

Advanced optical fibre gratings for nano-structural characterisation and biosensing applications

Abdulyezir Ayomipo Badmos

Doctor of Philosophy

Aston University

December 2016

© Abdulyezir Ayomipo Badmos, 2016

Abdulyezir Ayomipo Badmos asserts his moral right to be identified as the
author of this thesis

This copy of the thesis has been supplied on condition that anyone who consults it is understood to recognise that its copyright belongs to its author and that no quotation from the thesis and no information derived from it may be published without appropriate permission or acknowledgement.

Aston University

Advanced optical fibre gratings for nano-structural characterisation and biosensing applications

Abdulyezir Ayomipo Badmos
Doctor of Philosophy
December 2016

This thesis presents detailed investigation on the fabrication, spectral characterisation and applications of UV-inscribed optical fibre gratings devices. Of prominent significance is the characterisation of the optical fibre gratings devices with nanoparticles and biological recognition elements for novel developments in the field of optical biosensing.

A major contribution detailed in this thesis is the systematic study on fabrication, spectral characterisation and applications of different UV-inscribed in-fibre gratings. Specifically, uniform and apodized Fibre Bragg gratings (FBGs), normal and dual-peak long period fibre gratings (LPFGs), small-angle tilted fibre gratings (S-TFGs) and excessively tilted fibre gratings (Ex-TFGs) are presented. The holographic, phase-mask scanning and point-by-point methods are employed to fabricate these advanced optical fibre gratings using 244nm frequency-doubled Ar⁺ laser. Particular emphasis is laid on fabrication of dual-peak LPFGs in SMF-28 and thin-cladding single mode fibres of grating periods 140 μ m and 300 μ m respectively. Also, Ex-TFGs of different tilt angles are inscribed in single mode fibres using amplitude masks of different periods: 5.0 μ m, 6.6 μ m and 25 μ m.

Another important contribution from this study is the nano-structural characterisation of the in-fibre gratings with nanoparticles such as carbon nanotubes (CNT), zinc oxide (ZnO) and gold nanoparticles for power demodulation, sensitivity enhancement and polarisation dependent SPR excitation respectively. Refractive index (RI) sensors based on 81° Ex-TFGs with carbon nanotube (CNT) overlay deposition have been investigated. The CNT, a dark material, with high absorption of light and high RI is responsible for the power demodulation of the attenuation band while the 81°-TFG induces the wavelength shift as the surrounding medium RI changes. Results show high sensitivities of 557.29 nm/RIU and 95.54 dB/RIU for the wavelength shift and power demodulation respectively. Also, nano-deposition of zinc oxide (ZnO) on Ex-TFGs inscribed in two different fibre types has been investigated using dissimilar morphologies (direct ZnO overlay and PS-ZnO overlay) for enhanced RI sensing. Significant improvement in sensitivity of ~ 21% (~ 522 nm/RIU) is obtained. The polarisation dependence of Au-coated S-TFGs on excitation of surface plasmon resonance (SPR) has also been investigated.

Finally, the in-fibre gratings are surface-functionalized with bioreceptor elements such as enzymes (glucose oxidase) and antibody/antigen (Trx, IL-6). Enzyme functionalized biosensor based on dual-peak LPFG has been investigated for sugar concentration level and specific glucose detection and high sensitivities of ~4.67 nm/% and 12.21 \pm 0.19 nm/(mg/ml) are obtained respectively. Also, fibre optic biosensors based on antibody-functionalized 81°-TFGs have been presented for label-free specific recognition of interleukin-6 (IL-6) and thioredoxin (Trx) proteins. High saturation values ($\Delta\lambda_{\max}$) of 35.05nm and 33.19nm are obtained respectively. The specificity validation of the biosensors in the presence of other interfering proteins is investigated using human plasma and results show high specificity.

Key words: Optical fibre gratings, nano-structural functionalisation, optical biosensors, glucose detection, Interleukin-6, bioreceptor element, Thioredoxin.

Dedication

To Jeleelah, my darling and beloved wife,

And my lovely children...

...for their understanding and support!

Acknowledgements

Glory be to Allah, the Entirely Merciful, the Especially Merciful, without whom the successful completion of this programme is impossible. None of the favour of my Lord can I deny. I give all thanks and glory to Him for He is the Praiseworthy.

Thereafter, my profound gratitude goes to my supervisor, Prof Lin Zhang, who was extremely supportive throughout my research programme in Aston University. She patiently showed me how to tread the bumpy path of research and stood by me all along till the finish line. She is exceptionally awesome, I will forever be grateful to her.

My sincere gratitude goes to Dr Zhongyuan Sun, who taught me the fabrication of optical fibre gratings and guided me through many types of experimental measurements. Also, I will like to thank Dr Kaiming Zhou, Prof Qizhen Sun, Dr Zhijun Yan, Dr Petro Lutsyk, Prof Chengbo Mou, Dr Junxi Zhang, Dr Adenowo Gbadebo, Dr Guolu Yin, Changle Wang, Dr Sergey Sergeev and Dr Tom Allsop for their help and support throughout my study in Aston University.

Of much importance to my success in Aston University are the Academic Support Administrator, Mrs Helen Yard, who is always rendering her unflinching support whenever required; Research Student Administrator, Mrs Sandra Mosley and Mr Andrew Abbot, who is the 'heartbeat' of all Photonics Laboratories. I appreciate them for their contribution to my success both administratively and technically.

I will also like to acknowledge the collaboration with School of Life & Health Sciences, Aston University for their support and guidance on the biosensing experiments. Of much prominence is Dr Irudika Dias and her colleagues, I hereby acknowledge their immense contribution to the success of the biosensing (laboratory) experiments.

Finally, I will like to express my deepest gratitude to my parents who supported and encouraged me through thick and thin. I will also like to appreciate my family in Birmingham, Wale and Wunmi Badmos, a lovely couple that made my experience awesome. My gratitude also goes to my wife and children who are extremely supportive and understanding. They made my stay in the UK psychologically stable and gave me enough support to achieve greatness. I will forever adore them, especially my beautiful wife – Jeleelah. I also like to extend my profound gratitude to the Federal Government of Nigeria and the Management of Moshood Abiola Polytechnic, Abeokuta for the opportunity availed me to undergo my research programme in Aston University, UK.

Contents

Summary	2
Acknowledgements	4
Acronyms	9
List of Figures	11
List of Tables	18
Chapter 1. Introduction and Thesis structure	19
1.1 Introduction	19
1.2 Structure of thesis	22
References	24
Chapter 2. Review: historical background, photosensitivity, grating theory and fabrication techniques	26
2.1 Historical Background	26
2.2 Photosensitivity of optical fibre	30
2.2.1 Photosensitivity mechanism	30
2.2.2 Photosensitisation techniques	32
2.2.2.1 Colour centre model.....	32
2.2.2.2 Densification-compaction model.....	34
2.2.2.3 Stress relief model	34
2.2.3 Photosensitivity enhancement techniques	35
2.2.3.1 Hydrogen loading technique.....	35
2.2.3.2 Co-doping technique	36
2.2.3.3 Flame brushing technique	36
2.3 Couple mode theory	37
2.3.1 Backward Mode Coupling	39
2.3.2 Forward Mode Coupling	40
2.4 Phase matching conditions	42
2.4.1 Fibre Bragg grating (FBG)	45
2.4.2 Long period fibre grating (LPFG)	45
2.4.3 Tilted fibre gratings (TFGs)	46
2.5 Optical fibre grating fabrication techniques	48
2.5.1 Two-beam holographic inscription technique	48
2.5.2 Point-by-point inscription technique	50

2.5.3	Phase mask scanning technique	51
2.4	Chapter summary	53
	References	54
Chapter 3. Advanced optical fibre gratings: fabrication, spectral characteristics and sensing measurements		
3.1	Introduction	60
3.2	FBGs inscription and sensing characteristics	62
3.2.1	Using two-beam holographic technique	62
3.2.2	Using phase-mask scanning technique	66
3.2.3	Fabrication of (Gaussian) apodized Bragg gratings	68
3.2.4	FBG sensing characteristics	70
3.3	LPFGs inscription and sensing characteristic.....	75
3.3.1	Dual-peak LPFGs	78
3.3.2	LPFG thermal and SRI sensing characteristics	81
3.4	STFGs inscription and sensing characteristics	89
3.4.1	Fabrication of STFGs	89
3.4.2	Tilt angles inside and outside the fibre core	91
3.4.3	STFG SRI sensing characteristics	94
3.5	Ex-TFGs inscription and sensing characteristics	98
3.5.1	Fabrication and characterisation of Ex-TFGs	99
3.5.2	Sensitivity characteristics of Ex-TFGs	103
3.5.2.1	Thermal sensitivity of Ex-TFGs	104
3.5.2.2	SRI sensitivity of Ex-TFGs	107
3.5.2.3	Bend sensitivity of Ex-TFGs	110
3.6	Chapter conclusion	114
	References	116
Chapter 4. In-fibre grating based refractive index sensors with nanoparticle deposition.....		
4.1	Introduction	119
4.2	Refractive index (RI) sensors based on 81 ^o Ex-TFGs with carbon nanotube (CNT) deposition.....	120
4.2.1	RI sensor fabrication	120
4.2.2	Working Principle	122
4.2.3	Experimental setup	124
4.2.4	Results and discussion	125

4.2.5	Conclusion	127
4.3	Nano-deposition of zinc oxide (ZnO) on Ex-TFGs using discrete morphologies for enhanced RI sensing	128
4.3.1	Fabrication of 80° Ex-TFGs	129
4.3.2	Nanodeposition of ZnO on 80° Ex-TFGs	130
4.3.3	Experimental setup	134
4.3.4	Results and discussion	135
4.3.5	Conclusion	139
4.4	Plasmon-enhanced optical sensor based on gold-coated S-TFGs	140
4.4.1	Fabrication of plasmon-excited S-TFG sensor	140
4.4.2	Sensing principle	143
4.4.3	Results and discussion	144
4.4.4	Conclusion	146
4.5	Chapter conclusion	147
	References	148
 Chapter 5. In-fibre grating based biosensors for pathogen detection		152
5.1	Introduction	152
5.2	Enzyme-functionalized biosensor based on single mode 80µm-cladding dual-peak LPFG for glucose detection	153
5.2.1	Introduction	153
5.2.2	LPFG inscription and spectral characteristics	154
5.2.3	Enzyme functionalization of LPFG surface	156
5.2.4	Experimental setup for RI, sugar solution and glucose detection	159
5.2.5	Results and discussion	159
5.2.5.1	RI and sugar level detection measurements.....	159
5.2.5.2	Glucose detection with enzyme-functionalized dual-peak LPFG .	161
5.2.6	Conclusion.....	163
5.3	Label-free biosensor based on Trx-antibody immobilized 81°-TFG in 80µm-cladding B/Ge co-doped optical fibre for high-specific (Trx) detection	164
5.3.1	Introduction	164
5.3.2	Materials and methods	165
5.3.2.1	Ex-TFG inscription and antibody immobilization	165
5.3.2.2	Trx antigen-antibody interaction on fibre surface	166
5.3.3	Results and discussion	167
5.3.4	Conclusion	172
5.4	Fibre optic biosensor based on antibody-functionalized 81°-TFG for label-free specific recognition of interleukin-6 (IL-6) protein	173

5.4.1	Introduction	173
5.4.2	Materials and methods	174
5.4.2.1	Fabrication of the IL-6 immobilized 81 ^o -TFG biosensor	174
5.4.2.2	Chemical interaction on the surface-modified 81 ^o -TFG	175
5.4.3	Results and discussion	176
5.4.4	Conclusion	179
5.5	Chapter conclusion	180
	References	181
 Chapter 6. Conclusion and Future research		187
6.1	Conclusion	187
6.2	Future research	191
6.2.1	Label-free biosensor based on Ex-TFG in thin-core modal interferometer	191
6.2.2	Affinity surface plasmon resonance (SPR) biosensor	193
6.2.3	Bacteriophage-functionalized Ex-TFG biosensor for specific E-coli Detection	195
	References	197
	Publications	199

Acronyms

AFM	Atomic force microscope
APTES	(3-Aminopropyl) triethoxysilane
AuNPs	Gold Nanoparticles
BBS	Broadband source
B-Ge	Boron-germanium
CNT	Carbon nanotube
CW	Continuous wave
DI	deionized
DID	Drawing induced defects
DNA	Deoxyribonucleic acid
ELISA	Enzyme-linked immunosorbent assay
EMI	Electromagnetic interference
Ex-TFG	Excessively tilted fibre grating
FBG	Fibre Bragg grating
FBS	Fetal bovine serum
FWHM	Full width at half maximum
GEC	Germanium electron centre
GODC	Germanium oxygen-deficient centre
HE	Hybrid mode waves
IL-6	Interleukin-6
IR	Infrared ray
LPFG	Long period fibre grating
LP	Linear polarisation
LPMM	Length per millimetre
MZI	Mach-Zehnder interferometer
NADPH	Nicotinamide adenine dinucleotide phosphate
NBOHC	Non-bridging oxygen hole centre
NIR	Near infrared ray
NMP	N-Methyl-2-pyrrolidone
NMR	Nuclear magnetic resonance
NOV	Neutral oxygen vacancy
OH	Hydroxyl
OSA	Optical spectrum analyser
PBS	Phosphate buffered saline
PC	Polarisation controller
PDDA	Polydiallyldimethyl ammonium chloride
PM	Phase mask
PMC	Phase matching condition
P-OHC	Peroxy oxygen hole centre
PS	Polystyrene spheres
PSAM	Pilot symbol assisted modulation
PSS	Polyanion styrenesulfonate sodium salt
PVP	Polyvinyl pyrrolidone
PZT	Piezo-electric transducer
RFI	Radio frequency interference
RI	Refractive index
RIU	Refractive index unit
RPM	Revolution per minute
SA	Sodium acetate
SE	Standard error
SMF	Single mode fibre

SPP	Surface plasmon polariton
SPR	Surface plasmon resonance
SPW	Surface plasmon wave
SRI	Surrounding refractive index
STFG	Small-angle tilted fibre grating
STH	Self-trapped hole
TCSMF	Thin-core single mode fibre
TE	Transverse electric
TEM	Transmission electron microscope
TFG	Tilted fibre grating
TM	Transverse Magnetic
TNF- α	Tumor necrosis factor alpha
Trp-28	Tryptophan residues-28
Trx	Thioredoxin
TrxR	Thioredoxin reductase
UV	Ultra violet
WDM	Wavelength division multiplexer
ZnO	Zinc oxide

List of figures

Figure 2.1	Schematic of different point defects in germanium-doped silica (optical fibre).....	31
Figure 2.2	Photochemical reaction paths (a) single-photon process and (b) two-photon process.....	33
Figure 2.3	Schematics of optical fibre grating types and their phase matching conditions: (a) FBG; (b) LPFG; (c) TFG (at $\theta < 23.1^\circ$); (d) TFG (at $\theta = 45^\circ$); (e) TFG (at $\theta > 66.9^\circ$).....	44
Figure 2.4	Schematic of mode-coupling of Fibre Bragg Grating (FBG).....	45
Figure 2.5	Schematic of mode-coupling of Long Period Grating (LPFG).....	46
Figure 2.6	Schematic diagram of Tilted grating in fibre core.....	46
Figure 2.7	Schematic of mode-coupling of TFGs at different coupling angles	47
Figure 2.8	Schematic of optical setup of two-beam holographic inscription technique.....	49
Figure 2.9	Point-by-Point Inscription Technique; (a) optical setup; (b) Schematic diagram.....	51
Figure 2.10	Phase Mask Scanning Technique: schematic of UV diffraction beams by Phase Mask.....	52
Figure 3.1	Schematic diagram of optical setup for adjusting the Bragg wavelength in the holographic inscription technique.....	62
Figure 3.2	Typical transmission spectra of uniform-period Bragg gratings fabricated using two-beam holographic technique at wavelengths: (a) $\sim 2\mu\text{m}$; (b) $\sim 1550\text{nm}$; (c) $\sim 1310\text{nm}$; (d) $\sim 837\text{nm}$	63
Figure 3.3	Transmission spectra of uniform-period Bragg gratings fabricated using two-beam holographic technique showing different %Reflectance at wavelength $\sim 1454\text{ nm}$ (a) 4% (b) 20% (c) 50% (d) 90%.....	64
Figure 3.4	Plots of peak reflectance against exposure time with UV-power intensity set at 125mW: (a) FBGs at first trial; inset: residual plot (b) FBGs at second trial; inset: residual plot.....	66
Figure 3.5	UV diffraction pattern as taken during experiment (a) phase mask and (b) phase mask placed in near-contact to optical fibre.....	66
Figure 3.6	(a) Schematic of multi-wavelength phase-mask structure; (b) Transmission spectra of FBGs fabricated with multi-wavelength phase mask.....	67

Figure 3.7	Reflection spectrum of un-apodized Bragg grating showing side-lobes.....	69
Figure 3.8	Transmission and reflection spectra of Gaussian apodized Bragg gratings with centre wavelengths at (a) ~1544nm (b) ~1547nm (c) ~1552nm (d) ~1554nm.....	69
Figure 3.9	Experimental setup for FBG thermal characterisation.....	70
Figure 3.10	FBG thermal response at wavelengths (a) ~1310nm (80° - 0°C) and (b) ~1310nm (0° - 80°C); Insets: regular residual plots of each linear fit.....	71
Figure 3.11	(a) Transmission spectrum of FBG at ~1551nm showing spectra evolution to thermal variation; FBG thermal response at; (b) ~1535nm (c) ~1543nm (d) ~1551nm (e) ~1567nm. Insets: regular residual plots of each linear fit.....	72
Figure 3.12	Experimental setup for FBG strain characterisation.....	73
Figure 3.13	FBG strain response at: (a) ~1310nm and (b) ~1550nm. Insets: regular residual plots of each linear fit.....	74
Figure 3.14	Transmission spectra of LPFG ($\Lambda = 350\mu\text{m}$) before and after annealing. Inset: near mode field image as observed by near-infrared camera.....	76
Figure 3.15	Transmission spectra of LPFG ($\Lambda = 400\mu\text{m}$) with increasing UV exposure: (a) L = 5mm, (b) L = 10mm, (c) L = 12mm and (d) L = 15mm.....	78
Figure 3.16	Transmission spectra of LPFG ($\Lambda = 140\mu\text{m}$) measured during UV inscription: dual resonance peak (dashed line) were observed to coalesce in a single peak (solid line).....	79
Figure 3.17	(a) The simulation results of 80 μm diameter cladding size fibre with 4.8 μm core size; (b) Transmission spectra of UV-inscribed LPFGs ($\Lambda = 300\mu\text{m}$) in B/Ge co-doped thin cladding fibre: dual resonant peaks observed: trial 1; (c) trial 2.....	80
Figure 3.18	Transmission spectra of LPFGs measured during UV inscription in B/Ge co-doped thin-cladding fibre with period of (a) ($\Lambda = 250\mu\text{m}$) (b) ($\Lambda = 200\mu\text{m}$).....	81
Figure 3.19	Experimental setup for measuring thermal sensing of LPFGs.....	82
Figure 3.20	Experimental setup for measuring surrounding refractive index sensing of LPFGs.....	83
Figure 3.21	(a) Transmission spectra evolution of LPFG ($\Lambda = 140\mu\text{m}$) in response to SRI variation (b) Plots of wavelength shift of the dual peaks against surrounding refractive index variation.....	84

Figure 3.22	(a) Transmission spectra evolution of a dual peak LPFG ($\Lambda = 300\mu\text{m}$) in response to SRI variation (b) Plots of wavelength shift of the dual peaks against surrounding refractive index variation and (c) Plots of wavelength shift against temperature.....	85
Figure 3.23	(a) Plots of wavelength shift against surrounding refractive index variation (b) Plots of wavelength shift against temperature.....	86
Figure 3.24	(a) Transmission spectra evolution of LPFG ($\Lambda = 200\mu\text{m}$) in response to SRI variation (LP07) (b) Plots of wavelength shift against surrounding refractive index variation (c) Transmission spectra evolution of LPFG ($\Lambda = 200\mu\text{m}$) in response to thermal variation (LP08) (d) Plots of wavelength shift against temperature	88
Figure 3.25	Schematic of tilted fibre gratings by holographic technique.....	89
Figure 3.26	Schematic of tilted fibre gratings by scanning phase mask configurations: (a) tilt a normal FBG phase mask with the fibre fixed perpendicular to incident UV-beam (b) inscribe using phase mask with tilted diffraction patterns (c) tilt both fibre and phase mask at an angle θ to the incident UV-beam axis.....	90
Figure 3.27	Schematic of fringes distortion induced by tilted angle within (θ_{int}) and outside (θ_{ext}) the fibre core.....	91
Figure 3.28	Optical micro-image of the small-angle tilted grating (STFGs) structures UV-inscribed in SMF-28: (a) 5 degrees, (b) 8 degrees and (c) 10 degrees.....	92
Figure 3.29	Transmission spectra of STFGs (a) 5 degrees in SMF-800 (b) 5 degrees in SMF-28 (c) 8 degrees in SMF-28 (c) 10 degrees in SMF-28.....	93
Figure 3.30	Transmission spectra evolution of STFGs to SRI variations (a) 5° (c) 8° (e) 10° ; Plots of normalised area against SRI variation (b) 5° (d) 8° (f) 10° . Insets: randomly chosen enveloped area.....	95
Figure 3.31	(a) Transmission spectrum of STFGs at close range (12th -17th order cladding modes), (b) Spectra evolution of STFG in response to SRI variation and (c) Plots of wavelength shift against SRI variation.....	97
Figure 3.32	Schematic and vector phase matching diagram of Ex-TFGs.....	99
Figure 3.33	Schematic of tilted amplitude mask in close proximity to the optical fibre (a) front view (b) aerial view showing the zeroth order diffraction.....	100
Figure 3.34	Micro-images of Ex-TFGs inscribed in SMF-28 fibre with internal tilt angles at: (a) 75° (150 LPMM) (b) 79° (150 LPMM) (c) 81° (200 LPMM) (d) 83° (200 LPMM).....	101
Figure 3.35	Transmission spectra of 81° Ex-TFGs inscribed using amplitude masks of different periods: (a) $5\mu\text{m}$ (200 LPMM) (b) $6.6\mu\text{m}$ (150 LPMM) (c) $25\mu\text{m}$ (40 LPMM).....	102

Figure 3.36	Experimental setup for evaluating the thermal sensitivity of Ex-TFGs.....	104
Figure 3.37	(a) Zoomed transmission spectra of 83° Ex-TFG when launched with orthogonally polarised light (black line – TE; red line - TM); (b) Plots of wavelength shift against thermal variation for 83° Ex-TFG; (c) Plots of wavelength shift against thermal variation for 81° Ex-TFG (at ~ 1334nm and ~1554nm) and (d) Transmission spectra evolution of 81° Ex-TFG (TM - ~1550 nm) in response to thermal variation.....	105
Figure 3.38	(a) Transmission spectra evolution of 81° Ex-TFG (fabricated in B/Ge co-doped 80µm fibre with $\Lambda_{AM} = 25\mu\text{m}$) in response to thermal variation and (b) Plots of its wavelength shift against thermal variation showing linear correlation.....	106
Figure 3.39	Experimental setup for evaluating the SRI sensitivity of Ex-TFGs	107
Figure 3.40	(a) Plots of wavelength shift against SRI variation for 81° Ex-TFG (at ~ 1334nm and ~1554nm) and (b) Plots of wavelength shift against SRI variation for 75° Ex-TFG.....	108
Figure 3.41	(a) Transmission spectra evolution of 81° Ex-TFG (fabricated in B/Ge co-doped 80µm fibre with $\Lambda_{AM} = 25\mu\text{m}$) in response to SRI variation; (b) Plots of its wavelength shift against SRI variation; (c) Transmission spectra evolution of 83° Ex-TFG (fabricated in B/Ge co-doped 80µm fibre with $\Lambda_{AM} = 5\mu\text{m}$) in response to SRI variation and (d) Plots of its wavelength shift against SRI variation.....	109
Figure 3.42	(a) Experimental setup for bend sensing and (b) Schematic diagram of the four-point bend system with $a = 120\text{mm}$, $b = 40\text{mm}$, and bend depth, $h = 0 \sim 12.5\text{mm}$	110
Figure 3.43	Plot of curvature against bend depth using four-point bending system.....	112
Figure 3.44	(a) Transmission spectra evolution of 81° Ex-TFG ($\Lambda_{AM} = 6.6\mu\text{m}$) in response to bending (b) Plots of wavelength shift (nm) against curvature (1/m) (c) Transmission spectra evolution of 81° Ex-TFG ($\Lambda_{AM} = 25\mu\text{m}$) in response to bending (d) Plots of wavelength shift (nm) against curvature (1/m), inset: regression fitting analysis.....	112
Figure 4.1	Experimental setup for the CNT preparation.....	121
Figure 4.2	Schematic diagram of the CNT-coated 81° Ex-TFG RI sensor.....	123
Figure 4.3	Experimental setup of RI sensing of the CNT-coated 81°-TFG RI sensor.....	124
Figure 4.4	Transmission spectra evolution in response to SRI variation (a) bare 81°-TFG (b) CNT-coated 81°-TFG.....	126

Figure 4.5	(a) Plot of wavelength shift against SRI variation (81°-TFG, 'Sample 1') (b) Plot of wavelength shift against SRI variation (81°-TFG, 'Sample 2') (c) Plot of intensity variation against change in SRI (81°-TFG, 'Sample 1') (d) Plot of intensity variation against change in SRI (81°-TFG, 'Sample 2').....	127
Figure 4.6	Transmission Spectrum of 80° Ex-TFG with an unpolarised probe light source spanning from 1280 ~1680 nm. (Inset: zoomed spectra at ~ 1550 nm showing X- and Y-polarisation and unpolarised light).....	128
Figure 4.7	Transmittance and absorbance spectra of zinc oxide (ZnO) film....	131
Figure 4.8	Schematic of Ex-TFG structure with direct ZnO deposition on the fibre cladding (Morphology 1).....	131
Figure 4.9	Schematic of template-directed synthesis of ordered porous ZnO films (Morphology 2): (a) PS array template overlay, (b) deposition of porous ZnO, and (c) PS removal and formation of ZnO in the interstices of PS particles.....	133
Figure 4.10	Micrographs of 80° Ex-TFG: (a) bare fibre showing the excessively tilted fringes, (b) direct ZnO deposition (Morphology 1), and (c) ZnO in the interstices of PS array template (Morphology 2).....	134
Figure 4.11	(a) Spectra wavelength shift after PS-ZnO coating (in Air); (b) Spectra wavelength shift after ZnO coating (in Air); (c) Transmission Spectra evolution of 80° Ex-TFG to surrounding media of different refractive indices after PS-ZnO coating (Sample A); and (d) Transmission Spectra evolution of 80° Ex-TFG to surrounding media of different refractive indices after ZnO coating (Sample B).....	135
Figure 4.12	Plots of resonant wavelength shift of 80° Ex-TFGs (in SM-28 fibres) against SRI variation (Sample A): (a) X-polarisation before and after coating (Morphology 1); (b) Y-polarisation before and after coating (Morphology 1); (c) X-polarisation before and after coating (Morphology 2); and (d) Y-polarisation before and after coating (Morphology 2).....	137
Figure 4.13	Plots of resonant wavelength shift of 80°Ex-TFGs (in thin-cladding B/Ge doped fibres) against SRI variation (Sample B): (a) X-polarisation before and after coating (Morphology 1); (b) Y-polarisation before and after coating (Morphology 1); (c) X-polarisation before and after coating (Morphology 2); and (d) Y-polarisation before and after coating (Morphology 2).....	138
Figure 4.14	Transmission spectrum of the gold-coated 6°-TFG in air.....	141
Figure 4.15	Schematic of template-directed synthesis of ordered gold-film deposition: (a) PS array template overlay and (b) Gold-film coating on PS template.....	142
Figure 4.16	Transmission spectra of Au-coated 6°-TFG excited with (a) P-polarised light and (b) S-polarised light.....	144

Figure 4.17	Transmission spectra of Au-coated 6 ^o -TFG showing red-shift of the SPR as SRI changes (a) ns = 1.360 (b) ns = 1.380 (c) ns = 1.404 (d) ns = 1.412.....	145
Figure 4.18	Plots of SPR wavelength shift of 6 ^o -TFG against SRI variation; inset: regular residue plot.....	145
Figure 5.1	Enzyme functionalization of LPFG surface.....	156
Figure 5.2	Enzyme functionalization of LPFG surface: (a) Cleaning process (b) Silanization process and (c) Glucose-oxidase immobilization	157
Figure 5.3	Optical microscopic images of: (a) cleaned fibre, (b) silanized fibre, (c) enzyme-functionalized fibre observed under transmitted light, and (d) enzyme's (fluorescent) presence on fibre surface.....	158
Figure 5.4	Plots of resonant wavelength shift against surrounding medium RI variation of the 300 μ m period dual-peak LPFG in thin cladding fibre.....	159
Figure 5.5	(a) Transmission spectral evolution of 80 μ m-cladding dual-peak LPFG to varying concentration of turbinado sugar solution; (b) Plot of resonant wavelength shift of Peak 1 and Peak 2 against sugar solution.....	161
Figure 5.6	(a) Transmission spectral evolution of Peak 1 (of the dual-peak LPFG) to varying concentration of SA Buffer/D-(+)-Glucose solution at different concentration (inset: glucose solution (0.1 – 3.2 mg/ml)) and (b) Plots of resonant wavelength shift of the dual-peak LPFG against glucose concentration (inset: regular residual of Peak 2).....	162
Figure 5.7	Spectra wavelength shift after immobilization of Thioredoxin (Trx) antibody on fibre surface.....	166
Figure 5.8	Schematic of Thioredoxin (Trx) antigen-antibody reaction on fibre surface.....	167
Figure 5.9	Transmission spectra evolution of the 81 ^o -TFG biosensor in response to Thioredoxin (Trx) antigen-antibody interaction; red-shift from reference as sample concentration increases.....	168
Figure 5.10	Plot of resonant wavelength shift against variation in Thioredoxin-antigen solution concentration (1.50 – 25 ng/ml).....	169
Figure 5.11	Plot of resonant wavelength shift against variation in Thioredoxin-antigen solution concentration (0.07 – 2.5 ng/ml).....	170
Figure 5.12	(a) Spectra evolution of the 81 ^o -TFG biosensor in response to plasma concentrations, and (b) Plot of resonant wavelength shift of Trx-immobilized 81 ^o -TFG biosensor against variation in human plasma solution of different concentrations: (0.0625 – 1.0 mg/ml)	172
Figure 5.13	Spectra wavelength shift after immobilization of Interleukin-6 (IL-6) antibody on fibre surface.....	174

Figure 5.14	Schematic of Interleukin-6 (IL-6) antigen-antibody reaction on fibre surface.....	175
Figure 5.15	Transmission spectra evolution of the 81 ^o -TFG biosensor in response to Interleukin (IL-6) antigen-antibody interaction; red-shift from reference as sample concentration increases.....	176
Figure 5.16	Plot of resonant wavelength shift against variation in IL-6 antigen solution concentration (0.375 pg/ml – 25 pg/ml), (Inset: regular residual plot).....	177
Figure 5.17	Plot of resonant wavelength shift against variation in IL-6 antigen solution concentration (0.015 pg/ml – 2.5 pg/ml).....	178
Figure 5.18	Plot of resonant wavelength shift of IL-6 immobilized 81 ^o -TFG biosensor against variation in human plasma solution of different concentrations (0.0625 – 1.0 mg/ml).....	178
Figure 6.1	Schematic diagram of optical fibre sensor with a TCSMF sandwiched between two SMFs.....	191
Figure 6.2	Schematic of optical fibre undergoing PSAM deposition.....	192
Figure 6.3	Schematic diagram depicting principle of SPR biosensing.....	193
Figure 6.4	Schematic of SPR probing: (a) bio-molecular interaction occurring within a short distance from metal surface, (b) bio-molecular interaction occurring within the whole extent of the field of a SPW...	194
Figure 6.5	Hybrid fibre grating and plasmonic structure biosensor.....	194
Figure 6.6	Schematic of experimental procedure for covalent binding of T4 bacteriophage on Ex-TFGs samples for E. coli bacteria detection	196

List of tables

Table 3.1	Bragg gratings of different reflectance fabricated using two-beam holographic inscription technique.....	65
Table 3.2	Experimental results of LPFG ($\Lambda = 250\mu\text{m}$ and $200\mu\text{m}$) response to SRI variations.....	87
Table 3.3	Experimental results of STFG response to SRI variations (12th – 17th order cladding mode).....	97
Table 3.4	Amplitude masks and optical fibre grating parameters.....	101

Introduction and Thesis structure

1.1 Introduction

The emergence of optical fibre brought about an era of technological revolution with a variety of application devices developed in the field of optical communication and optical sensing. Basically, optical fibre works by the principles of total internal reflection guiding light rays through the core of the fibre with minimal loss to the surrounding. Since signals are transmitted as light instead of electric current, optical fibre is immune to both electromagnetic interference (EMI) and radio frequency interference (RFI) with advantages of light weight, low insertion loss and high temperature tolerance. Moreover, the discovery of the photosensitivity characteristic of optical fibres have further revolutionized their telecommunication and sensing applications [1].

Photosensitivity in optical fibre generally refers to sensitivity to electromagnetic radiation, usually light. This phenomenon is manifested by light-induced refractive index changes providing a practical method for inscribing gratings in the core of the glass fibre which are predominantly used in telecommunication and optical sensing. Photosensitivity has been a major factor since it was first discovered in germanium-silica (Ge-doped) fibres [2] and researchers have developed various methods of enhancing the photosensitivity of fibres.

Low-temperature hydrogen loading of germane-silicate fibres at high pressure [3] is the most commonly used technique for enhancing photosensitivity in optic fibre and it is widely used to enhance grating inscription in optic fibre. Over the last few decades,

persistent research has led to three main fabrication methods: holographic inscription [4], phase mask scanning [5-7] and point-by-point technique [8]. Also, optical fibre gratings have been broadly classified into three categories: fibre Bragg gratings (FBGs) [2], long period fibre gratings (LPFGs) [9] and tilted fibre gratings (TFGs) [10, 11].

Fibre Bragg gratings (FBGs), whose periods are usually much less than one micrometre, are a series of distributed Bragg reflectors constructed in an optical fibre that reflect particular light wavelengths and transmit all other wavelengths. FBGs are based on forward to backward core mode coupling and characterised by wavelength selective reflection function in form of filtering. Contrary to the contra-directional coupling in FBGs, LPFGs with periods of hundreds of micrometres induce co-directional coupling in an optical fibre where the guided mode is coupled to the cladding modes and are characterised by loss filtering function.

TFGs are fabricated by tilting the grating planes relative to the perpendicular of the fibre axis and their characteristics depend on the angle of tilt which can either be small (S-TFG) or large (Ex-TFG). S-TFGs are characterised by strong enhancement of the cladding mode resonances at the expense of the Bragg resonance spreading through the transmission window which ensure backward coupling of the guided core mode to the cladding modes. Meanwhile, Ex-TFGs are excessively tilted fringes inscribed in the fibre core which couple the guided core mode to forward-propagating higher order cladding modes with optical polarisation properties. Considering the different mode coupling mechanism, tilted grating structures can offer different but desirable device functions for many in-fibre systems thereby finding applications in laser systems and optical sensing [12].

In recently years, optical fibre gratings are becoming increasingly attractive for biochemical and bio-sensing applications. This is because they offer high-performance alternative to conventional technologies, either for measuring a variety of physical parameters or for performing high-sensitivity bio-chemical analysis. Optical fibre-based biosensors offer label-free platforms for bioreceptor element and conduits for excitation light. They have inherent selectivity for specific analyte and are classified according to the bioreceptor element employed for sensing.

Previous researches have reported couple of bioreceptor-based optical biosensors to monitor analyte-receptor interactions which majorly include enzyme-based optical biosensors [13-15], antibody/antigen optical biosensors [16], DNA biosensors based on optical fibre gratings [17-19], and biomimetic-receptor optical biosensors [20]. Also, various optical fibre grating modifications have brought about unique features in bio-

sensing such as micro fibre Bragg gratings (mFBGs) [21], long period fibre gratings (LPFGs) [18, 22], tilted fibre gratings (TFGs) [12, 14], LPFGs in photonic crystal fibres [23], and surface plasmon resonance (SPR) [24].

The ever increasing demand for biochemical/bio-sensing platforms with unique features of label free, real time, selectivity, specificity and in-situ detection have given optical fibre grating biosensors significant analytical roles in medical diagnosis, food processing, life science and environmental monitoring. The demand for these high function optical fibre grating biosensors coupled with their wide range of applications are the motivation of this thesis.

1.2 Thesis structure

Basically, this thesis describes the significant contribution of optical fibre gratings to biochemical and bio-sensing applications. It consists of six chapters and the detailed contents of each chapter are as listed:

Chapter 1 briefly introduces the thesis contents and laid out the structure of the thesis for easy navigation.

Chapter 2 encompasses the study of literature review on UV photosensitivity of silica glass fibres which prompted the emergence of optical fibre grating. It delves deep into the history and development of fibre grating technologies with brief explanations on the three different fabrication techniques for fibre grating inscription. It also presents the theoretical principles behind the mode coupling mechanisms, emphasizing on the phase matching conditions for each grating type.

Chapter 3 will present the research outcomes on the fabrication and optical characterisation of different types of advanced optical fibre gratings employing the existing facilities available in Aston University. It will begin with the fabrication of FBGs with different central wavelengths spanning across 800nm to beyond 2 μ m using two different inscription techniques: two-beam holographic and phase mask scanning. Also, Gaussian apodized FBGs will be presented and the response of FBGs to thermal and strain perturbations will be verified. The second session of this chapter will address the fabrication of LPFGs with particular emphasis on the characteristics of LPFGs with periods near dispersion turning points and explore their sensing characteristics. While the third session will explain in details the fabrication and sensing characteristics of small angle tilted gratings (S-TFGs), the fourth session will focus on experimental investigation of Ex-TFGs with different tilt angles and their response to temperature, bending and surrounding refractive index (SRI) sensing.

Chapter 4 will discuss the significant contribution to the analysis and nano-characterisation of in-fibre grating based refractive index (RI) sensors. It will present the detailed investigation of the effect of nanoparticle-coated (specifically carbon nanotube and zinc oxide) optical fibre gratings on their spectral characteristics and response to external perturbations. It will also present Au-coated S-TFGs excited plasmon sensor for observable SPR signature and employed for SRI sensing.

Chapter 5 intends exploring the bio-sensing applications of optic fibre gratings using different bio reception elements. The first section will present enzyme functionalized biosensor based on single mode, thin cladding dual-peak LPFG for sugar level and

specific glucose detection. The two other sessions intend presenting novel investigation on level-detection of specific antibody/antigens; thioredoxin (Trx) and interleukin-6 (IL-6) which are essential proteins in human body.

Chapter 6 will present the overall thesis conclusion and proffer suggestions for imminent future research.

References

- [1] K.O. Hill, G. Meltz, "Fibre Bragg technology fundamentals and overview", *Journal of Lightwave Technology*, vol. 15(8), pp. 1263-1276, 1997.
- [2] K.O. Hill, Y. Fujii, D. C. Johnson and B. S. Kawasaki, "Photosensitivity in optical fibre waveguides: Application to reflection filter fabrication", *Applied Physics Letters*, vol. 32, pp. 647-649, 1978.
- [3] P.J. Lemaire, R. M. Atkins, V. Mizrahi and W. A. Reed, "High pressure H₂ loading as a technique for achieving ultrahigh UV photosensitivity and thermal sensitivity in GeO₂ doped optical fibres", *Electronics Letters*, vol. 29(13), pp. 1191-1193, 1993.
- [4] G. Meltz, W. W. Morey, and W. H. Glenn, "In-fibre Bragg grating tap in Optical Fibre Communication," San Francisco, California, USA: *Optical Society of America Technical Digest series 1*, vol. TuG1, 1990.
- [5] D. Z. Anderson, V. Mizrahi, T. Erdogan and A. E. White, "Production of in-fibre gratings using a diffractive optical element," *Electronics Letters*, vol. 29(6), pp. 566-568, 1993.
- [6] J. R. Armitage, "Fibre Bragg reflectors written at 262nm using a frequency quadrupled diode-pumped Nd³⁺: YLF laser " *Electronics Letters*, vol. 29(13), pp. 1181-1183, 1993.
- [7] B. Malo , K. O. Hill, F. Bilodeau, D. C. Johnson, and J. Albert, "Bragging gratings fabricated in mono-mode photosensitive optical fibre by UV exposure through a phase mask," *Appl. Phys. Lett.*, vol. 62, pp. 1035-1037, 1993.
- [8] B. Malo, K. O. Hill, F. Bilodeau, D. C. Johnson and J. Albert, "Point-by-Point Fabrication of Micro-Bragg Gratings in Photosensitive Fibre Using Single Excimer Pulse Refractive-Index Modification Techniques," *Electronics Letters*, vol. 29(18), pp. 1668-1669, 1993.
- [9] A. M. Vengsarkar, P. J. Lemaire, J. B. Judkins, V. Bhatia, T. Erdogan and J. E. Sipe, "Long-period fibre gratings as band-rejection filters," *Journal of Lightwave Technology*, vol. 14(1), pp. 58-65, 1996.
- [10] T. Erdogan, and J. E. Sipe, "Tilted fibre phase gratings," *J. Opt. Soc. Am. A*, vol. 13, pp. 296-313, 1996.
- [11] K. Zhou, L. Zhang, X. Chen, I. Bennion, "Low thermal sensitivity grating devices based on Ex-45° tilting structure capable of forward-propagating cladding modes coupling," *Journal of Lightwave technology*, vol. 24, pp. 5087-5094, 2006.
- [12] J. Albert, L.-Y. Shao, C. Caucheteur, "Tilted fibre Bragg grating sensors," *Laser & Photonics Reviews*, vol. 7, pp. 83-108, 2012.
- [13] J. H. Kim, S. Y. Lim, D. H. Nam, J. Ryu, S. H. Ku, C. B. Park, "Self-assembled, photoluminescent peptide hydrogel as a versatile platform for enzyme-based optical biosensors," *Biosens. Bioelectron.* vol. 26(5), pp. 1860-1865, 2011.

- [14] B. Luo, Z. Yan, Z. Sun, J. Li, L. Zhang, "Novel glucose sensor based on enzyme-immobilized 81° tilted fibre grating," *Optical Express*, vol. 22(25), 2014 DOI:10.1364/OE.22.030571
- [15] A. Deep, U. Tiwari, P. Kumar, V. Mishra, S. C. Jain, N. Singh, P. Kapur, L. M. Bharadwaj, "Immobilization of enzyme on long period grating fibres for sensitive glucose detection," *Biosens. Bioelectron.* vol. 33, 190-195, 2012.
- [16] M. P. DeLisa, Z. Zhang, M. Shiloach, S. Pilevar, C. C. Davis, J. S. Sirkis, W. E. Bentley, "Evanescent wave long-period fibre Bragg grating as an immobilized antibody biosensor," *Anal. Chem.* vol. 72(13), 2895-2900, 2000.
- [17] H. S. Jang, K. N. Park, J. P. Kim, S. J. Sim, O. J. Kwon, "Sensitive DNA biosensor based on a long-period grating formed on the side-polished fibre surface," *Opt. Express* vol. 17, 3855-3860, 2009.
- [18] X. Chen, L. Zhang, K. Zhou, E. Davies, K. Sugden, "Real-time detection of DNA interactions with long-period fibre-grating-based biosensor," *Opt. Lett.* vol. 32, 2541-2543, 2007.
- [19] H. M. R. Goncaives, L. Moreira, L. Pereira, P. Jorge, C. Gouveia, P. Martins-Lopes, J. R. A. Fernandes, "Biosensor for label-free DNA quantification based on functionalized LPGs," *Biosens. Bioelectron.* vol. 84, 30-36, 2015.
- [20] R. T. Piervincenzi, W. M. Reichert, H. W. Hellinga, "Genetic engineering of a single-chain antibody fragment for surface immobilization in an optical biosensor," *Biosens. Bioelectron.* vol. 13, 305-312, 1998.
- [21] D. Sun, T. Guo, Y. Ran, Y. Huang, B. O. Guan, "In-situ DNA hybridization detection with a reflective microfibre grating biosensor," *Biosens. Bioelectron.* vol. 61, 541-546, 2014.
- [22] G. Quero, M. Consales, R. Severino, P. Vaiano, A. Boniello et al., "Long period fibre grating nano-optrode for cancer biomarker detection," *Biosens. Bioelectron.* vol. 80, 590-600, 2016.
- [23] Z. He, F. Tian, Y. Zhu, N. Lavlinskaia, H. Du, "Long-period gratings in photonic crystal fibre as an optofluidic label-free biosensor," *Biosens. Bioelectron.* vol. 26, 4774-4778, 2011.
- [24] Y. Shevchenko, G. CamciUnal, D. Cuttica, M. Dokmeci, J. Albert, "Surface plasmon resonance fibre sensor for real-time and label-free monitoring of cellular behaviour," *Biosens. Bioelectron.* vol. 56, 359-367, 2014.

Chapter 2

Review: Historical background, photosensitivity, Grating theory and fabrication techniques

2.1 Historical background

The evolution of optical fibre photosensitivity could be traced back to Communication Research Centre, Canada, where fibre photosensitivity was first observed in germanium-doped silica fibre by Hill and co-workers [1]. They were initially carrying out an experiment to study nonlinear effects in a specially designed optical fibre where intense visible light from an argon ion laser was launched into the core of the fibre. With prolonged exposure, it was observed that the intensity of the light back-reflected from the fibre increased significantly with time thereby increasing the fibre attenuation. It was a standing wave pattern formed by the interference between 4% back reflection from the cleaved fibre end and the forward propagating light. Spectral measurement showed that the increased attenuation of transmission light was as a result of a permanent refractive index variation being photo-induced into the core of this special fibre. Consequently, this structure coupled some of the forward propagating light in the core mode into the backward propagating mode. This periodic refractive index variation, also named “Hill grating”, was the first observation of fibre Bragg gratings (FBGs) and a milestone in research on the nonlinear properties of germanium-doped silica fibre.

This phenomenon left a couple of researchers confused for about a decade but some still endeavour to delve into the mechanism behind it [2, 3]. The main reasons being that it was difficult to repeat the original experiments and the phenomenon observed was stigmatized to emanate only from the experiments which was limited to the one “magic” fibre at the Communication Research Centre, Canada. Also, the writing wavelength of the spectral region of the “Hill gratings” was confined within the visible part of the spectrum (argon ion writing wavelength – 488nm), which was of no importance to telecommunication, signal processing and sensing in near-IR region. During the early 1980s, scientists were investigating on second-harmonic generation in germanium-doped silica optical fibres with zero second-order nonlinear coefficients. Sasaki, Ohmori [4] and Fujii *et al.* [5] reported another nonlinear phenomenon of sum frequency generation. Stolen *et al.* [6] and Farries *et al.* [7] illustrated some experiments to support a mechanism for phase-matched generation of second harmonic (SH) light in the fibre. Thereafter, the observation from Stone *et al.* [8] demonstrated that virtually all germanium-doped silica fibres are sensitive to argon ion laser light radiation; this prompted resurgence in the field of optical fibre gratings.

In 1989, persistent research brought about a major breakthrough – a new fabrication method called the side inscription method later known as Two-beam holographic method [9]. Bragg gratings were inscribed by this method using the ultraviolet laser at 244nm single-photon absorption. It was demonstrated how two interfering 244nm single-photon UV laser beams could be used to inscribe gratings that would reflect a wide wavelength range of light (750nm - 1650nm) by illuminating the fibre core from the side. The Bragg resonance wavelength is dependent on the angle between the two interfering beams. Therefore, with this method, fibre gratings of any wavelength could be fabricated simply by changing the interfering angle of the two beams. The wavelength for reflection gratings could also be extended to any wavelength region of interest (1300 - 1500nm), permitting their usage in modern telecommunications and sensing systems. Thereafter, R. Kashyap *et al.* [10] demonstrated the first fibre laser operating from the reflection of the erbium-doped germane-silicate fibre grating at 1500nm.

However, one persistent problem of this breakthrough is the weakness of the fibre grating. This is because, normally, the UV induced refractive index change in standard single mode optical fibres is only around -3×10^{-5} . Since then, several treatment methods have been devised to increase the refractive index changes in optical fibre. These treatments make possible efficient reflectors of hundred wavelengths long. A prominent effort came from Lemaire and his colleagues, who reported a simple fibre treating

technique to enhance the photosensitivity by a low temperature and high pressure hydrogen treatment (also called hydrogen loading) before the UV exposure [11].

The year 1993 was the most important in the history of FBGs, with the discovery of two more enabling technologies: the phase mask and hydrogen-loading. The phase mask technique was invented by Hill and two other groups in Bell Labs and British Telecom [12, 13]; which eventually made commercial productivity of fibre gratings a reality. The second crucial development was the discovery that the diffusion of molecular hydrogen gas in optical fibre at relatively high pressure and for a duration long enough to saturate the fibre led to an extremely large enhancement in the photosensitivity of the fibres to UV light [11].

As a rapidly maturing technology finding applications in several fields, reliability of FBGs became a major concern to users. In 1994, the first chirped in-fibre Bragg grating for compensation of optical fibre dispersion was reported by Hill et al. [14]. Moreover, many new modified fibre gratings such as sampled gratings [15], apodized FBGs [16], Moiré gratings [17] and phase shift gratings [18] were also reported. Then, in 1996, Vengsarkar et al. presented the first long period fibre grating (LPFG) as band rejection filter [19]. These are fibre gratings with much longer periods than FBGs, such that mode coupling occurs in the forward direction instead of backwards. The resulting filter is a band-pass transmission filter and the phase matching condition depends on the difference between the effective indices of the modes being coupled. The consequence of the phase matching condition of LPFGs is that the resonant wavelength of a given mode coupling pair becomes highly dispersive. In that case, the resonant wavelength sensitivity to a given perturbation can either be positive, negative or near zero and can generally be optimised for a given sensing application [20].

Recently, availability of micro-structured fibres in several shapes and forms has opened up new sensing modalities which have led to the development of polarisation maintaining (PM) fibres [21]. In 2000, the first 45°- tilted fibre grating (TFG), used as in-line polarimeter, was demonstrated by P. S. Westbrook [22] while in 2005, Zhou et al. [23], demonstrated the use of 45°-TFGs as in-fibre polariser. Also, in early 2006, Zhou et al reported the first excessively tilted fibre grating (Ex-TFG) used as sensors with high RI sensitivity and low thermal sensitivity [24].

Perhaps it is worth mentioning that there are significantly new additions to the trend of optical fibre discoveries as each day goes by. Lots of articles relating to photosensitivity and fibre gratings are often being published in journals and proceedings of conferences.

Prominent among recent discoveries is the ultra-fast pulsed (femtosecond) laser, which can write into any object that is transparent at the laser wavelength. The focusing strength and ultra-short pulses of femtosecond laser ensure that the bandgap of the material is reached and its properties altered as a result. Also, the possibility of using phase mask scanning technique together with ultrafast lasers to inscribe different grating types in several materials has been demonstrated [25].

2.2 Photosensitivity of optical fibre

As earlier mentioned, the discovery of photosensitivity in silica by Hill et al [1] occurred while investigating non-linear effects in germanium doped silica fibre but light reflection from the cleaved end of the fibre was observed. The reflected light interfered with the forward propagating light and, as a result, set up a standing wave along the fibre length which changes the refractive index of the fibre. This change in refractive index acted as a reflector to the incoming radiation thereby increasing the standing wave amplitude and the periodic refractive index modulation till saturation was attained. The resulting structure acted like a narrowband ($< 200\text{MHz}$) filter limited to operate at the original laser wavelength.

Photosensitivity of optical fibre, therefore, refers to the induced change in refractive index of fibre core after exposure to ultra-violet (UV) light with specific wavelength. It is a couple of complex photo-chemical, photo-mechanical and thermo-chemical mechanism. Although, it was initially discovered in the germanium-doped silica glass fibre, many other doped silica fibres, such as europium [26], cerium [27], phosphorus [28] and erbium/germanium [29] have also shown different degrees of photosensitivity. Despite all, the germanium-doped fibre exhibit most photosensitivity to UV exposure. Therefore, the photosensitivity mechanism in germanium doped silica glass fibre will only be focused on in this session of the thesis.

2.2.1 Photosensitivity mechanisms

A variety of mechanisms have been proposed to explain the phenomenon behind the index changes but the dependence of this phenomenon on the various fabrication methods indicates its complexity. The photosensitive behaviour of doped amorphous silica varies with composition and fabrication methods thereby impacting the molecular structure of the silica matrix. Nearly all materials have defects and that of amorphous silica is no exception. While defects in the structure of silica used for optical transmission are kept at barest minimum so as to reduce losses caused by the associated absorption bands, they also play important role in photosensitivity. The defects of material are fatal in some applications such as high speed rotating turbine, but are useful in other applications such as germanium-doped optical fibres and semiconductor materials. These point defects, also known as colour centres, arise from intrinsic material defects or are induced by processing methods like drawing of fibre.

The predominant modified chemical vapour deposition system for the preparation of germanium-doped preform instil several incompatible chemical reactions in the preform

leading to lots of sub-oxides and defects in the silica host tetrahedral matrix. Also, the fibre drawing process induces new defect centres known as drawing induced defects (DIDs) [30, 31]. With germanium having two different stable oxidization states, +2 and +4, perturbations such as high temperature during the preform fabrication process affect the stability of its sub-oxide (GeO_2) while GeO exists mainly in the fibre core in form of 2-coordinated Ge or the Ge-Si (or Ge-Ge) wrong bonds, which are defect precursors [32]. The different point defects in germanium doped optical fibre are as shown in Figure 2.1.



Figure 2.1: Schematic of different point defects in germanium-doped silica (optical fibre).

As shown in the figure, the GODCs are germanium oxygen-deficient centres which are responsible for photosensitivity in optical fibre. Ge(1) and Ge(2) are trapped electron centres (or hole centres) and have their absorption bands at 281nm and 213nm respectively [33, 34]. Also, GODCs have two absorption bands: a single-photon absorption process due to singlet to singlet transition at 240nm and a two-photon absorption process which is weak absorption band with singlet to triplet transition at 480nm [35]. The other point defects are: the peroxy oxygen hole centre (P-OHC), the

non-bridging oxygen hole centre (NBOHC) and hole/trap centre or electron centre (GeE') with absorption bands at 260nm, 600nm and 195nm respectively [36]. Besides causing photosensitivity, all these absorption bands created by the point defects also incur transmission loss, nonlinear transmission [37, 38] and fibre fusing effect [39] on the optical fibre.

2.2.2 Photosensitisation techniques

Photosensitivity being a complex mechanism cannot possibly be explained by a single theoretical model therefore, several models have been proposed for better understanding of the concept of photosensitivity in optic fibre. These models include colour centre model [40, 41], mechanical effects like compaction/densification model [42] or stress relief/relaxation model [42, 43], electron charge migration model [44], permanent electric dipole model [45] and ionic migration model [46]. Meanwhile, this session will only briefly review colour centre model, stress relief/relaxation model and compaction/densification model among others.

2.2.2.1 Color center model

Color center model otherwise known as the defects center model was first proposed by Hand and Russell using the Kramers-Kronig relation [45]. This model is based on the principle that the photo-induced refractive index variation in optical fibre is as a result of electron excitation and conversion of defect centers in the germanium-doped fibre. Pure amorphous silica forms a tetrahedral structure in which silicon atom bonds to four oxygen atoms in a quasi-periodic structure. Within this regular structure, deviation from the normal tetrahedral lattice occurs. Similarly, germanium has a valence of four and, therefore, can act as a direct replacement in the silica matrix. The two dominant absorption bands for germanium-doped fibre are at 195nm (6.35eV) and 240nm (5.1eV) and are associated with the point defects GeE' and GODC respectively [47, 48]. When the germanium content is increased, the concentration of the related germanium oxygen deficiency centers (GODCs) also increases. Ge^{2+} defect with absorption at 241nm and the neutral oxygen vacancy (also known as NOV, a Ge-Ge bond or Si-Ge bond) with absorption at 245nm are the two defects significantly causing the increment. The absorption related to the GODCs is bleached when exposed to UV, indicating the defects are modified upon UV exposure resulting in the formation of new defects with new absorption bands. It has been experimentally shown [40] that the photon-induced refractive index change while responding to UV light near 240nm induces photochemical

reactions between GODC defects and GeE' . These reactions can be identified as two processes. Firstly, the single-photon process in which the wrong bond based GODC absorbs a photon (5.16eV) and subsequently converts to GeE' and GeO_3^+ as expressed in Fig. 2.2(a) [49, 50]. The emergence of GeE' liberates an electron which has been trapped elsewhere in the matrix thereby forming an additional defect such as the Ge(1). Secondly, the two-photon process where the 2-coordinated Ge based GODC absorbs two photons and initially generates a self-trapped hole center (STH) together with a 'Ge' electron center (GEC) which is finally converted to GeE' as expressed in Figure 2.2(b) [50].

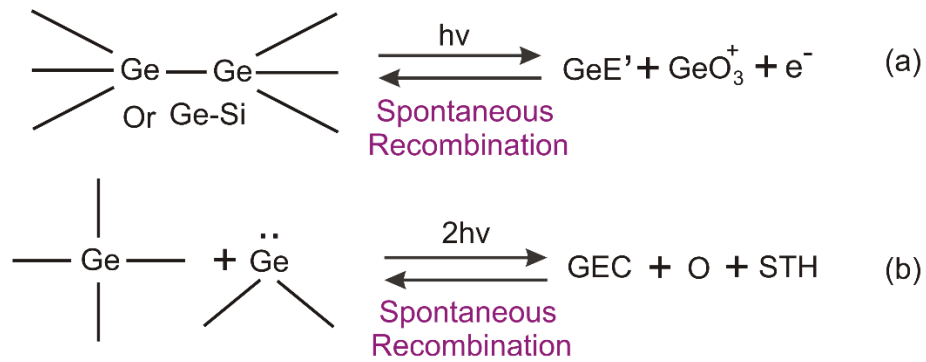


Figure 2.2: Photochemical reaction paths (a) single-photon process and (b) two-photon process.

The changes in refractive index are closely linked with changes of absorption in UV region. Also, some other mechanisms occur, possibly based around thermal effects, stress modification or compaction of the silica resulting in additional levels of index modification. In fact, densification has been shown to occur in UV exposed germane-silicates with resultant variations of stress and refractive index [51].

2.2.2.2 Densification-compaction model

This model assumes that the refractive index change is caused by the UV-induced compaction/densification. It is based on structural changes of the glass matrix and was initiated by Fiori and Devine in the compaction effect of amorphous silica film [52]. In a study of silica glasses for lithography applications, it was observed that UV induced densification was proportional to the softening temperature for number of different silica based glasses [53]. UV-induced densification in germanium-doped silica preforms and fibres was indeed observed by using atomic force microscope (AFM) [54], transmission electrons microscope (TEM) [55] and indirectly through changes in Raman spectra [56]. Compaction of the core occurs when an increase in refractive index causes an increase in the tensile stress in the core.

In contrary to the stress relief model, during the Bragg grating growth in the fibre and perform, it was observed that the tension increased strongly [55, 57]. This process is the combination of compaction (increasing the RI) and tensile stress effect on fibre core (reducing the RI). After some analysis of the contributions to the light induced RI change due to the compaction and photo-elastic effect, it was observed that the total Bragg grating RI modulation is smaller than that of the compaction induced RI modulation by 30%-35%, because of negative index effect of photo-elastic [42].

2.2.2.3 Stress relief model

When the refractive index of silica glass changes due to the stress-optic effect, the relief of built-in thermo-elastic stress which is caused by the UV exposure changes the RI of the fibre core [58]. Optical fibres may have highly stressed region depending on material properties and manufacturing procedures. Obviously, the residual stress arises from fibre cladding and core region having different thermal expansion coefficients. During the drawing and cooling process of the fibre the residual stress will be restored and the resulting tension can cause the reduction in refractive index (RI).

Optical fibre with a core having higher thermal expansion coefficient than that of its cladding ($\alpha_{T-core} > \alpha_{T-clad}$) will be restricted by the cladding glass as the core of the fibre cools down due to contraction. It will be a reverse situation if the core has a lower thermal expansion when compared to the cladding. When the stress integrate over the fibre is zero, the residual stress in the different regions will depend on the ratio of their area. The drawing tension will be applied to the region that first solidifies and the remaining glass with the lower transition temperature will solidify once the temperature has sufficiently

decreased. As the drawing tension gradually reduces, the fibre will contract thereby resulting in a compressive stress in the regions with lower transition temperature [59]. Estimated refractive index change due to stress relation in highly stressed fibre is in the order of $\Delta n \sim 10^{-3}$ [60].

2.2.3 Photosensitivity enhancement techniques

Standard communication fibre (SMF- 28) has very low photosensitivity and, therefore, needs to be enhanced. This is because it has low germanium dopant (around 3 mol%) and the UV induced saturable index change in the fibre is only about 3×10^{-5} [61]. Meanwhile, germanium is not the only dopant that can be added to the silica matrix in order to enhance photosensitivity. It is, however, frequently convenient to use germanium because it provides greater design and fabrication flexibility besides increasing the refractive index of silica. But to avoid the undesirable effects of excessive germanium doping levels, additional co-dopants (such as boron) may be used which has been found to enhance photosensitivity as well [52].

2.2.3.1 Hydrogen loading technique

The technique of hydrogen loading has been developed to improve photosensitivity without altering the physical properties of the glass. This is a good alternative to increasing dopant levels in germano-silicate glasses. It involves the use of high pressure to diffuse hydrogen into the silica matrix [11]. Permanent index changes, as high as 2×10^{-2} , is induced in the planar waveguide when loaded glass is exposed to UV [62]. This technique has been shown to effectively enhance photosensitivity in both germanium doped and germanium-free fibres. Also, it has the advantage that hydrogen in the unexposed glass diffuses out without altering the physical properties of the glass.

However, the main disadvantage of hydrogenation is that out-diffusion of hydrogen begins as soon as the sample is removed from a high pressure atmosphere. OH group in silica have a characteristic absorption at $1.4 \mu\text{m}$ which extends to the 1550nm telecommunications wavelength band. Hydrogen loading and UV irradiation are known to also form such OH groups within the silica matrix, so the technique can increase transmission loss in the resultant structures. Obviously, the spare hydrogen will cause critical loss at the communication windows. One alternative proposed to avoid this problem is to use deuterium whose chemical properties are almost identical to hydrogen, and then the infrared loss band will be moved away from the telecommunication transmission window.

2.2.3.2 Co-doping technique

The initial discovery of photosensitivity in optic fibre is as a result of the presence of germanium as a dopant in the core of the fibre. Therefore, doping or co-doping with other additional materials could be an alternative method to enhance the photosensitivity. Co-doping silica fibres with B_2O_3 and GeO_2 results in highly photosensitive fibres [52]. The addition of B_2O_3 , with concentration less than 10 mol%, to GeO_2 doped silica does not alter the 240nm UV absorption band characteristic for germanium doped fibres. But for higher B_2O_3 concentration, the 240nm absorption band is reduced (17-18 mol% GeO_2). In B_2O_3 - SiO_2 glass, UV absorption starts to increase at ~190nm and there is no absorption band at 240nm [63]. This co-doping mechanism is attributed to densification enhancement due to stress effect [64]. Actually, the enhancement of the photosensitivity of germane-silicate fibre is not only limited to the Boron co-doping, there are also other materials as co-dopants. Tin (Sn) co-doped fibre and Nitrogen (N_2) co-doped fibre are typical examples. But there are some problems limiting their fabrications and applications. In comparison to boron (B) co-doping, tin (Sn) co-doping does not introduce any significant loss at the telecommunication transmission window [65, 66].

2.2.3.3 Flame brushing technique

Flame brushing, which has the same photosensitizing principle as the hydrogenation technique, involves localized heating of fibres and waveguides using hydrogen rich flame. This technique results in enormous increase in the UV absorption spectra. During this process, the fibre is treated in a flame fuelled with hydrogen and oxygen at an estimated temperature of ~1700 °C for about 20mins. Essentially, the increased photosensitivity is due to in-diffusion of hydrogen and hydroxyl molecules into the fibre core which react with germane-silicate to produce GODC defect centres, enlarge the absorption band of 240nm, and finally increase UV induced RI modulation [67]. Despite having numerous advantages - such as low loss at the desired telecommunication transmission window, short treatment time, permanent enhancement and localization of photosensitivity - the major drawback of this method which is mechanical degradation of the fibre after prolonged processing overshadows the benefits.

2.3 Couple mode theory

Couple-mode theory has been widely accepted as approximate solution for the quantitative analysis of diffraction efficiency and spectral dependence of optical fibre gratings. It is a simple but accurate model for describing the characteristics and optical properties of in-fibre gratings. The comprehensive derivation of this theory has earlier been provided by Yariv [68], Kogelnik [69], and Erdogan [70, 71]. This thesis will only give a brief theoretical discussion based on the model proposed by Erdogan.

Considering the transverse component of the electric field as a superposition of the ideal modes in an ideal waveguide without any perturbation represented by the Eqn. (2.1) below:

$$\text{Equation 2.1} \quad \vec{E}^T(x, y, z, t) = \sum_m [A_m(z) \exp(i\beta_m z) + B_m(z) \exp(-i\beta_m z)] \vec{e}_m^T(x, y) \exp(-i\omega t)$$

Where the coefficients $A_m(z)$ and $B_m(z)$ are slightly varying amplitudes of the m^{th} mode (travelling in the +z and -z directions respectively), $\vec{e}_m^T(x, y)$ is the transverse mode field (described by a bound-core, cladding or radiation mode), and β is the propagation constant. The propagation constant can further be expressed as,

$$\text{Equation 2.2} \quad \beta = \frac{2\pi}{\lambda} n_{eff}$$

Where n_{eff} represents the effective refractive index (RI) of the m^{th} mode.

Mode coupling occurs in the presence of a dielectric perturbation and the amplitudes $A_m(z)$ and $B_m(z)$ of the m^{th} mode evolve along the z direction as expressed by the following equations:

Equation 2.3

$$\frac{dA_m}{dz} = i \sum_q A_q (C_{qm}^T + C_{qm}^L) \exp[i(\beta_q - \beta_m)z] + i \sum_q B_q (C_{qm}^T - C_{qm}^L) \exp[-i(\beta_q + \beta_m)z]$$

Equation 2.4

$$\frac{dB_m}{dz} = -i \sum_q A_q (C_{qm}^T - C_{qm}^L) \exp[i(\beta_q + \beta_m)z] - i \sum_q B_q (C_{qm}^T + C_{qm}^L) \exp[-i(\beta_q - \beta_m)z]$$

Where C_{qm}^T and C_{qm}^L are the transverse and longitudinal coupling coefficients between q and m modes respectively.

The longitudinal coefficient C_{qm}^L is analogous to that of the transverse coefficient, C_{qm}^T , but for fibre modes the longitudinal coefficient C_{qm}^L is usually neglected since $C_{qm}^T \gg C_{qm}^L$. The transverse coefficient can then be expressed as,

$$\text{Equation 2.5} \quad C_{qm}^T(z) = \frac{\omega}{4} \iint_{\infty} \Delta\varepsilon(x, y, z) \cdot \vec{e}_q^T(x, y) dx dy$$

$$\text{Equation 2.6} \quad \Delta\varepsilon(x, y, z) = 2n_{eff} \delta n_{eff}(x, y, z)$$

Where $\Delta\varepsilon(x, y, z)$ is the permittivity perturbation with a value of approximately $2n\delta n$ and δn is the effective RI variation with smaller value compared with the local index, n , in the ideal fibre.

In an ideal waveguide, with no perturbation, $\Delta\varepsilon = 0$, the coupling coefficient $C_{qm}^T(z) = 0$, and the transverse mode are orthogonal without exchanging any form of energy. When a photosensitive fibre is exposed to a spatially varying pattern of UV light, it produces the refractive index change $\delta n_{eff}(z)$ which is expressed by the Eqn. (2.7) as,

$$\text{Equation 2.7} \quad \delta n_{eff}(z) = \bar{\delta n}_{eff}(z) \left[1 + v \cos\left(\frac{2\pi}{\Lambda} z + \phi(z)\right) \right]$$

Where $\bar{\delta n}_{eff}(z)$ is the “dc” index change spatially averaged over a grating period or the slowly varying envelope of the grating, Λ is the grating period, $\phi(z)$ describes the grating chirp and v is the fringe visibility of the index change. UV-induced index change, $\delta n_{eff}(x, y, z)$, is approximately uniform across the core and negligible outside the core of most fibre gratings. It can, therefore be replaced by $\bar{\delta n}_{co}(z)$. From Eqns. (2.6) and (2.7), the general coupling coefficient may be written as

$$\text{Equation 2.8} \quad C_{qm}^T(z) = \psi_{qm}(z) + 2k_{qm}(z) \cos\left(\frac{2\pi}{\Lambda} z + \phi(z)\right)$$

Where $\psi_{qm}(z)$ and $k_{qm}(z)$ in Eqn. (2.8) are the “dc” and “ac” coupling coefficients respectively and are given by:

Equation 2.9
$$\psi_{qm}(z) = \frac{\omega n_{eff}}{2} \bar{\delta} n_{eff}(z) \iint_{core} \vec{e}_q^T(x, y) dx dy$$

Equation 2.10
$$k_{qm}(z) = \frac{v}{2} \psi_{qm}(z)$$

2.3.1 Backward Mode Coupling

The dominant interaction, in the backward mode coupling, is near the wavelength at which reflection occurs from a mode of amplitude $A(z)$ to an identical counter-propagating mode of amplitude $B(z)$. Under such conditions equations (2.3) and (2.4) are simplified to the following equations [70]:

Equation 2.11
$$\frac{dR}{dz} = i\hat{\psi}R(z) + ikS(z)$$

Equation 2.12
$$\frac{dS}{dz} = -i\hat{\psi}S(z) - ik^*R(z)$$

Where k is “ac” coupling coefficient, $\hat{\psi}$ is the general “dc” self-coupling coefficient and the amplitudes are R and S .

Equation 2.13
$$R(z) = A(z) \exp\left(i\delta z - \frac{\phi(z)}{2}\right)$$

Equation 2.14
$$S(z) = B(z) \exp\left(-i\delta z + \frac{\phi(z)}{2}\right)$$

Equation 2.15
$$\hat{\psi} = \delta + \psi - \frac{1}{2} \frac{d\phi(z)}{dz}$$

Where the detuning, δ is independent of z and defined as

Equation 2.16
$$\delta = \beta - \frac{\pi}{\Lambda} = \beta - \beta_d = 2\pi n_{eff} \left[\frac{1}{\lambda} - \frac{1}{\lambda_d} \right]$$

Here, $\lambda_d = 2n_{eff}\Lambda$ is the “design wavelength” for Bragg scattering by an infinitesimally weak grating ($\delta n_{eff} \rightarrow 0$). For a single-mode Bragg grating, the following equations are simplified relations

Equation 2.17

$$\psi = \frac{2\pi}{\lambda} \bar{\delta n}_{eff}$$

Equation 2.18

$$k = k^* = \frac{\pi}{\lambda} v \bar{\delta n}_{eff}$$

For a uniform grating along z axis, $\bar{\delta n}_{eff}$ is constant and $d\phi(z)/dz = 0$, meaning there is no indication of grating chirp. Thus k, ψ and $\hat{\psi}$ are constants. This simplifies equations (2.11) and (2.12) into coupled first-order ordinary differential equations with constant coefficients. The closed form may be found when appropriate boundary conditions are specified.

2.3.2 Forward Mode Coupling

In forward mode coupling, a forward propagating mode with amplitude $A_1(z)$ is strongly coupled into a co-propagating mode of amplitude $A_2(z)$ close to the wavelength in which forward mode coupling occurs. Equations (2.3) and (2.4) may be modified by retaining the terms that involve the amplitudes of these two modes and assuming necessary synchronous approximation to derive the following equations,

Equation 2.19

$$\frac{dR}{dz} = i\hat{\psi}R(z) + ikS(z)$$

Equation 2.20

$$\frac{dS}{dz} = -i\hat{\psi}S(z) + ik^*R(z)$$

Where R and S are new amplitudes and can be defined by the following expressions:

Equation 2.21

$$R(z) = A_1(z) \exp\left(i(\psi_{11} + \psi_{22})\frac{z}{2}\right) \exp\left(i\delta z - \frac{\phi}{2}\right)$$

Equation 2.22

$$S(z) = A_2(z) \exp\left(-i(\psi_{11} + \psi_{22})\frac{z}{2}\right) \exp\left(-i\delta z + \frac{\phi}{2}\right)$$

Where ψ_{11} and ψ_{22} are “dc” coupling coefficients as defined earlier in equation (2.9), k being the “ac” coupling coefficient as earlier stated, $k = k_{21} = k_{12}^*$ and $\hat{\psi}$ is the general “dc” self-coupling coefficient which is defined by the expression below:

Equation 2.23

$$\hat{\psi} = \delta + \left(\frac{\psi_{11} + \psi_{12}}{2} \right) - \frac{1}{2} \frac{dQ}{dz}$$

When the detuning δ is assumed to be constant along the z axis, it becomes defined by the expression

Equation 2.24

$$\delta = \frac{1}{2}(\beta_1 - \beta_2) - \frac{\pi}{\Lambda} = \pi \Delta n_{eff} \left[\frac{1}{\lambda} - \frac{1}{\lambda_d} \right]$$

where $\lambda_d = \Delta n_{eff} \Lambda$ is termed the “*design wavelength*” for any grating approaching zero index modulation. For Bragg gratings the grating condition is given as $\delta = 0$, or $\lambda = \lambda_d = \Delta n_{eff} \Lambda$. In contrast to single mode Bragg grating, uniform forward coupling grating has constant $\hat{\psi}$ and k ; while k may need to be evaluated numerically and not simply calculated as stated in Eqn. (2.18). Since the forward coupled grating equations are coupled first order differential equations with constant coefficient, closed form solutions can be found when given necessary boundary conditions [70].

2.4 Phase matching conditions

With the existence of any perturbation in an optic fibre, the bound-wave tends to be coupled to the counter-propagating or co-propagating modes. Optic fibre grating is classified depending on which mode the bound-wave is coupled. When coupled to the counter-propagating mode, it is called backward-coupled grating since it couples light to opposite direction. Bragg gratings (FBG) of uniform and chirped structures and tilted fibre gratings (TFG) with small tilted angles are typical examples of this category. But when coupled to the co-propagating mode, it is termed forward-coupled grating since coupling occurs among the same directional modes. Long period fibre grating (LPFG) and excessively tilted fibre grating (Ex-TFG) are examples of this category.

For the coupled modes, either backward-coupled or forward-coupled, the phase mismatch factor is referred to as a detuning and is given by the expression below;

Equation 2.25
$$\Delta\beta = \beta_i \pm \beta_d - \frac{2\pi}{\Lambda_g} N \cos \theta$$

where β_i and β_d are the propagating constants for the incident and diffracted modes respectively, Λ_g is the period of the grating, θ is the grating tilted angle and N is an integer number. Essentially, the " \pm " sign defines the propagation direction along " $\mp z$ " axis. The phase mismatch factor, $\Delta\beta$ must be zero for a significant amount of energy to be transferred. This is termed the phase-matching condition and therefore Eqn. (2.25) becomes

Equation 2.26
$$\beta_i \pm \beta_d = \frac{2\pi}{\Lambda_g} N \cos \theta$$

For counter-propagation (backward-coupled), β_i and β_d both have identical signs whereas for co-propagating, (forward-coupled), β_i and β_d have opposite signs. This shows that the sign of β_i and that of β_d determine with which mode the phase is matched. In most cases, first-order diffraction is dominant, therefore, N is always assumed to be unity [68]. The resonant wavelength is satisfied by the following expression:

Equation 2.27
$$\lambda = \left(n_i^{eff} \pm n_d^{eff} \right) \frac{\Lambda_g}{\cos \theta}$$

Another approach to understanding the phase-matching condition (PMC) is to see it as conservation of energy. The vector equation of PMC is given by these expressions:

$$\text{Equation 2.28} \quad \vec{K}_x = \vec{K}_{core} + \vec{K}_G$$

$$\text{Equation 2.29} \quad \vec{K}_{core} = n_{core} \frac{2\pi}{\lambda}$$

$$\text{Equation 2.30} \quad \vec{K}_G = n_{core} \frac{2\pi}{\Lambda} \cos \theta$$

$$\text{Equation 2.31} \quad \vec{K}_x = n_x \frac{2\pi}{\lambda}$$

The core mode is represented by the wave vector \vec{K}_{core} , the grating by wave vector \vec{K}_G , and x can be core, cladding or radiation, so, \vec{K}_x is the wave vector of core, cladding or radiation mode depending on the subscript applicable.

Various types of optical fibre gratings and their phase matching conditions are as shown in Figure 2.3. It shows that PMC theory can be used in different types of grating to know the propagating directions and the applicable resonance wavelengths. Phase matching condition for TFG is a bit complex and can be viewed from the principle of total internal reflection with tilted angle range between 23.1° and 66.9° in air. A comprehensive explanation on critical condition and mode coupling range that led to the choice of tilt-angle range in different media can be found in [72]. Considering total internal reflection effect at the interface of the cladding of a silica fibre and air, below this angle range, light will be coupled to backward propagating cladding modes while above the angle range light is coupled to forward propagating cladding modes.

In line with the above explanation, TFGs can be classified into three types: TFGs with tilted angles $\theta < 23.1^\circ$, which couple forward propagating core-mode to backward-propagating cladding modes; TFGs with tilted angles $23.1^\circ < \theta < 66.9^\circ$, which couple fundamental core-mode to radiation modes; and TFGs with tilted angles $\theta > 66.9^\circ$, which couple core-mode to forward-propagating cladding modes [23, 72].

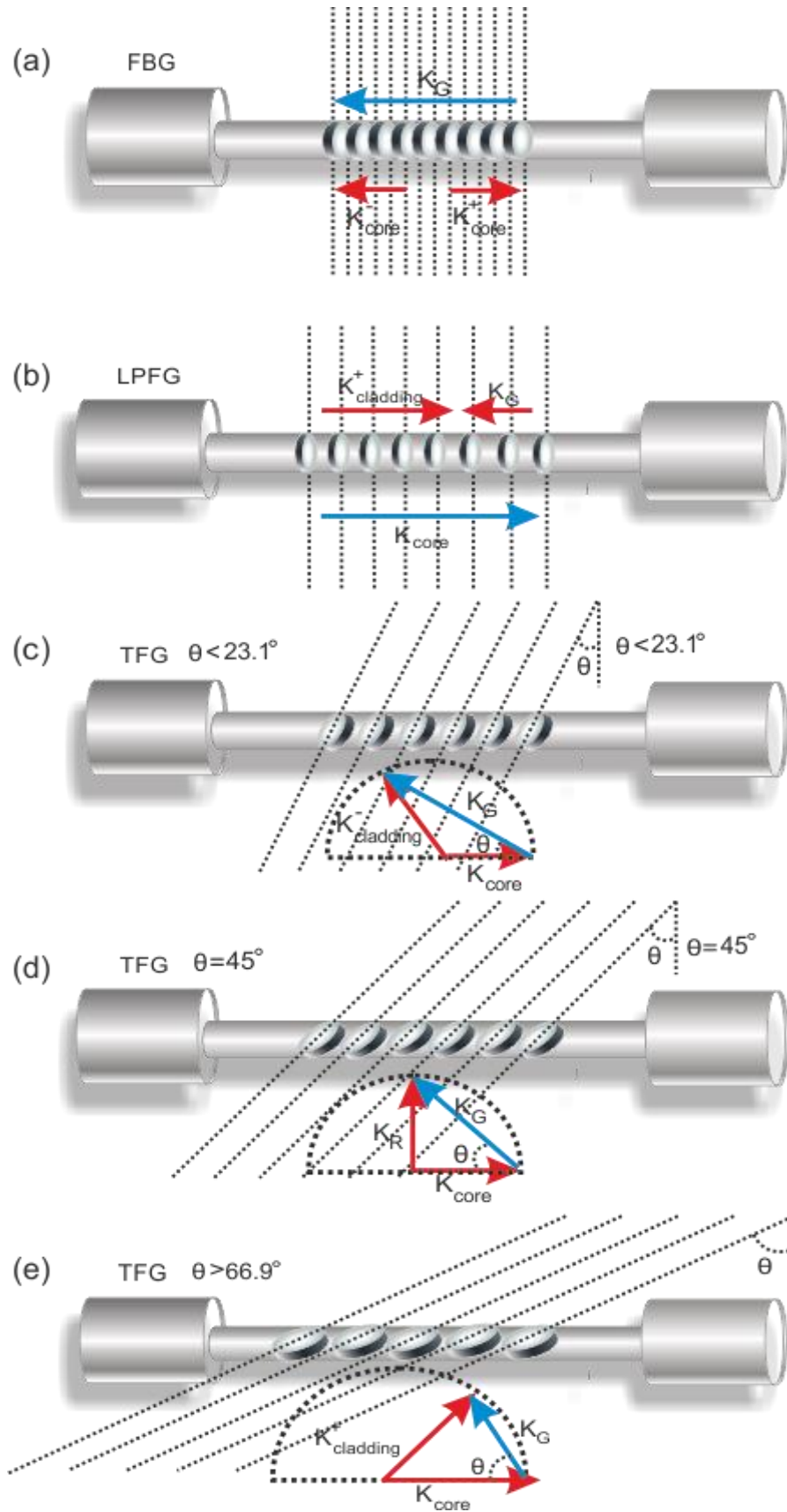


Figure 2.3: Schematics of optical fibre grating types and their phase matching conditions: (a) FBG; (b) LPFG; (c) TFG (at $\theta < 23.1^\circ$); (d) TFG (at $\theta = 45^\circ$); (e) TFG (at $\theta > 66.9^\circ$).

2.4.1 Fibre Bragg grating (FBG)

For Fibre Bragg grating (FBG) inscribed in a single-mode fibre, the only dominant interaction is the energy transfer between the forward and backward propagating core-modes as shown in Figure 2.4. FBG has periodic index modulation pattern, which are symmetric, along fibre axis with a period in sub-micrometer range. In the case of backward-coupling exhibited by normal FBG ($\theta = 0^\circ$), the Bragg wavelength is given by the expression,

Equation 2.32
$$\lambda_B = 2n_{eff}\Lambda$$

where n_{eff} is the effective index of the core and Λ is the period of the index modulation.

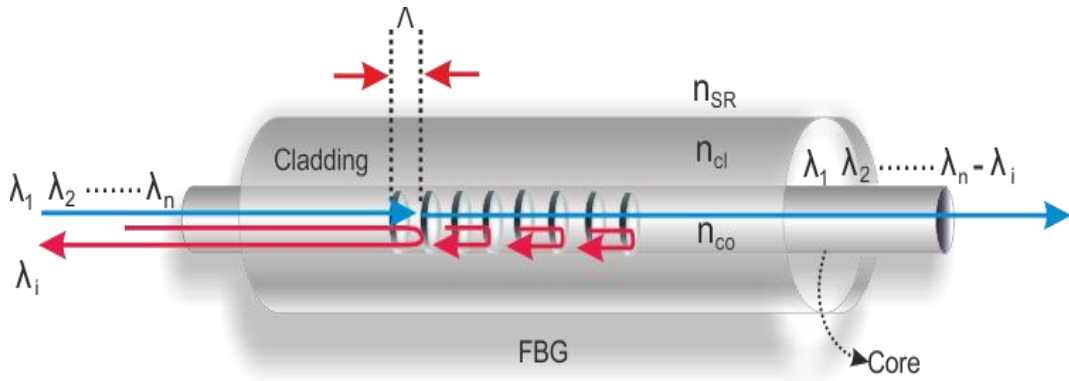


Figure 2.4: Schematic of mode-coupling of Fibre Bragg Grating (FBG).

2.4.2 Long period fibre grating (LPFG)

Long period fibre grating (LPFG) exhibits forward-mode coupling between the core and the cladding modes as shown in Figure 2.5. The resonant wavelength for coupling between the core and cladding modes satisfies the expression below;

Equation 2.33
$$\lambda_{res} = (n_{co}^{eff} - n_{cl,m}^{eff}) \cdot \Lambda$$

With n_{co}^{eff} and $n_{cl,m}^{eff}$ being the effective indices corresponding to the core and the m^{th} cladding modes respectively. The grating period of a forward-coupled grating at any particular wavelength is much larger than that of a backward-coupled grating because

the differences between core and cladding mode effective indices are far less than unity. LPFGs have period in hundreds of microns [19].

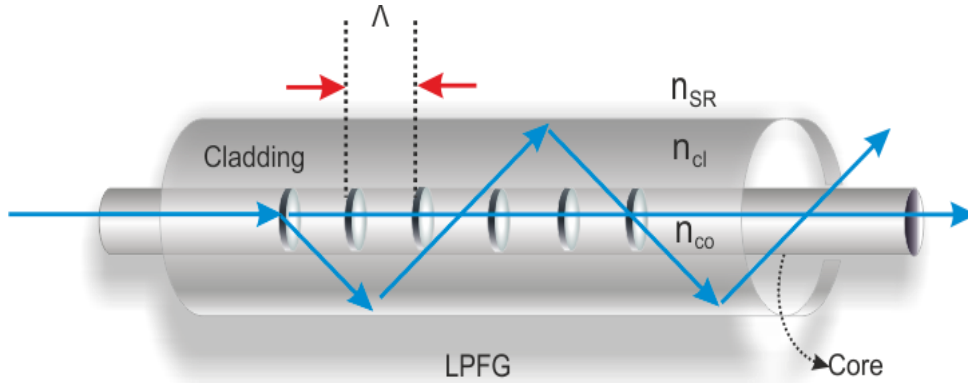


Figure 2.5: Schematic of mode-coupling of long period fibre grating (LPFG).

2.4.3 Tilted fibre gratings (TFGs)

Tilted fibre grating (TFG) exhibits more complex mode coupling unlike FBG and LPFG as depicted in Figure 2.6. Since there is existence of an angle, the resonant wavelength is given by [73, 74],

Equation 2.34
$$\lambda_{co-cl} = (n_{co}^{eff} \pm n_{cl,m}^{eff}) \cdot \frac{\Lambda_g}{\cos \theta}$$

where n_{co}^{eff} and $n_{cl,m}^{eff}$ are the effective indices corresponding to the core and m^{th} cladding mode respectively. The grating period along the fibre axis is expressed as,

Equation 2.35
$$\Lambda = \frac{\Lambda_g}{\cos \theta}$$

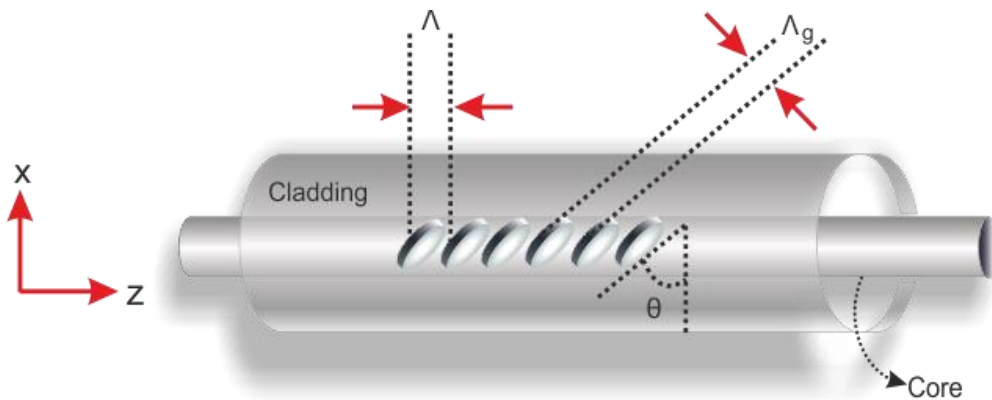


Figure 2.6: Schematic diagram of Tilted grating in fibre core.

The sign "+" or "-" in equation (2.34) indicates the direction of the mode propagate towards "-z" or "+z" axis respectively. As earlier explained, the schematic diagram in Figure 2.7 shows mode-coupling of TFG at different coupling angles.

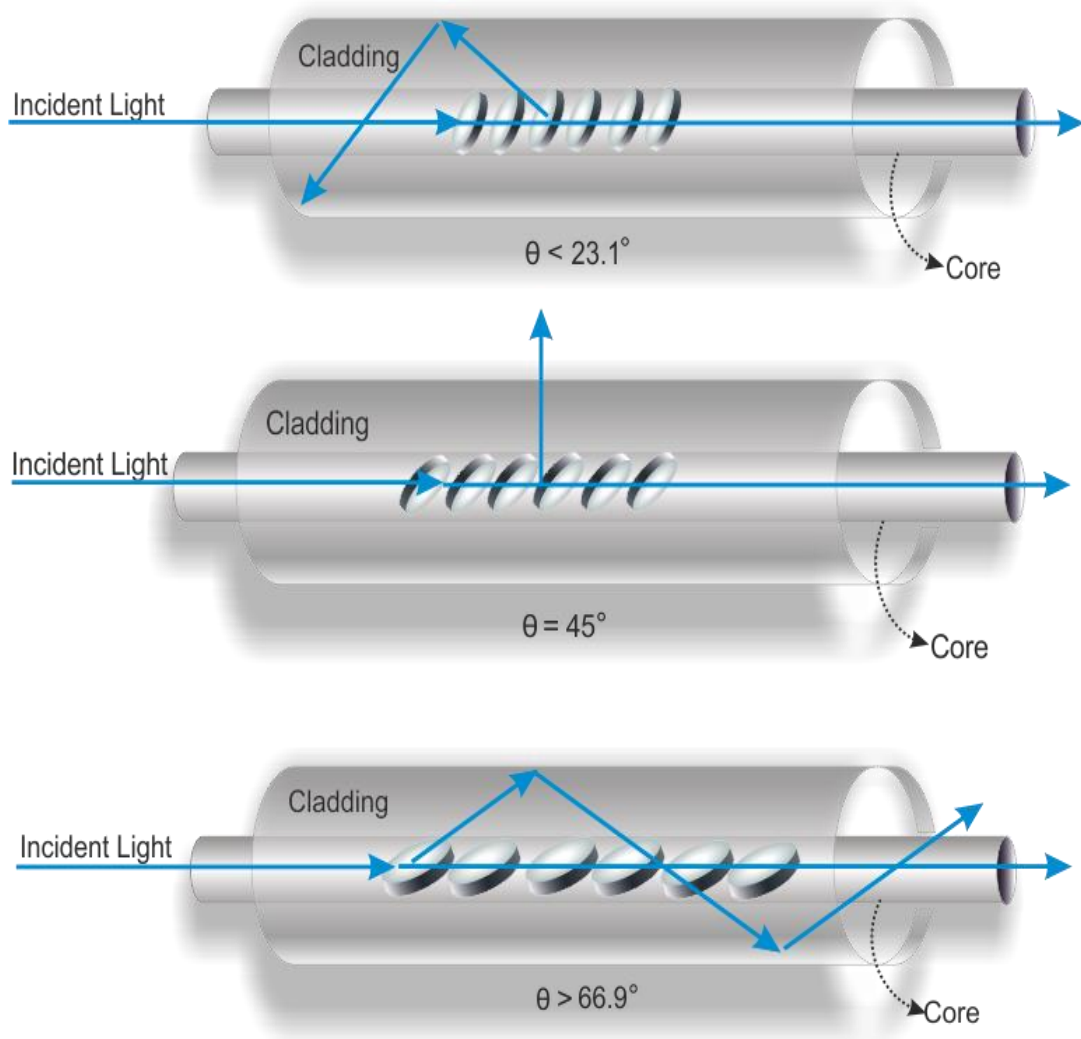


Figure 2.7: Schematic of mode-coupling of TFGs at different coupling angles.

2.5 Optical fibre grating fabrication techniques

Optical fibre grating requires different fabrication techniques depending on the characteristic of the grating in question. Each technique has its merit, limitation and specification requirement of the grating to be fabricated. It suffices to reiterate the fact that all other techniques evolved from the standing wave inscription technique as a result of persistent research activities and desire for improvement. Presently, the established optical fibre grating fabrication techniques are classified into three: Two-beam Holographic Technique, Point-by-Point Technique, and Phase Mask Technique. All these three techniques are up and running in the Aston Institute of Photonic Technologies (AIPT) Laboratories at Aston University. The couple of laboratory activities and experimental results enumerated in this thesis made use of all these fabrication techniques.

2.5.1 Two-beam holographic inscription technique

The two-beam holographic method is an external inscription approach to inscribing gratings in photosensitive fibres. It involves the splitting of an incident UV-laser light into two beams with equivalent intensity. The light passes through a 50:50 amplitude (beam) splitter and reflected by two highly reflective mirrors indicated as M_1 and M_2 in Figure 2.8. The reflected beams recombine to produce the interfering fringes. The stripped optical fibre is placed in the interference area, and subsequently a refractive index modulation is induced in the core of the fibre. The interfering beams are normally focused to enhance the intensity to the fibre core by the use of two cylindrical lenses inserted in the two optical paths. The distance between the mirrors and the splitter could be adjusted to get desired inscription wavelength [9]. Gratings fabricated in this manner are much more efficient with no limitation in designing the Bragg wavelength and chirp.

The shortfall of this technique is that the total length of fabricated grating is limited by the size of the two interfering beams. Also, inherent with this system is the 'self-chirping' of the gratings which occurs due to the beam profile producing a non-uniform exposure over the length of the grating, exhibiting some oscillations located at the short wavelength side of the Bragg resonance.



Figure 2.8: Schematic of optical setup of two-beam holographic inscription technique.

Unlike the standing wave technique, the period of interference pattern depends not just on the wavelength of incident light but also the angle between the two beams. The mathematical relationship between the Bragg wavelength and the system parameter is expressed as [9]:

Equation 2.36
$$\Lambda = \frac{\lambda_{uv}}{2 \sin\left(\frac{\theta}{2}\right)}$$

Equation 2.37
$$\lambda = 2n_{eff} \Lambda_s$$

Equation 2.38
$$\lambda = \frac{n_{eff} \lambda_{uv}}{\sin\left(\frac{\theta}{2}\right)}$$

The distance from the beam splitter to fibre holder is fixed (labelled as L_0 in Figure (2.8)), but the angle between the two beams can be adjusted by changing the positions of mirrors 1 and 2 (since the arm-length $L_1 = L_2$ for uniform-period FBG) and can be expressed as,

$$\text{Equation 2.39} \quad \frac{\theta}{2} = \tan^{-1} \left(\frac{L_1}{\sqrt{2L_0} - L_1} \right)$$

Substituting equation (2.38) into (2.39), the mathematical relationship between the Bragg wavelength and the system parameter is finally obtained as,

$$\text{Equation 2.40} \quad \lambda_B = \frac{n_{eff} \lambda_{uv}}{\sin \left(\tan^{-1} \left(\frac{L_1}{\sqrt{2L_0} - L_1} \right) \right)}$$

2.5.2 Point-by-point inscription technique

This technique is so named because the grating is written a point at a time in the fibre core. Each index perturbation of the grating is individually photo-imprinted in the fibre core by directly modulating the UV beam. It is limited by the focused spot size of UV-beam hence difficult to control translation stage movement accurately enough to write FBG structures. Therefore, this technique is mainly used to fabricate long-period fibre gratings with periods ranging from $10\mu m$ to $600\mu m$. With a focus lens placed between slit and fibre, Malo et al. fabricated a third order FBG at 1536nm using a modified point-by-point inscription technique and the image of slit was shadowed inside the fibre core as grating [75]. Also, the point-by-point inscription technique had been reported for direct FBG inscription in Aston University using infrared femtosecond laser [76, 77] likewise reported was femtosecond laser microfabrication of subwavelength structures in photonics [78].

As shown in Figure 2.9, unlike the phase mask inscription technique, an additional lens is required so as to reduce the spot size of the UV-beam. The UV-beam is focused on the fibre core by the two orthogonally placed cylindrical lens while inscribing the gratings in the core of the fibre. The PC-controlled shutter modulates the UV-laser power by

intermittently switching on and off as the translation stage move along the fibre at a 50:50 duty cycle to achieve point-by-point inscription. This technique also finds application in femtosecond laser inscription of fibre gratings and micro-structures.

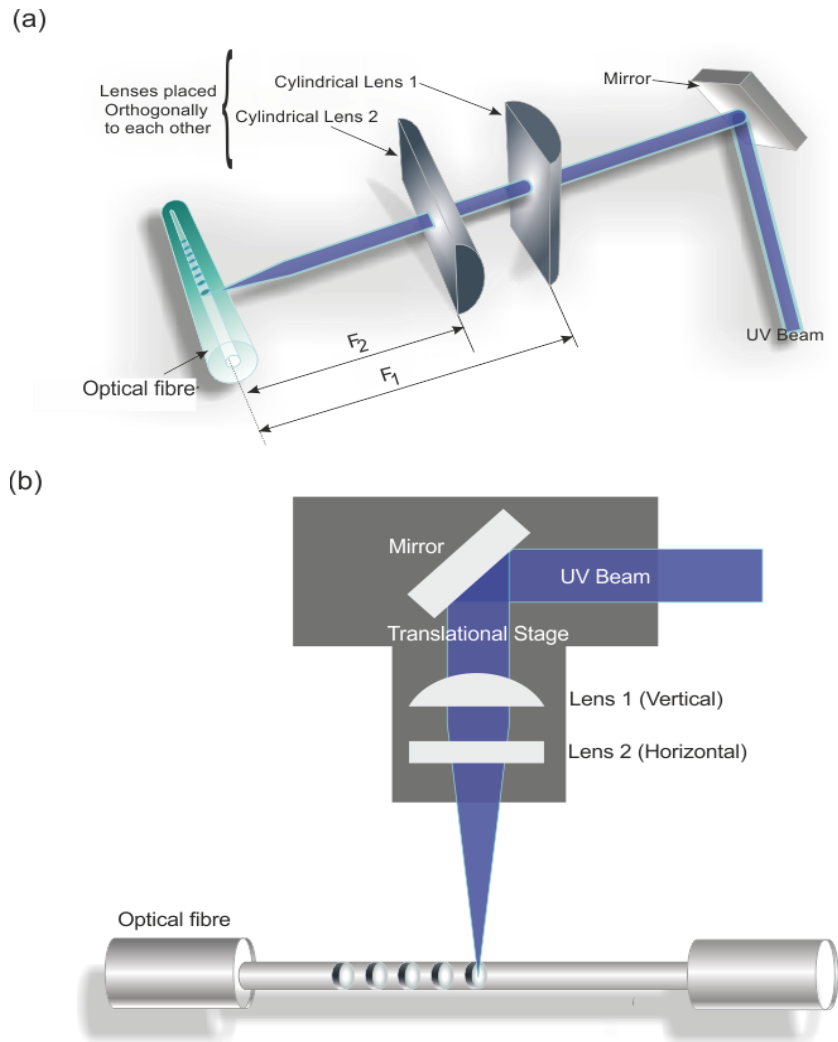


Figure 2.9: Point-by-Point Inscription Technique; (a) optical setup; (b) Schematic diagram.

2.5.3 Phase mask scanning technique

The phase mask (PM) is a one-dimensional periodic surface relief pattern etched into fused silica substrate that is transparent to UV light. It is one of the fastest and most effective techniques for reproducing fibre grating inscription. In this technique, the phase mask is employed as a diffractive optical element used for spatially modulating the incident UV-beam. To start with, the optical fibre is placed very close to the corrugations

of the phase mask for effective inscription as shown in Figure 2.10. The UV beam is diffracted into several orders by the periodic corrugations, when it passes through the phase mask. Approximately 80% UV laser intensity is divided equally into +1 and -1 orders diffraction beams which interfere to generate a periodic pattern that can effectively inscribe Bragg grating in the core of the fibre. Phase mask has been optimised to achieve zero-order suppression to less than 4% of the intensity of the transmitted light by controlling the depth of corrugation and choosing the amplitude of the periodic surface-relief pattern with the π phase modulation at the wavelength of incident UV beam [12, 13, 79].

For minimum zeroth-order diffraction, the depth of corrugations is given by the equation below. Where the wavelength of the UV beam is λ_{uv} , and $n_s(\lambda_{uv})$ is the refractive index of the fibre at the wavelength of incident UV light. The period of the fibre grating is determined by that of phase mask (half of the period of phase mask) and is independent of the UV-light inscription wavelength.

Equation 2.41
$$d = \frac{\lambda_{uv}}{2(n_s(\lambda_{uv}) - 1)}$$

Equation 2.42
$$\Lambda_g = \frac{\Lambda_{PM}}{2}$$

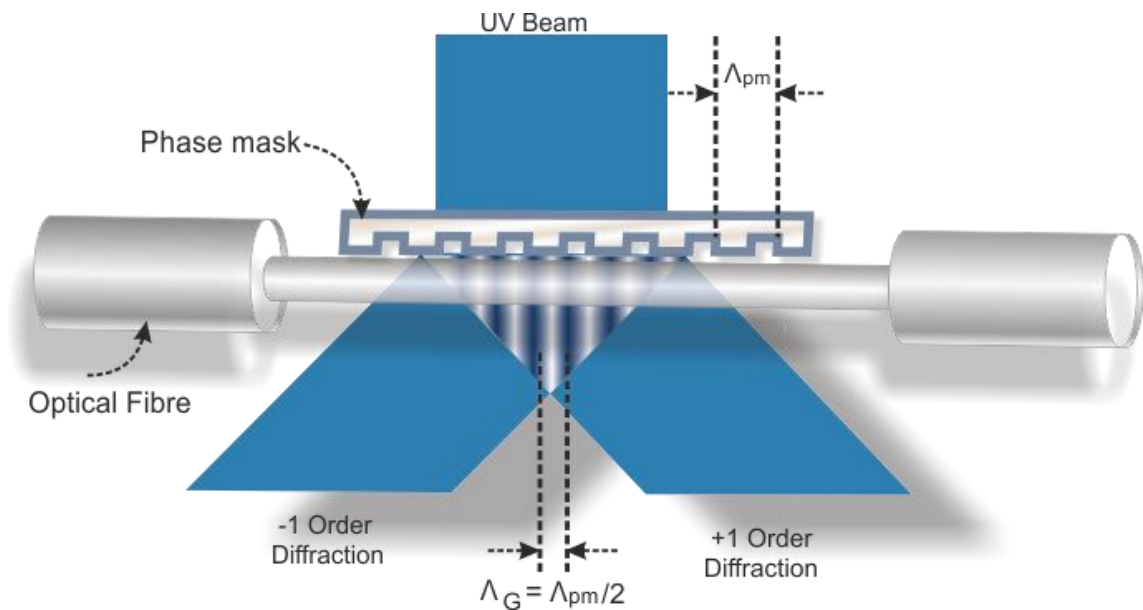


Figure 2.10: Phase Mask Scanning Technique: schematic of UV diffraction beams by Phase Mask.

2.6 Chapter conclusion

This chapter has discussed extensively the historical emergence of optical fibre gratings while also reviewing the photosensitivity property of optical fibre which is as a result of its UV-absorption characteristic mainly due to the existence of point defects in germanium-doped silica glass fibre. Various photosensitivity enhancement techniques are also discussed. The chapter goes further to discuss the couple mode theory as approximate solution for quantitative analysis of diffraction efficiency and spectra dependence of optical fibre gratings. The phase matching conditions for each type of optical fibre gratings are also reviewed. Finally, the three prominent optical fibre grating inscription techniques - two-beam holographic technique, phase-mask scanning technique and point-by-point inscription technique – have also been reviewed.

References

- [1] K.O. Hill, Y. Fujii, D. C. Johnson and B. S. Kawasaki, "Photosensitivity in optical fibre waveguides: Application to reflection filter fabrication", *Applied Physics Letters*, vol. 32, pp. 647-649, 1978.
- [2] J. Bures, J. Lapiere, and D. Pascale, "Photosensitivity Effect in Optical Fibres - a Model for the Growth of an Interference Filter," *Applied Physics Letters*, vol. 37(10), pp. 860-862, 1980.
- [3] D.K.W. Lam, and B.K. Garside, "Characterisation of Single-Mode Optical Fibre Filters," *Applied Optics*, vol. 37(10), pp. 860-862, 1980.
- [4] Y. Sasaki and Y. Ohmori, "Phase-matched sum-frequency light generation in optical fibres," *Applied Physics Letters*, vol. 39, pp. 466-468, 1981.
- [5] Y. Fujii, B. S. Kawasaki, K. O. Hill, and D. C. Johnson, "Sum-frequency light generation in optical fibres," *Opt. Lett.*, vol. 5, pp. 48-50, 1980.
- [6] R. H. Stolen and H. W. K. Tom, "Self-organized phase-matched harmonic generation in optical fibres," *Opt. Lett.*, vol. 12, pp. 585-587, 1987.
- [7] M. C. Farries, P. St J. Russell, M. E. Fermann, and D. N. Payne, "Second-harmonic generation in an optical fibre by self-written X⁽²⁾ grating," *Electronics Letters*, vol. 23, pp. 322-324, 1987.
- [8] J. Stone, "Photo-refractivity in GeO [sub 2]-doped silica fibres," *Journal of Applied Physics*, vol. 62, pp. 4371-4374, 1987.
- [9] G. Meltz, W. W. Morey, and W. H. Glenn, "In-fibre Bragg grating tap in Optical Fibre Communication," *San Francisco, California, USA: Optical Society of America Technical Digest series 1*, vol. TuG1, 1990.
- [10] R. Kashyap, J. R. Armitage, R. Wyatt, S. T. Davey and D. L. Williams, "All-fibre narrowband reflection gratings at 1500nm", *Electronics Letters* vol. 26(11), pp. 730-732., 1990.
- [11] P. J. Lemaire, R. M. Atkins, V. Mizrahi and W. A. Reed, "High pressure H₂ loading as a technique for achieving ultrahigh UV photosensitivity and thermal sensitivity in GeO₂ doped optical fibres," *Electronics Letters*, vol. 29(13), pp. 1191-1193, 1993.
- [12] D. Z. Anderson, V. Mizrahi, T. Erdogan and A. E. White, "Production of in-fibre gratings using a diffractive optical element," *Electronics Letters*, vol. 29(6), pp. 566-568, 1993.
- [13] J. R. Armitage, "Fibre Bragg reflectors written at 262 nm using a frequency quadrupled diode-pumped Nd₃: YLF laser " *Electronics Letters*, vol. 29(13), pp. 1181-1183, 1993.

- [14] K. O. Hill, F. Bilodeau, B. Malo, T. Kitagawa, S. Thériault, D. C. Johnson, J. Albert, and K. Takiguchi, "Chirped in-fibre Bragg gratings for compensation of optical-fibre dispersion," *Optics Letters*, vol. 19(17), pp. 1314-1316, 1994.
- [15] B. J. Eggleton, P. A. Krug, L. Poladian and F. Ouellette, "Long periodic superstructure Bragg gratings in optical fibres," *Electronics Letters*, vol. 30(19), pp. 1620-1622, 1994.
- [16] B. Malo, S. Theriault, D. C. Johnson, F. Bilodeau, J. Albert and K. O. Hill, "Apodised in-fibre Bragg grating reflectors photo-imprinted using a phase mask " *Electronics Letters*, vol. 31(3), pp. 223-225, 1995.
- [17] D. C. J. Reid, C. M. Ragdale, I. Bennion, J. Buus and W. J. Stewart, "Phase-shifted Moire grating fibre resonators", *Electronics Letters*, vol. 26(1), pp. 10-12, 1990.
- [18] R. Kashyap, P.F. McKee, and D. Armes, "UV written reflection grating structures in photosensitive optical fibres using phase-shifted phase masks " *Electronics Letters*, vol. 30(23), pp. 1977-1978, 1994.
- [19] A. M. Vengsarkar, P. J. Lemaire, J. B. Judkins, V. Bhatia, T. Erdogan and J. E. Sipe, "Long-period fibre gratings as band-rejection filters," *Journal of Lightwave Technology*, vol. 14(1), pp. 58-65, 1996.
- [20] V. Bhatia, "Application of long-period gratings to single and multi-parameter sensing," *Opt. Express*, vol. 4(11), pp. 457-466, 1999.
- [21] W. Berlandi, T. M. Monro, K. Furusawa, J. C. Baggett, N. G. R. Broderick, and D. J. Richardson, "Sensing with microstructure optical fibres", *Meas. Sci. Technol.*, vol. 12(7), pp. 854-858, 2001.
- [22] P.S. Westbrook, T. A. Strasser, and T. Erdogan, "In-Line Polarimeter Using Blazed Fibre Gratings," *Optics and Photonics News*, vol. 12(12), pp. 50-50, 2001.
- [23] K. Zhou, X. F. Chen, A. G. Simpson, L. Zhang and I. Bennion, "High Extinction Ratio In-Fibre Polariser Based on a 45°-Tilted Fibre Bragg Grating," presented at the Optical Fibre Communication Conference and Exposition and The National Fibre Optic Engineers Conference, Anaheim, California: Optical Society of America., 2005.
- [24] K. Zhou, L. Zhang, X. Chen, I. Bennion, "Optic sensors of high refractive-index responsivity and low thermal cross sensitivity that use fibre Bragg gratings of 80° tilted structures," *Optics Letters*, vol. 31(9), pp. 1193-1195, 2006.
- [25] S. J. Mihailov C. W. Smelser, D. Grobnc, "Formation of Type I-IR Type II-IR gratings with an ultrafast IR laser and a phase mask," *Opt. Express*, vol. 13(14), pp. 5377-5386, 2005.
- [26] K. O. Hill, M. A. Saifi, M. J. Andrejco, W. I. Way, A. Von Lehman, A. Y. Yan, Chinlon Lin, F. Bilodeau, "Photosensitivity in Eu^{2+} : Al_2O_3 -Doped-Core Fibre: Preliminary Results and Application to Mode Converters " p. PD3, 1991.

- [27] T. Taunay, P. Bernage, M. Douay, W. X. Xie, G. Martinelli, P. Niay, J. F. Bayon, E. Deleuaque, and H. Poignant, "Ultraviolet-enhanced photosensitivity in cerium-doped alumino-silicate fibres and glasses through high-pressure hydrogen loading," *J. Opt. Soc. Am. B.*, vol. 14, pp. 912-925, 1997.
- [28] B. Malo, J. Albert, F. Bilodeau, T. Kitagawa, D. C. Johnson and K. O. Hill, "Photosensitivity in phosphorus-doped silica glass and optical waveguides," *Applied Physics Letters*, vol. 65, pp. 394-396, 1994.
- [29] F. Bilodeau, D. C. Johnson, B. Malo, K. A. Vineberg, K. O. Hill, T. F. Morse, A. Kilian, and L. Reinhart, "Ultraviolet-light photosensitivity in Er³⁺ Ge-doped optical fibre," *Opt. Lett.*, vol. 15, pp. 1138-1140, 1990.
- [30] P. Kaiser, "Drawing-induced coloration in vitreous silica fibres," *J. Opt. Soc. Am.*, vol. 64, pp. 475-481, 1974.
- [31] Y. Hibino and H. Hanafusa, "Defect structure and formation mechanism of drawing-induced absorption at 630 nm in silica optical fibres," *Journal of Applied Physics*, vol. 60, pp. 1797-1801, 1986.
- [32] J. M. Jackson, M. E. Wells, G. Kordas, D. L. Kinser, and R. A. Weeks, "Preparation effects on the UV optical properties of GeO₂ glasses," *Journal of Applied Physics*, vol. 58, pp. 2308-2311, 1985.
- [33] T. E. Tsai, D. L. Griscom, E. J. Friebele "On the Structure of Ge-Associated Defect Centers in Irradiated High Purity GeO₂ and Ge-Doped SiO₂ Glasses," *Defect and Diffusion Forum*, vol. 53-54, pp. 469, 1987.
- [34] T. E. Tsai and D. L. Griscom, "Defect centers and photo-induced self-organization in Ge-doped silica core fibre," pp. 14-28, 1991.
- [35] V. B. Neustruev, "Color centers in germanosilicate glass and optical fibres," *Journal of Physics: Condensed Matter*, vol. 6, pp. 6901, 1994.
- [36] T-E. Tsai, D. L. Griscom, and E. J. Friebele, "Radiation-induced defect centers in high-purity GeO₂ glass," *Journal of Applied Physics*, vol. 62, pp. 2264-2268, 1987.
- [37] P. S. Russell, L. J. Poyntz-Wright and D. P. Hand, "Frequency doubling, absorption, and grating formation in glass fibres: effective defects or defective effects?" pp. 126-139, 1991.
- [38] L. J. Poyntz-Wright, et al., "Nonlinear transmission and color-center dynamics in germanosilicate fibres at 420-540 nm" *Opt. Lett.*, vol. 13, pp. 1023-1025, 1988.
- [39] D. P. Hand and P. S. Russell, "Solidarity thermal shock waves and optical damage in optical fibres: the fibre fuse," *Opt. Lett.*, vol. 13, pp. 767-769, 1988.
- [40] R. M. Atkins and T. Erdogan, "248-nm induced UV spectral changes in optical fibre perform cores: Support for a color center model of photosensitivity," *Electron. Lett.* vol. 29, pp. 385-387, 1993.

- [41] P. S. Russell, D. P. Hand, Y. T. Chow and L. J. Poyntz-Wright, "Optically induced creation, transformation, and organization of defects and color centers in optical fibres," pp. 47-54, 1991.
- [42] H. G. Limberger, P. Y. Fonjallaz, R. P. Salathe and F. Cochet, "Compaction- and photo-elastic induced index changes in fibre Bragg gratings," *Applied Physics Letters*, vol. 68(22), pp. 3069-3071, 1996.
- [43] D. Wong, S.B. Poole, and M.G. Sceats, "Stress-birefringence reduction in elliptical-core fibres under ultraviolet irradiation," *Optics Letters*, vol. 17(12), pp. 1773-1775, 1992.
- [44] A. E. Attard, "Fermi level shift in $\text{Bi}_{12}\text{SiO}_{20}$ via photon-induced trap level occupation," *Journal of Applied Physics*, vol. 71, pp. 933-937, 1992.
- [45] D. P. Hand and P. St. J. Russell "Photo-induced refractive-index changes in germanosilicate fibres," *Optic Letters*, vol. 15(2), pp. 102-104, 1990.
- [46] N. M. Lawandy, "Light induced transport and delocalization in transparent amorphous systems," *Optics Communications*, vol. 74(3-4), pp. 180-184, 1989.
- [47] H. Hosono, M. Mizuguchi, H. Kawazoe, "Correlation between GeE' Centers and Optical Absorption Bands in $\text{SiO}_2:\text{GeO}_2$ glasses," *Japanese Journal of Applied Physics*, vol. 35, pp. L234-L236, 1996.
- [48] R. M. Atkins and V. Mizrahi, "Observations of changes in UV absorption bands of single-mode germanosilicate core optical fibres on writing and thermally erasing refractive index gratings," *Electronics Letters*, vol. 28, pp. 1743-1744, 1992.
- [49] H. Hosono, Y. Abe, D. L. Kinser, R. A. Weeks, K. Muta, and H. Kawazoe, "Nature and origin of the 5-eV band $\text{SiO}_2:\text{GeO}_2$ glasses," *Physical Review B*, vol. 46, pp. 11445-11451, 1992.
- [50] J. Nishii, K. Fukumi, H. Yamanaka, K. Kawamura, H. Hosono, and H. Kawazoe, "Photochemical reactions in $\text{GeO}_2:\text{SiO}_2$ glasses induced by ultraviolet irradiation: Comparison between Hg lamp and excimer laser," *Physical Review B*, vol. 52, pp. 1661-1665, 1995.
- [51] M. Douay, W.X. Xie, T. Taunay, P. Bernage, P. Cordier, B. Pommellec, L. Dong, J. F. Bayon, H. Poignant, and E. Delevaque, "Densification Involved in the UV-based Photosensitivity of Silica glasses and Optical fibres," *IEEE Journal of Lightwave Technology*, vol. 15(8), pp. 1329-1342, 1997.
- [52] D. L. Williams, B. J. Ainslie, J. R. Armitage, R. Kashyap, and R. Campbell, "Enhanced UV photosensitivity in boron co-doped germanosilicate fibres," *Electronics Letters*, vol. 29(1), pp. 45-47, 1993.
- [53] N. F. Borrelli, C. M. Smith, D. C. Allan, "Excimer-laser-induced densification in binary silica glasses," *Opt. Lett.*, vol. 24, pp. 1401-1403, 1999.
- [54] B. Pommellec, P. Niay, P. Cordier and E. Delevaque, Optical Materials, "UV induced densification during Bragg grating inscription in $\text{Ge}:\text{SiO}_2$ preforms," vol. 4(4), pp. 441-449, 1995.

- [55] P. Cordier, S. Dupont, M. Douay, G. Martinelli P. Bernage and P. Niay, "Evidence by transmission electron microscopy of densification associated to Bragg grating photo-imprinting in germanosilicate optical fibres," *Applied Physics Letters*, vol. 70(10), pp. 1204-1206, 1997.
- [56] E. M. Dianov, V. G. Plotnichenko, V. V. Koltashev, Yu N. Pyrkov, N. H. Ky, H. G. Limberger, R. P. Salathe, "UV-irradiation induced structural transformation of germanosilicate glass fibre," *Opt. Lett.*, vol. 22, pp. 1754-1756, 1997.
- [57] P. Y. Fonjallaz, H. G. Limberger, R. P. Salathé, F. Cochet, and B. Leuenberger, "Tension increase correlated to refractive-index change in fibres containing UV-written Bragg gratings," *Opt. Lett.*, vol. 20, pp. 1346-1348, 1995.
- [58] M. G. Sceats, G. R. Atkins, S. B. Poole, "Photolytic index changes in optical fibres," *Annual Rev. Mater. Sci.*, vol. 23, pp. 381-410, 1993.
- [59] Y. Park, K. Oh, U. C. Paek, D. Y. Kim, and C. R. Kurkjian, "Residual Stresses in a Doubly Clad Fibre with Depressed Inner Cladding (DIC)," *J. Lightwave Technol.*, vol. 17, pp. 1823-1834, 1999.
- [60] M. G. Sceats, P. A. Krug, "Photo-viscous annealing - dynamics and stability of photo-refractivity in optical fibres," *SPIE proc.*, vol. 2044, pp. 113-120, 1993.
- [61] I. Bennion, J. A. R. Williams, L. Zhang, K. Sugden and N. J. Doran, "UV-written in-fibre Bragg gratings," *Optical and Quantum Electronics*, vol. 28(2), pp. 93-135, 1996.
- [62] M. Svalgaard, and K. Faerch, "High Index Contrast UV-Written Waveguides," in *proceedings of 12th European Conference of Integrated Optics*, Grenoble, 2005, pp. 522-525.
- [63] L. Dong, J. Pinkstone, P. St. J. Russell, D. N. Payne, "Ultraviolet absorption in modified chemical vapor deposition preforms," *J. Opt. Soc. Am. B*, vol. 11, pp. 2106-2111, 1994.
- [64] I. Camlibel, D. A. Pinnow, and F. W. Dabby, "Optical aging characteristics of borosilicate clad fused silica core fibre optical waveguides," *Appl. Phys. Lett.*, vol. 26, pp. 185-187, 1975.
- [65] L. Dong, J. L. Cruz, L. Reekie, M. G. Xu and D. N. Payne, "Enhanced photosensitivity in Tin co-doped germanosilicate optical fibres," *Photonics Technology Letters, IEEE*, vol. 7, pp. 1048-1050, 1995.
- [66] N. H. Ky, H. G. Limberger, R. P. Salathé, F. Cochet and L. Dong, "Effects of drawing tension on the photosensitivity of Sn Ge- and B/Ge co-doped core fibres" *Opt. Lett.*, vol. 23, pp. 1402-1404, 1998.
- [67] F. Bilodeau, B. Malo, J. Albert, D. C. Johnson, K. O. Hill, Y. Hibino, M. Abe, and M. Kawachi, "Photosensitisation of optical fibre and silica-on-silica/silica waveguides," *Opt. Lett.*, vol. 18, pp. 953-955, 1993.
- [68] A. Yariv, "Coupled-mode theory for guided-wave optics" *IEEE Quantum Electron*, vol. 9, pp. 919-933, 1973.

- [69] H. Kogelnik, and C. W. Shank, "Coupled wave theory of distributed feedback lasers," *Appl. Phys.*, vol. 43, pp. 2327-2335, 1972.
- [70] T. Erdogan, "Fibre grating spectra," *Lightwave Technol.*, vol. 15, pp. 1277-1294, 1997.
- [71] T. Erdogan, "Cladding-mode resonances in short- and long- period fibre grating filters " *Opt. Soc. Am.*, vol. A14, pp. 1760-1773, 1997.
- [72] K. Zhou, L. Zhang, X. Chen, I. Bennion, "Low Thermal Sensitivity Grating Devices Based on Ex-45° Tilting Structure Capable of Forward-Propagating Cladding Modes Coupling," *Journal of Lightwave technology*, vol. 24, pp. 5087-5094, 2006.
- [73] K. Lee, and T. Erdogan, "Fibre mode coupling in transmissive and reflective tilted fibre gratings," *Appl. Opt.*, vol. 39, pp. 1394-1404, 2000.
- [74] T. Erdogan, and J. E. Sipe, "Tilted fibre phase gratings," *J. Opt. Soc. Am. A*, vol. 13, pp. 296-313, 1996.
- [75] B. Malo, K. O. Hill, F. Bilodeau, D. C. Johnson and J. Albert, "Point-by-Point Fabrication of Micro-Bragg Gratings in Photosensitive Fibre Using Single Excimer Pulse Refractive-Index Modification Techniques," *Electronics Letters*, vol. 29(18), pp. 1668-1669, 1993.
- [76] A. Martinez, M. Dubov, I. Khrushchev and I. Bennion, "Direct writing of fibre Bragg gratings by femtosecond laser," *Electronics Letters*, vol. 40(19), pp. 1170 – 1172, 2004.
- [77] A. Martinez, I. Y. Khrushchev and I. Bennion, "Thermal properties of fibre Bragg gratings inscribed point-by-point by infrared femtosecond laser," *Electronics Letters*, vol. 41(4), pp. 176 – 178, 2005.
- [78] V. Mezentsev, J. S. Petrovic, M. Dubov, I. Bennion, J. Dreher, H. Schmitz and R. Grauer, "Femtosecond laser microfabrication of subwavelength structures in photonics," *Proc. SPIE 6459, Laser-based Micro- and Nanopackaging and Assembly*, 64590B, 2007 (doi:10.1117/12.705800).
- [79] B. Malo , K. O. Hill, F. Bilodeau, D. C. Johnson, and J. Albert, "Bragging gratings fabricated in mono-mode photosensitive optical fibre by UV exposure through a phase mask," *Appl. Phys. Lett.*, vol. 62, pp. 1035-1037, 1993.

Chapter 3

Advanced Optical Fibre Gratings: Fabrication, spectral characteristics and Sensing measurements

3.1 Introduction

This chapter discusses the fabrication of fibre Bragg gratings (FBGs), Long period fibre gratings (LPFGs), small-angle tilted fibre gratings (S-TFGs) and excessively tilted fibre gratings (Ex-TFGs) with their sensing characteristics. The three typical fabrication techniques earlier described – two-beam holographic, phase mask scanning and point-by-point methods – are experimentally used for the gratings inscription. The chapter starts with the first session describing the theoretical concept behind FBG and the two different techniques employed for the UV inscription: two-beam holographic and phase mask scanning.

The second session discusses LPFGs fabricated with different grating periods and shows the characteristics of LPFGs with periods near dispersion turning points and their sensing characteristics. While the third session explains in details the fabrication and sensing characteristics of small angle tilted fibre gratings, the fourth session discusses that of Ex-TFGs with different tilt angles. All experimental results analysis has utilised the confidence interval (95%) and Standard error (SE) for data point and linear fitting

error analysis respectively. Also, each of the experiments was repeated at least three times to ascertain good repeatability and reproducibility for comprehensive data analysis.

This chapter further describes the theories that underpin the response of various optical fibre gratings to external perturbations such as temperature, strain, bending and refractive index variations. In addition, the dependence of grating inscription on some parameters like grating length, mode order etc. are also discussed.

3.2 FBGs inscription and sensing characteristics

This section details the experimental procedure behind the fabrication of fibre Bragg gratings (FBGs) with two different inscription techniques: two-beam holographic and phase mask scanning methods. The objectives of these experiments are to demonstrate different FBGs fabrication methods, investigate spectral profiles of FBGs of different wavelengths, and evaluate their sensing characteristics.

3.2.1 Using two-beam holographic technique

As earlier explained, the uniform-period Bragg gratings fabricated with this technique are not limited in the Bragg wavelength design and are much more efficient. The only acknowledged disadvantage is a limitation in length of grating which is imposed by the size of the two interfering beams. As earlier shown in Figure 2.8, the two cylindrical lenses focus the two beams on the photosensitive single-mode fibre to enhance the power intensity. And these interfering UV-beams produce a uniform-period grating in the core of the optical fibre. With L_0 fixed in position, the grating wavelength changes when arm-length (L_1) is made to vary. According to [1], different grating wavelengths can be predicted using a reference grating. This is achievable with the optical setup shown in Figure 3.1 where mirrors M_1 and M_2 are movable to new positions M'_1 and M'_2 with the new arm-length at $L_1 = L_{ref} + x$, where x is the displacement measured with accuracy of $0.01mm$ using a micrometre driver.

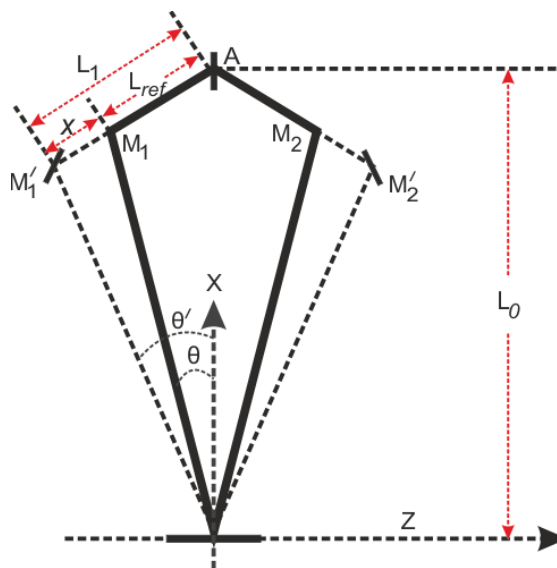


Figure 3.1: Schematic diagram of optical setup for adjusting the Bragg wavelength in the holographic inscription technique.

Substituting the new arm-length into eqn. 2.42, a new expression, which is used to predict the new grating wavelength during fabrication, can then be obtained in Eqn. 3.1 as,

Equation 3.1

$$\lambda_B = \frac{n_{eff} \lambda_{uv}}{\sin \left(\tan^{-1} \left(\frac{L_{ref} + x}{\sqrt{2}L_0 - (L_{ref} + x)} \right) \right)}$$

For the experiment, if the initial parameters were set for a displacement of $\Delta x = 0.01mm$; L_1 (reference) = 142mm and fixed length at $L_0 = 522mm$, it yields $\Delta\lambda_B = 20nm$. These parameters were used to fabricate and achieve different typical optical transmission wavelengths at four regions: $\sim 850nm$ (high attenuation; first communication window), $\sim 1310nm$ (zero dispersion; ‘O band’), $\sim 1550nm$ (lowest attenuation; ‘C-band’), and $\sim 2\mu m$ (mid-infra-red region). In general, hydrogen loaded single-mode fibre (SMF-28: core diameter of $\sim 8.2\mu m$ and cladding diameter of $\sim 125 \pm 0.7\mu m$) was used to UV-inscribe the FBGs in these wavelength regions. The typical transmission spectra of the fabricated gratings using two-beam holography method are as presented in Figure 3.2 below, showing the Bragg responses in the four wavelength regions.

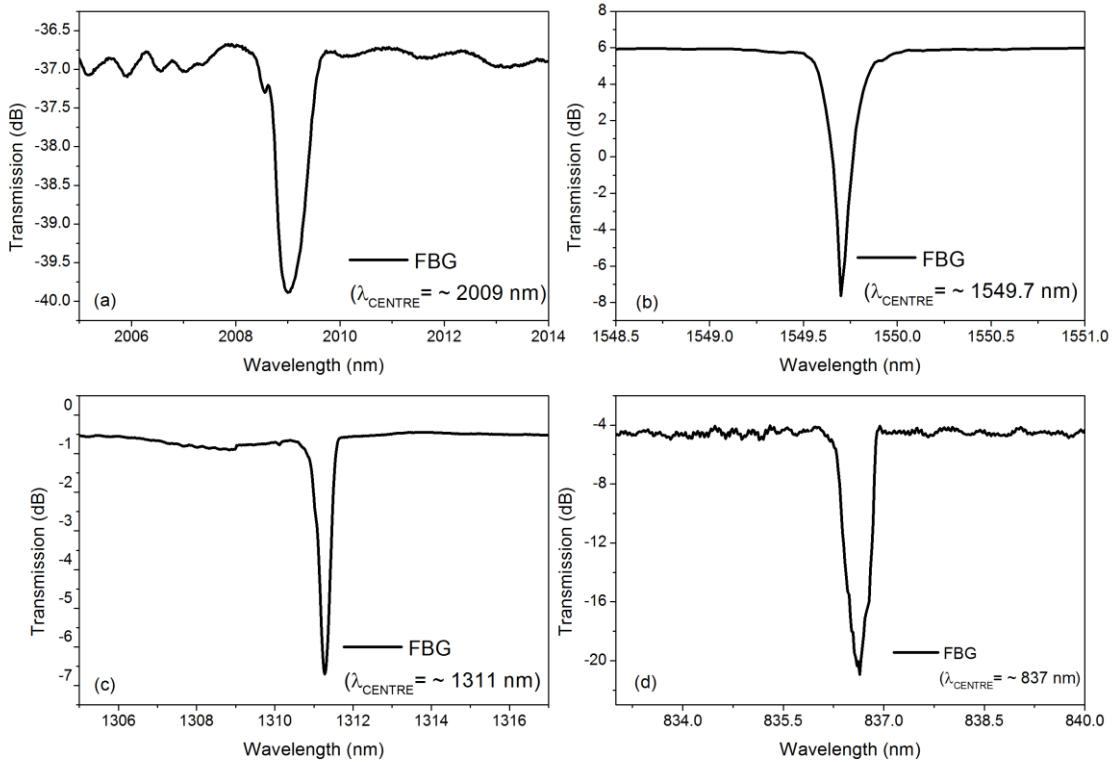


Figure 3.2: Typical transmission spectra of uniform-period Bragg gratings fabricated using two-beam holographic technique at wavelengths: (a) $\sim 2\mu m$; (b) ~ 1550 nm; (c) ~ 1310 nm; (d) ~ 837 nm.

Also, this inscription method was used to write Bragg gratings specifically at centre wavelength 1454 nm in hydrogen-loaded SMF-28 with the writing UV laser power set at 95mW. The reflectance of the FBGs ranges from as low as 4% to as high as 99% at an interval of approximately 10%. Figure 3.3 shows the transmission spectra of some selected FBGs with different reflectance as achieved by the two-beam holographic method and note, the gratings were thermal annealed at 80°C for 24 hours to stabilise the response property.

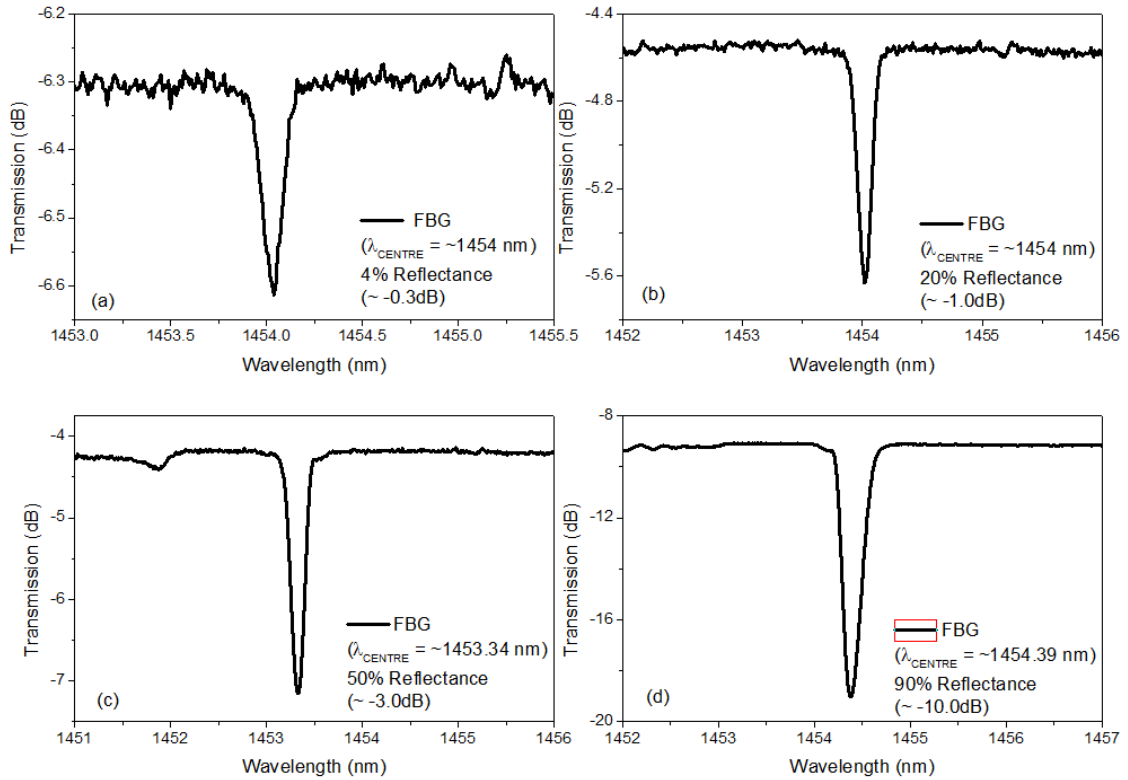


Figure 3.3: Transmission spectra of uniform-period Bragg gratings fabricated using two-beam holographic technique showing different %Reflectance at wavelength ~ 1454 nm (a) 4% (b) 20% (c) 50% (d) 90%.

From figure 3.3 it can be seen that the bandwidths (FWHM at 3dB points) of the four FBGs with different reflectance are between ~0.3nm - ~0.5nm. During the fabrication, the transmission spectra of the FBGs were monitored in real-time on the optical spectrum analyser (OSA). Thereafter, the grating transmittance was utilised for the reflectivity of the FBG using the relationships,

Equation 3.2
$$T = 10 \log_{10} \left(\frac{I}{I_0} \right) dB$$

Equation 3.3
$$T = 100\% - R$$

where T and R are the transmittance and reflectance of the gratings respectively, I is the power intensity (dB) and I_o is the reference power intensity. Table 3.1 shows the calculated values and the experimental outcomes with deviation in centre wavelength to accuracy of $\pm 0.5\text{nm}$. Also, the measurements of grating reflectance as a function of exposure time and writing intensity were recorded during the fabrication. The plots of peak reflectance against exposure time for two trials are as shown in Figure 3.4. Despite using different fabrication methods, the experimental outcomes obtained here are in good agreement with the modelling and experimental results in [2].

Table 3.1: Bragg gratings of different reflectance fabricated using two-beam holographic inscription technique.

FBG Trials	Centre Wavelength (nm)	Reflectance (dB)		Reflectance (%)	% Error
		Calculated Value	Experimental Outcome		
TR1	1454.04	~-0.20	~-0.30	4	0.5000
TR2	1454.16	~-0.20	~-0.28	4	0.4000
TR1	1454.12	~-0.50	~-0.50	10	0.0000
TR2	1454.04	~-0.50	~-0.50	10	0.0000
TR1	1454.15	~-0.97	~-0.90	20	0.0722
TR2	1454.02	~-0.97	~-1.00	20	0.0309
TR1	1454.15	~-1.55	~-1.55	30	0.0000
TR2	1454.42	~-1.55	~-1.57	30	0.0129
TR1	1454.31	~-2.20	~-2.39	40	0.0864
TR2	1453.82	~-2.20	~-2.35	40	0.0682
TR1	1453.34	~-3.00	~-3.00	50	0.0000
TR2	1454.44	~-3.00	~-3.15	50	0.0500
TR1	1454.31	~-4.00	~-4.00	60	0.0000
TR2	1453.57	~-4.00	~-3.90	60	0.0250
TR1	1455.30	~-5.22	~-5.47	70	0.0479
TR2	1453.94	~-5.22	~-5.46	70	0.0728
TR1	1454.09	~-6.90	~-7.90	80	0.1449
TR2	1455.91	~-6.90	~-7.50	80	0.0870
TR1	1456.15	~-10.00	~-9.54	90	0.0460
TR2	1454.38	~-10.00	~-9.92	90	0.0080
TR1	1454.26	~-13.00	~-13.00	96	0.0000
TR2	1454.34	~-13.00	~-13.11	96	0.0085

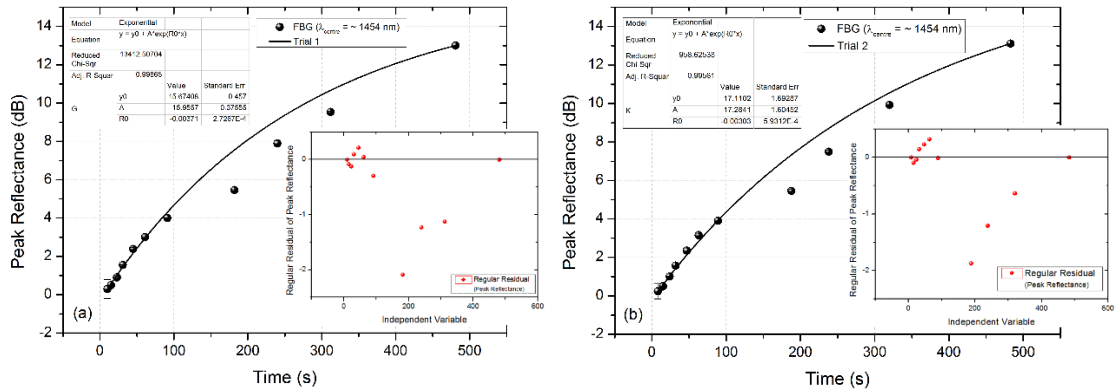


Figure 3.4: Plots of peak reflectance against exposure time with UV-power intensity set at 125mW: (a) FBGs at first trial; inset: residual plot (b) FBGs at second trial; inset: residual plot.

3.2.2 Using phase-mask scanning technique

This inscription technique involves moving the translational UV-beam across the phase mask placed in near-contact to the optical fibre for the fabrication of uniform Bragg grating and complex gratings such as Gaussian apodized Bragg gratings. This fabrication technique allows for less crucial spatial and temporal coherence of the UV-source with great simplicity and reproducibility. Its main advantage is the capability of making high quality complex grating structures. The phase mask has been optimised to suppress the light diffraction energy at zeroth order and maximise diffraction efficiency at each of the diffracted first order (± 1). Figure 3.5(a) shows the image of UV diffraction pattern by the phase-mask indicating the zeroth order (as suppressed) and the diffracted first order (± 1) as maximised while Figure 3.5(b) shows the diffraction pattern with the phase mask placed in near-contact to the optical fibre as taken during the course of the experiment.

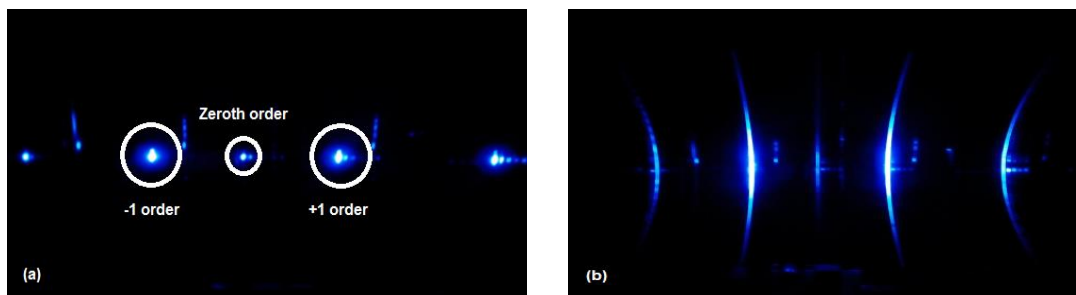
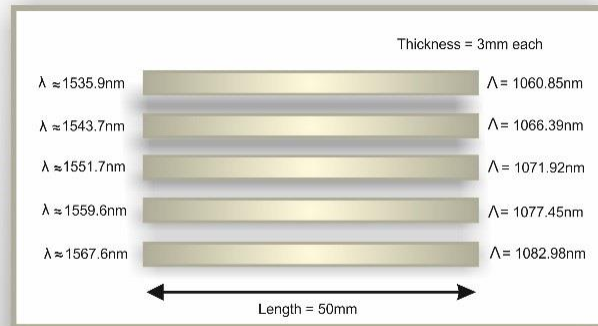


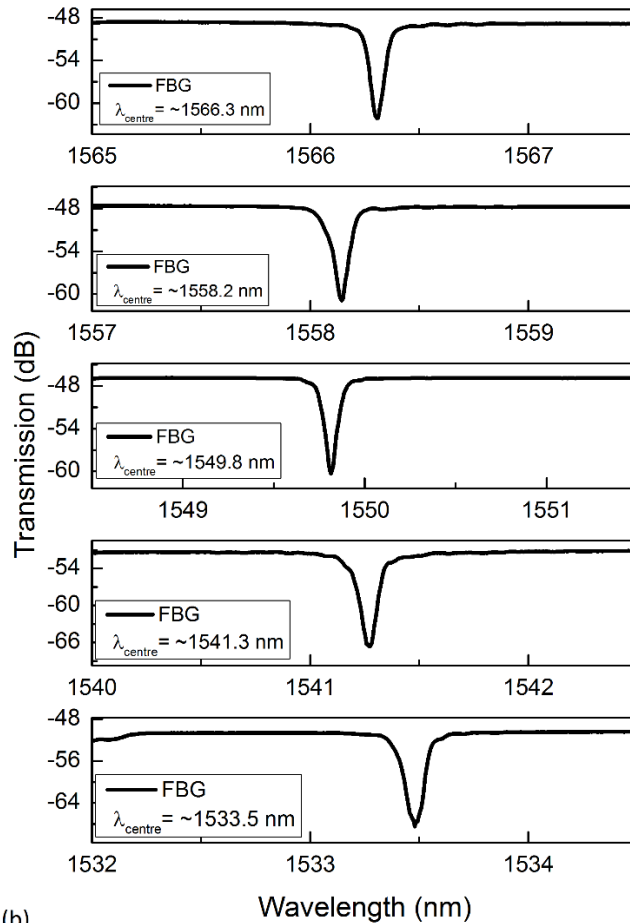
Figure 3.5: UV diffraction pattern as taken during experiment (a) phase mask and (b) phase mask placed in near-contact to optical fibre.

The main limitation of this method is the non-flexibility of writing Bragg gratings at different wavelengths as obtained in the holography method. The Bragg wavelength is

fixed by the period of the phase mask so FBGs at different wavelengths are only inscribed using different phase masks. A phase mask of multiple wavelengths, with scanning length of 50mm, was used to fabricate FBGs at different wavelengths. Figure 3.6(a) shows the structure and specification profile of the multi-wavelength phase mask.



(a)



(b)

Figure 3.6: (a) Schematic of multi-wavelength phase-mask structure; (b) Transmission spectra of FBGs fabricated with multi-wavelength phase mask.

Standard single-mode fibre (SMF-28e Corning), hydrogen loaded in a hydrogen gas chamber set at low temperature (20-70°C) and high pressure (150 atm) which results in hydrogen molecules diffusing into the fibre core so as to enhance photosensitivity, was used for the fabrication of uniform FBGs at the five indicated wavelengths. The stripped fibre was fixed in position on the stage and the phase-mask adjusted to each of the five wavelength for inscription. Figure 3.6(b) shows the transmission spectra of the FBGs fabricated using the multi-wavelength phase mask. After inscription, the FBGs were subjected to thermal annealing at 80°C for 48 hours so as to out-gas the hydrogen from the fibre core and stabilize the grating properties. Consequently, there is slight blue-shift in the centre wavelength to the tune of ~ 0.5nm and a reduction in intensity. This couple with the instability in the writing UV-power drift the centre wavelength to the shorter wavelength by between ~1.3nm – ~2.4nm. Also, stretching the fibre during the inscription process introduces slight strain which vanishes when the fibre is relaxed after UV exposure causing blue-shift in the Bragg centre wavelength. After the fabrication, the spectral profile of the FBG was taken using a broadband source and optical spectrum analyser (OSA) which displays the transmitted spectrum.

3.2.3 Fabrication of (Gaussian) apodized Bragg gratings

The existence of a series of side-lobes on either side of the central reflection peak in the reflection spectrum of a finite length Bragg grating necessitates apodization. Apodization is an optical filtering technique which filters out the unwanted side-lobes. Some applications - such as wavelength division multiplexing (WDM) systems where the side-lobes induce cross talk between information channels - requires lowering or possibly eliminating these side-lobes by apodization. Apodized fibre gratings are known to have very sharp spectra responses and offer improvement to the dispersion compensation characteristics of chirped Bragg grating by linearizing the group delay and eliminating the modulation associated with the side-lobes [3]. A narrow UV writing beam is required when an introduction of a precise apodization profile into the grating is desired however, the writing efficiency decreases as a result [1].

The apodized FBGs were fabricated using the existing experimental setup in Aston Institute of Photonics technologies (AIPT) clean room where the phase mask (multi-wavelength) was mounted on a computer-controlled piezo-electric transducer (PZT) stage. The stage is moved relative to the photosensitive fibre thereby incorporating phase-shifts into the fibre grating during the UV inscription which makes it capable of introducing profiled coupling coefficient in form of complex grating structures. Figure 3.7 shows the reflection spectrum of typical FBG with the side-lobes. Hydrogen loaded SMF-

28 fibres were used for the Gaussian apodized Bragg gratings and their transmission and reflection spectra were recorded using an OSA as shown in figure 3.8 below. Annealing of apodized Bragg gratings was under 80°C for 48 hours like that of the uniform Bragg gratings. As clearly seen, the side-lobes are significantly suppressed when the Bragg grating is apodized with a Gaussian profile.

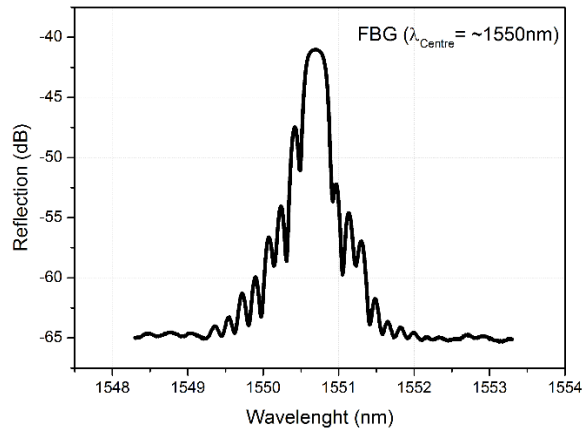


Figure 3.7: Reflection spectrum of un-apodized Bragg grating showing side-lobes.

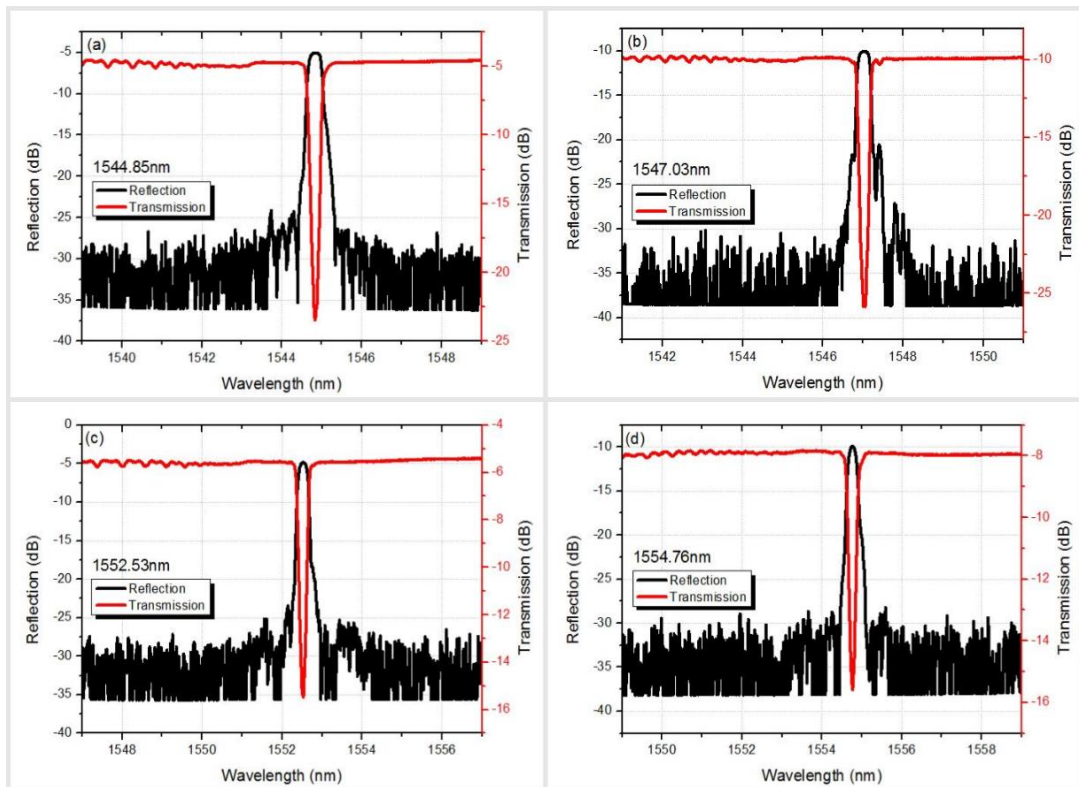


Figure 3.8: Transmission and reflection spectra of Gaussian apodized Bragg gratings with centre wavelengths at (a) ~1544nm (b) ~1547nm (c) ~1552nm (d) ~1554nm.

3.2.4 FBG sensing characteristics

The Bragg wavelength shifts when subjected to external perturbations like temperature, strain or pressure which results in changes in the grating pitch and refractive index. This is due to the dependence of the Bragg grating resonance on the effective index of the fibre core and the periodicity of the grating as shown by the expression in Eqn. 3.4 below,

$$\text{Equation 3.4} \quad \Delta\lambda_B = 2 \left\{ \Lambda \frac{\partial n_{eff}}{\partial T} + n_{eff} \frac{\partial \Lambda}{\partial T} \right\} \Delta T + 2 \left(\Lambda \frac{\partial n_{eff}}{\partial l} + n_{eff} \frac{\partial \Lambda}{\partial l} \right) \Delta l$$

The first term in eqn. 3.4 represents the thermal effect on the optical fibre which corresponds to grating space change and the thermo-optical effect on the effective refractive index. The thermo-optical effect is expressed in the Eqn. 3.5 as [4],

$$\text{Equation 3.5} \quad \Delta\lambda_B = \lambda_B (\alpha_\Lambda + \alpha_n) \Delta T$$

$$\text{Equation 3.6} \quad \alpha_n = \left(\frac{1}{\Lambda} \right) \left(\frac{\partial \Lambda}{\partial T} \right)$$

$$\text{Equation 3.7} \quad \alpha_\Lambda = \left(\frac{1}{n_{eff}} \right) \left(\frac{\partial n_{eff}}{\partial T} \right)$$

Where Eqn. 3.6 expresses the fibre thermal expansion coefficient, Eqn. 3.7 represents the thermo-optical coefficient. The sensing characterisation of FBG to thermal response was experimentally investigated using the earlier fabricated FBGs at $\sim 1310nm$ (holography technique) and $\sim 1500nm$ (phase mask scanning technique) wavelengths.



Figure 3.9: Experimental setup for FBG thermal characterisation.

The temperature sensing experimental setup is as shown in Figure 3.9 where the FBGs are fixed on a metal heated plate (Peltier) in succession. The grating region, which is approximately $\sim 12\text{mm}$ in length, is centred on the Peltier to ensure the whole grating structure is subjected to thermal variation. The broadband source (BBS) transmits light through the FBGs while the temperature controller (Light Wave LDT-5910B) sets the temperature range from 0°C to 80°C and the spectral response at each temperature was displayed and recorded on the OSA for spectral analysis. The centre wavelength shifts as the temperature increases. Figure 3.10 shows the thermal response of FBG at centre wavelength $\sim 1310\text{ nm}$ respond to temperature increment ($0^\circ - 80^\circ\text{C}$) and decrement ($80^\circ - 0^\circ\text{C}$) with a plot of wavelength shift against temperature. This temperature sensor has a sensitivity of $10.0 \pm 0.1\text{ pm}/^\circ\text{C}$ ($80^\circ - 0^\circ\text{C}$) and $9.30 \pm 0.21\text{ pm}/^\circ\text{C}$ ($0^\circ - 80^\circ\text{C}$) with coefficients of determination 0.998 and 0.992 respectively. The insets are the residual plots of the FBG response to thermal change which show suitability of a linear model.

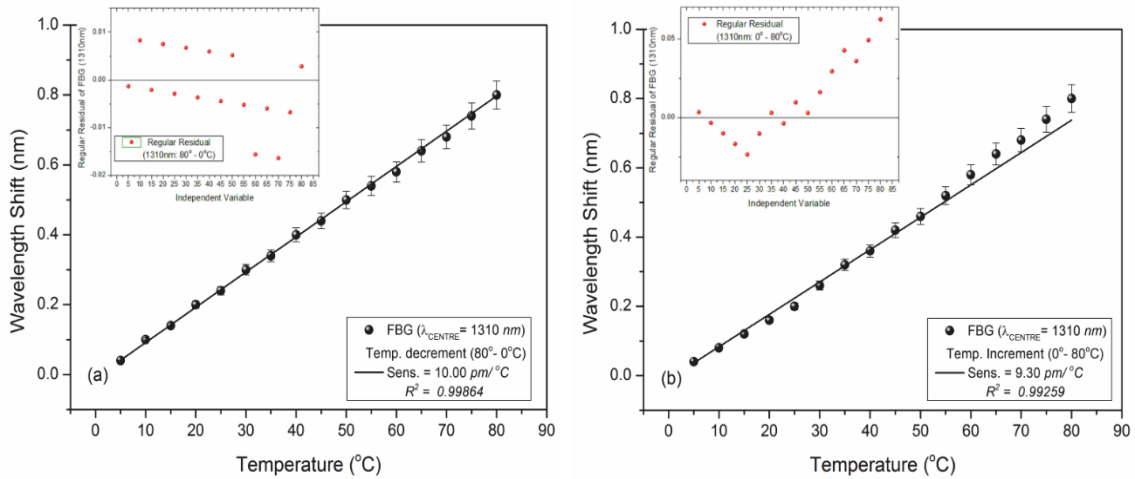


Figure 3.10: FBG thermal response at wavelengths (a) $\sim 1310\text{nm}$ ($80^\circ - 0^\circ\text{C}$) and (b) $\sim 1310\text{nm}$ ($0^\circ - 80^\circ\text{C}$); Insets: regular residual plots of each linear fit.

The sensitivity of the FBGs fabricated with the multi-wavelength phase mask to thermal variation was also investigated. Figure 3.11(a) shows the spectra evolution of the FBG to thermal variation as temperature increases from $0^\circ - 80^\circ\text{C}$. Slightly higher sensitivities were recorded for the FBGs at 1500 nm range compared to that at 1310 nm as obvious in Figure 3.11(b-e). The recorded sensitivities are $11.10 \pm 0.19\text{ pm}/^\circ\text{C}$ (1567nm); $10.80 \pm 0.35\text{ pm}/^\circ\text{C}$ (1551nm); $10.10 \pm 0.37\text{ pm}/^\circ\text{C}$ (1543nm) and $\sim 10.71 \pm 0.18\text{ pm}/^\circ\text{C}$ (1535nm). The results are in good agreement with literature [5] as linear correlation exists between the variables. The insets are the regular residual plots showing random scatter-residuals that do not contradict the linear assumption. The overall results also indicate that FBG at longer wavelength have higher thermal sensitivity.

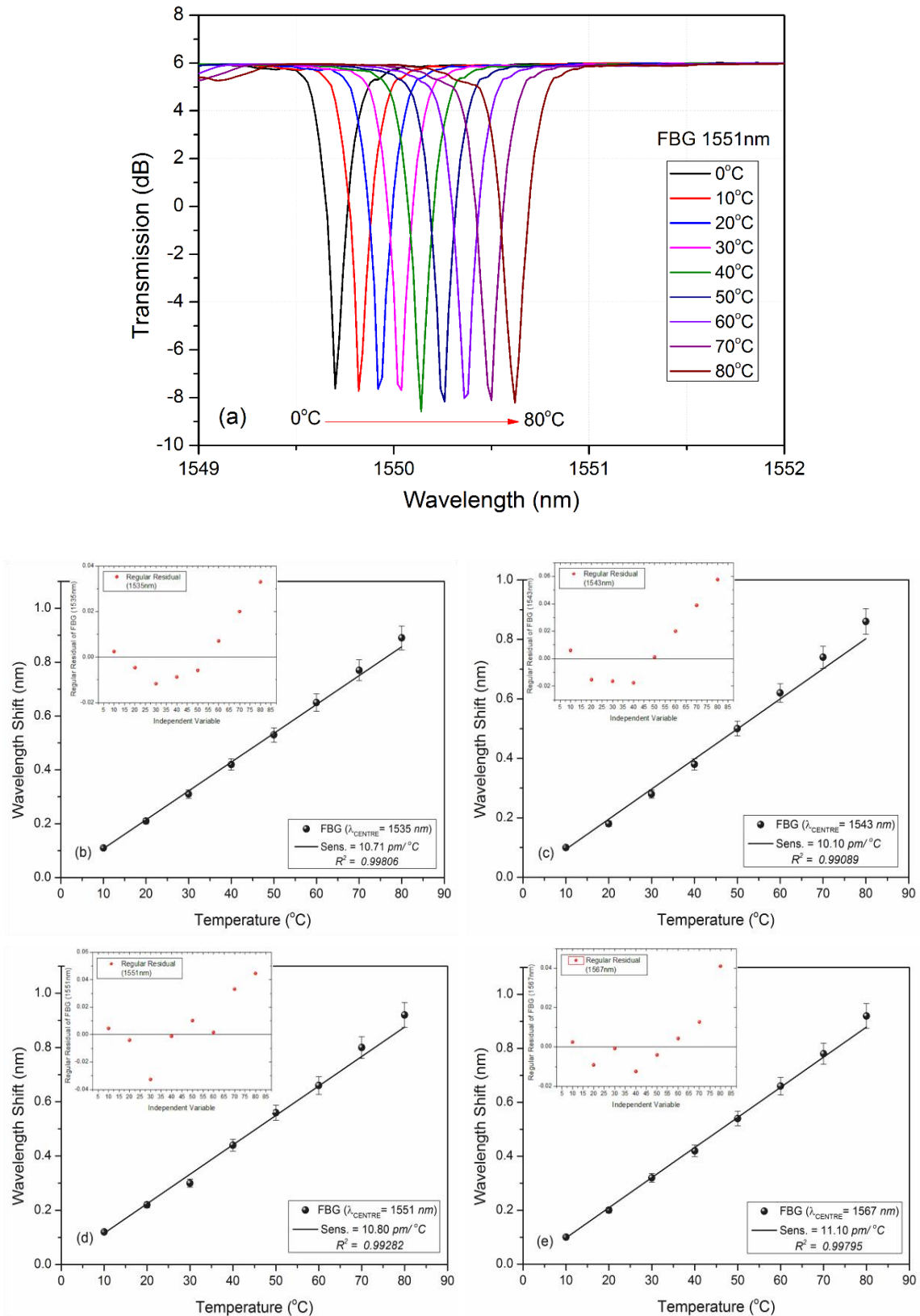


Figure 3.11: (a) Transmission spectrum of FBG at ~1551nm showing spectra evolution to thermal variation; FBG thermal response at; (b) ~1535nm (c) ~1543nm (d) ~1551nm (e) ~1567nm. Insets: regular residual plots of each linear fit.

The effect of strain on an optical fibre is represented by the second term in eqn. 3.4. The FBG wavelength shifts, due to the strain expansion, change the effective refractive index and the grating spacing. The strain effect term is expressed in Eqn. 3.8 as [4],

Equation 3.8
$$\Delta\lambda_B = \lambda_B (1 - p_e) \varepsilon_z$$

Where the effective strain-optic constant p_e is expressed as

Equation 3.9
$$p_e = \frac{n_{eff}^2}{2} (p_{12} - \nu(p_{11} + p_{12}))$$

The components of strain-optic tensor are p_{11} and p_{12} , while ν is the Poisson's ratio. The experimental setup for strain sensing is as shown in Figure 3.12 where the FBG was firmly (not too tight) clamped on a 3D translational stage at each end separated at a set distance of 'x cm' (usually set at ~ 40 cm for my experiments) to ensure grating region is centralised and suspended freely in air. One end of the translational stage was fixed in position while force was applied through the other end to strain the grating. This was achieved by turning the micrometre adjustment knob (capable of longitudinal motion) attached to the translational stage from ~ 0mm – ~ 0.35mm at interval of ~ 0.05mm away from the fixed end thereby pulling the grating apart to induce a total strain of 750µε. The reference was set at ~ 0mm (in air) on the micrometre and all measurements taken are with respect to the reference. Light was transmitted from a broadband light source through the FBGs and the spectra profile displayed on the optical spectrum analyzer.



Figure 3.12: Experimental setup for FBG strain characterisation.

The experimental results from strain response of FBGs at 1310 nm and 1550 nm are as plotted in Figure 3.13. From the figure it can be clearly seen that the FBG at 1310 nm has a sensitivity of $1.05 \pm 0.07 \text{ pm}/\mu\epsilon$ while that at 1550 nm has a slightly higher sensitivity of $1.18 \pm 0.06 \text{ pm}/\mu\epsilon$. Both strain sensors have resolution of approximately ± 0.05 . The results obtained are in good agreement with earlier report on FBG strain sensing [6].

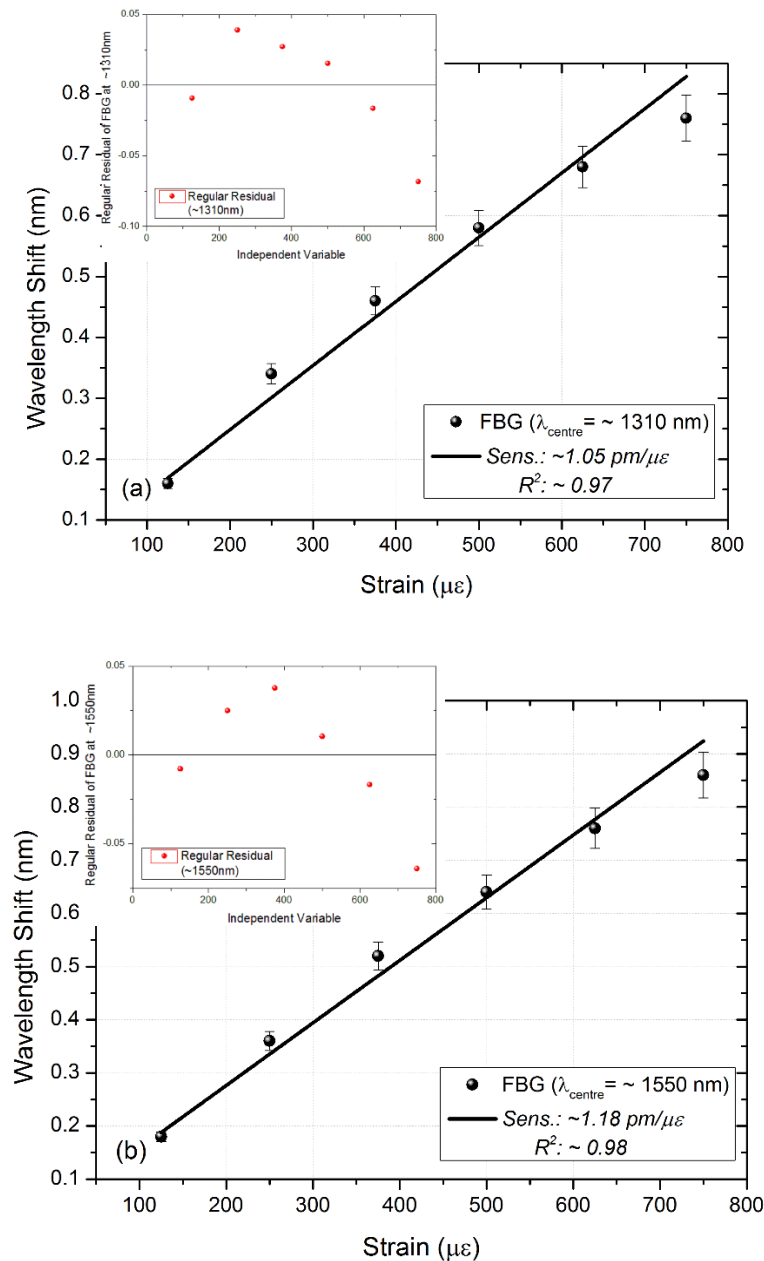


Figure 3.13: FBG strain response at: (a) $\sim 1310 \text{ nm}$ and (b) $\sim 1550 \text{ nm}$. Insets: regular residual plots of each linear fit.

3.3 LPFGs inscription and sensing characteristics

This section presents theoretical and experimental investigation of long-period fibre gratings (LPFG). The theory literarily explains the principle that underpin the characteristics of LPFGs. While the experiments confirm such principles, they also detail the fabrication of LPFGs at different periods and investigate their response to external perturbations such as temperature and refractive index variations.

As earlier mentioned, LPFGs have long grating periods ranging from $\sim 10\mu\text{m}$ to $\sim 600\mu\text{m}$ which enables them to couple light from fundamental core mode to co-propagating cladding modes. There have been several techniques reported for the fabrication of LPFGs [7-11], but the most prevalent ones remain the point-by-point and amplitude mask scanning inscriptions. All LPFGs fabricated and reported in this thesis made use of the point-by-point inscription (earlier discussed in session 2.5.3) using a 244nm frequency-doubled UV-laser. LPFGs with different grating periods (Λ) at $140\mu\text{m}$, $250\mu\text{m}$, $350\mu\text{m}$, $400\mu\text{m}$, were UV-inscribed in hydrogen-loaded single-mode standard telecom fibre (SMF-28, Corning). As discussed in session 2.2.3, hydrogen loading technique entails diffusing hydrogen molecules into the fibre cladding and core at low temperature and high pressure. This hydrogen-diffusion increases the refractive indices of both fibre cladding and core which consequently shifts the grating resonance. While this effect could be meagre in Bragg gratings with annealing for 48 hours at 80°C shifting the Bragg resonance for only about $\sim 0.5\text{nm}$, it could be as much as over $\sim 100\text{nm}$ shift in long period fibre gratings.

The LPFG ($\Lambda = 350\mu\text{m}$) fabricated in hydrogen-loaded SMF-28 was used to investigate the effect of hydrogen out-diffusion from the fibre core and cladding. During fabrication, the transmission spectrum of the LPFG was monitored on the OSA (YOKOGAWA: AQ6370D) and recorded as 'before annealing'. In order to stabilize the grating structure, the LPFG was annealed for 48 hours at 80°C to out-diffuse the residual hydrogen molecules in the fibre core and cladding, which were not part of the photochemical reaction during the grating inscription. The transmission spectra of the LPFG before and after annealing are optically characterised using supercontinuum laser source (Fianium) and OSA spanning across wavelength range 1200nm to 1700 nm shown in Figure 3.14.

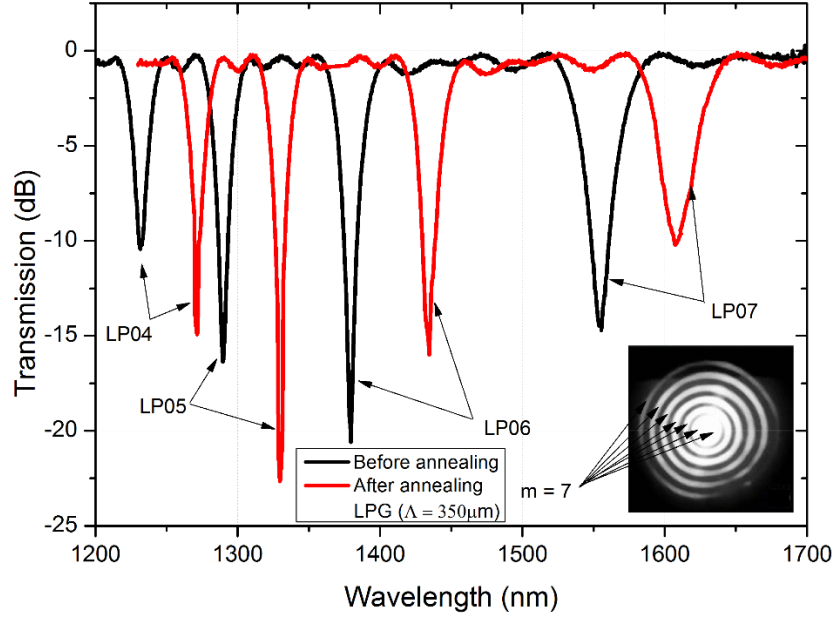


Figure 3.14: Transmission spectra of LPFG ($\Lambda = 350\mu\text{m}$) before and after annealing. Inset: near mode field image as observed by near-infra-red camera.

It can be clearly seen that resonant wavelengths red-shift after annealing when the hydrogen molecules have been out-diffused from the fibre. The higher order modes $LP07$ and $LP06$ have relatively larger red-shifts of $\sim 95\text{nm}$ and $\sim 54\text{nm}$ respectively when compared with lower order modes $LP04$ and $LP05$ which have red-shift of $\sim 39\text{nm}$ and $\sim 41\text{nm}$ respectively. Also, the higher order modes $LP06$ and $LP07$ both witnessed a reduction in attenuation band of around $\sim 5\text{dB}$ after annealing while the lower order modes $LP04$ and $LP05$ witnessed increment in attenuation band of $\sim 5\text{dB}$ and $\sim 7\text{dB}$ respectively. This as a result of change in coupling coefficient before and after annealing which is caused by variation in UV-induced index modulation. The factors that determine the shift in direction of the resonant wavelength peaks when subjected to temperature change are: fibre dispersion factor (γ) and the thermal dependence of the waveguide dispersion ($\Gamma_{thermal}$). When the cladding mode order is less than or equal to 7 ($m \leq 7$), the value of fibre dispersion factor is positive, therefore subsequent peaks shift direction only depends on the value of $\Gamma_{thermal}$ which can be expressed as [15],

Equation 3.10

$$\Gamma_{thermal} = \frac{\xi_{co} n_{co}^{eff} - \xi_{cl} n_{cl,m}^{eff}}{n_{co}^{eff} - n_{cl,m}^{eff}}$$

where ξ_{co} and ξ_{cl} are the thermo-optic coefficients of the fibre core and cladding materials, respectively. Since the effective refractive index of core in hydrogenated fibre, is always larger than the refractive index of cladding, then the denominator of the above

expression $(n_{co}^{eff} - n_{cl,m}^{eff})$ is always positive. After annealing, the core effective RI (n_{co}^{eff}) will decrease sharply compare with the cladding effective RI ($n_{cl,m}^{eff}$). Also, the numerator $(\xi_{co} n_{co}^{eff} - \xi_{cl} n_{cl,m}^{eff})$ will be positive and all the resonant wavelength peaks ($m \leq 7$) will red-shift. This is as a result of the change in coupling coefficient as the UV-induced index modulation changed after the annealing.

Meanwhile, to determine which cladding modes are linearly polarised (LP) and have maximum coefficient of coupling to the fundamental core mode [12], the LPFG ($\Lambda = 350\mu m$) was connected to a tunable laser, (TSL-210: Santec) having a tunable range 1530nm - 1630nm, to one end of the LPFG sample as a single wavelength light source. The other end of the LPFG sample was cleaved at the grating end to observe the near mode field with the help of a near infra-red camera (IR camera 72904). As can be seen in Figure 3.14 inset, the intensity distribution of the near mode field pattern as observed at the longest wavelength (~1609nm) indicates that the resonant dips were coupled from the fundamental core mode $LP01$ to co-propagating cladding modes $LP04$, $LP05$, $LP06$, and $LP07$ as labelled in the figure.

The fibre can be modelled as a two waveguide structure; the first being high-index core surrounded by lower-index cladding and the second is the cladding surrounded by air. The minimum transmission of the attenuation band is governed by the expression in Eqn. 3.11 [13]:

$$\text{Equation 3.11} \quad T_m = 1 - \sin^2(\kappa_i L)$$

where κ_i is the coupling coefficient for the i^{th} cladding mode which can be determined by the overlap integral of the core and cladding mode, and L is the length of the LPFG. Theoretical analysis has shown that efficient coupling exists only between fundamental core mode and co-propagating cladding modes with large overlap integral (have similar electric field profile) [14]. The coupling strength of the LPFG is proportional to the length of scans when the scan velocity and the UV power are kept constant/unchanged. This was experimentally investigated using LPFG ($\Lambda = 400\mu m$) fabricated in hydrogen-loaded SMF-28. The spectra transmission is captured for different lengths of UV exposure with further scanning. At first, as the shape of transmission changes the resonance wavelengths shift to longer wavelengths. With continuous UV exposure, the coupling coefficient of $LP06$ reaches maximum where the core mode is wholly coupled to the fibre

cladding at that resonant wavelength (λ_{06}) which results in the largest resonance attenuation.

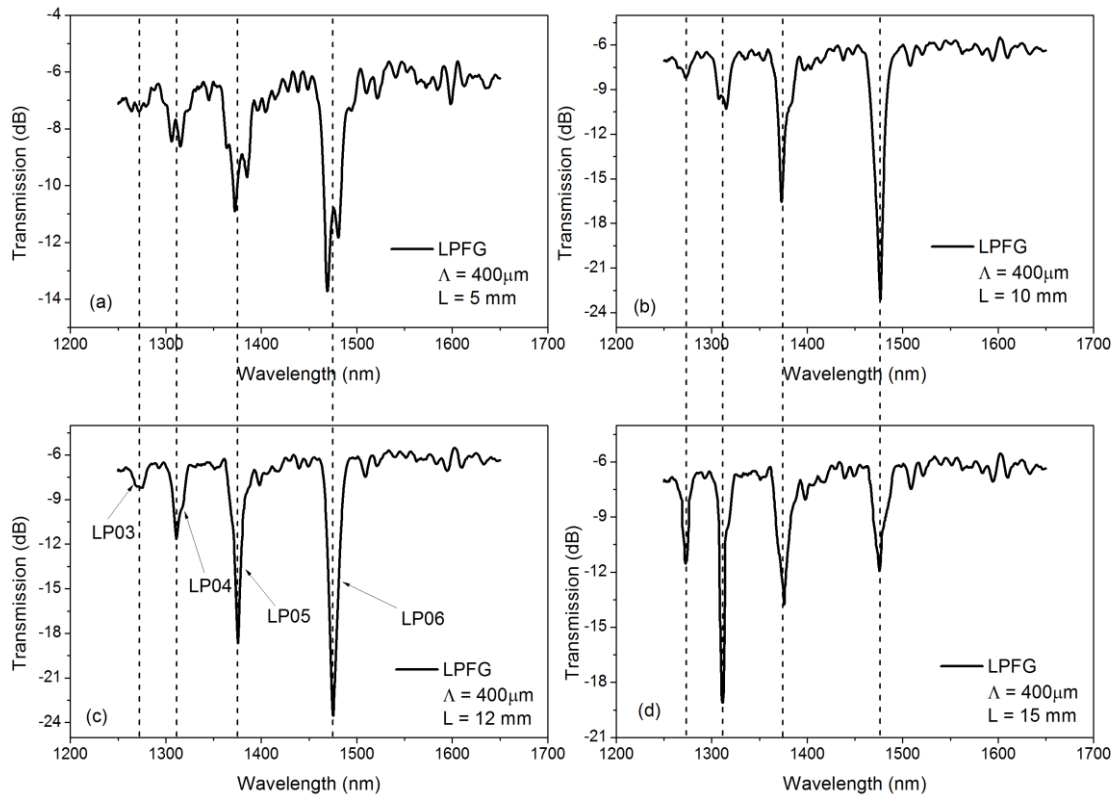


Figure 3.15: Transmission spectra of LPFG ($\Lambda = 400\mu\text{m}$) with increasing UV exposure: (a) $L = 5\text{mm}$, (b) $L = 10\text{mm}$, (c) $L = 12\text{mm}$ and (d) $L = 15\text{mm}$.

Then, with further UV exposure, the coupling coefficient at (λ_{06}) begins to reduce as the core mode is gradually coupled back into the fibre core. At this point the resonance wavelength builds up more at the shorter wavelength till resonant wavelength $LP04$ becomes maximum resonance attenuation. The transmission spectra are as shown in Figure 3.15 where the dependence of transmission on grating length (UV exposure) is been experimentally evaluated.

3.3.1 Dual-peak LPFGs

Shu et al. [15] pointed out that for each mode that exhibits a turning point in its phase matching curve, a specific LPFG period corresponds to two resonant attenuation bands which results in coupling to a single cladding mode characterised by dual attenuation peaks in the transmission spectrum. These turning points appear at longer wavelengths for lower order modes with gradual shift to shorter wavelengths as the mode order increases and they determine the condition of maximum sensitivity for each cladding

modes. In other words, LPFG can be optimised for high sensitivity at a particular wavelength by selecting a cladding mode and period close to the turning point. Therefore, it is anticipated that LPFG dual resonant peaks can be achieved when the core mode is coupled to a single cladding mode provided the grating period is smaller than, but close to, that of the turning point [15]. The dual resonant peak feature has been proven to be visible for LPFGs with relatively short periods ($\Lambda \leq 160\mu\text{m}$) in an extended wavelength range of $\sim 900\text{nm} - \sim 2\mu\text{m}$.

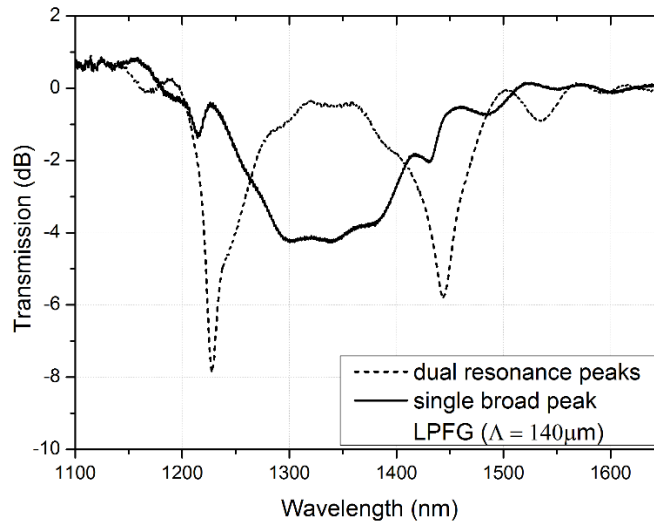


Figure 3.16: Transmission spectra of LPFG ($\Lambda = 140\mu\text{m}$) measured during UV inscription: dual resonance peak (dashed line) were observed to coalesce in a single peak (solid line).

Experimentally, a period (Λ) of $140\mu\text{m}$ was chosen to generate dual resonant peak LPFGs with corresponding mode order $m = 13$, UV-inscribed in a hydrogen-loaded SMF-28 (Corning). The prolonged UV-exposure reported in [15] was investigated with the LPFG ($\Lambda = 140\mu\text{m}$) where the resonance attenuation is close to the dispersion turning point. The two resonant peaks moved closer to each other and eventually coalesce as shown by the solid line in Figure 3.16. Experimental observation has shown that the turning points occurred at a shorter wavelength with increasing mode order. Despite the coalescence at fabrication, sensing measurements separate the dual resonance peaks as presented in the next session.

A reduction in the cladding radius shifts the dispersion turning point to longer wavelength range compared with the standard SMF-28 of $62.5\mu\text{m}$ cladding radius [16]. Analysis of the dual peak LPFGs UV-inscribed in $80\mu\text{m}$ diameter cladding fibre with $4.8\mu\text{m}$ core size was made. Due to the reduction in the fibre cladding diameter ($80\mu\text{m}$), the dispersion turning point of cladding mode has shifted to lower order cladding mode compared with the normal $125\mu\text{m}$ cladding fibre. As the simulated result has shown (Fig. 3.17(a)), at the

near-infrared range, the turning point started from cladding mode $HE_{1,4}$. According to the calculation result, the dual-peak would appear at the $HE_{1,6}$ with the wavelength of 1520nm and 1740nm, and there is a peak of $HE_{1,5}$ at around 2320nm. LPFGs of period $300\mu\text{m}$ were UV inscribed (95mW) in a non-hydrogenated boron-germanium (B/Ge) co-doped thin cladding ($40\mu\text{m}$ radius) fibre (Nortel) at a speed of 0.1mm/s and grating length of 24mm . The experimental outcome shows successful dual resonant peak LPFGs fabricated as far as in near infra-red region. Figure 3.17(a)(b) shows the transmission spectra of the LPFGs ($\Lambda = 300\mu\text{m}$) with the little variation in centre wavelengths due to unstable UV-laser power. Also, these LPFGs were specially selected for sensitivity measurements as presented in the next session.

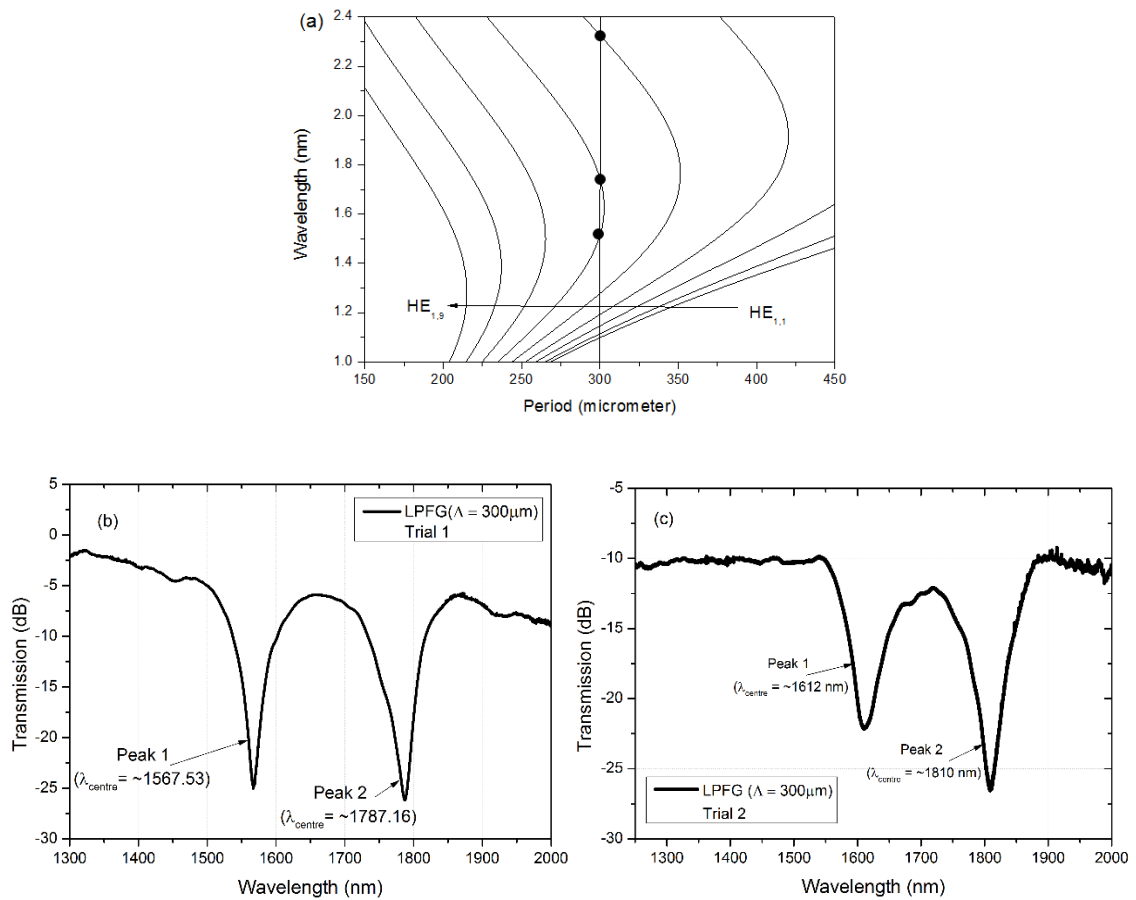


Figure 3.17: (a) The simulation results of $80\mu\text{m}$ diameter cladding size fibre with $4.8\mu\text{m}$ core size; (b) Transmission spectra of UV-inscribed LPFGs ($\Lambda = 300\mu\text{m}$) in B/Ge co-doped thin cladding fibre: dual resonant peaks observed: trial 1; (c) trial 2.

Furthermore, LPFGs ($\Lambda = 250\mu\text{m}$ and $200\mu\text{m}$) were inscribed in the B/Ge co-doped thin cladding fibre. The transmission spectrum of that of LPFGs ($\Lambda = 250\mu\text{m}$) was probed further into the mid infra-red region where some resonant peaks were discovered and

subjected to sensing. Figure 3.18 shows the transmission spectra of the LPFGs ($\Lambda = 250\mu\text{m}$ and $200\mu\text{m}$) as observed on the OSA.

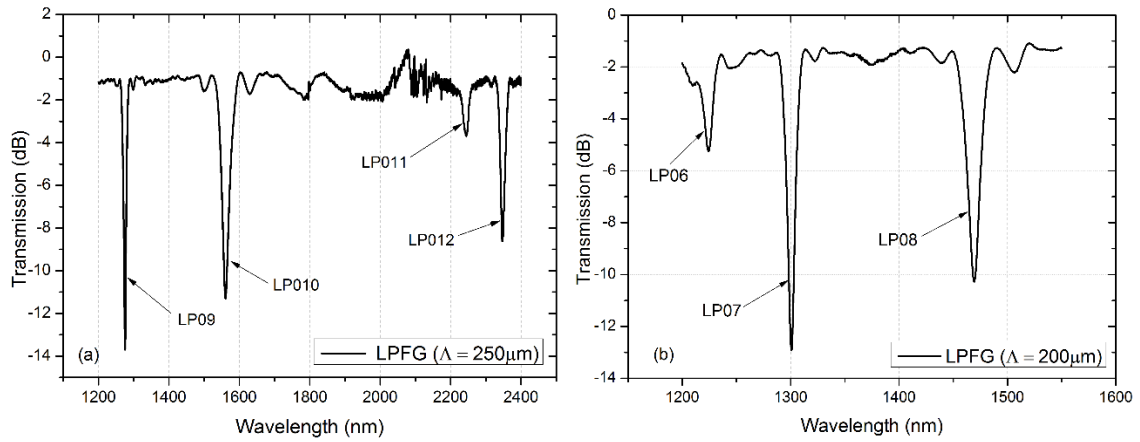


Figure 3.18: Transmission spectra of LPFGs measured during UV inscription in B/Ge co-doped thin-cladding fibre with period of (a) ($\Lambda = 250\mu\text{m}$) (b) ($\Lambda = 200\mu\text{m}$).

3.3.2 LPFG thermal and SRI sensing characteristics

Long-period fibre gratings are known to be important sensors of environmental conditions (such as temperature, strain, surrounding refractive index variation, pressure and so on). This session focuses mainly on experimental evaluation of LPFGs as sensors of temperature and surrounding refractive index (SRI) variation with theoretical explanation behind the principles.

Deriving analytic expressions for the thermal sensitivity ($d\lambda_{res}/dT$) and SRI sensitivity ($d\lambda_{res}/dn_{sur}$) requires the differentiation of Eqn. 2.34 as follows [15],

Equation 3.12
$$\frac{d\lambda_{res}}{dT} = \lambda_{res} \cdot \gamma \cdot (\alpha + \Gamma_{thermal})$$

Equation 3.13
$$\frac{d\lambda_{res}}{dn_{sur}} = \lambda_{res} \cdot \gamma \cdot \Gamma_{sur}$$

where α is the thermal expansion coefficient of the fibre, γ (known as general sensitivity factor) describes the waveguide dispersion which is expressed by Eqn. 3.14 as [17],

Equation 3.14

$$\gamma = \frac{\frac{d\lambda_{res}}{d\Lambda}}{n_{co}^{eff} - n_{cl,m}^{eff}}$$

With thermal dependence of the waveguide ($\Gamma_{thermal}$) already expressed by eqn. 3.10, the SRI dependence of the waveguide (Γ_{sur}) can be expressed as [15],

Equation 3.15

$$\Gamma_{sur} = -\frac{u_m^2 \lambda_{res}^3 n_{sur}}{8\pi r_{cl}^3 n_{cl} (n_{co}^{eff} - n_{cl,m}^{eff}) (n_{cl}^2 - n_{sur}^2)^{3/2}}$$

where r_{cl} and n_{cl} are the radius and refractive index (RI) of the fibre cladding respectively, u_m is the m^{th} root of the zeroth-order Bessel function of the first order kind. As earlier explained, it is worth noting that at each turning points, $|d\lambda_{res}/d\Lambda| \rightarrow \infty$ and therefore $|\gamma| \rightarrow \infty$ making the turning point a determinant for the condition of maximum sensitivity for each cladding mode [18].

The sensing characteristics of LPFGs was investigated experimentally using the two different sets of dual peak LPFGs ($\Lambda = 140\mu m$ and $\Lambda = 300\mu m$) earlier presented. The experimental setup for the thermal sensing for LPFGs is as shown in Figure 3.19 where the LPFGs are laid flat (to prevent the effect of strain and bending) on the Peltier and caged to prevent heat escape. The temperature controller adjusts the temperature from 10° to 80°C at intervals of 10°C. One end of the LPFG is connected to the supercontinuum light source and the other end to the OSA for spectral measurement. It is worthy of noting that for the thermal sensing, all measurements were taken with air as the surrounding medium



Figure 3.19: Experimental setup for measuring thermal sensing of LPFGs.

The SRI experimental setup is as shown in Figure 3.20, the LPFG was mounted on a translational stage at each end and suspended across a micrometre stage to which was attached the test solution platform. Series of index gels (Cargille Laboratory) with different refractive indices ranging from 1.300 to 1.444 were applied to the LPFGs and their spectral evolution in response to SRI variation was recorded and evaluated. In order to prevent wavelength shift induced by bending and axial strain, the translational stages on which the LPFGs are firmly clamped are ensured to be of equal height. The index gels were intermittently dropped on glass slides in which the grating is submerged for the sensing measurement. Once surrounded by the gel, the wavelength shift was instantaneous as observed on the optical spectrum analyzer (OSA). For measurement accuracy, the grating was rinsed with methanol after administering each index gel to remove residual oil sticking to the fibre prior to applying subsequent gels and ensure it returned to initial state in air (reference point).



Figure 3.20: Experimental setup for measuring surrounding refractive index sensing of LPFGs.

The coalesced dual-peak LPFG ($\Lambda = 140\mu\text{m}$) was subjected to thermal sensing over a temperature range $10^{\circ} - 80^{\circ}\text{C}$ at 10°C interval, but due to its broad spectrum no meaningful measurement could be taken from the experiment. However when subjected to SRI measurement, it responded with high sensitivity. It was submerged in index gels with refractive index ranging from 1.300 – 1.440 one at a time. The transmission spectra evolution of the response of the LPFG to the SRI variation was captured on the OSA as shown in Figure 3.21(a). As could be observed in the figure, with the submergence of the LPFG in the first index gel (1.300) the dual peak separated from the single coalesced attenuation band confirming that the dual peak actually coalesce during fabrication.

The two peaks continue to drift apart as the SRI increases in value and their wavelength shift was plotted against the varying SRI as shown in Figure 3.21(b). The resonance peak drifting towards the shorter wavelength is termed 'Peak 1' while the other that drifts towards longer wavelength is termed 'Peak 2' for ease of analysis and referral. Peak 1

showed a sensitivity of $-278.20 \pm 20.59 \text{ nm/RIU}$ for index range 1.300 – 1.395 and $-1541.10 \pm 144.35 \text{ nm/RIU}$ for index range 1.404 – 1.440 while Peak 2 recorded a higher sensitivity of $569.70 \pm 32.56 \text{ nm/RIU}$ for index range 1.300 – 1.395 and $4400.40 \pm 692.31 \text{ nm/RIU}$ for index range 1.404 – 1.440. Experimentally, the LPFG ($\Lambda = 140\mu\text{m}$) has been shown to exhibit high sensitivity to surrounding refractive index variation.

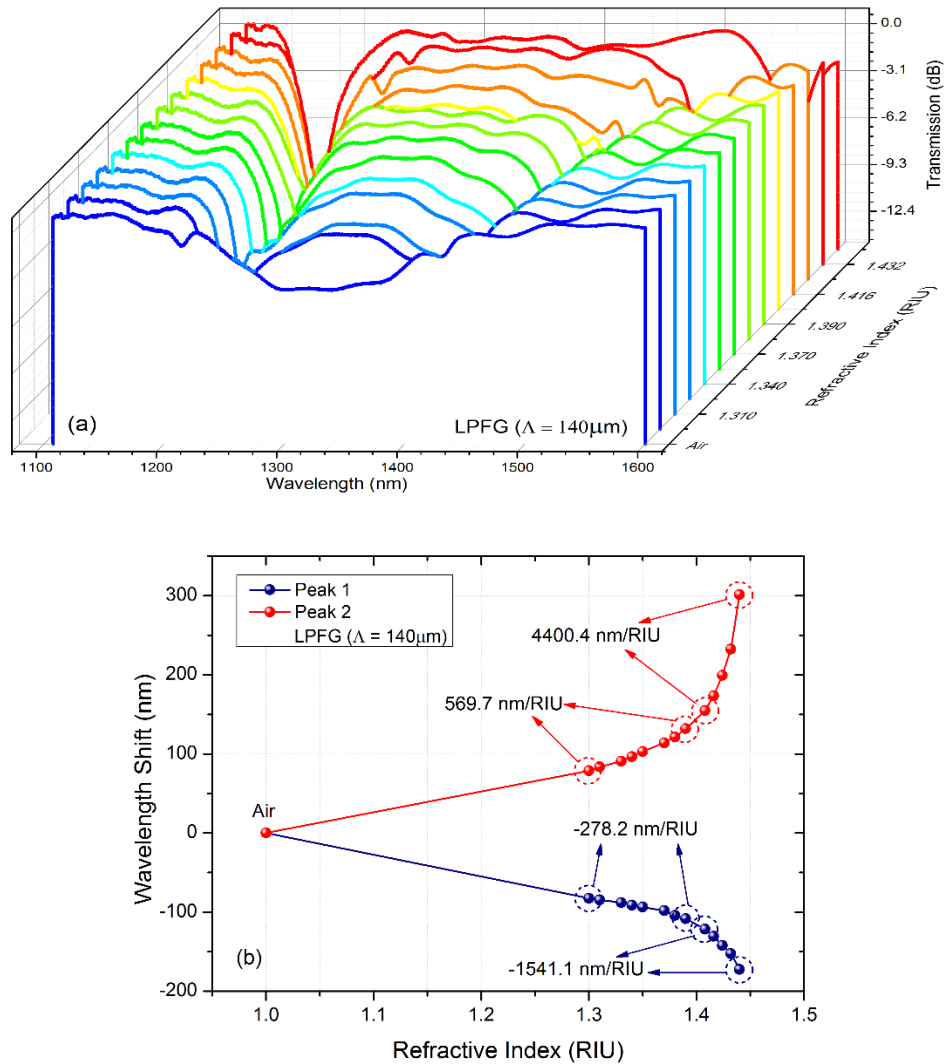


Figure 3.21: (a) Transmission spectra evolution of LPFG ($\Lambda = 140\mu\text{m}$) in response to SRI variation (b) Plots of wavelength shift of the dual peaks against surrounding refractive index variation.

The dual-peak LPFG ($\Lambda = 300\mu\text{m}$) inscribed in B/Ge co-doped thin cladding fibre was also subjected to thermal and SRI sensing. Since this LPFG was not overexposed to UV-light, distinct dual-peaks are directly observable in its transmission spectrum as earlier shown in Figure 3.17. The dual-peak LPFG was used for SRI sensing by intermittently submerging it in index gels with refractive index ranging from 1.300 – 1.412. As the SRI increases along the selected range, its spectra evolution was observed on the OSA as shown in Figure 3.22(a). Figure 3.22(b) shows the plot of wavelength shift

against surrounding refractive index where the first peak 'Peak 1' showed a sensitivity of $-330.17 \pm 43.41 \text{ nm/RIU}$ ($R^2: 0.95$) for index range 1.300 – 1.360 and $-707.21 \pm 44.35 \text{ nm/RIU}$ for index range 1.360 – 1.412 while higher sensitivities of $654.19 \pm 74.70 \text{ nm/RIU}$ for index range 1.300 – 1.360 and $1725.30 \pm 152.43 \text{ nm/RIU}$ for index range 1.360 – 1.412 were recorded for the second peak 'Peak 2'.

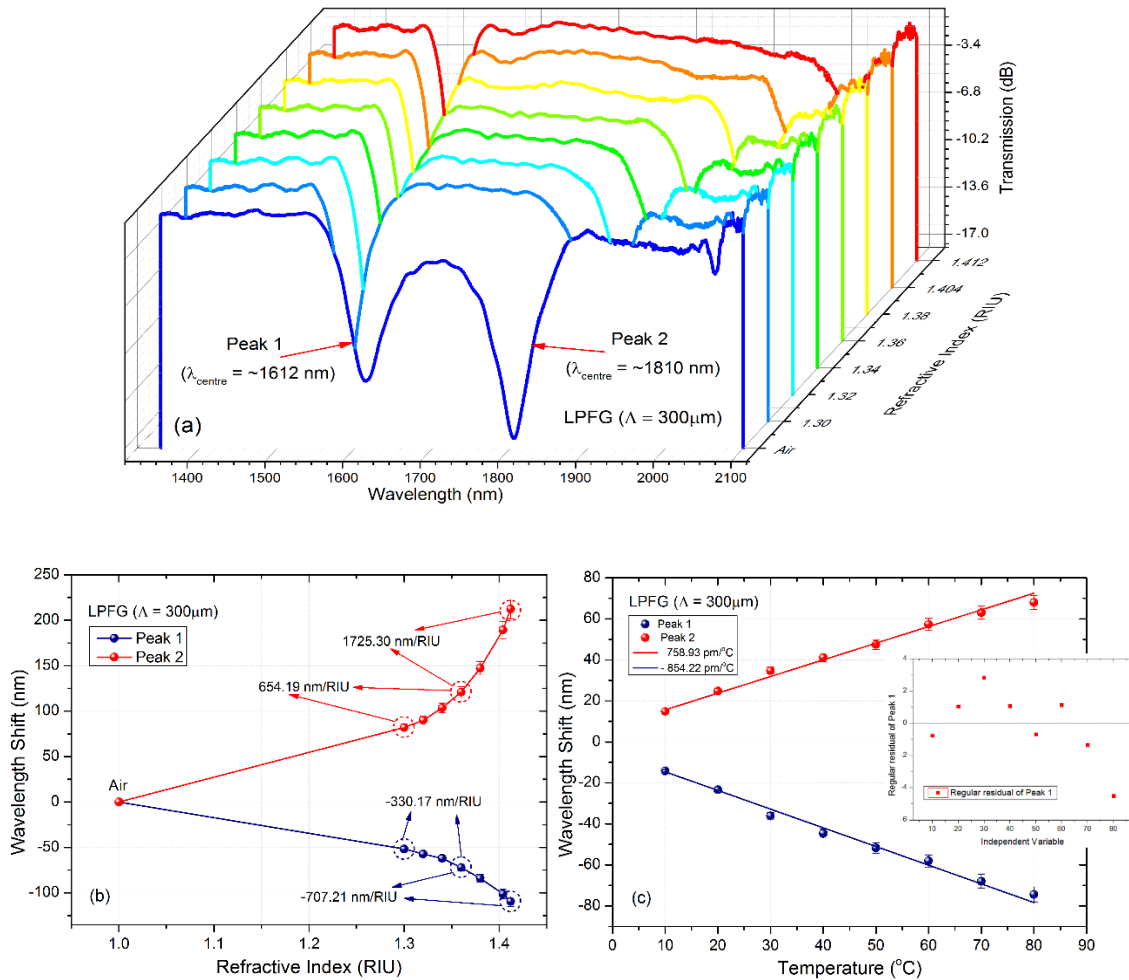


Figure 3.22: (a) Transmission spectra evolution of a dual peak LPFG ($\lambda = 300\mu\text{m}$) in response to SRI variation (b) Plots of wavelength shift of the dual peaks against surrounding refractive index variation and (c) Plots of wavelength shift against temperature.

The dual peak LPFG was also subjected to thermal sensing ($10^{\circ} - 80^{\circ}\text{C}$) and results shown in Figure 3.22(c) indicates linear correlation for both peaks with the regular residual plot showing random scatter-residuals in support of the linear assumption. Peak 1 recorded thermal sensitivity of $-854.22 \pm 32.71 \text{ pm/}^{\circ}\text{C}$ while Peak 2 have thermal sensitivity of $758.93 \pm 29.79 \text{ pm/}^{\circ}\text{C}$. So far, the obtained experimental results of LPFG sensitivity to single and multi-parameter sensing are in good agreement with results earlier reported in [18, 19].

In comparison to the dual-peak LPFGs, the normal LPFGs at period $250\mu\text{m}$ and $200\mu\text{m}$ inscribed in the same $80\mu\text{m}$ -cladding B/Ge co-doped fibre under the same condition were also subjected to SRI and thermal sensing. Results show lower sensitivities to both SRI and thermal response when compared to those obtained with the dual-peak LPFGs. Firstly, the LPFG ($\Lambda = 250\mu\text{m}$) with resonant dips probed well into the mid infrared region was submerged in index gel with RI range 1.300 – 1.448. The experimental results are as plotted in Figure 3.23(a) where the wavelength shift in response to SRI increment of each cladding mode can be observed as distinct. The sensitivity results are detailed in Table 3.2 below. Also the LPFG was subjected to thermal sensing and the results are as presented in Figure 3.23(b) where the recorded sensitivity for each cladding modes are: $-332.91 \pm 6.13 \text{ pm}/^\circ\text{C}$ (LP09), $-288.18 \pm 7.03 \text{ pm}/^\circ\text{C}$ (LP010), $-231.20 \pm 8.63 \text{ pm}/^\circ\text{C}$ (LP011) and $-153.53 \pm 0.44\text{pm}/^\circ\text{C}$ (LP012).

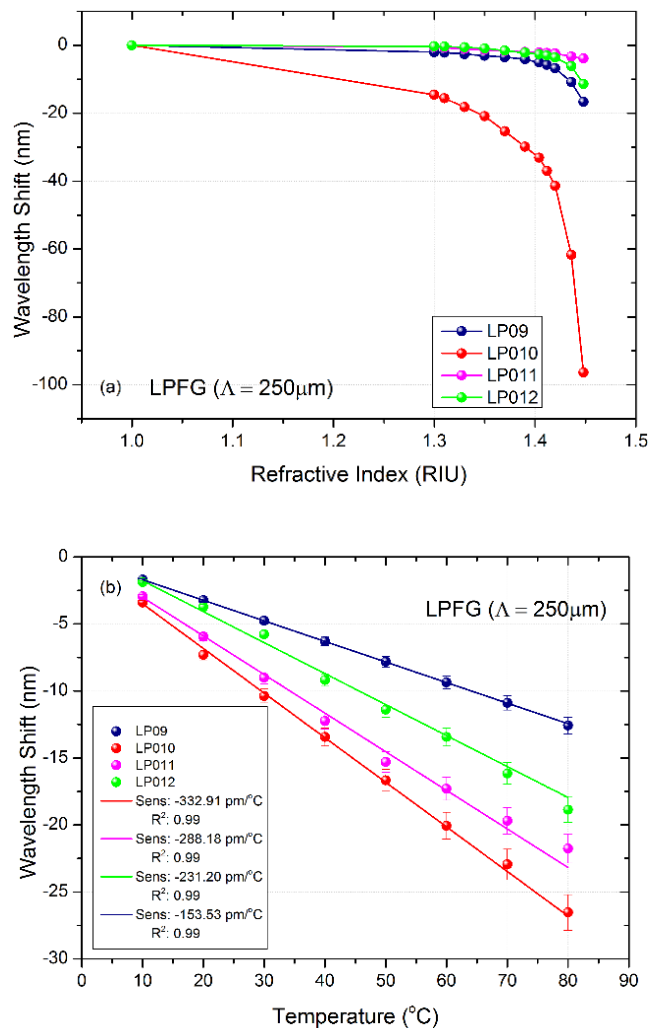


Figure 3.23: (a) Plots of wavelength shift against surrounding refractive index variation (b) Plots of wavelength shift against temperature.

Table 3.2: Experimental results of LPFG ($\Lambda = 250\mu\text{m}$ and $200\mu\text{m}$) response to SRI variations

LPFG Period (μm)	Mode order	Sensitivity (nm/RIU)	Determination Coefficient (R^2)	SRI Range (RIU)
250	LP09	-23.07 ± 0.91	0.99	1.300 – 1.390
		-258.69 ± 41.55	0.91	1.404 – 1.448
	LP10	-167.72 ± 12.36	0.97	1.300 – 1.390
		-1391.85 ± 259.17	0.87	1.404 – 1.448
	LP11	-15.81 ± 0.60	0.99	1.300 – 1.390
		-43.01 ± 4.42	0.96	1.404 – 1.448
LP12	-20.85 ± 2.71	0.92	1.300 – 1.390	
	-189.44 ± 41.71	0.83	1.404 – 1.448	
200	LP06	-3.82 ± 0.15	0.99	1.300 – 1.380
		-35.03 ± 11.64	0.86	1.404 – 1.448
	LP07	-11.94 ± 1.35	0.96	1.300 – 1.380
		-110.03 ± 21.61	0.86	1.404 – 1.448
	LP08	-53.74 ± 9.01	0.92	1.300 – 1.380
		-400.07 ± 84.60	0.85	1.404 – 1.448

Also, the LPFG ($\Lambda = 200\mu\text{m}$) was also observed for SRI and thermal variation and the experimental results (SRI) is as enumerated in Table 3.2. It is observed that the LPFGs are more sensitive to the SRI region $1.404 - 1.448$ which is in good agreement with literature [18, 19]. Figure 3.24(a) shows the spectra evolution of the LPFG ($\Lambda = 200\mu\text{m}$) in response to SRI increment while Figure 3.24(b) shows the plot of wavelength shift against the refractive index variation. The thermal response of the LPFG is depicted by the transmission spectra shift as shown in Figure 3.24(c) and the plot of wavelength shift against temperature is as presented in Figure 3.24(d). The recorded thermal sensitivity for each cladding modes are: $-211.39 \pm 1.49 \text{ pm}/^\circ\text{C}$ (LP06), $-139.44 \pm 1.10 \text{ pm}/^\circ\text{C}$ (LP07), and $-124.28 \pm 1.59 \text{ pm}/^\circ\text{C}$ (LP08).

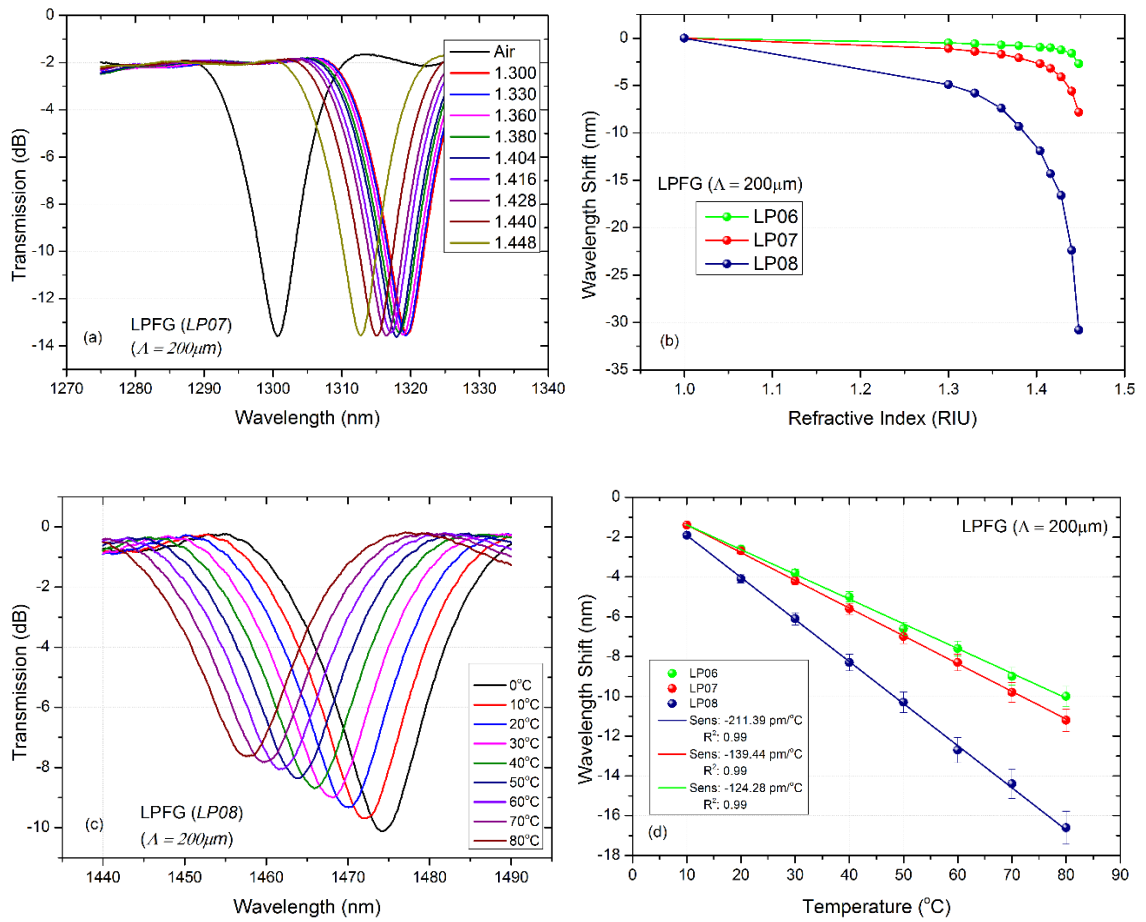


Figure 3.24: (a) Transmission spectra evolution of LPFG ($\lambda = 200\mu\text{m}$) in response to SRI variation (LP07) (b) Plots of wavelength shift against surrounding refractive index variation (c) Transmission spectra evolution of LPFG ($\lambda = 200\mu\text{m}$) in response to thermal variation (LP08) (d) Plots of wavelength shift against temperature.

3.4 STFGs inscription and sensing characteristics

This section of the thesis explains the fabrication of different tilted gratings with tilt-angles varying from 2° to 10° while also discussing their response to refractive index variations as experimentally observed. Tilting the grating planes at a small angle relative to the fibre axis results in leaky modes of the cladding as a result of the interaction of the periodic perturbation with the core guided light. This brings about the enhancement of the cladding mode resonances at the expense of the Bragg resonance. In other words, when the grating planes are at tilted angle to the fibre axis, reflections get off axis and each grating plane emits some light towards the fibre cladding which collectively bring up the emergence of backward propagating cladding mode at the phase matched wavelength. This has all the resonances occupy a spectra window ranging from around $\sim 10\text{nm}$ to $\sim 200\text{nm}$ depending on the fabrication parameters. As an important advantage, a single STFG can be used for many sensing modalities by choosing which resonance responds better by providing the highest sensitivity to a particular external perturbation.

3.4.1 Fabrication of STFGs

The fabrication of STFGs is quite similar to that of the typical FBG fabrication. The same conventional inscription techniques: phase mask scanning and two beam holography, are also applicable but at slightly tilted angles. Firstly, using the holographic technique [20] ensures the fibre is placed within the interference fringe area formed by two intense UV-laser beams with the fibre placed at an angle to the normal of the interfering fringe patterns.

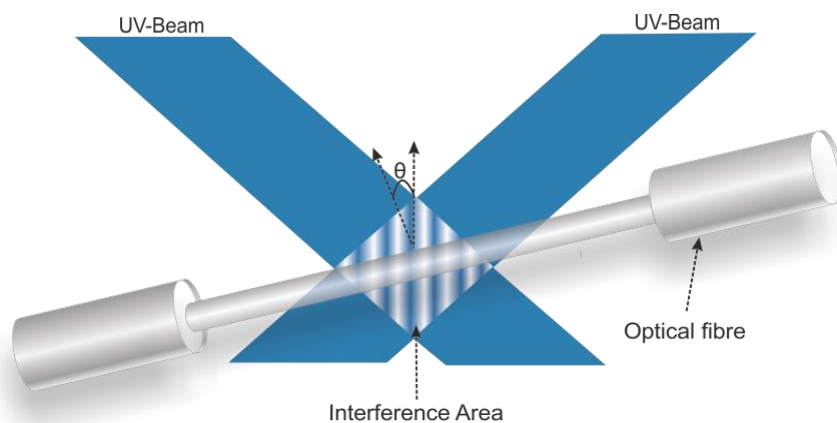


Figure 3.25: Schematic of tilted fibre gratings by holographic technique.

As shown in Figure 3.25, the tilted gratings are inscribed with the fibre placed right within the interference area at an angle θ , which is the tilt angle between normal of the axis

fibre and the interference fringe area. The main shortfalls of this technique, as earlier pointed out, are the limitation in grating length dictated by the width of laser beam and high coherent laser source required for inscription.

Secondly, interference patterns can be generated by a diffractive phase mask and placed in close proximity to the fibre [21]. The period of the grating is as fixed by the phase mask and due to the close proximity of the fibre, a low coherent UV source can be easily employed. There exists three variants to this inscription idea as described in [13, 22]: one is tilting a normal FBG phase mask with the fibre fixed perpendicular to incident UV-beam (Figure 3.26(a)), the other is inscribing using phase mask with tilted diffraction patterns (Figure 3.26(b)), and finally tilting both fibre and normal phase mask at an angle θ to the incident UV-beam axis (Figure 3.26(c)).

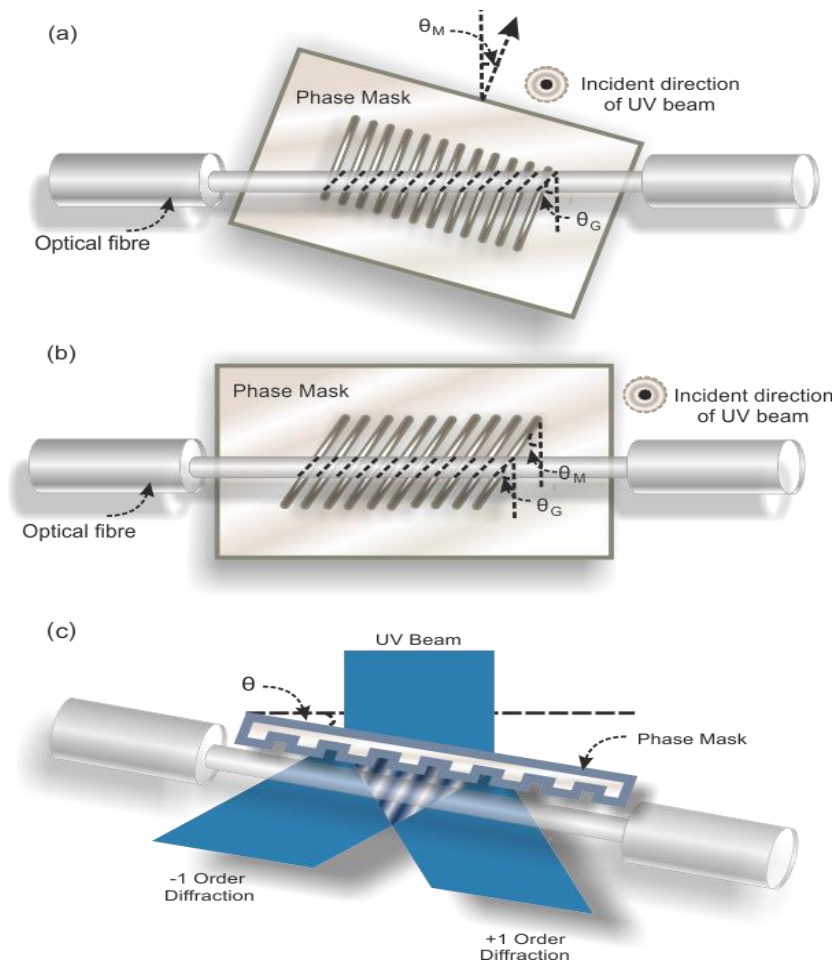


Figure 3.26: Schematic of tilted fibre gratings by scanning phase mask configurations: (a) tilt a normal FBG phase mask with the fibre fixed perpendicular to incident UV-beam (b) inscribe using phase mask with tilted diffraction patterns (c) tilt both fibre and phase mask at an angle θ to the incident UV-beam axis.

3.4.2 Tilt angles inside and outside the fibre core

The cylindrical nature of optical fibre enables only light in direction perpendicular to its central axis inscribe directly in the fibre core without any distortion. Uniform FBG inscription is a good example where the interference fringe of the UV-beam is perpendicular to the fibre axis. So, the fringes inside and outside the fibre are both the same. However, with a slight tilt at any angle with respect to the fibre axis, the interference fringe within the fibre core will be distorted. In other words, the tilted angle of the grating in the fibre core will be different from that of the interference fringe outside the fibre because of the refraction experienced by the UV beam at the air-cladding interface.

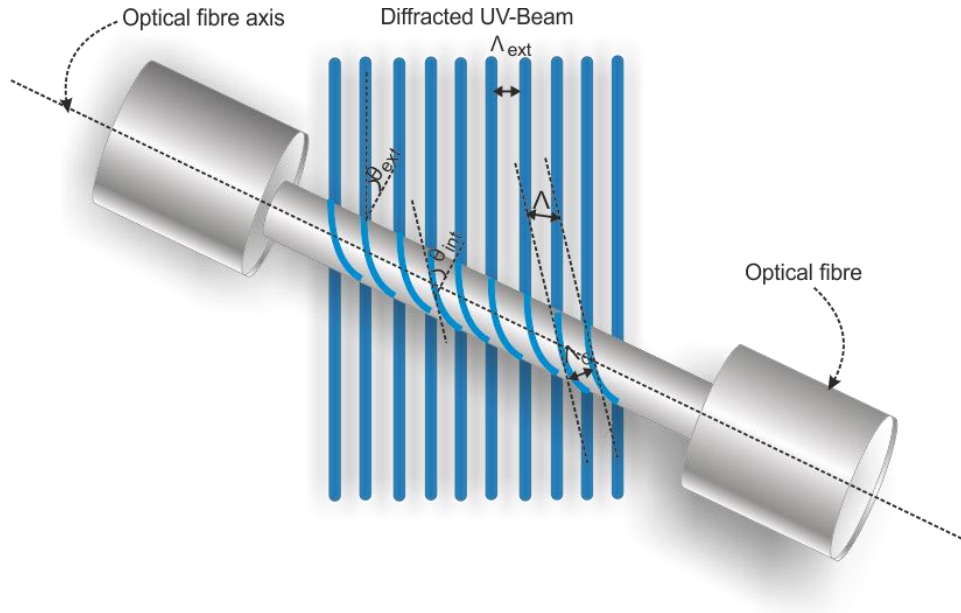


Figure 3.27: Schematic of fringes distortion induced by tilted angle within (θ_{int}) and outside (θ_{ext}) the fibre core.

Figure 3.27 illustrates the effect of the fringe distortion as a result of the tilt angle with the segregation of the angles into internal and external. The relationship between the internal ' θ_{int} ' and external ' θ_{ext} ' angles is expressed as [23]:

Equation 3.16
$$\theta_{int} = \frac{\pi}{2} - \tan^{-1} \left[\frac{1}{n_{UV} \tan(\theta_{ext})} \right]$$

where n_{UV} is the refractive index of the fibre at wavelength of UV laser. Also, the relationship between the period of internal interference fringe and external interference fringe could be expressed as:

Equation 3.17

$$\Lambda = \frac{\Lambda_{ext}}{\cos \theta_{ext}} = \frac{\Lambda_G}{\cos \theta_{int}}$$

Equation 3.18

$$\Lambda_G = \frac{\Lambda_{PM} \cos \theta_{int}}{2 \cos \theta_{ext}}$$

where the periods of the grating in the fibre core and that of the external UV interference fringes are denoted by Λ_G and Λ_{ext} respectively. All the aforementioned configurations are suitable for small angle tilted fibre grating fabrication but the ones used for the experiments reported in this thesis are: the tilt normal FBG phase mask (Figure 3.26(a)) and phase mask with tilted diffraction patterns (Figure 3.26(b)) with moderate CW laser (CW frequency-doubled Argon ion laser). However, phase masks at two different centre wavelengths (830nm and 1550nm) were employed. Figure 3.28 shows the micro-images of the small-angle tilted grating structures UV-inscribed in standard communication fibre (SMF-28) as observed under an optical microscope (Zeiss Axioskop 2 mot plus). External tilt angles of 3.5°, 5.5° and 7° are used to obtain internal fringes at ~5°, ~8° and ~10° respectively.

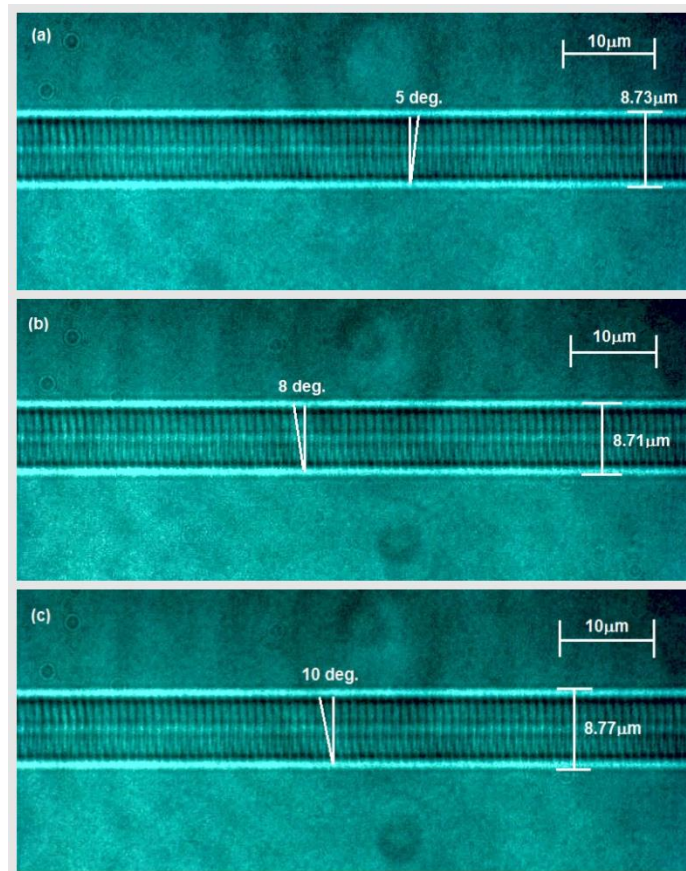


Figure 3.28: Optical micro-image of the small-angle tilted grating (STFGs) structures UV-inscribed in SMF-28: (a) 5 degrees, (b) 8 degrees and (c) 10 degrees.

The small-angle tilted fibre gratings were first inscribed in hydrogen-loaded SM-800 fibre with varying angles, 2, 5, 8 and 10 degrees using a phase mask of period $0.5742\mu\text{m}$ and centre wavelength at 830nm . Thereafter, another sets of STFGs were fabricated with similar tilt angles in hydrogen loaded SMF-28 using the multi-wavelength phase mask earlier reported in session 3.2.2 choosing the centre wavelength 1551.7nm with a period of 1071.92nm . The STFGs were successfully inscribed in the fibres and some selected transmission spectra are as shown in Figure 3.29. In comparison, FBG which has only one strong resonance at the wavelength that corresponds to the Bragg condition for this grating period in that particular fibre together with a large number of additional weak resonances in its transmission spectrum but these weak resonances are not obvious in the reflection spectrum due to the stripping away of the cladding modes power by the lossy jacket. In contrast, the S-TFG transmission spectrum shows appearance of the core mode and numerous cladding-mode resonances spreading through its transmission spectrum. However, the counter-propagating cladding modes attenuate rapidly and are therefore not observable in the reflection spectrum. These cladding modes are enhanced at the expense of the Bragg resonance. The STFGs were annealed at 80°C for 48 hours to stabilize the grating structures. It is also observed that as the angle increases the bulk cladding modes move towards the shorter wavelength.

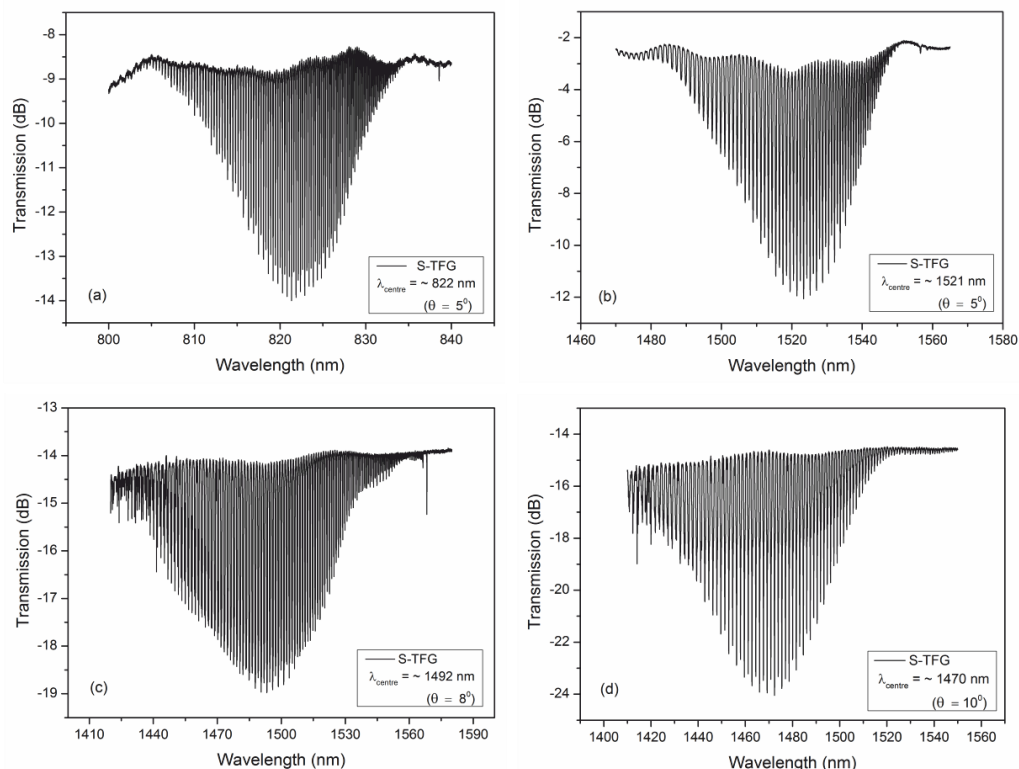


Figure 3.29: Transmission spectra of STFGs (a) 5 degrees in SMF-800 (b) 5 degrees in SMF-28 (c) 8 degrees in SMF-28 (c) 10 degrees in SMF-28.

3.4.3 STFG SRI sensing characteristics

Since STFGs are capable of coupling the core-guided light into the backward propagating cladding modes so that the evanescent fields of the modes penetrate the outer medium, they are employed for surrounding refractive index (SRI) sensing. As the index of the ambient medium increases steadily from the index of air (~ 1.000) to that of silica (~ 1.446), the cladding mode resonances gradually disappear. This is because at that instance the cladding modes are no longer total-internally reflected by the cladding boundary and thus the modes are termed as 'lossy'. As the surrounding refractive index (n_{sur}) changes from 1.000 (air) to 1.300, the centre wavelength of each resonant dips shifts towards the longer wavelength (red-shifts) with no significant change in attenuation. But as the surrounding index variation increases from 1.300 to 1.440, they not only red-shift but their attenuation band also progressively reduce to form a smooth loss curve [24].

According to [24], this can be theoretically explained by assigning to any resonance λ_m a discrete cladding mode with an effective index of $n_{eff,m}$ which readily decreases with decrease in λ_m . Therefore, when the surrounding refractive index gradually increases till it reaches the value $n_{eff,m}$, this mode becomes weakly guided, due to the decrement in overlap integral between the fundamental guided mode and the $n_{eff,m}$ cladding mode, thereby reducing the amplitude of the coupling coefficient and consequently the amplitude of this resonant dip. But as soon as n_{sur} equals $n_{eff,m}$ the cladding no longer supports the guided-mode and the coupling becomes a continuum of radiation modes. The lower and upper envelope curves (ξ_{lower} and ξ_{upper}) and the normalised area ($A_{normalised}$) of the closed field delimited by ξ_{lower} and ξ_{upper} can be determined by the expression in Eqn. 3.19 as [24]:

$$\text{Equation 3.19} \quad A_{normalised} = \frac{\int_{\lambda_{min}}^{\lambda_{max}} [\xi_{upper}(\lambda) - \xi_{lower}(\lambda)] d\lambda}{\int_{\lambda_{min}}^{\lambda_{max}} [\xi_{upper}^{n_{ref}}(\lambda) - \xi_{lower}^{n_{ref}}(\lambda)] d\lambda}$$

where $\xi_{upper}^{n_{ref}}$ and $\xi_{lower}^{n_{ref}}$ are the upper and lower envelope curves for a particular SRI with $n_{ref} = n_{sur}$; then, λ_{min} and λ_{max} are the limits of the spectra window of interest. This avails opportunity to monitor the bulk evolution of the area ($A_{normalised}$) assumed by the cladding modes collectively, instead of limiting observation only to individual wavelength shifts as the SRI varies.

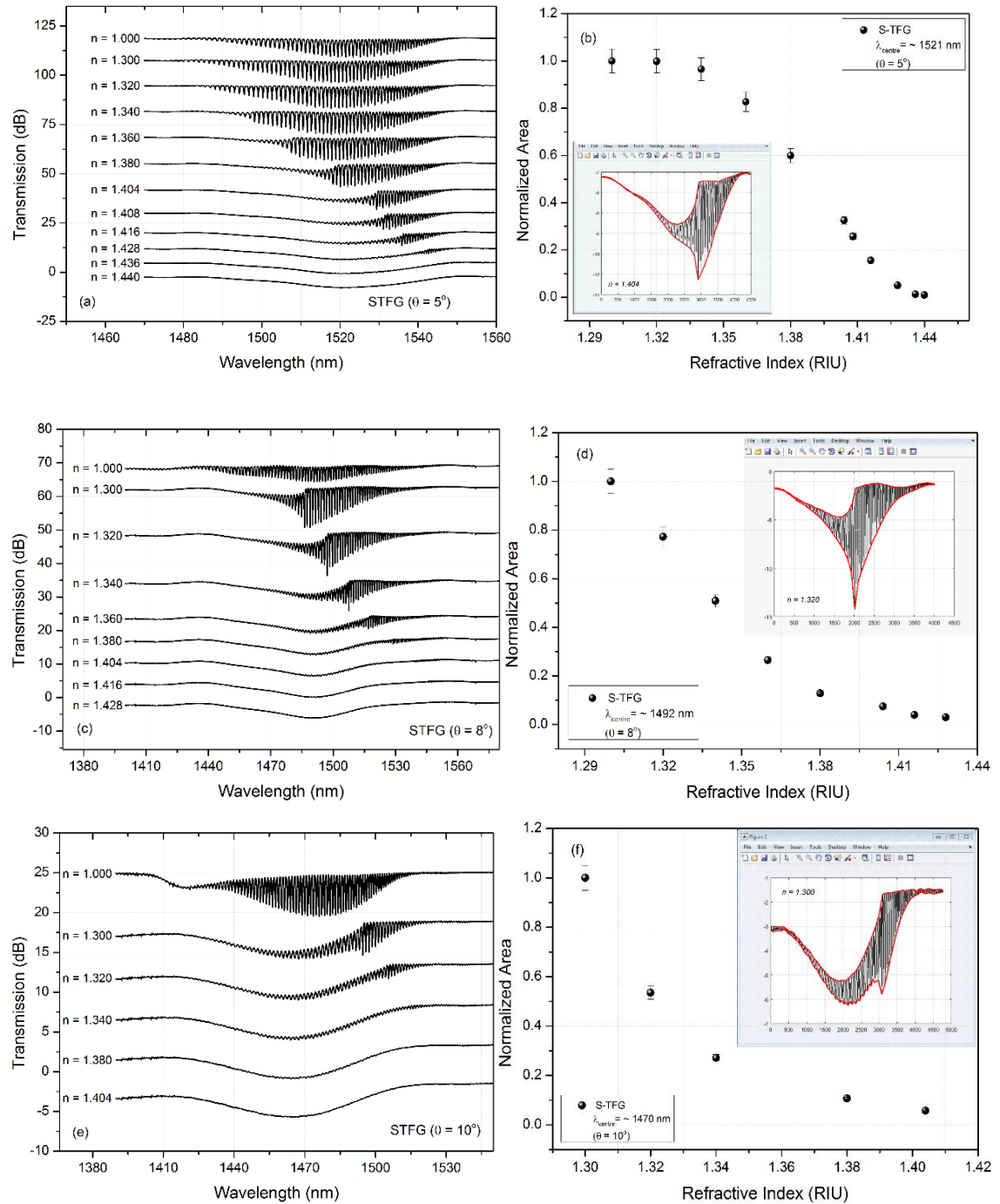


Figure 3.30: Transmission spectra evolution of STFGs to SRI variations (a) 5° (c) 8° (e) 10° ; Plots of normalised area against SRI variation (b) 5° (d) 8° (f) 10° . Insets: randomly chosen enveloped area.

It can be observed that as the external refractive index increases, the upper and lower envelope curves draw closer therefore the value of $A_{normalised}$ decreases. Figure 3.30 shows the results obtained for three different STFGs at 5° , 8° and 10° . The evolution of the transmission spectra as the SRI increases are as shown in Figure 3.30(a), (c) and (e) and the normalised area plot as derived from MATLAB programming of Eqn. 3.19 are as shown in Figure 3.30(b), (d) and (f). The insets are randomly picked SRI points where $n_{ref} = n_{sur}$ to depict the upper and lower envelopes round the area of interest.

The limit of spectra window observed for the 5° STFG is between $\sim 1482nm - \sim 1555 nm$ while that of the 8° STFG lies within $\sim 1435nm - \sim 1559 nm$ and finally that of 10° STFG lies in the range $\sim 1420nm - \sim 1530nm$. Also, it is observed that the normalised area decreases as the SRI increases. The experimental result analysis utilizes confidence interval (95%) for error analysis as the experiment was repeated three times to ascertain good repeatability. The experimental results obtained are in good agreement with literatures [24, 25].

Experiments have also been performed for closer look into individual resonant peak response to the SRI variation. The same index gel (Cargille oil) of different RI ranging 1.300 to 1.436 were employed but only the $12^{th} - 17^{th}$ order cladding modes (mode order determined through simulation software) were chosen for close observation (Figure 3.31(a)). It was observed that as the SRI increases, each of the cladding modes red-shifts gradually until the SRI value gets closer to that of the cladding and the mode becomes lossy as earlier explained. The experimental result confirms this statements and the spectra shift are as observed in Figure 3.31(b). The plot of wavelength shifts against the SRI variations is as shown in Figure 3.31(c) and sensitivity results obtained are detailed in Table 3.3. It is observed that the sensitivity decrease with increase in mode order which means that the cladding modes at shorter wavelengths are observed to be slightly more sensitive that those at longer wavelengths.

Table 3.3: Experimental results of STFG response to SRI variations (12th – 17th order cladding mode)

Cladding mode Orders	Sensitivity (nm/RIU)	Determination Coefficient (R ²)	SRI Range (RIU)
12 th	4.90 ± 0.97	0.89	1.300 – 1.360
	2.44 ± 0.31	0.97	1.380 – 1.416
13 th	4.85 ± 0.78	0.93	1.300 – 1.360
	2.44 ± 0.31	0.97	1.380 – 1.416
14 th	4.55 ± 0.91	0.89	1.300 – 1.360
	1.85 ± 0.52	0.86	1.380 – 1.416
15 th	4.35 ± 0.78	0.91	1.300 – 1.360
	1.67 ± 2.34E-12	1.00	1.380 – 1.416
16 th	3.90 ± 0.67	0.92	1.300 – 1.360
	1.61 ± 0.31	0.93	1.380 – 1.416
17 th	3.25 ± 0.62	0.90	1.300 – 1.360
	1.97 ± 0.11	0.99	1.380 – 1.416

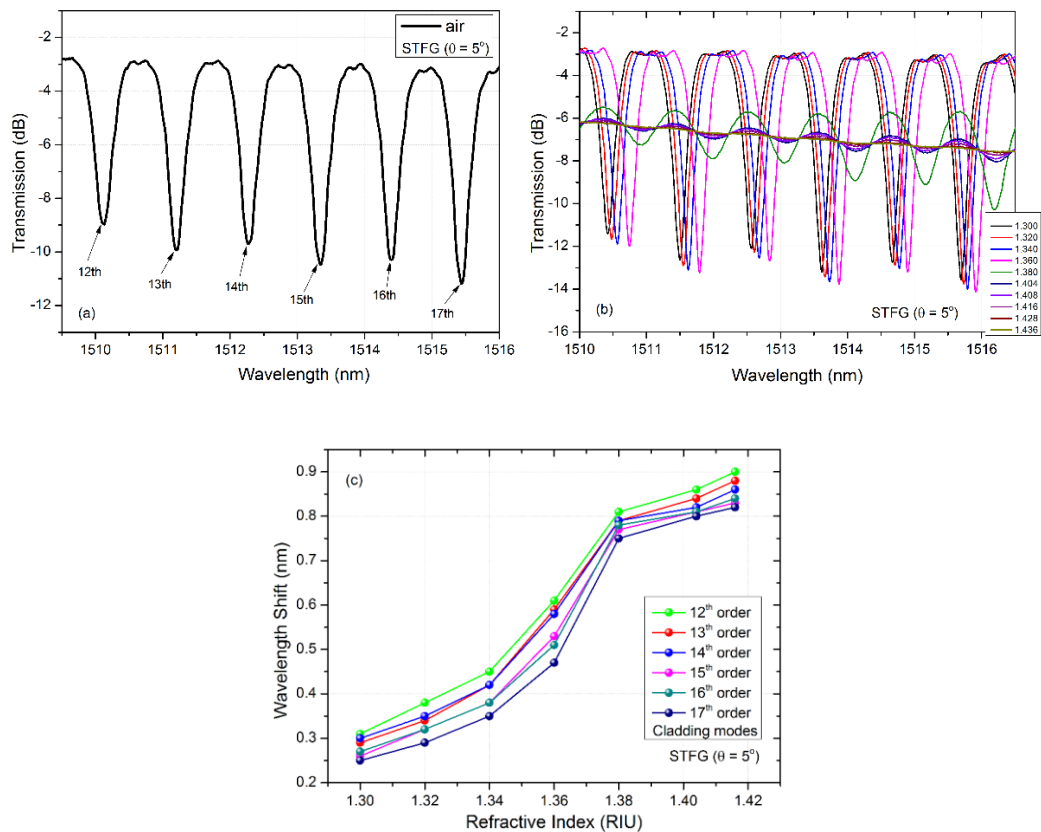


Figure 3.31: (a) Transmission spectrum of STFGs at close range (12th -17th order cladding modes), (b) Spectra evolution of STFG in response to SRI variation and (c) Plots of wavelength shift against SRI variation.

3.5 Ex-TFGs inscription and sensing characteristics

This section explains the fabrication and optical measurements carried out with excessively tilted fibre gratings (Ex-TFGs) with brief reference to theory behind the principles. The objectives of these experiments are to demonstrate the fabrication of Ex-TFGs, investigate their spectral profile with respect to polarisation properties, and evaluate their sensing characteristics to external perturbations like temperature, bending and refractive index variations.

Optical fibre gratings that can couple light from the fundamental core mode to the forward propagating cladding modes have approximately a thousand time higher sensitivity than the backward propagating ones [26]. LPFGs and Ex-TFGs are the only two types of gratings that perfectly exhibit such principle. While LPFGs have been explored extensively as attenuation filters and environmental detectors [15, 16, 19, 27], Ex-TFGs are only recently reported by Zhou et al. as showing high SRI sensitivity to aqueous solutions with low thermal cross-sensitivity [28, 29]. Due to the asymmetric structure induced by the excessively tilted index fringes in the fibre core, light in the core mode is coupled into higher order forward-propagating cladding modes. The birefringence induced by the tilt angle splits this light into two sets of polarisation dependent modes resulting in dual-peak resonances in the transmission spectrum when probed with unpolarised light.

The phase matching condition of Ex-TFG determines the wavelength of the strongest coupling between the core and the co-propagating cladding modes as given by the expression in Eqn. 3.20 below [29],

$$\text{Equation 3.20} \quad \lambda = \left(n_{co}^{eff}(\lambda) - n_{cl,m}^{i,eff}(\lambda) \right) \frac{\Lambda_G}{\cos \theta} \quad i = TE \text{ or } TM$$

where λ is the resonant wavelength, n_{co}^{eff} is the effective index of the core mode at the resonant wavelength, $n_{cl,m}^{i,eff}$ is the effective index of m^{th} TE/TM cladding mode at the resonant wavelength, Λ_G is the normal period of grating and θ is the tilt-angle of the grating. The axial period (Λ), the normal period (Λ_G) and the tilt angle of the Ex-TFG are related by the expression,

$$\text{Equation 3.21} \quad \Lambda = \frac{\Lambda_G}{\cos \theta}$$

Therefore, Eqn. 3.20 can be re-written by substituting the expression for the axial period of grating as,

$$\text{Equation 3.22} \quad \lambda = \left(n_{co}^{eff}(\lambda) - n_{cl,m}^{i,eff}(\lambda) \right) \Lambda \quad i = TE \text{ or } TM$$

Eqn. 3.22 shows that the resonant wavelength of Ex-TFG is mainly determined by the axial period of grating and the effective refractive indices of both core and cladding modes. Figure 3.32 further expatiates eqn. 3.22 by distinct schematic and vector phase matching diagram of the excessively tilted structures.

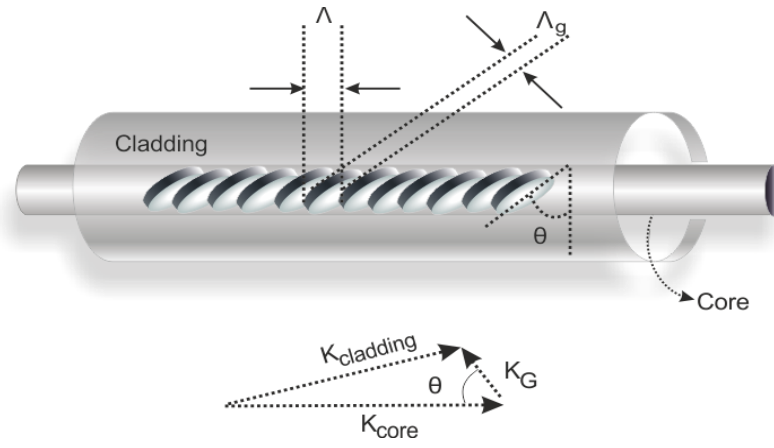


Figure 3.32: Schematic and vector phase matching diagram of Ex-TFGs.

3.5.1 Fabrication and characterisation of Ex-TFGs

As earlier discussed in session 2.4.3, an Ex-TFG must have excessively tilted structures at an angle close to or greater than 70° . These highly asymmetric index fringe structures induce birefringence in the fibre core of the Ex-TFG resulting in all coupled cladding modes degenerating into two sets of orthogonally polarised states. This causes pronounced polarisation dependent loss as a result of the mode split. Meanwhile, due to their relatively small period (typically in tens of micron (μm)) and the excessively tilted angle, Ex-TFGs cannot be fabricated with point-by-point inscription technique. A more realistic method would be using amplitude mask tilted to desired angle. The fabrications reported in this thesis made use of custom-designed amplitude masks (Edmund Optics, USA) with periods: $5 \mu\text{m}$ (200 LPMM), $6.6 \mu\text{m}$ (150 LPMM) and $25 \mu\text{m}$ (40 LPMM). These periods are so designed to ensure grating response generated from high order cladding modes coupling are centred in the C-L band. The zeroth order diffraction of UV-beam propagated through the amplitude mask is used to inscribe the excessively tilted

structures in the fibre core, thus the fibre grating and the amplitude mask have the same axial period. Figure 3.33 shows the front and aerial view of the amplitude mask in close proximity to the optical fibre during fabrication.

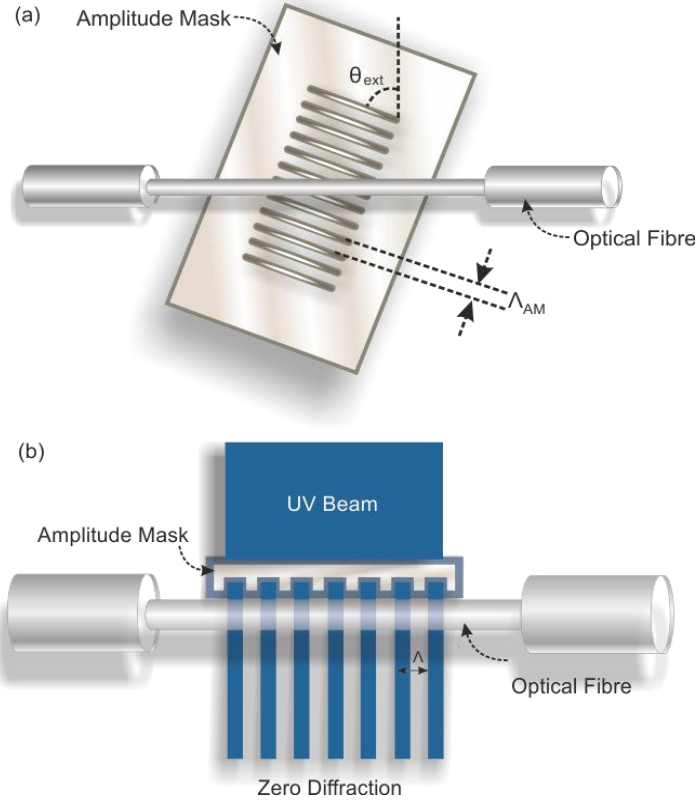


Figure 3.33: Schematic of tilted amplitude mask in close proximity to the optical fibre (a) front view (b) aerial view showing the zeroth order diffraction.

By substituting Eqn. 3.16 into 3.18, the grating period, the external tilted angle and the period of the amplitude mask is related by the expression given below,

$$\text{Equation 3.23} \quad \Lambda_G = \frac{\Lambda_{AM} \cos\left(\frac{\pi}{2} - \tan^{-1}\left[\frac{1}{n_{UV} \tan(\theta_{ext})}\right]\right)}{\cos \theta_{ext}}$$

where n_{UV} is the refractive index of the fibre at wavelength of UV laser (244 nm), Λ_G and Λ_{AM} are the grating period of the fibre and the amplitude mask respectively and θ_{ext} is the tilt angle of the amplitude mask. Three amplitude masks with different periods (5.0 μm , 6.6 μm , and 25 μm) were used for the fabrication of Ex-TFGs. The details of the amplitude masks, their axial and normal periods with respect to internal and external tilt-angles are as listed in Table 3.4 below which are only limited to two internal angles of 75° and 81°. For the whole experiment, four different angles (internal), 75°, 79°, 81° and

83° were fabricated in hydrogen loaded single-mode fibre (SMF-28) and non-hydrogenated B/Ge co-doped thin cladding fibres.

Table 3.4: Amplitude masks and optical fibre grating parameters

Period of mask	Tilted angle of amplitude mask	Axial Grating period inside the fibre	Normal Grating period inside the fibre	Tilted angle of grating in fibre core
5.0µm (200 LPMM)	68.0°	13.35 µm	3.46 µm	75.0°
5.0µm (200 LPMM)	76.5°	21.42 µm	3.35 µm	81.0°
6.6µm (150 LPMM)	68.0°	17.62 µm	4.55 µm	75.0°
6.6µm (150 LPMM)	76.5°	28.27 µm	4.43 µm	81.0°
25.0µm (40 LPMM)	68.0°	66.74 µm	17.30 µm	75.0°
25.0µm (40 LPMM)	76.5°	107.09 µm	16.75 µm	81.0°

The micro-images of the excessively tilted fringe structures as observed under optical microscope (100×) are as shown in Figure 3.34. The micro-images are those of amplitude masks of two different periods, 5µm and 6.6µm, showing the four angles of tilt used for the fabrication. The Ex-TFGs were annealed for 48 hours at 80°C temperature after the inscription to stabilize the grating.

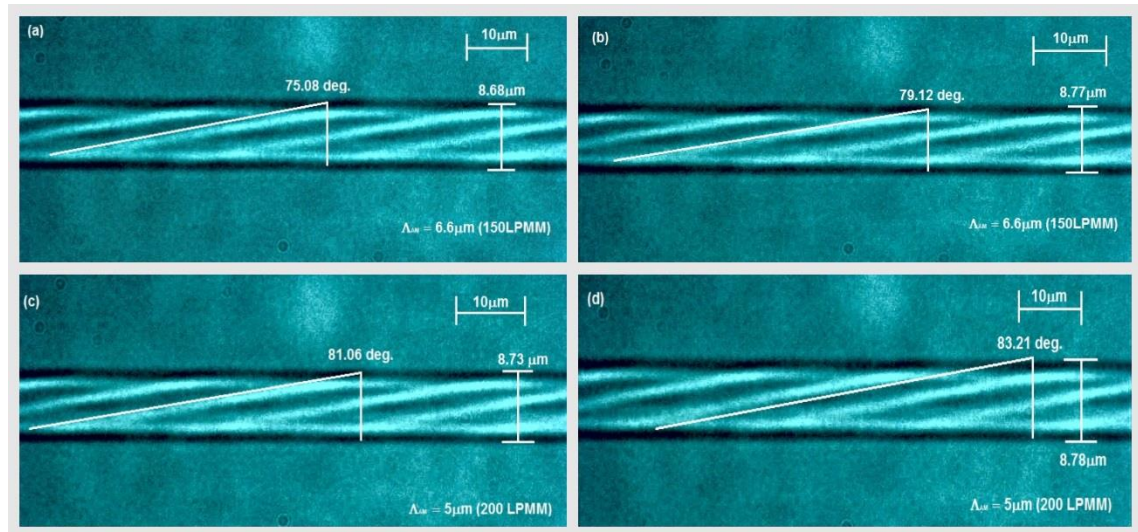


Figure 3.34: Micro-images of Ex-TFGs inscribed in SMF-28 fibre with internal tilt angles at: (a) 75° (150 LPMM) (b) 79° (150 LPMM) (c) 81° (200 LPMM) (d) 83° (200 LPMM).

During fabrication, one end of the optical fibre was connected to light from a supercontinuum laser (Fianium ultra-fast laser) propagated through an in-fibre polariser and a polarisation controller as the UV-beam inscribed excessively tilted fringes in the fibre core which was monitored real-time on the optical spectrum analyser (AQ6370D: YOKOGAWA) connected to the other end of the fibre. Figure 3.35 shows the transmission spectra of 81° Ex-TFG in SMF-28 fibre with different axial and normal grating periods as achieved by different amplitude masks when probed with unpolarised light. Since the gratings were fabricated under same conditions of hydrogen loading, UV-inscription power (145mW), scanning speed, exposure time and alignment, then the difference in spectra characteristic is as a result of difference in the grating periods. It can be observed that the grating with the lowest period (5 μ m) has the highest number of cladding modes in the transmission spectra window (1200 - 1600nm). This implies that as the grating period increases, the cladding resonant dips decreases because of the increment in the periodic gap between the resonant dips. Loss of approximately -6dB was incurred due to lossy connections from the laser source to the sink.

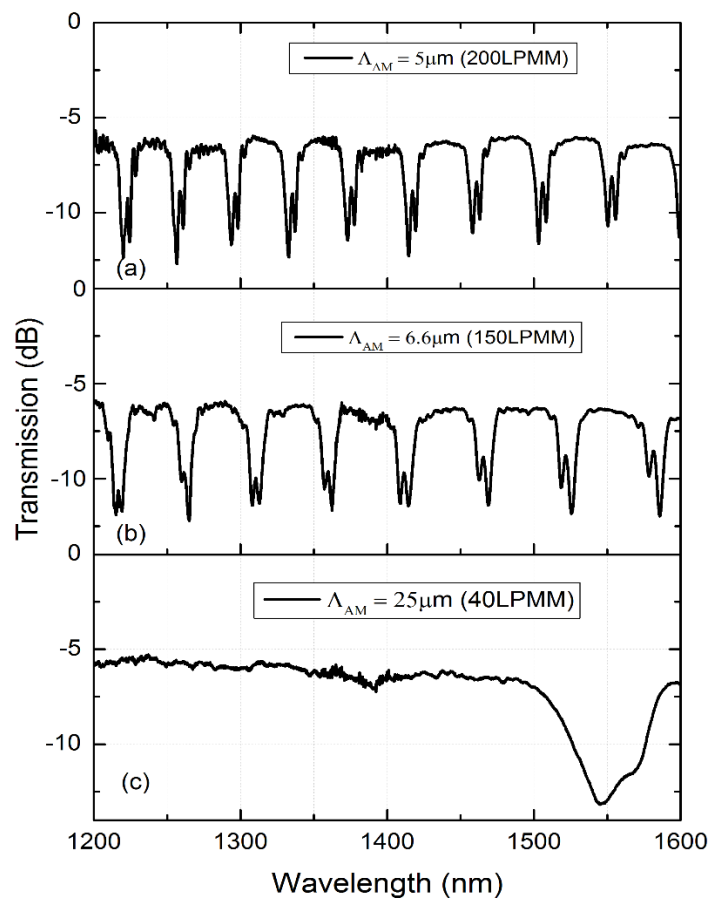


Figure 3.35: Transmission spectra of 81° Ex-TFGs inscribed using amplitude masks of different periods: (a) 5 μ m (200 LPMM) (b) 6.6 μ m (150 LPMM) (c) 25 μ m (40 LPMM).

3.5.2 Sensitivity characteristics of Ex-TFGs

All the parameters, axial period of grating (Λ) and the effective refractive indices of both core (n_{co}^{eff}) and cladding modes ($n_{cl,m}^{i,eff}$), that determine the resonant wavelength of Ex-TFGs are sensitive to environmental perturbations, like temperature, bending and SRI, and the resulting induced resonant wavelength change is a modification of Eqn. 3.22 into an expression given as [29],

$$\text{Equation 3.24} \quad \lambda' = \left(n_{co}^{eff}(\lambda') - n_{cl,m}^{i,eff}(\lambda') \right) \Lambda + \left(\delta n_{co}^{eff} - \delta n_{cl,m}^{i,eff} \right) \Lambda + \left(n_{co}^{eff}(\lambda') - n_{cl,m}^{i,eff}(\lambda') \right) \delta \Lambda$$

where the resonant wavelength, after the change due to environmental condition, is denoted as λ' ; the change in effective index of core is denoted as δn_{co}^{eff} , the change in effective index of cladding modes is represented by $\delta n_{cl,m}^{i,eff}$ and finally, the change in grating axial period under environmental perturbation is $\delta \Lambda$. Consequently, the resulting wavelength shift is given as

$$\text{Equation 3.25} \quad \Delta \lambda = \lambda' - \lambda = \frac{1}{1 - \left(\frac{dn_{co}^{eff}}{d\lambda} - \frac{dn_{cl,m}^{i,eff}}{d\lambda} \right) \Lambda} \left(\frac{\delta n_{co}^{eff} - \delta n_{cl,m}^{i,eff}}{n_{co}^{eff}(\lambda) - n_{cl,m}^{i,eff}(\lambda)} + \frac{d\Lambda}{\Lambda} \right) \lambda$$

The first term in Eqn. 3.24 is the dispersion factor (γ), the second is the environmental dependence of waveguide dispersion (Γ) and the third is material expansion (α) caused by environmental change. Then, Eqn. 3.24 can be rewritten as,

$$\text{Equation 3.26} \quad \Delta \lambda = \gamma (\Gamma + \alpha) \lambda$$

When the Ex-TFG is subjected to thermal perturbation, the thermal dependence of waveguide dispersion is defined by Eqn. 3.27 as,

$$\text{Equation 3.27} \quad \Gamma_{temp} = \frac{\left(\xi_{co} n_{co}^{eff} - \xi_{cl} n_{cl,m}^{i,eff} \right)}{\left(n_{co}^{eff}(\lambda) - n_{cl,m}^{i,eff}(\lambda) \right)}$$

where the thermo-optic coefficients of core and cladding materials are denoted as ξ_{co} and ξ_{cl} respectively. Also, the surrounding refractive index (SRI) dependence of waveguide dispersion can be expressed as [30],

Equation 3.28

$$\Gamma_{SRI} = \frac{(-\delta n_{cl,m}^{eff})}{n_{co}^{eff}(\lambda) - n_{cl,m}^{eff}(\lambda)}$$

Equation 3.29

$$\Gamma_{SRI} = -\frac{u_m^2 \lambda^2 \Delta n_{sur}}{8\pi^3 r^3 n_{cl,m}^{eff} (n_{cl}^2 - n_{sur}^2)^{3/2}}$$

Equation 3.30

$$\Delta\lambda = \gamma \Gamma_{SRI} \lambda$$

where u_m^2 is the root of the zeroth order Bessel function, n_{sur} is the RI of surrounding medium, λ is the operating wavelength of cladding mode, r is the radius of the optical fibre cladding, and n_{cl} is the index of cladding. Eqn. 3.29 shows Γ_{SRI} is a negative value which means the SRI sensitivity has an opposite sign to the general sensitivity γ factor expressed in Eqn. 3.14. The simplified form of the SRI sensitivity of Ex-TFG is as expressed in Eqn. 3.30.

3.5.2.1 Thermal sensitivity of Ex-TFGs

The thermal response of Ex-TFGs has been evaluated using the experimental setup in Figure 3.36. Each Ex-TFG was subjected to thermal evaluation by mounting it on the surface of a temperature tuneable Peltier enclosed in a box to forestall external influence on the measurement. The temperature was tuned from 0°C - 80°C at an incremental interval of 10°C. In the setup, an in-fibre polariser and polarisation controller were employed to ascertain easy switching between polarisation states making it easy for a polarisation state to be evaluated at a time.



Figure 3.36: Experimental setup for evaluating the thermal sensitivity of Ex-TFGs.

The transmission spectra of Ex-TFG at 83° with axial grating period of 27.44 μm when launched with orthogonal polarised light have one peak fully excited and the other suppressed at a point in time. The zoomed spectra of a pair of dual peak around ~1550 nm is as shown in Figure 3.37(a) indicating the TM and TE modes. According to calculations in [31], for SMF-28 fibre the resonance mode at around ~1550 nm should be 35th cladding mode and the wavelength of TM-mode should be shorter than that of the TE-mode. The linearly fitted result in Figure 3.37(b) shows that the TM-mode recorded a slightly higher sensitivity of 8.44 ± 0.04 pm/°C (R²: 0.99) than that of the TE-mode which is 7.27 ± 0.05 pm/°C (R²: 0.99). Apart from the 83° Ex-TFG, another 81° Ex-TFG also fabricated in SMF-28 was selected for thermal sensing at two different centre wavelengths (~ 1334 nm and ~1554 nm) for comparison. According to [30], the dual peak around 1330 nm and 1550 nm are 37th and 34th cladding modes respectively.

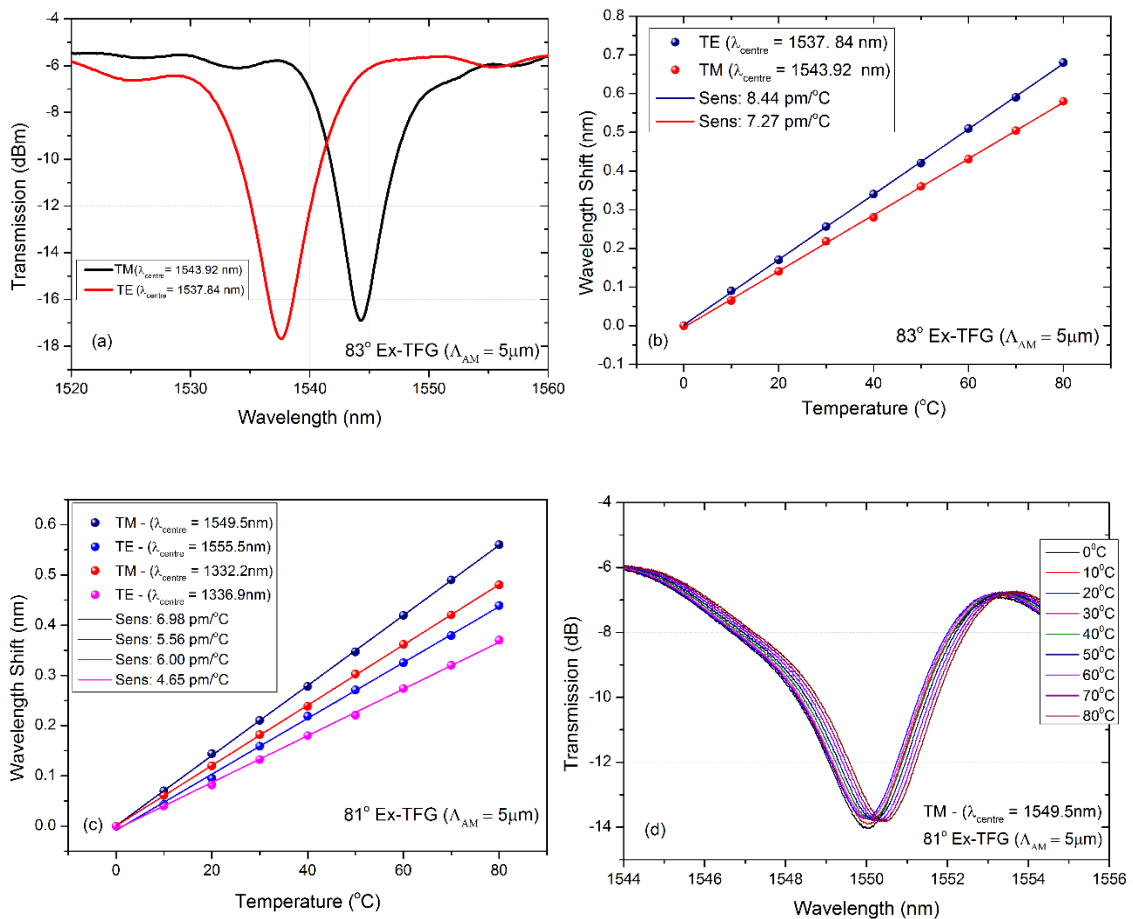


Figure 3.37: (a) Zoomed transmission spectra of 83° Ex-TFG when launched with orthogonally polarised light (black line – TE; red line - TM); (b) Plots of wavelength shift against thermal variation for 83° Ex-TFG; (c) Plots of wavelength shift against thermal variation for 81° Ex-TFG (at ~ 1334nm and ~1554nm) and (d) Transmission spectra evolution of 81° Ex-TFG (TM - ~1550 nm) in response to thermal variation.

The fitted results in Figure 3.37(c) indicate the various sensitivities of the TM and TE modes at the two wavelengths. As expected, the dual peak at ~ 1550 nm centre wavelength exhibit slightly higher thermal sensitivity than that at ~ 1330 nm. For the dual peak at ~ 1550 nm, TM-mode has a thermal sensitivity of 6.98 ± 0.03 pm/ $^{\circ}$ C (R^2 : 0.99) and TE-mode has 6.00 ± 0.02 pm/ $^{\circ}$ C (R^2 : 0.99). The results at ~ 1330 nm are: TM-mode 5.56 ± 0.07 pm/ $^{\circ}$ C (R^2 : 0.99) and TE-mode 4.65 ± 0.05 pm/ $^{\circ}$ C (R^2 : 0.99). The obtained results are in good agreement with earlier report in [30]. Figure 3.37(d) is merely the transmission spectra evolution of the TM mode at ~ 1550 nm in response to the thermal variation.

Also, an 81° Ex-TFG fabricated in B/Ge co-doped thin cladding fibre using amplitude mask with period $25\mu\text{m}$ was subjected to thermal sensing. Because the number of cladding modes is affected directly by the cladding radius, the mode number decreases as the cladding radius reduces [30]. Thus, for same mode order, the cladding mode effective index of a fibre with a smaller radius will significantly be lower than that of a fibre with larger cladding radius. This also improves the sensitivity of the fibre as the SRI sensitivity is inversely proportional to the radius of the fibre as indicated in Eqn. 3.29. However, because of the larger period of the amplitude mask ($25\mu\text{m}$), the spectrum is broader than conventional Ex-TFGs and segregating the polarisation states becomes a challenge. The TM-mode was focused on and used for the thermal sensing. Figure 3.38(a) shows the transmission spectra evolution of the TM mode at ~ 1550 nm in response to the thermal variation spanning over 20nm as it drifts from 0°C to 80°C . Linearly fitted result in Figure 3.38(b) indicates a sensitivity of 236.77 ± 2.87 pm/ $^{\circ}$ C (R^2 : 0.99) which is much higher than those earlier reported for FBGs and LPFGs combined.

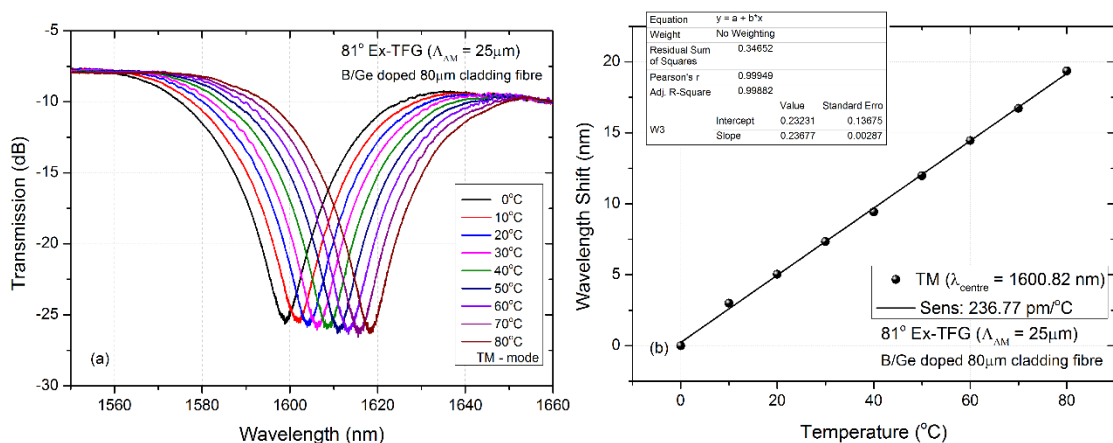


Figure 3.38: (a) Transmission spectra evolution of 81° Ex-TFG (fabricated in B/Ge co-doped $80\mu\text{m}$ fibre with $\Lambda_{AM} = 25\mu\text{m}$) in response to thermal variation and (b) Plots of its wavelength shift against thermal variation showing linear correlation.

3.5.2.2 SRI sensitivity of Ex-TFGs

The SRI sensing capability of Ex-TFGs has also been evaluated using the experimental setup shown in Figure 3.39 below, the setup only differs from that of thermal sensing by the replacement of the Peltier and temperature controller with two translational stages at each end of the fibre holding it firmly across a test-platform attached to a micrometre stage. The two translational stages are set at same height and the grating firmly clamped (not too tight) on each to avoid wavelength shift induced by bending and axial strain. Series of index gel (from Cargille laboratory) with different refractive indices ranging from 1.300 to 1.390 were applied to the grating intermittently.



Figure 3.39: Experimental setup for evaluating the SRI sensitivity of Ex-TFGs.

At the commencement of each experimental stage, a new flat glass substrate is placed on the test platform attached to the micrometre stage. The index gel was placed on this glass substrate and the micrometre stage moves vertically upward to submerge the grating, which is already hanging in air across the test platform, into the index gel without imposing any force on it. Immediately the grating is fully submerged in the index gel the wavelength shift is instantaneously obvious on the display screen of the optical spectrum analyser (OSA). After each index gel measurement, the glass substrate was constantly replaced by a new one and the residual gel rinsed off the surface of the grating with methanol thereby restoring it to initial position in air as previously displayed on the OSA.

The plots of wavelength shift against surrounding refractive index (SRI) variation from 1.305 -1.385 for the 34th TM and TE cladding modes of 81^o Ex-TFG is as shown in Figure 3.40(a). The two different centre wavelengths (~ 1334 nm and ~1554 nm) of the 81^o Ex-TFG earlier evaluated for thermal sensing were also probed for SRI sensing. The experimental results confirm that the SRI sensitivity of an Ex-TFG is cladding mode dependent and thus increases with the order of the cladding modes. From the figure, the results shown indicate that the TM-modes have slightly higher sensitivity than the TE-

modes at the two different centre wavelengths: at ~ 1550 nm, TM-mode has sensitivities of 153.11 nm/RIU (1.305 – 1.345) and 658.62 nm/RIU (1.365 – 1.385); TE-mode has slightly lower sensitivities of 124.08 nm/RIU (1.305 – 1.345) and 622.05 nm/RIU (1.365 – 1.385) whereas at ~ 1330 nm, TM-mode has sensitivities of 100.92 nm/RIU (1.305 – 1.345) and 306.50 nm/RIU (1.365 – 1.385); TE-mode has slightly lower sensitivities of 85.23 nm/RIU (1.305 – 1.345) and 279.05 nm/RIU (1.365 – 1.385). The general trend of Ex-TFGs response to SRI variation is that the SRI sensitivity increases with increasing SRI values and reaches maximum when the SRI value drifts towards the effective index of the cladding mode. Unlike the linear correlation exhibited by the thermal sensitivity, the SRI sensitivity exhibits a nonlinear correlation in form of exponential fitting. However, the sensitivity is fathomed linearly within a set of SRI range that are linearly related. Also a 75° Ex-TFG was subjected to SRI sensing and the recorded wavelength shift plot is as shown in Figure 3.40(b). The TM-mode is recorded to have sensitivities of 143.54 nm/RIU (1.30 – 1.35) and 488.00 nm/RIU (1.36 – 1.38) and TE-mode has sensitivities of 127.89 nm/RIU (1.30 – 1.35) and 438.00 nm/RIU (1.36 – 1.38). The obtained results are in good agreement with those earlier obtained in [30].

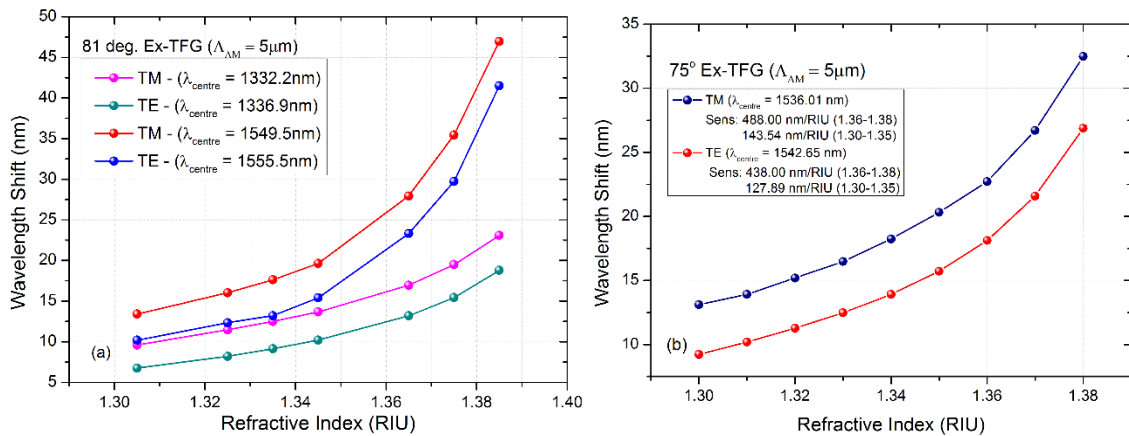


Figure 3.40: (a) Plots of wavelength shift against SRI variation for 81° Ex-TFG (at ~ 1334 nm and ~ 1554 nm) and (b) Plots of wavelength shift against SRI variation for 75° Ex-TFG.

Furthermore, the 81° Ex-TFG fabricated in B/Ge co-doped thin cladding fibre using amplitude mask with period $25\mu\text{m}$ was also subjected to SRI sensing. The higher period coupled with the reduced radius of fibre cladding enhanced the sensitivity outcome greatly. As shown in Figure 3.41(a) the transmission spectra evolution is a giant ~ 80 nm drift away from air at SRI value of 1.385. The entire wavelength shift plot against the SRI variation was shown in Figure 3.41(b) to record sensitivities of 354.88 nm/RIU (1.305 – 1.345) and 931.02 nm/RIU (1.345 – 1.404). Also, another 83° Ex-TFG fabricated in B/Ge co-doped thin cladding fibre using amplitude mask with period $5\mu\text{m}$ was used for SRI

sensing. Its spectra evolution is as presented in Figure 3.41(c) indicating around ~40 nm shift from air over RI range of (1.300- 1.370). The wavelength shift plots in Figure 3.41(d) show high sensitivities of 827.84 nm/RIU (1.34 -1.37) and 643.20 nm/RIU (1.34 -1.37) for the TM and TE modes respectively. The results align with theoretical perceptions and results obtained in [30].

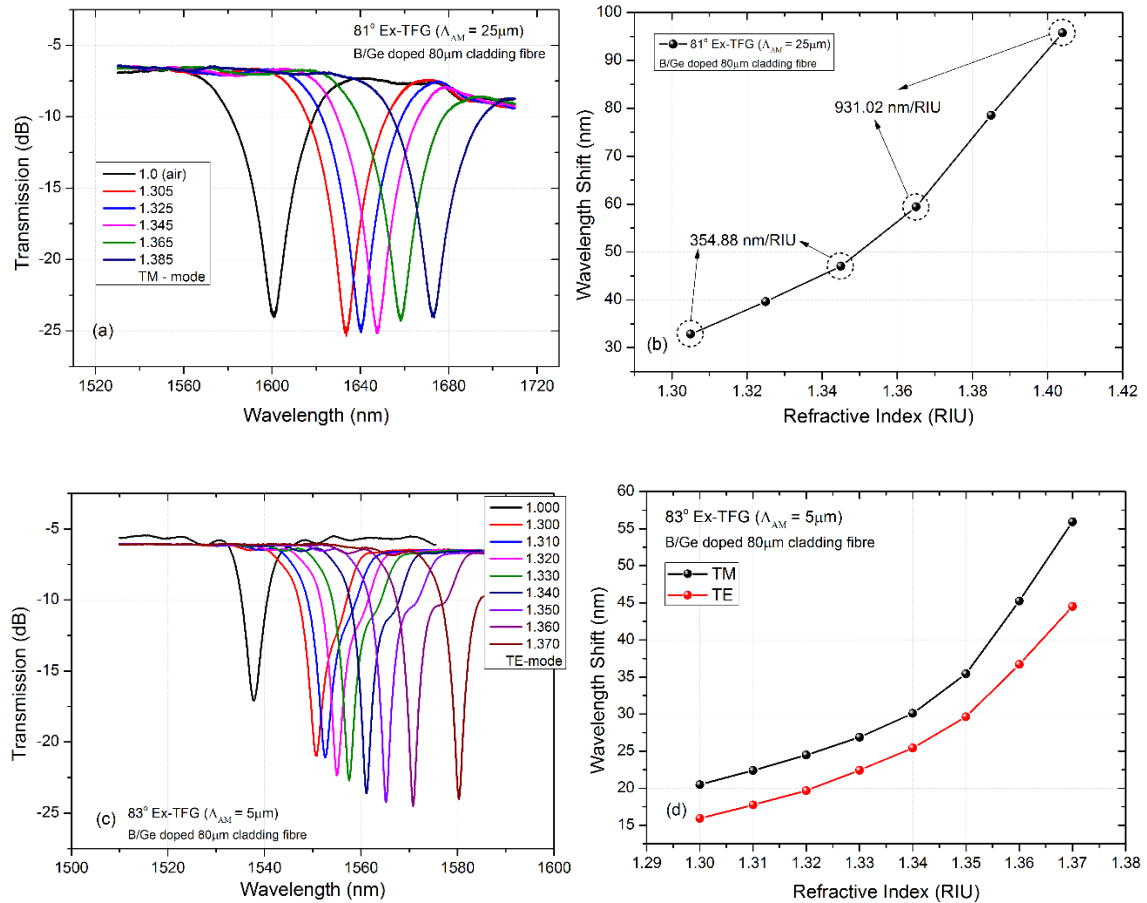


Figure 3.41: (a) Transmission spectra evolution of 81° Ex-TFG (fabricated in B/Ge co-doped 80 μm fibre with $\Lambda_{AM} = 25 \mu\text{m}$) in response to SRI variation; (b) Plots of its wavelength shift against SRI variation; (c) Transmission spectra evolution of 83° Ex-TFG (fabricated in B/Ge co-doped 80 μm fibre with $\Lambda_{AM} = 5 \mu\text{m}$) in response to SRI variation and (d) Plots of its wavelength shift against SRI variation.

3.5.2.3 Bend sensitivity of Ex-TFGs

The bend characteristic of Ex-TFGs has not previously been reported since they do not offer any spectacular bending sensitivity compared with LPFGs which have been demonstrated as bend sensors measuring curvature by detecting bending induced wavelength shifts [32, 33]. However, with a view to improving the bending characteristics, this session investigates the response of Ex-TFGs to bending induced structural shape deformation using two Ex-TFGs of different periods. Two different 81° Ex-TFGs were fabricated using amplitude masks of periods 6.6 μm and 25 μm on SMF-28 with axial grating periods of 28.27 μm and 107.09 μm respectively. The experimental setup for bend sensing is as shown in Figure 3.42(a) below where light from a supercontinuum laser is transmitted through the in-fibre polariser and polarisation controller to one end of the Ex-TFG which is clamped loosely to a steel rule stationed on the four-point bend system.



Figure 3.42: (a) Experimental setup for bend sensing and (b) Schematic diagram of the four-point bend system with $a = 120\text{mm}$, $b = 40\text{mm}$, and bend depth, $h = 0 \sim 12.5\text{mm}$

The other end of the fibre is connected directly to the OSA (AQ6370D) where measurements were recorded. Figure 3.42(b) illustrated the schematic of the four-point bend system showing its geometric configuration. The SMF-28 containing the 81° Ex-TFG in the centre was loosely attached to a steel rule of 0.5mm thickness, 20mm width and 200mm length. The fibre was loosely attached so as to eliminate effect of axial strain. As shown in the figure, depressing the centre micrometer driver with a depth (h) the fibre was bent. The resulting bend curvature has a near linear relationship with the depressing bend depth (h) and can be expressed as [1],

$$\text{Equation 3.31} \quad \begin{cases} R^2 = (R - h_0)^2 + \left(\frac{a}{2}\right)^2 \\ \left(\frac{b}{2}\right)^2 + [-h - (R - h)]^2 = R^2 \end{cases}$$

where R is the bend radius, h is the bend depth which is accurately read from the micrometer driver, a and b are the spacing of the two sets of forced points as shown in Figure 3.43(b). Simplifying Eqn. 3.31 yields,

$$\text{Equation 3.32} \quad \left(\frac{a}{2}\right)^2 - 2R \left[R + h - \sqrt{R^2 - \left(\frac{b}{2}\right)^2} \right]^2 + \left[R + h - \sqrt{R^2 - \left(\frac{b}{2}\right)^2} \right]^2 = 0$$

With $R \gg a, b$ and h , and with $a \gg b$ and h , an approximate expression reduces Eqn. 3.32 to,

$$\text{Equation 3.33} \quad \frac{1}{R} = \frac{8h}{a^2 - b^2}$$

It is obvious from Eqn. 3.33 that there exist a linear relationship between the bend curvature and bend depth. Figure 3.43 shows the plot of the bend curvature ($1/R$) against the bend depth (h) confirming the linear approximation defined in Eqn. 3.33. The two 81° Ex-TFGs fabricated using amplitude masks of periods 6.6 μm and 25 μm on SMF-28 were subjected to bend sensing for sensitivity comparison. The transmission spectra evolution of the 81° Ex-TFG ($\lambda_{AM} = 6.6\mu\text{m}$) in response to bending is as shown in Figure 3.44(a) as the bending depth increases from 0 – 12.5mm. The plot of wavelength shift against curvature for both TM and TE-modes exhibit linear correlation giving sensitivities

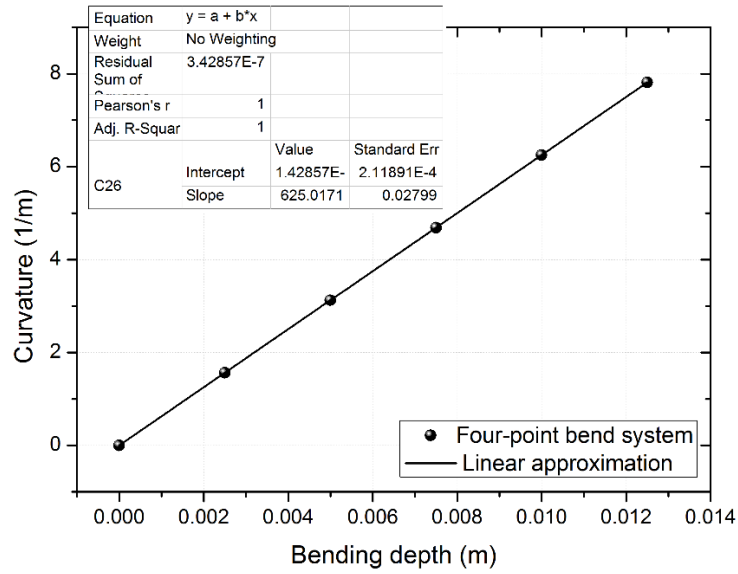


Figure 3.43: Plot of curvature against bend depth using four-point bending system.

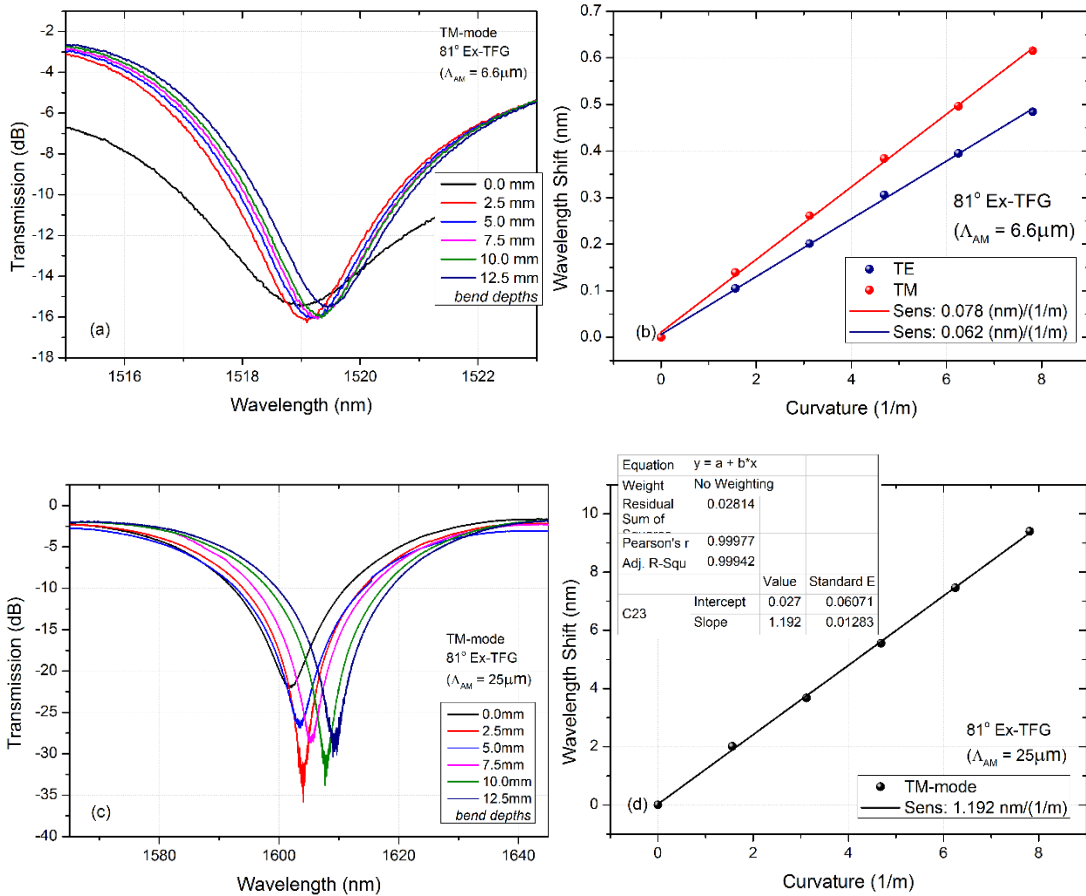


Figure 3.44: (a) Transmission spectra evolution of 81° Ex-TFG ($\Lambda_{AM} = 6.6\mu\text{m}$) in response to bending (b) Plots of wavelength shift (nm) against curvature (1/m) (c) Transmission spectra evolution of 81° Ex-TFG ($\Lambda_{AM} = 25\mu\text{m}$) in response to bending (d) Plots of wavelength shift (nm) against curvature (1/m), inset: regression fitting analysis.

0.078 ± 0.001 (nm)/(1/m) and 0.062 ± 0.001 (nm)/(1/m) respectively as shown in Figure 3.44(b). However, the 81° Ex-TFG ($\Lambda_{AM} = 25\mu m$) gives a higher sensitivity of 1.192 ± 0.013 (nm)/(1/m) due to the increase in axial grating period which is close to that of an LPFG. The transmission spectra evolution of the 81° Ex-TFG ($\Lambda_{AM} = 25\mu m$) in response to the bend depth is as shown in Figure 3.44(c) and the shift of its wavelength against curvature is plotted in Figure 3.44(d).

3.6 Chapter conclusion

In this chapter, extensive experimental study on the fabrication, spectral features and sensing characteristics of different advanced optical fibre gratings have been demonstrated and presented. Firstly, it has been demonstrated that two different fabrication techniques - holography and phase mask scanning - can be employed for the UV-inscription of FBGs. The holographic technique has been employed to write FBGs at different percentage reflectivity ranging from $\sim 4\%$ - $\sim 96\%$ while the phase mask scanning has been used for fabrication of complex Gaussian apodized FBGs at different wavelength ranges between $1544\text{ nm} - 1554\text{ nm}$. Then, the responses of FBGs to thermal and strain sensing have been remarkably shown to be $\sim 11\text{ pm}/^\circ\text{C}$ and $\sim 1.18\text{ pm}/\mu\epsilon$ respectively.

Similar with the FBGs, a 244nm Ar⁺ laser has also been used to fabricate LPFGs at different grating periods - $140\mu\text{m}$, $250\mu\text{m}$, $300\mu\text{m}$, $350\mu\text{m}$, and $400\mu\text{m}$ – using the point-by-point inscription technique. In particular, dual-peak LPFGs with periods ($300\mu\text{m}$) near dispersion turning points have been fabricated in $80\mu\text{m}$ cladding fibre and investigated for optimum sensitivity to external perturbations. The dual-peak LPFGs have recorded high sensitivities of $\sim 4400\text{ nm}/\text{RIU}$ and $\sim 854.22\text{ pm}/^\circ\text{C}$ for SRI and thermal sensing respectively. For comparison, normal LPFGs with periods $200\mu\text{m}$ and $250\mu\text{m}$ were inscribed in same $80\mu\text{m}$ cladding fibre and subjected to thermal and SRI sensing. Lower sensitivities of $\sim 1391.85\text{ nm}/\text{RIU}$ and $\sim 332.91\text{ pm}/^\circ\text{C}$ were obtained for SRI and thermal sensing respectively.

Furthermore, TFGs have been fabricated at different angles using phase-masks and amplitude masks for STFGs and Ex-TFGs respectively. While a session detailed the spectral features and sensing characteristics of STFGs another discussed at length the fabrication of Ex-TFGs with amplitude masks of different axial periods and tilt angles. STFGs were employed for SRI sensing due to their ability to couple core-guided mode into backward propagating cladding modes. The collective responses of the cladding modes to variation in SRI were presented as plot of normalised area against RI. Sensitivity of $\sim 4.9\text{ nm}/\text{RIU}$ was obtained for 12th order cladding mode when individual cladding modes are zoomed for close investigation.

Meanwhile, the transmission spectra of Ex-TFGs shows dual-peak attenuation bands corresponding to two orthogonal polarisation states. These two polarisation states are confirmed to be TE and TM resonant peaks when linear polarised light with different azimuth angles were launched through the Ex-TFG. The sensing characteristics of Ex-

TFGs to thermal, SRI and bend sensing were also examined. Specifically, thermal sensitivities of $8.44 \text{ pm}/^\circ\text{C}$ and $6.98 \text{ pm}/^\circ\text{C}$ were obtained for 83° -TFG and 81° -TFG respectively while SRI sensitivities of $\sim 658.62 \text{ nm}/\text{RIU}$ and $\sim 488.00 \text{ nm}/\text{RIU}$ were obtained for 81° -TFG and 75° -TFG respectively. Bend sensing of Ex-TFGs was carried out and reported for 81° -TFG. Two different 81° Ex-TFGs were fabricated using amplitude masks of periods $6.6\mu\text{m}$ and $25\mu\text{m}$ in SMF-28 with axial grating periods of $28.27\mu\text{m}$ and $107.09\mu\text{m}$ respectively. Improved sensitivity of $1.192 \text{ nm}/(1/\text{m})$ was obtained for 81° Ex-TFG ($\Lambda_{AM} = 25\mu\text{m}$) as against $0.078 \text{ nm}/(1/\text{m})$ obtained for 81° Ex-TFG ($\Lambda_{AM} = 6.6\mu\text{m}$).

References

- [1] Y. Liu, "Advanced fibre gratings and their applications," Ph.D. Thesis, Photonics Research group Aston University, Birmingham, pp 77- 165, 2001.
- [2] H. Patrick and S. L. Gilbert, "Growth of Bragg gratings produced by continuous-wave ultraviolet light in optical fibre," *Optics Letters*, vol. 18(18), pp 1483-1486, 1993.
- [3] J. Albert, K. O. Hill, B. Malo, S. Theriault, F. Bilodeau, D. C. Johnson and L. E. Erickson, "Apodization of the spectral response of fibre Bragg gratings using a phase mask with variable diffraction efficiency," *Electron. Letter*, vol. 31(3), pp.222-223, 1995.
- [4] G. Meltz and W. W. Morey, "Bragg grating formation and germanosilicate fibre photosensitivity," International Workshop on Photo-induced Self-Organization Effects in Optical Fibre, Quebec City, Quebec, May 10-11, *Proceedings SPIE*, vol. 1516, pp 185-199, 1991.
- [5] A. D. Kersey, M. A. Davis, H. J. Patrick, M. LeBlanc, K. P. Koo, C. G. Askins, M. A. Putnam and E. J. Friebele, "Fibre grating sensors," *J. Lightwave Technol.* 15, 1442–1463, 1997.
- [6] A. D. Kersey, T. A. Berkoff and W. W. Morey, "High resolution fibre Bragg grating based strain sensor with interferometric wavelength shift detection," *Electron. Lett.* 28, 236 –238, 1992.
- [7] B. Malo, K. O. Hill, F. Bilodeau, D. C. Johnson and J. Albert, "Point-By-Point Fabrication Of Micro-Bragg Gratings in Photosensitive Fibre Using Single Excimer Pulse Refractive-Index Modification Techniques," *Electron. Lett.* vol. 29(18), pp.1668-1669, 1993.
- [8] H. J. Patrick, C. G. Askins, R. W. McElhanon and E. J. Friebele, "Amplitude mask patterned on an excimer laser mirror for high intensity writing of long period fibre gratings," *Electron. Lett.* vol. 33(13), pp.1167-1168, 1997.
- [9] S. Yamasaki, M. Akiyama, K. Nishide, A. Wada and R. Yamauchi, "Characteristics of long period fibre grating utilizing periodic stress relaxation," *IEICE Transactions on Electronics*, vol. E83-C(3), pp.440-443, 2000.
- [10] E. M. Dianov, V. I. Karpov, M. V. Grekov, K. M. Golant, S. A. Vasiliev, O. I. Medvedkov and R. R. Khrapko, "Thermo-induced long-period fibre gratings," *IEE conference publication*, No.448, pp.53-56, 1997.
- [11] D. D. Davis, T. K. Gaylord, E. N. Glytsis, S. G. Kosinski, S. C. Mettler and A. M. Vengsarkar, "Long-period fibre grating fabrication with focused CO₂ laser pulses," *Electron. Lett.* vol. 34(3), pp.302-303, 1998.
- [12] S. A. Vasil'ev, E. M. Dianov, A. S. Kurkov, O. I. Medvedkov and V. N. Protopopov, "Photoinduced in-fibre refractive-index gratings for core-cladding mode coupling," *Quantum Electron*, 27(2), pp 146-149, 1997.
- [13] R. Kashyap, "Fibre Bragg Gratings," 2nd Ed., Academic Press, Burlington, 2011.
- [14] T. Erdogan, "Cladding mode resistances in short and long period fibre grating filters," *J. Opt. Soc. Am.* 14, pp 1760-1773, 1997.

- [15] X. Shu, L. Zhang and I. Bennion, "Sensitivity Characteristics of Long-Period Fibre Gratings," *J. Lightwave technol.*, vol. 20(2), pp 255-266, 2002.
- [16] X. Chen, K. Zhou, L. Zhang and I. Bennion, "Dual-peak long-period fibre gratings with enhanced refractive index sensitivity by finely tailored mode dispersion that uses the light cladding etching technique," *Applied Optics* vol. 46(4), pp 451-455, 2007.
- [17] T. W. MacDougall, S. Pilevar, C. W. Haggans and M. A. Jackson, "Generalized expression for the growth of long period gratings," *IEEE Photon. Technol. Lett.*, vol. 10, pp 1449-1451, 1998.
- [18] V. Bhatia and A. M. Vengsarkar, "Optical fibre long-period grating sensors," *Opt. Lett.*, vol. 21(9), pp 692-694, 1996.
- [19] V. Bhatia, "Applications of long-period gratings to single and multi-parameter sensing," *Opt. Lett.*, vol. 4, pp 457-466, 1999.
- [20] G. Meltz, W. W. Morey, and W. H. Glenn, "In-fibre Bragg grating tap in optical fibre communication," San Francisco, California, USA: *Optical Society of America Technical Digest* series 1, vol. TuG1, 1990.
- [21] D. Z. Anderson, V Mizrahi, T Erdogan and A. E. White, "Production of in-fibre gratings using a diffractive optical element," *Electronics Letters*, vol. 29(6), pp. 566-568, 1993.
- [22] A. Othonos and K. Kalli, "Fibre Bragg gratings, fundamentals and applications in telecommunications and sensing," Artech House, London, 1999.
- [23] S. J. Mihailov, R. B. Walker, T. J. Stocki and D.C. Johnson, "Fabrication of tilted fibre grating polarisation –dependent loss equalizer," *Electron. Lett.* vol. 37, pp. 284-286, 2001.
- [24] G. Laffont and P. Ferdinand, "Tilted short-period fibre-Bragg-grating-induced coupling to cladding modes for accurate refractometry", *Meas. Sci. Technol.* vol. 12, pp. 765-770, 2001.
- [25] C. Chan, C. Chen, A. Jafari, A. Laronche, D. J. Thomson and J. Albert, "Optical fibre refractometer using narrowband cladding-mode resonance shifts," *Applied Optics* vol. 46(7), pp. 1142-1149, 2007.
- [26] G. Nemova and R. Kashyap, "Theoretical model of a planar integrated refractive index sensor based on surface plasmon-polariton excitation with a long period grating," *J. Opt. Soc. Am. B*, vol. 24, pp. 2696-2701, 2007.
- [27] A. M. Vengsarkar, P. J. Lemaire, J. B. Judkins, V. Bhatia, T. Erdogan and J. E. Sipe, "Long-period fibre gratings as band-rejection filters," *Journal of Lightwave Technology*, vol. 14(1), pp. 58-65, 1996.
- [28] K. Zhou, L. Zhang, X. Chen and I. Bennion, "Optic sensors of high refractive-index responsivity and low thermal cross sensitivity that use fibre Bragg gratings of 80° tilted structures," *Optics Letters*, vol. 31(9), pp. 1193-1195, 2006.
- [29] K. Zhou, L. Zhang, X. Chen and I. Bennion, "Low Thermal Sensitivity Grating Devices Based on Ex-45° Tilting Structure Capable of Forward-Propagating Cladding Modes Coupling," *Journal of light-wave technology* vol. 24, pp. 5087-5094, 2006.
- [30] Z. Yan, Z. Sun, K. Zhou, B. Luo, J. Li, H. Wang, Y. Wang, W. Zhao, and L. Zhang, "Numerical and experimental analysis of sensitivity enhanced RI sensor based on Ex-TFG in thin cladding fibre," *Journal of Lightwave Technology*, vol. 33(14), pp. 3023-3027, 2015.

- [31] Z. Yan, "Advanced tilted fibre gratings and their applications," Ph.D. Thesis, Aston Institute of Photonics technologies, Aston University, Birmingham, pp 151- 182, 2014.
- [32] H. J. Patrick, C. C. Chang and S. T. Vohra, "Long-period fibre gratings for structure bend sensing," *Electron. Lett.* vol. 34(18), pp.1773-1775, 1999.
- [33] H. J. Patrick and S. T. Vohra, "Directional shape sensing using sensitivity of long period fibre gratings," OFS-13, Korea, pp.561-564, 1999.

Chapter 4

In-fibre grating based refractive index sensors with nanoparticle deposition

[1, 2]

4.1 Introduction

The nanoparticle deposition on the surface of optical fibres alters their spectral characteristics and response to external perturbation. This chapter discusses significant contribution to the analysis and nano-characterisation of in-fibre grating based refractive index (RI) sensors.

The nanoparticles employed here are: Carbon nanotubes (CNT), Zinc oxide (ZnO), Polystyrene Spheres (PS) array and Gold nanoparticles (AuNPs). The optical characteristics of each of these nanoparticles were explored for spectral characterisation of the in-fibre gratings for sensing applications. These sensors find practical applications in bio/chemical detection due to their high RI sensitivity, low temperature cross-sensitivity, low cost power-based demodulation and strong mechanical strength.

4.2 Refractive index (RI) sensors based on 81° Ex-TFGs with carbon nanotube (CNT) deposition [1]

This session presents highly sensitive ambient refractive index (RI) sensors based on 81° excessively tilted fibre gratings (81°Ex-TFGs) structure UV-inscribed in SMF-28 fibre (62.5µm cladding radius) with carbon nanotube (CNT) overlay deposition. Two separate 80°Ex-TFGs were fabricated and evaluated as RI sensor which are termed as 'Sample1' and 'Sample2' respectively. Although the two 81°Ex-TFGs were fabricated under the same design conditions, due to the instability in the UV-source during grating inscription, their spectral characteristics are expected to be slightly different. The sensing mechanism is based on the ability of CNT to induce change in transmitted optical power and the highly sensitive structure of 81°Ex-TFGs to ambient refractive index. The thin CNT film with high refractive index enhances significant interaction between the cladding modes and the surrounding medium. Consequently, the surrounding medium RI change induces not only the resonant wavelength shift but also the strength of the attenuation band in the transmission spectrum. The result shows that the change in transmitted optical power produces a corresponding linear reduction in attenuation band strength with increment of RI values. The low thermal sensitivity property of the 81° Ex-TFGs offers reduction in thermal cross-sensitivity and enhances specificity of the sensor.

4.2.1 RI sensor fabrication

The fabrication process of the RI sensors includes two steps: Ex-TFG fabrication, and CNT deposition on grating area of fibre. Firstly, the Ex-TFGs were inscribed by a 244nm UV source from a frequency doubled Argon laser (Coherent Sabre Fred) using a custom-designed amplitude mask of period 6.6µm as earlier discussed in session 3.5.1. The period of the amplitude mask was specially designed to ensure that the generated grating responses from higher order cladding modes are centred in the C-L band of the frequency windows. The standard telecom fibre (SMF-28) samples were hydrogen loaded under high temperature (80°C) and high pressure (150 bars) for 48 hours to enhance UV- photosensitivity prior to the TFG inscription. During the inscription process the amplitude mask was tilted at ~ 77° external angle in order to achieve excessively tilted fringes at ~ 81° in the fibre core. Post the UV inscription, the Ex-TFGs were annealed at ~ 80°C for 48 hours to outgas the hydrogen and stabilize the grating structures.

Secondly, the CNT deposition was overlaid by a relatively simple and effective method on the grating area of the 81° Ex-TFGs for easy repeatability of the sensor. The CNT

solution was prepared by dispersing 0.5 mg of CNT powder in 10 ml of N-methyl-2-pyrrolidone (NMP) solution and sonicated in water bath (20 kHz, 200 W, 1 h, Nanoruptor, Diagenode SA, Liege, Belgium). NMP was used because of its efficiency in the direct dispersion of hydrophobic materials (CNT) at lower concentrations (< 0.02 mg/ml) [3]. Polyvinyl pyrrolidone (PVP) polymer (1 mg/ml) was added as dispersion agent in order to enhance the concentration of CNTs within the resulting dispersion [4]. Thereafter, the CNT-PVP-NMP solution was centrifuged for 30 minutes at 10 000 RPM with MLS-50 rotor (Optima MaxXP Benchtop Ultracentrifuge, Beckman Coulter, Brea, California, USA) with a view to removing residual CNT bundles and achieving a highly uniform dispersion. Figure 4.1 shows the experimental setup for the preparation of a well-dispersed CNT of 0.2mg/ml concentration. After the preparation, the well-dispersed CNT solution was deposited on the 81° Ex-TFGs using dip-draw method which entails placing the fibres in a micro-capillary tube filled with the CNT dispersion for a couple of minutes and repeated several times to achieve a CNT thickness of 2nm on the fibre surface. The entire surface of the grating region (of grating length 24mm) was totally submerged in the CNT solution and allowed to dry in air at atmospheric pressure for 24 hours. This method is found to be cost effective as it only entails the mechanical transfer of cold nanomaterials with no heating required [5]. CNTs being cylindrical carbon molecules structured with diameter of few nanometres and high surface area for absorption of water molecules and aqueous solutions, have been reported to have their refractive index (the effective dielectric property of CNT) vary with changes in RI of ambient medium [6].



Figure 4.1: Experimental setup for the CNT preparation.

4.2.2 Working Principle

The working principle of Ex-TFG based RI sensors includes two aspects: wavelength shift and intensity variation. The Ex-TFG induces two different sets of birefringence cladding modes (TM/TE resonance peaks) coupling and the strongest coupling between the fundamental core mode and the co-propagating cladding modes is expressed by the phase matching condition stated in Eqn. 3.20 but modified to show the factors on which the effective indexes of core and cladding depend in the expression below,

$$\text{Equation 4.1} \quad \lambda_{m,res} = \left(n_{co}^{eff}(\lambda_{m,res}, n_1, n_2) - n_{cl,m}^{i,eff}(\lambda_{m,res}, n_2, n_{SRI}) \right) \frac{\Lambda_G}{\cos \theta} \quad i = TE \text{ or } TM$$

Where $\lambda_{m,res}$ is the resonance wavelength due to coupling between fundamental core mode and the m^{th} cladding mode, n_{co}^{eff} is the effective index of the fundamental core mode, $n_{cl,m}^{i,eff}$ is the effective index of m^{th} cladding mode at the resonance wavelength, n_{SRI} is the refractive index of ambient medium, n_1, n_2 are the RI of the core and cladding respectively.

For intensity variation based sensing, the principle is as follows: when the surrounding RI changes, it leads to a variation in the amount of attenuation of the cladding modes which would result in change in the attenuation depth of the attenuation band. Therefore, the sensing of the RI of the external surrounding medium can be obtained by monitoring the amount of attenuation in the attenuation bands of the Ex-TFGs. And for wavelength shift based sensing, as the RI of surrounding medium varies there exists a corresponding variation in the effective index of the cladding modes, and then the resonant wavelength will shift according to Eqn. 4.1. When the RI of the ambient medium is less than that of the cladding mode, then with every increase in RI of the ambient medium the effective RI of the cladding also increases while that of the fundamental core remains constant resulting in red shift of the resonance wavelength.

Meanwhile, with additional thin film (CNT layer) on the cladding of the 81°Ex-TFGs, the sensors can be modelled as a four layer cylindrical waveguide. They can be modified to incorporate additional dielectric layer between cladding of finite thickness and the surrounding medium of infinite thickness. The schematic diagram in Figure 4.2 shows the sensors as model of four-layer cylindrical waveguide.

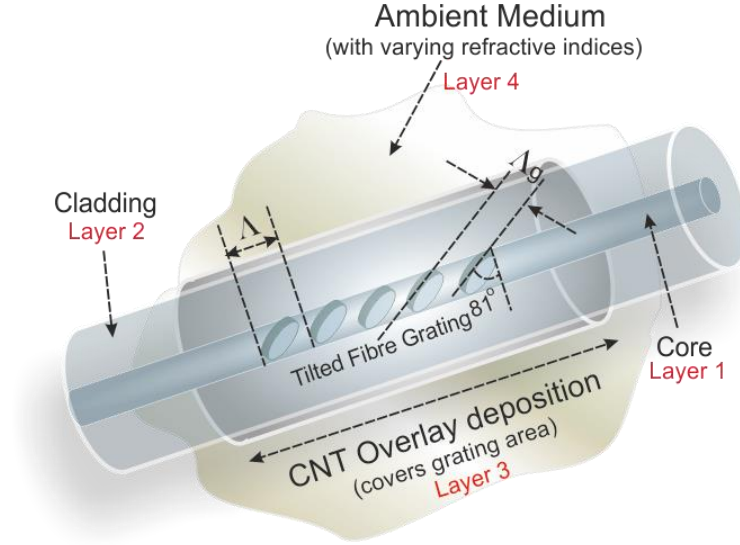


Figure 4.2: Schematic diagram of the CNT-coated 81° Ex-TFG RI sensor.

The 81° Ex-TFGs, now surrounded by medium of higher RI, will have a portion of the power of cladding mode reflected by the CNT layer while the remaining are transmitted [7]. Quantification of the amount of reflectance of the cladding mode at the fibre cladding/CNT layer interface can be obtained as follows [8]:

Equation 4.2
$$R = \left| \frac{r_{23} + r_{34} e^{-\tilde{k}_{cnt}}}{1 + r_{23} r_{34} e^{-\tilde{k}_{cnt}}} \right|^2$$

Equation 4.3
$$r_{23} = \frac{n_{clad} - \tilde{n}_{cnt}}{n_{clad} + \tilde{n}_{cnt}}$$

Equation 4.4
$$r_{34} = \frac{\tilde{n}_{cnt} - n_{SR}}{\tilde{n}_{cnt} + n_{SR}}$$

Equation 4.5
$$\tilde{k}_{cnt} = \frac{4\pi\tilde{n}_{cnt}d_{cnt}}{\lambda} = \frac{4\pi n d_{cnt}}{\lambda} - i \frac{4\pi k d_{cnt}}{\lambda} = \beta_{cnt} - i a d_{cnt}$$

where $a = 4\pi k/\lambda$ is the absorption coefficient of the thin CNT layer, n_{clad} and n_{SR} are the RIs of the cladding and the surrounding medium respectively. The reflection coefficient of the interface between each two layers in Eqns. 4.3 and 4.4 is denoted by $r_{i,j}$, and $\tilde{n}_{cnt} = n - ik$. Figure 4.2 shows each distinct layer as components of the sensor and from Eqns. (4.2 - 4.5), the reflectance (R) would vary with n_{SR} which consequently leads to variation in the coupling strength of the cladding modes resulting in change in depth of the attenuation band. Precisely, the sensors are based on the principle that both

the intensity and the wavelength of the CNT-coated 81°-TFG change with changes in the RI of ambient medium. The CNT overlay which is a dark material with high absorption of light and high RI is responsible for the decrement of the attenuation band while the 81°-TFG, being highly sensitive to ambient RI variations, induces the wavelength shift as the surrounding medium RI changes.

4.2.3 Experimental setup

The experimental setup to characterise the CNT coated Ex-TFG based RI sensors, as shown in Figure 4.3, includes a broadband light source (Fianium ultrafast fibre laser-super continuum- range 950nm to far infrared), an optical spectrum analyser (OSA, Model 86140 Agilent), micrometre stage, an in-fibre polariser and a polarisation controller. Light from the super-continuum laser was transmitted through a polariser linked to the polarisation controller (manual fibre paddle polarisation controller) and then through the sample (CNT coated Ex-TFG) with the transmission spectrum displayed on the OSA with resolution of 0.06 nm and average power of -33.2dB. The polarisation controller makes switching from the TE to TM of the cladding modes possible and each mode is subjected to variation in the surrounding RI. The transmission spectra of 81°-TFG ranging from 1250 to 1650 nm was captured on the OSA. As particular with Ex-TFGs, the peaks split into two which is as a result of the coupling of the two sets of cladding modes of orthogonal polarisation when measured using unpolarised light [9]. A pair of the dual-peak cladding modes with the spectrum centred around 1550-1580 nm was selected for the refractive index sensing.



Figure 4.3: Experimental setup of RI sensing of the CNT-coated 81°-TFG RI sensor.

The test solution used for this experiment was prepared from the dissolution of +D+ glucose (purchased from Sigma Aldrich) in de-ionized water and stirred under room temperature of about $22 \pm 0.1^\circ C$ until a saturated glucose solution was formed. Different

concentration of the glucose solution was obtained by varying the percentage concentration of the glucose powder and the volume of the de-ionized water. The refractive index of each solution was obtained using a digital refractometer with resolution of 0.001. To demonstrate the effect of the CNT film on the Ex-TFGs, the RI sensing performance between bare Ex-TFGs and the CNT coated Ex-TFGs were compared. The RI solution ranges from 1.300 to 1.370 for the experiment with the bare fibre while that for the CNT deposited fibre ranges from 1.344 – 1.392. This was because the experiments were carried out at different points in time and new solutions have to be prepared. All the measurements were carried out at room temperature. Since Ex-TFGs are less sensitive to temperature compared to LPFGs, temperature-induced perturbation that leads to cross-sensitivity is minimal. However, the thermal response of the sensors was also evaluated.

During the experiment, the CNT-coated 81°Ex-TFG which was mounted on a translational stage at each end have its grating area centred on the test platform attached to the micrometre stage. A new glass slide was repeatedly placed on the test platform as each solution was applied to the grating area for the RI measurement. Note, the CNT coated grating region was totally submerged in the glucose solution and the transmission spectra was monitored on the OSA. After each measurement, the CNT-coated 81°Ex-TFG was rinsed with methanol and the spectral movement was monitored to initial position in air. Using both the in-fibre polariser and polarisation controller enabled switching from one orthogonal state to the other (TE and TM cladding modes) during the experiment.

4.2.4 Results and discussion

With the CNT overlay on the grating region of the 81°Ex-TFG, the sensor, as shown in Figure 4.4, clearly display distinct power levels as well as resonant wavelength shifts with test solutions of different RI. It is observed that as the ambient RI varies lower reflectance occurs at higher RI values and higher reflectance at lower RI values. In other words, as the RI of the ambient solution increases, the intensity minima of the attenuation bands of the orthogonal TE and TM cladding mode decreases. The experiment was repeated three times and each time the distinct power level was imminent. This shows that with the CNT overlay on the fibre, the cladding modes extend well into the radiation mode. Then the amount of reflectance at the cladding/CNT boundary would depend on the surrounding medium RI as described in Eqn. 4.2. Also, the wavelength notably shifts towards the longer wavelengths (red-shift) as RI of surrounding medium increases.

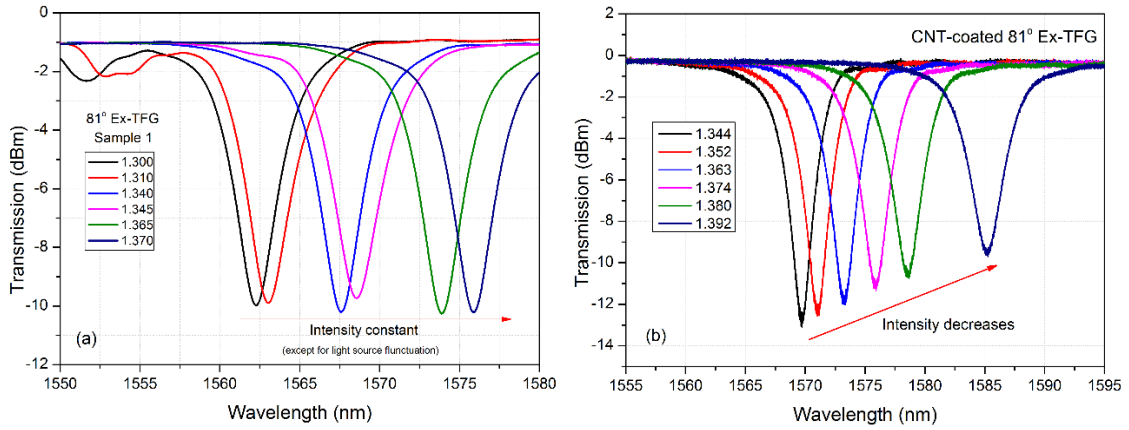


Figure 4.4: Transmission spectra evolution in response to SRI variation (a) bare 81°-TFG (b) CNT-coated 81°-TFG.

Figure 4.5(a) shows the plot of wavelength shift against variation in SRI for 81°Ex-TFG, ‘Sample 1’; TM-mode recorded sensitivities of 241.79 ± 16.32 nm/RIU (1.344 – 1.374) and 557.29 ± 22.85 nm/RIU (1.374 – 1.392) while TE-mode recorded sensitivities of 207.38 ± 11.14 nm/RIU (1.344 – 1.374) and 523.48 ± 23.84 nm/RIU (1.374 – 1.392). As shown in Figure 4.5(b), the second sample ‘Sample 2’ has its TM-mode recorded sensitivities of 222.45 ± 9.16 nm/RIU (1.344 – 1.374) and 519.38 ± 8.33 nm/RIU (1.374 – 1.392) and its TE-mode recorded sensitivities of 199.31 ± 10.73 nm/RIU (1.344 – 1.374) and 439.19 ± 6.52 nm/RIU (1.374 – 1.392).

Meanwhile, the intensity plot of TE/TM cladding modes against RI of ambient solution of the samples were also observed experimentally. For both samples, there exists positive correlation between the intensity variation and change in SRI as shown in Figures 4.5(c) and (d). For ‘Sample 1’ sensitivities of 70.65 ± 0.89 dB/RIU and 47.71 ± 0.71 dB/RIU were recorded for TM-mode and TE-mode respectively. Also, ‘Sample 2’ recorded sensitivities of 95.54 ± 1.62 dB/RIU and 64.03 ± 1.18 dB/RIU for TM-mode and TE-mode respectively. The power demodulation characteristic of CNT when used as RI sensing element as shown by above results are in good agreement with those reported in [10]. However, the results of Sample 1 give a 50 percent sensitivity increment while those of Sample 2 give over 100 percent increment in comparison with CNT-deposited LPFG earlier obtained in [10] within similar surrounding index of refraction range.

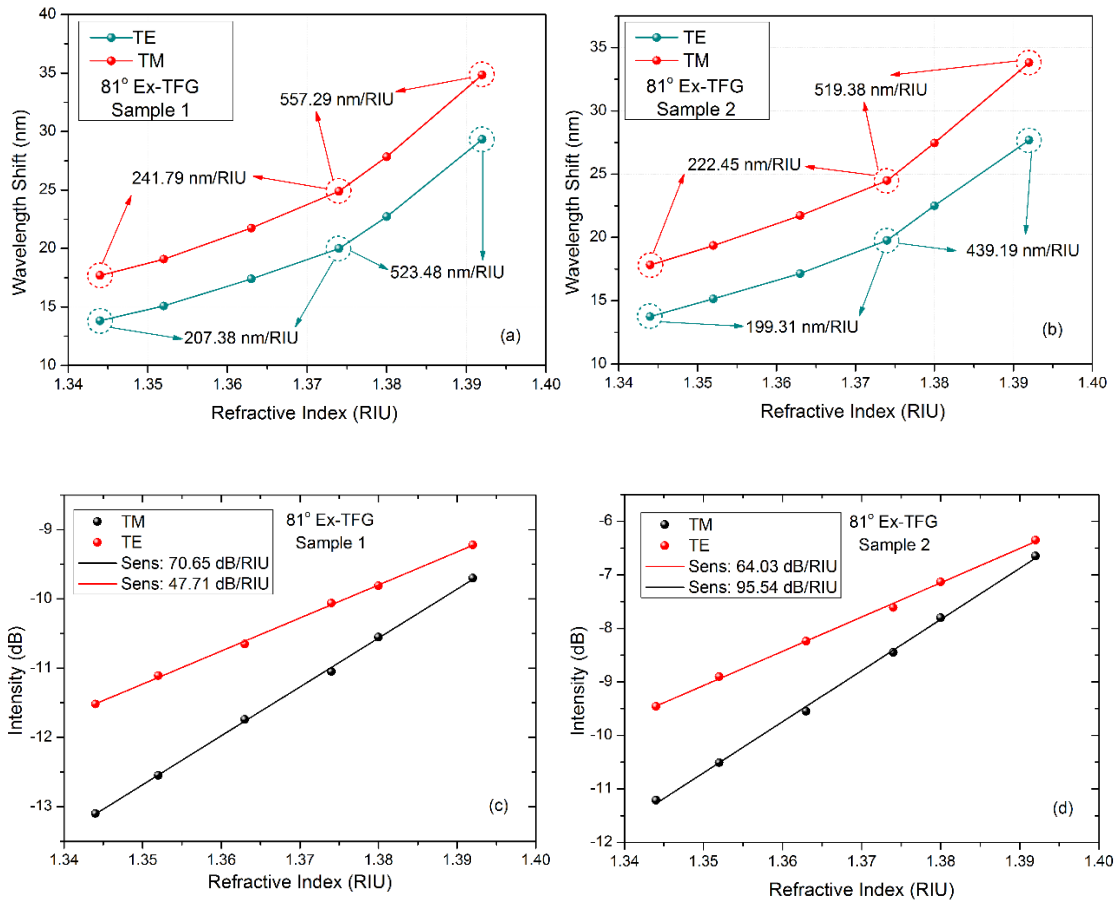


Figure 4.5: (a) Plot of wavelength shift against SRI variation (81° Ex-TFG, 'Sample 1') (b) Plot of wavelength shift against SRI variation (81° Ex-TFG, 'Sample 2') (c) Plot of intensity variation against change in SRI (81° -TFG, 'Sample 1') (d) Plot of intensity variation against change in SRI (81° Ex-TFG, 'Sample 2').

4.2.5 Conclusion

In summary, a highly sensitive ambient refractive index (RI) sensor based on excessively tilted fibre grating (81° Ex-TFGs) structures UV-inscribed in SMF-28 with carbon nanotube (CNT) overlay deposition has been demonstrated. The surrounding RI change has not only induced the resonant wavelength shift but also the power intensity change of the attenuation band in the transmission spectrum. For the wavelength demodulation, the sensors achieved high sensitivities of 557.29 nm/RIU (1.374–1.392) and 519.38 nm/RIU (1.374–1.392) range for the TM-modes of Samples 1 and 2 respectively. Also, for the intensity demodulation, sensitivities of 70.65 dB/RIU and 95.54 dB/RIU were obtained for the TM-modes of Samples 1 and 2 respectively.

4.3 Nano-deposition of zinc oxide (ZnO) on Ex-TFGs using discrete morphologies for enhanced RI sensing [2]

The inherent ability of excessively tilted grating structures (Ex-TFGs), photo-induced in optical fibre, to couple light from fundamental core mode to co-propagating higher order cladding modes made them a viable alternative for chemical and biochemical sensing. Recent findings have exploited the numerous advantages of optical fibre based refractive index (RI) sensors such as compactness, immunity to electromagnetic interference, high resolution, large evanescent field and ability to withstand harsh conditions. Prominent amongst such findings are fibre based interferometer [11-13], optical micro-fibre and fibre tapering [14-16], Surface Plasmon Resonance (SPR) based fibre sensors [17, 18], nanomaterial-coated optic fibre gratings [1, 19, 20] and multimode interference [21].

The asymmetric structure of Ex-TFGs induced by their excessively tilted fringes exhibits pronounced birefringence which degenerates the normal cladding modes into two sets of orthogonal polarisation dependent modes [9, 22]. These sets of orthogonal polarisation dependent modes appear as dual attenuation peaks at specific wavelengths across the transmission spectrum. The evanescent fields of Ex-TFGs cladding modes extend way beyond the cladding perimeter diffusing into the surrounding, thereby making them sensitive to the optical properties of such surrounding materials. Attempts to enhance this inherent property have instigated the nanodeposition of materials on the fibre surface with a view to enhancing their optical properties in response to external perturbations [1, 19]. Furthermore, the enhanced sensitivity of higher order cladding modes is as a result of their phase matching curve (PMC) having smaller gradient and operating closer to the dispersion turning point. This implies that small variation in any parameter induces large resonant wavelength shifts. Also, the higher order modes interrogate material farther away from the fibre core therefore any changes in overlay/film thickness and/or surrounding refractive indices have large effect on sensitivity [10]. As earlier iterated, Ex-TFGs exhibit low thermal cross sensitivity and higher responsivity to aqueous solutions compared with long period gratings.

Metal oxides have a wide range of properties, their physical structures affect the surface energy and hence influence their chemical (absorption) properties. Since structural defects in transition metal oxides greatly influence their catalytic properties, their application for chemical and biochemical sensing becomes viable. Zinc oxide, being a typical metal oxide, has numerous favourable properties such as wide bandgap, good transparency and high electron mobility. These properties have been explored for chemical sensing [23], gas sensing [24, 25], and biomedical detection [26]. Several findings, both theoretical and experimental, have shown that nm-thick thin film coating of

higher RI than the cladding facilitates the transition between cladding guided modes and the overlay guided mode thereby causing enormous attenuation-band shift in the transmission spectrum [27-29]. Nanodeposition of ZnO, which has a higher RI (1.929 at 1450 nm) [25] than the cladding of an optical fibre, on the surface of Ex-TFGs is therefore expected to improve its RI sensing properties.

The significance of this session of the thesis lies in the investigation and detection of improved optical sensitivity properties after the nanodeposition of zinc oxide (ZnO) on the surface of Ex-TFGs using two dissimilar morphologies. The first of which is a direct overlay of ZnO on the surface of the Ex-TFGs by dip-draw coating method with subsequent annealing under high temperature (200°C) and the other uses Polystyrene spheres (PS) array template for ZnO deposition under room temperature. Optical fibres of two different cladding diameters (80µm and 125µm) were used to ascertain variation in enhanced sensitivity and detect the most desirable morphology for each fibre type. Significant improvements of up to ~10-20% in sensitivity compared to the bare fibre were obtained with either morphology. Also, the investigation was limited to ambient RI below the cladding RI (1.30 – 1.38) where Ex-TFG have been demonstrated to be of high sensitivity [30].

4.3.1 Fabrication of 80°Ex-TFGs

The fabrication of the Ex-TFGs follows the same procedure as already discussed in session 4.2.1, however, an amplitude mask of period 5µm (200LPMM) was used for the scanning. Firstly, 80°Ex-TFGs were UV inscribed in H₂-loaded SMF-28 with grating length of ~12mm. These sets of Ex-TFGs are termed 'Sample A' for ease of analysis and discussion. Figure 4.6 shows the transmission spectrum of a Sample A 80°Ex-TFGs spanning across ~ 1280nm – 1680 nm when probed with unpolarised light, while the inset depicts the polarisation states of one paired peaks when probed with polarised and unpolarised light centred at ~1555nm. The black attenuation resonant dip indicates the fast-axis mode fully excited when the Ex-TFG is probed with X-polarised light, then the red resonant dip represents the slow-axis mode fully coupled when probed with Y-polarised light and finally the equal polarisation is achieved with unpolarised light exhibiting two equally coupled peaks (blue) of ~3dB intensity. The phase matching condition (PMC) for Ex-TFG resonant mode coupling is as expressed in Eqn. 4.1 and the sensitivity of the Ex-TFG to variation in SRI is explained by the dependence of the PMC on the effective index of the cladding modes which in turn is dependent on the difference between cladding and the ambient medium [30].

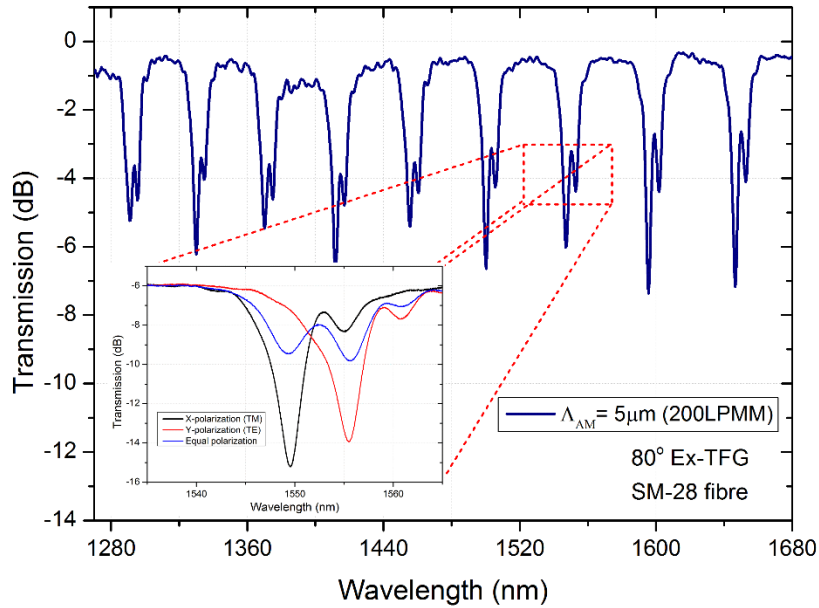


Figure 4.6: Transmission Spectrum of 80° Ex-TFG with an unpolarised probe light source spanning from 1280 ~1680 nm. (Inset: zoomed spectra at ~ 1550 nm showing X- and Y-polarisation and unpolarised light).

Secondly, ‘Sample B’ is a set of 80°Ex-TFGs that were UV inscribed in B/Ge co-doped thin cladding fibre (80μm B/Ge CA3596/877F/C - Nortel) using the same technique and parameters. The fibre is already co-doped to enhance photosensitivity, hence the inscription was made directly on the fibre without further hydrogen loading. The transmission spectrum of Sample B is similar to that of Sample A shown above. Analysis have shown that RI sensitivity significantly increases when a fibre of reduced cladding size is used. This is because the dispersion turning point moves to the lower order cladding modes when the fibre cladding radius is reduced and the number of guided cladding modes decreases. For a particular cladding mode order, the smaller the cladding radius the lower the cladding mode effective index and thus the more sensitive [30, 31].

4.3.2 Nanodeposition of ZnO on 80°Ex-TFGs

In order to deposit ZnO-nanoparticle layers on the fibre gratings we used ZnO nanoparticles (form: dispersion; 721085 ALDRICH; 40 wt. %) diluted in ethanol. We diluted the initially purchased ZnO nanoparticles up to 5 v/v % with neat ethanol. Basically, the deposition of ZnO on the grating region of the 80°Ex-TFGs followed two dissimilar morphologies. The first morphology entails deposition of ZnO nanoparticles by dip-draw coating and then annealing under high temperature (200°C). The film has a average thickness of approximately 80 ± 30 nm which was estimated via transmittance of the ZnO films in the range of 320-360 nm (Figure 4.7) and literature data [32-34]. The

transmittance spectra of ZnO films were measured with a Lambda 1050 UV/VIS/NIR (Perkin Elmer) spectrometer.

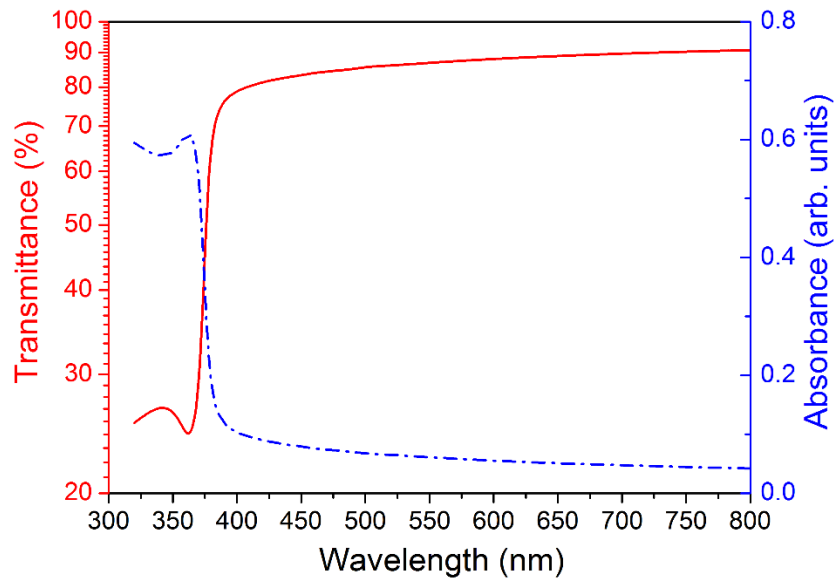


Figure 4.7: Transmittance and absorbance spectra of zinc oxide (ZnO) film.

The improvement of the adhesion between the fibre and the ZnO necessitated the high temperature for annealing (200°C). Figure 4.8 shows the schematic of the optical fibre revealing the excessively tilted fringes and the ZnO overlay. Each one of the 80°Ex-TFGs inscribed in SM-28 fibre (Sample A) and B/Ge co-doped thin-cladding fibre (Sample B) was coated using this morphology and the subsequent optical measurements were recorded and analyzed. Note, before coating the 80°Ex-TFGs their response to SRI variation was first measured for sensitivity comparison.

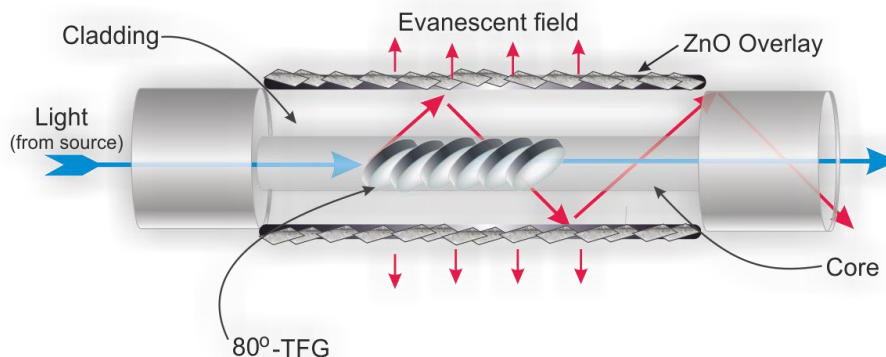


Figure 4.8: Schematic of Ex-TFG structure with direct ZnO deposition on the fibre cladding (Morphology 1).

The second morphology made use of closely-assembled monolayer (~500nm in diameter) Polystyrene spheres (PS) array template for ZnO deposition under room temperature. The monolayer PS colloidal crystals with closely-packed arrays were first prepared on a well cleaned glass substrate (2 × 2 cm) by spin coating of the PS colloidal suspension. The formed PS monolayer colloidal crystals were then transferred onto de-ionized water surface (or lift-off on water surface) as previously described in [35].

The monolayer PS colloidal crystals were finally picked up by the 80°Ex-TFGs using dip-draw coating method. The formed PS particles on the fibre grating are very stable due to the strong Van der Waals force from the monolayer PS colloidal crystals. The 80°Ex-TFGs were allowed to dry at room temperature for 12 hours to allow for total evaporation of water molecules. Thereafter, the PS-coated 80°Ex-TFGs were immersed in the earlier diluted dispersion of ZnO nanoparticles and left to dry for another 12hrs at room temperature.

Prior to optical measurements, the PS colloidal monolayer coated with the ZnO nanostructures was immersed in methylene chloride (CH₂Cl₂) solution for 5 min to dissolve/remove the PS spheres and the ZnO nanoparticles were left to assume the interstices of the PS spheres. Figure 4.9(a)-(c) depict the schematic of all the aforementioned procedures.

The monographs of the 80°Ex-TFGs identifying the two different morphologies employed for this investigation as observed under an optical microscope (Zeiss Axioskop 2 mot plus) are as shown in Figure 4.10. The first of the micrographs shows the excessively tilted fringes in the core of the fibre tilted at ~80° (Figure 4.10(a)), the second shows the zinc nanoparticle directly deposited on the fibre surface (Morphology 1) (Figure 4.10(b)) and the third shows ZnO in the interstices of PS array template (Morphology 2) (Figure 4.10(c)).

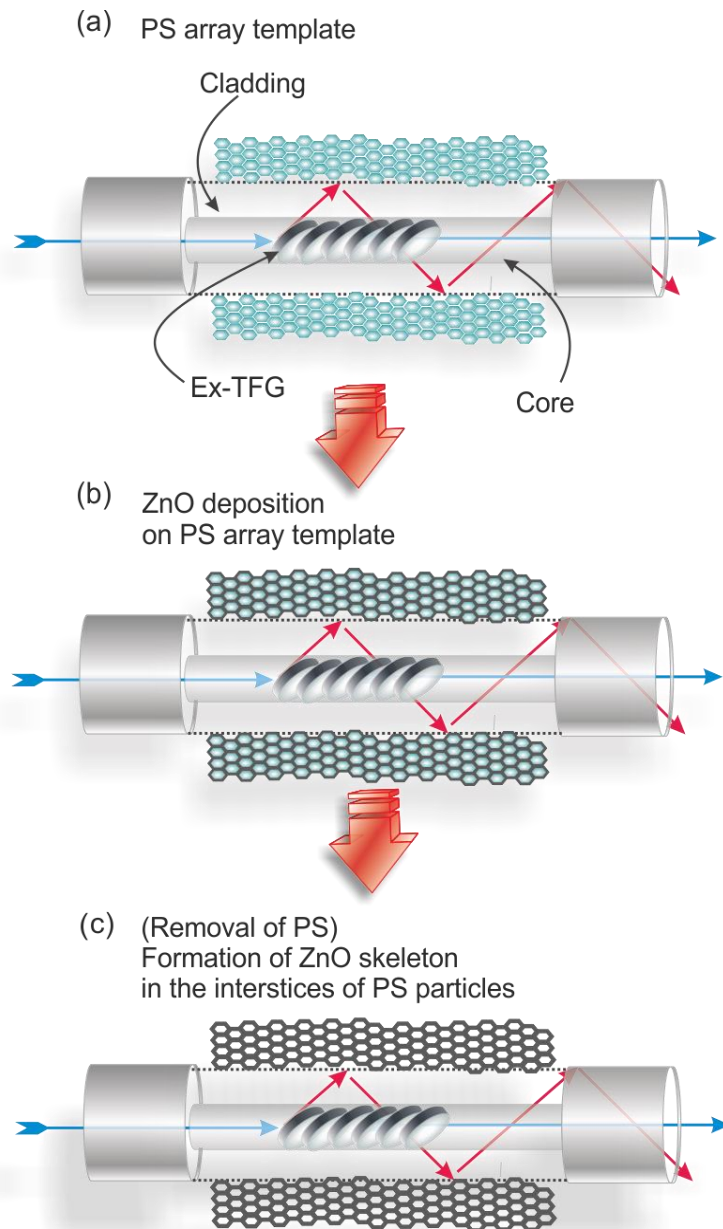


Figure 4.9: Schematic of template-directed synthesis of ordered porous ZnO films (Morphology 2): (a) PS array template overlay, (b) deposition of porous ZnO, and (c) PS removal and formation of ZnO in the interstices of PS particles.

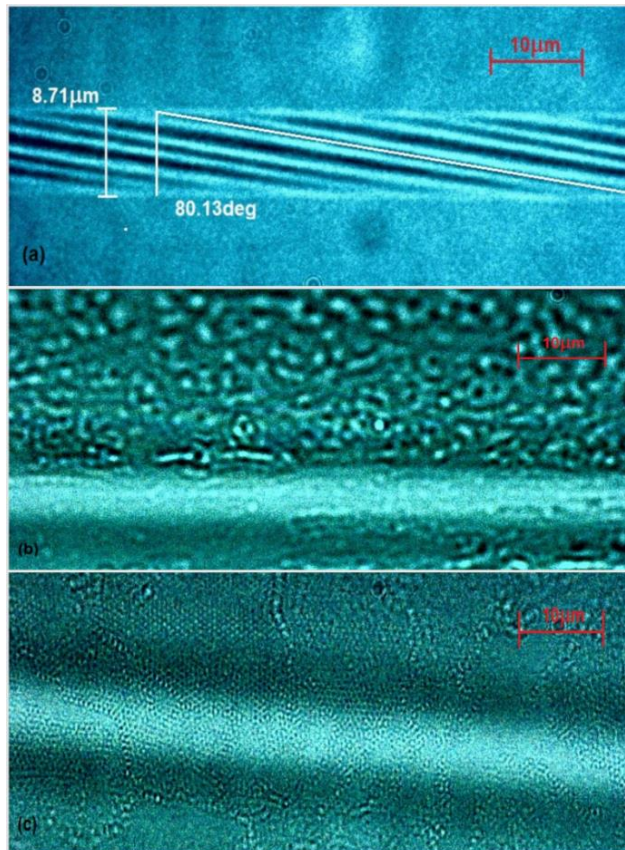


Figure 4.10: Micrographs of 80° Ex-TFG: (a) bare fibre showing the excessively tilted fringes, (b) direct ZnO deposition (Morphology 1), and (c) ZnO in the interstices of PS array template (Morphology 2).

4.3.3 Experimental setup

As earlier mentioned, the response of the 80° Ex-TFGs to SRI variation was first measured prior to coating with either identified morphology for sensitivity comparison. Here, the SRI measurement made use of series of index gel (Cargille Laboratory) of different refractive index values as test solutions. The experimental set up is the same as the one earlier reported for CNT-coated 81° Ex-TFG in Figure 4.3. In preparation for subsequent application of the index gels, the grating surface was intermittently rinsed off with methanol to remove the residual index gel and allowed to reset to reference before the next gel was applied. The spectrum recorded in air was used as reference and subsequent spectra movement due to application of the various index gels were analyzed with respect to the reference as displayed on the OSA.

4.3.4 Results and discussion

After the nanodeposition of ZnO on the fibre surface, the thermal annealing, which is one factor that distinguishes the two morphologies, greatly affects the film morphology. For the first morphology (direct ZnO overlay), the thermal process at $\sim 200^\circ\text{C}$ led to further oxidation of the ZnO nanoparticles inducing wavelength shift and attenuation variation of the resonant bands of the 80°Ex-TFGs . The ZnO overlay acts as mirror to the evanescence field thereby recoupling part of the light back into the fibre core mode which results in the reduction of the attenuation band compared to the bare 80°Ex-TFGs as shown in Figure 4.11(b). Besides the obvious reduction in attenuation band, the central wavelength red-shifted around ~ 4 nm away from that of the bare fibre. Thus direct coating of the 80°Ex-TFGs with ZnO leads to a red-shift of the central wavelength and a reduction in attenuation bands of the cladding modes. The attenuation band reduction is consistent with the results earlier reported for LPFG overlaid with Langmuir-Blodgett [36], TiO_2 [37] and CNT [1] thin films.

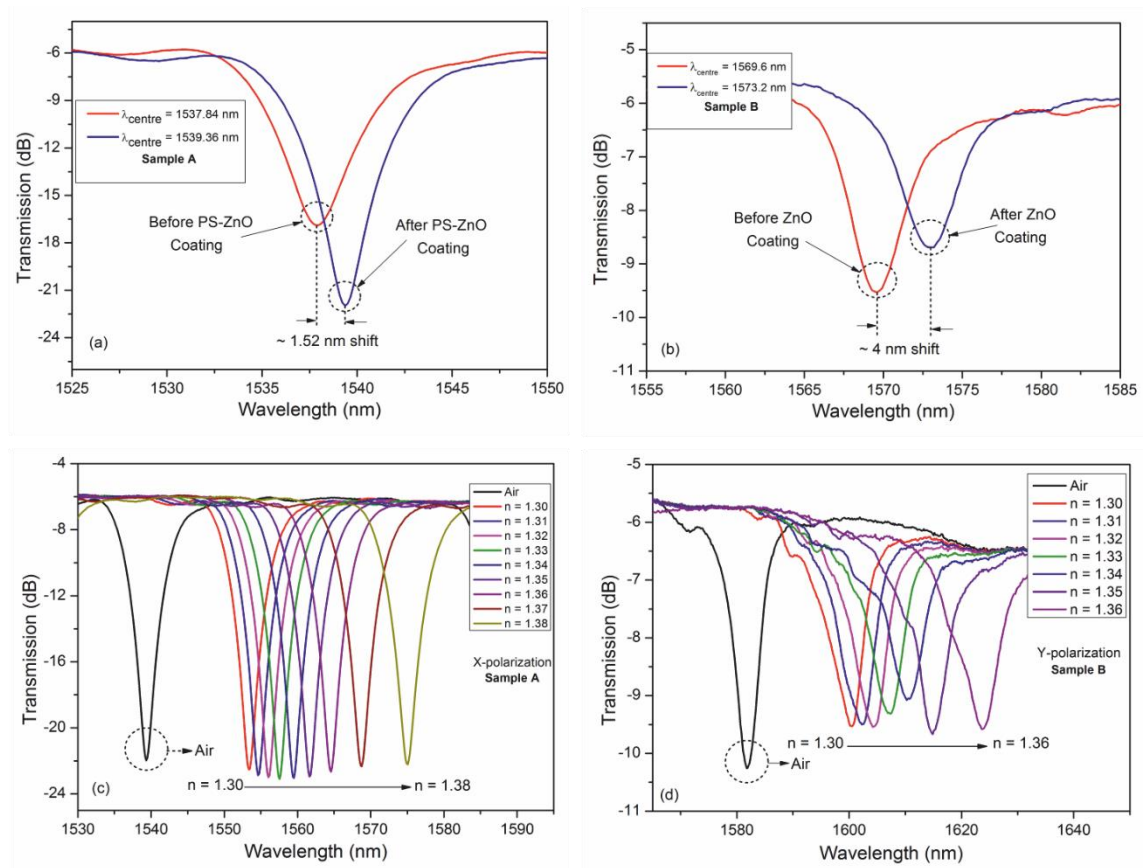


Figure 4.11: (a) Spectra wavelength shift after PS-ZnO coating (in Air); (b) Spectra wavelength shift after ZnO coating (in Air); (c) Transmission Spectra evolution of 80° Ex-TFG to surrounding media of different refractive indices after PS-ZnO coating (Sample A); and (d) Transmission Spectra evolution of 80° Ex-TFG to surrounding media of different refractive indices after ZnO coating (Sample B).

Meanwhile, the second morphology which made use of PS-array templates at room temperature, left a skeletal ZnO in the interstices of the PS particles after the PS removal, thereby weakening the reflective capacity of the metal oxide. This results in an increase in attenuation band compared to the bare 80°Ex-TFGs and a red-shift of ~ 1.52 nm as shown in Figure 4.11 (a). Figures 4.11 (c) and 4.11 (d) show the transmission spectra evolution of Samples A and B respectively as they were exposed to RI variations.

Numerical simulations results in [30] have shown that the effective index of cladding mode is affected by the interaction between the evanescence field of guided mode and the ambient medium. As the fibre cladding reduces, the dispersion turning point moves to the lower order cladding mode, consequently, SRI sensitivity increases enormously. Since the number of guided cladding modes is determined by the cladding radius, Samples A which has a larger cladding radius (62.5 μm) than Sample B (40 μm) is expected to exhibit different characteristics to each overlay morphology in conformity with the simulations.

Also, according to [38], when the fibre is coated with an overlay of a particular thickness, numerical simulation of effective index of the cladding modes as a function of the overlay thickness at a fixed wavelength draws two conclusions: firstly, the higher order cladding modes than the one guided by the overlay will shift their effective index value towards the immediate lower value. Secondly, the lower order cladding modes than those guided by the overlay will shift their effective index value to higher values. Consequently, the effective index returns to its original state thereby recovering the effective index distribution of cladding modes before overlay deposition. In other words, the fibre grating responds to the perturbation of overlay deposition by recovering the effective index distribution of the cladding modes each time a cladding mode is guided by the overlay. This is a repeated phenomenon each time a new mode is guided by the overlay.

Ideally, it is the cladding mode with highest effective index that is guided by the overlay but for the fact that this waveguides (80°Ex-TFGs) are lossy, the mode guided by the overlay may not be the one with highest state of energy. In other words, the thicker the overlay deposition, the lossier the waveguides which may result in lower effective index modes being guided by the overlay [38]. This explains why the direct ZnO overlay morphology on Sample A has a less significant SRI sensitivity increment of ~ 4.26% (~ 484.5 nm/RIU: 1.345-1.385) compared to the bare fibre as shown in Figure 4.12 (a) and (b) (X-pol and Y-pol respectively). Meanwhile, the second morphology (PS-ZnO) have an appreciable sensitivity improvement of ~ 19% increment (X-pol: 1.30-1.34) and ~ 10% increment (~ 409.5 nm/RIU: 1.35- 1.38) as shown in Figure 4.12 (c) and (d). This is in

conformity with the simulated results in [38] and it is therefore suitable to use the PS-ZnO morphology for Sample A if sensitivity improvement is to be optimised.

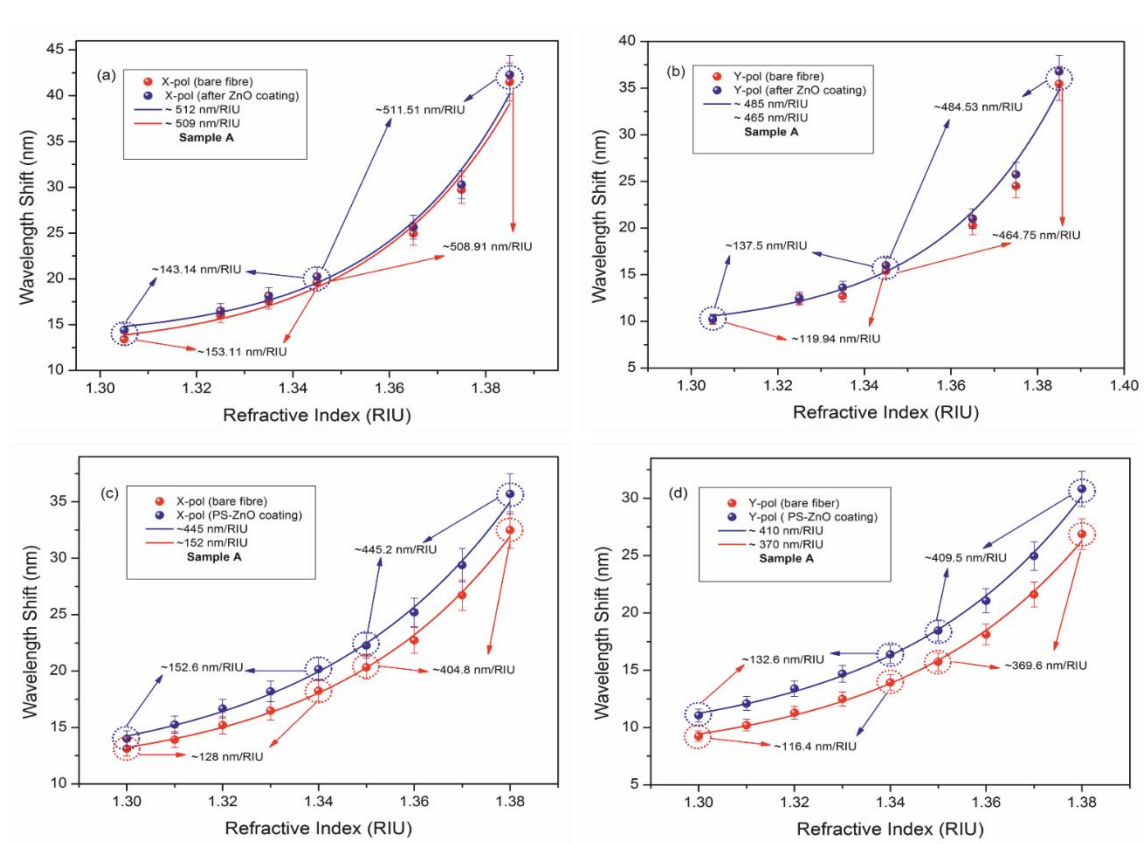


Figure 4.12: Plots of resonant wavelength shift of 80° Ex-TFGs (in SM-28 fibres) against SRI variation (Sample A): (a) X-polarisation before and after coating (Morphology 1); (b) Y-polarisation before and after coating (Morphology 1); (c) X-polarisation before and after coating (Morphology 2); and (d) Y-polarisation before and after coating (Morphology 2).

However, due to the reduction in cladding size and different dopant type and concentration of Sample B, both morphologies used for this waveguides show appreciable SRI sensitivity increment. Figure 4.13 (a) and (b) show the transmission spectrum response of the (direct) ZnO coated 80°Ex-TFGs with sensitivity enhancement of ~ 14.5% (~ 535 nm/RIU: 1.33-1.36) with respect to the bare fibre. Also, Figure 4.13 (c) and (d) show the response of 80°Ex-TFGs which uses the PS-ZnO morphology having an even higher SRI sensitivity improvement of ~ 21% (~ 522 nm/RIU: 1.33-1.36). It suffices to infer that although either morphology can be used for Sample B, the PS-ZnO morphology still have the most appreciable sensitivity increment. These results are also in good agreement with theoretical simulations in [28], [31] and [38]. Also, the experiments were carried out for repeatability assurance. Due to the enormity of the data and the preferred sensitivity increment range, SRI experiments using only Samples A

and B with PS-ZnO morphology were repeated three times to ascertain the repeatability of the sensors. The sensors give repeatability standard deviations of 0.09 and 0.10 for Samples A and B respectively.

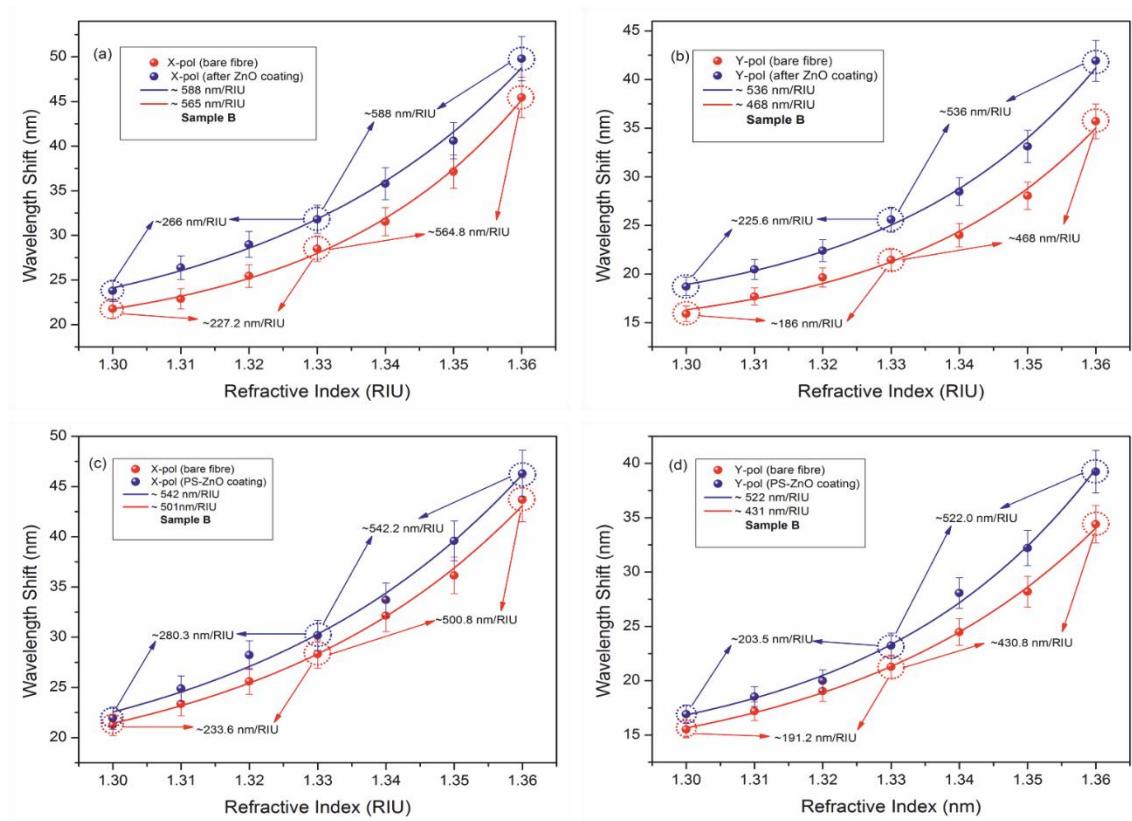


Figure 4.13: Plots of resonant wavelength shift of 80°Ex-TFGs (in thin-cladding B/Ge doped fibres) against SRI variation (Sample B): (a) X-polarisation before and after coating (Morphology 1); (b) Y-polarisation before and after coating (Morphology 1); (c) X-polarisation before and after coating (Morphology 2); and (d) Y-polarisation before and after coating (Morphology 2).

4.3.5 Conclusion

The nanodeposition of ZnO on excessively tilted grating structures (Ex-TFGs) in single-mode fibre using discrete morphologies have been investigated for enhanced refractive index sensing. Also, the 80°Ex-TFGs have been shown to exhibit relatively higher sensitivity to SRI with ZnO coating. Samples A with higher cladding radius (62.5µm) showed a less significant SRI sensitivity increment of ~ 4.26% (~ 484.5 nm/RIU) compared to the bare 80°Ex-TFGs when the direct ZnO overlay morphology was employed, however, it exhibited a significant improvement in sensitivity by ~ 19% (1.3-1.34) and ~10% (~ 409.5 nm/RIU: 1.35- 1.38) with respect to the bare fibre Ex-TFG when PS-ZnO morphology was employed. Meanwhile, due to the reduction in cladding size (40µm) and different dopant type and concentration of Sample B fibre, it showed improved sensitivities to both morphologies: sensitivity enhancement of ~ 14.5% (~ 535 nm/RIU: 1.33-1.36) for the direct ZnO overlay and a higher SRI sensitivity improvement of ~ 21% (~ 522 nm/RIU: 1.33-1.36) for the PS-ZnO morphology with respect to the bare fibre Ex-TFG. Experimentally, the sensors give repeatability standard deviations of 0.09 and 0.10 for Samples A and B respectively. With the advantage of low thermal cross-sensitivity, high mechanical strength and light weight, these sensors are viable alternatives in chemical, biochemical, environmental and food processing applications.

4.4 Plasmon-enhanced optical sensor based on gold-coated S-TFGs

Evanescent optical waveguide sensors used as refractometry and sensing of changes in functionalised coatings with comparable sensitivities have been experimentally and theoretically investigated [39-42]. One prominent way of achieving such a waveguide is the use of surface plasmon polaritons (SPPs) that are confined by metal dielectric interface [43]. In order to achieve plasmon resonance, the optical field within the fibre must have non-zero amplitude at the fibre interface with a specific value of axial propagation constant [44]. Earlier reported findings relied on tapered fibres, metal-coated side polished fibres, or multimode fibres for the interaction between guided core light and the metal film [39, 40].

Recent findings have used LPFGs to excite a particular cladding mode whose effective index is perturbed by a plasmon resonance of metal coating on the fibre [41] and small angle tilted fibre gratings (S-TFGs) with cladding modes having non-zero evanescent fields extending beyond the cladding diameter into the metal film [45]. The unique properties of these waves coupled with the highly controlled excitation by S-TFGs combined to make high resolution sensors for infinitesimal changes occurring at fibre-metal interface. This finding experimentally investigates plasmon-excited S-TFG sensor by utilizing already established theoretical procedures.

4.4.1 Fabrication of plasmon-excited S-TFG sensor

The fabrication of the plasmon-excited S-TFG sensor comprises two different stages: the S-TFG fabrication and the gold film deposition on the S-TFG. Firstly for the fabrication of S-TFG, the various fabrication procedures of small angle tilted fibre gratings (S-TFGs) have been extensively discussed in session 3.41 and the particular method employed for the fabrication of all S-TFGs reported in this thesis has been identified. However, it is important to state that these STFGs were fabricated in hydrogen loaded SMF-28 using a phase mask with centre wavelength 1552nm and a period of 1071.92nm. After successful inscription, the STFGs were annealed at 80°C for 48 hours to stabilize the grating structures. For a normal FBG, the Bragg resonance is always the longest in wavelength and strongest in resonance since the effective index of the single core guided mode is the largest; however, when the grating planes are slightly tilted (in this case at 6°) the effect is an enhancement of cladding mode resonances spread across the shorter wavelength at the expense of the reduction in Bragg resonance as shown in Figure 4.14.

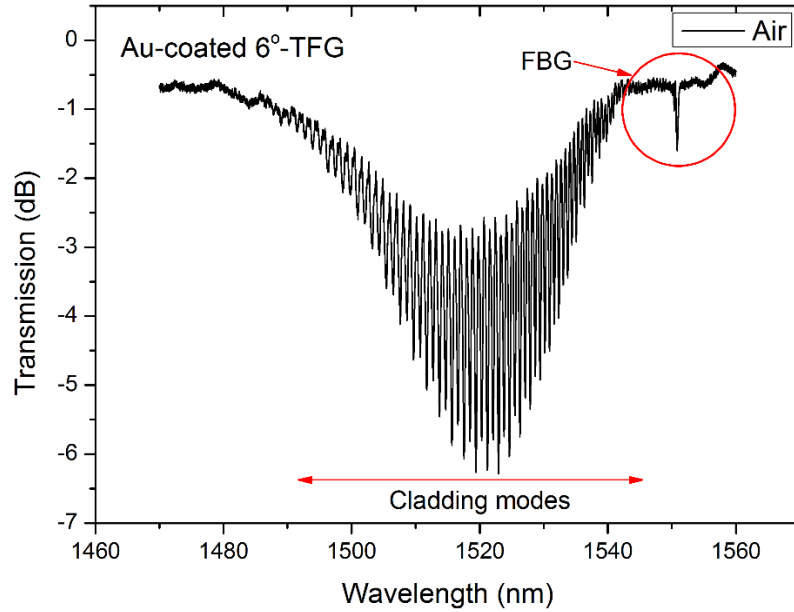


Figure 4.14: Transmission spectrum of the gold-coated 6°-TFG in air.

The second fabrication stage is the gold (Au) film deposition on the surface of the S-TFG using thermal evaporation. Prior to the Au film deposition, closely-assembled monolayer Polystyrene spheres (PS) array with diameter 750nm was deposited on the fibre surface under room temperature by dip-draw coating method (Figure 4.15(a)). The deposited PS template are very stable and attractive due to the Van der Waals force existing within its crystal and could attach the gold film to the fibre surface. The 6°-TFGs fibre samples were allowed to dry at room temperature for 12 hours to allow for total evaporation of water molecules. Thereafter, the process of gold film coating commenced. Gold wire, purchased from Kurt J. Lesker Company with 0.5mm diameter and 99.99% purity, was used for the growth and characterisation of gold thin films on the surface of the S-TFGs.

The thermal evaporation process entails heating a solid material (the gold wire) beyond its evaporation point and causing the vapour particles to be deposited on the sample (S-TFG). Usually, the process takes place inside a vacuum so as to prevent interaction between emitted vapour particles and atmospheric impurities. In this experiment, Aston University's Moorfield evaporator was used to deposit gold film on the S-TFG. To start with, the material (gold wire) for evaporation is placed in a boat of electrically conductive highly thermally resistive material (such as Tungsten or Molybdenum).

The boats were preheated at a temperature below the evaporation point of the gold wire before deposition. Preheating is necessitated in order to eject any impurity absorbed into the chamber wall which would have otherwise been emitted alongside the main material during evaporation.

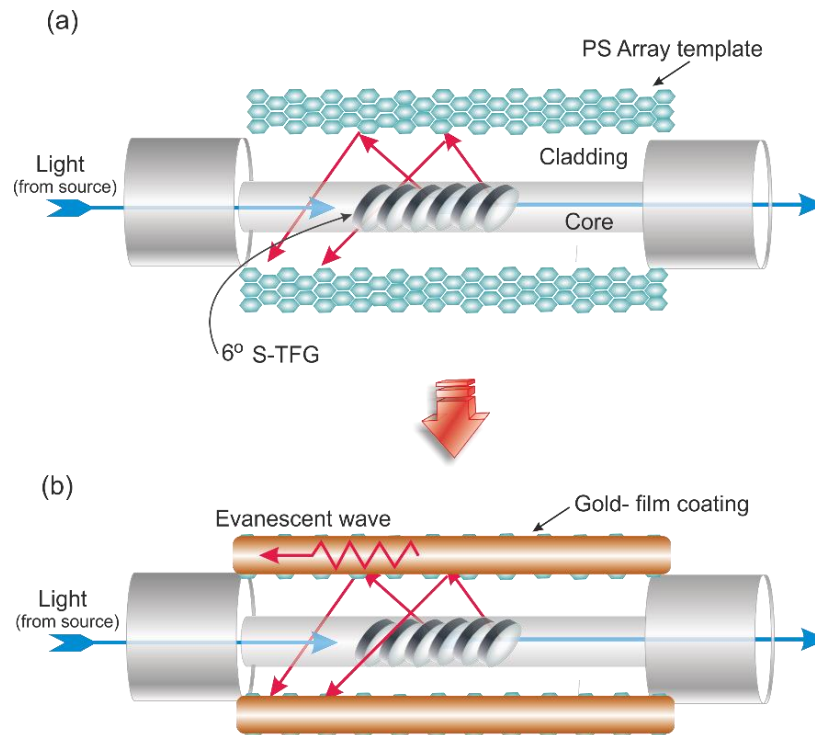


Figure 4.15: Schematic of template-directed synthesis of ordered gold-film deposition: (a) PS array template overlay and (b) Gold-film coating on PS template

The deposition was patterned using shadow masks and the film thickness evaluated by a quartz crystal thickness monitor which gives real time film thickness and deposition rates. The gold wire has a melting point of 1064°C and the temperature was achieved with a voltage of 1.5V and power of 8W. Subsequent evaporation process was done with higher voltage (2.5V) and power (44W) so as to achieve faster rate of deposition. With the higher voltage and power, the gold wire heats up and evaporates resulting in vapour which travels across the length of the chamber till it comes in contact with the target sample (S-TFG). The vapour cools off forming a solid state thin film on the surface of the S-TFG. The fibre was coated as uniformly as possible by rotating the fibre holder at angle 180° between coating process. However, since the fibre is cylindrical, the film uniformity on the fibre surface cannot be totally guaranteed which leads to some polarisation dependence of the light transmission. Figure 4.15(b) shows the gold-film overlay covering the PS template on the surface of the fibre. After the gold-film deposition, the PS colloidal monolayer was dissolved/removed by immersing the Au-coated 6° -TFGs in methylene chloride (CH_2Cl_2) solution for 5 minutes. The film thickness as indicated real time by the quartz crystal is 44nm which is the thickness of the two sides that directly faced the sputtering target.

4.4.2 Sensing principle

An S-TFG has its grating plane slightly tilted (internal tilt of 6°) from the fibre axis which enables it to couple the core mode light to a multitude of counter propagating cladding modes. The counter propagating cladding modes are not reflected back (like FBG) but rather rapidly attenuated by the fibre cladding. Coupling to the surface plasmon resonance (SPR) occurs when the axial component of the cladding mode is equivalent to that of an SPR wave. The Au-coated S-TFG is with the versatility that a single grating design can sufficiently generate wavelength-dependent set of cladding modes that can individually interrogate the metal film at various angles of incidence. Whenever a cladding mode couples to an SPR, it experiences more attenuation than other surrounding modes indicating the SPR signature. The effective index of the i^{th} cladding mode (n_{clad}^i) is determined from the resonance position (λ_{clad}^i) that satisfy the following phase matching condition [46]:

$$\text{Equation 4. 6} \quad \lambda_{clad}^i = (n_{eff}^i + n_{clad}^i) \frac{\Lambda}{\cos \theta}$$

where n_{eff}^i is the effective index of the core mode at wavelength λ_{clad}^i , Λ is the grating period and θ is the internal tilt angle of the S-TFG. The effective index of the surface plasmon N_{eff}^{SP} can be determined from the dielectric constant of the metal (ϵ_m) and the refractive index of the surrounding medium n_s as expressed in Eqn. 4.7 below [47],

$$\text{Equation 4. 7} \quad N_{eff}^{SP} = \sqrt{\frac{\epsilon_m n_s^2}{\epsilon_m + n_s^2}}$$

The SPR signal depends on polarisation of the input light source [48] which is maximised for P-polarised light corresponding to complete extinction of a fractional part of the cladding mode resonances. It is obvious in Figure 4.16(a) that when the P-polarised light is transmitted through the S-TFG, the effective index of the SPR is found where the cladding mode resonances are attenuated most in the transmission spectra. However, for the S-polarised light, the SPR effect is not excited and the transmission spectrum remain similar to that of uncoated S-TFG as shown in Figure 4.16(b). This Au-coated S-TFG has the advantage that each of the cladding modes can be individually investigated by simply changing the wavelength of the guided light with each mode striking the cladding boundary at different angle of incidence. This result is in agreement with those obtained in [48] where effect of polarisation was extensively discussed.

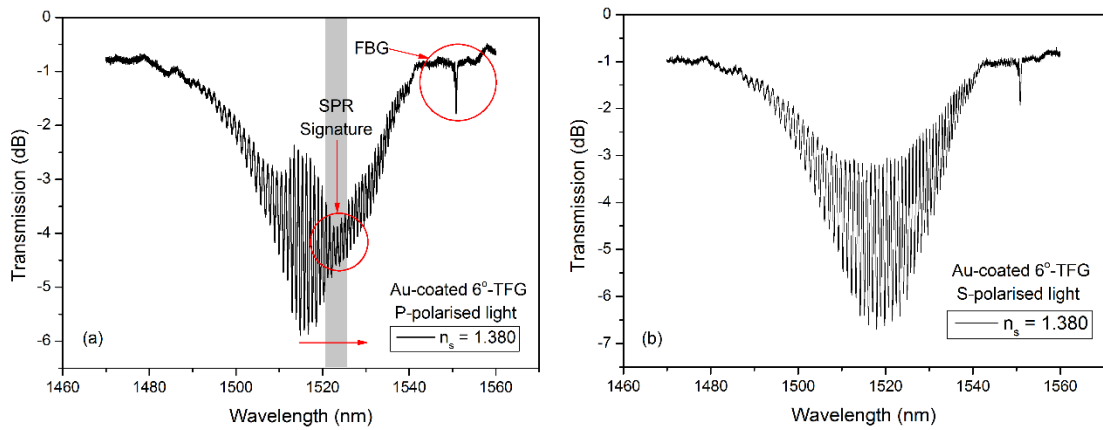


Figure 4.16: Transmission spectra of Au-coated 6°-TFG excited with (a) P-polarised light and (b) S-polarised light.

4.4.3 Results and discussion

In similar manner as described in [48], for the gold film thickness of 44nm, the plasmon has effective index close to the gold index-gel boundary which can be calculated using Eqn. 4.7. As shown in Figure 4.16, the Au-coated 6°-TFG excites a large number of cladding modes but amongst these modes, only those who have their effective index and polarisation state equal to that of the SP will be able to transfer energy across the metal layer. When the Au-coated 6°-TFGs is immersed in index gels (Cargille) of different refractive indices (RIs), the SPR is observed to red-shift as the surrounding RI increases.

The experimental result shows the loss of a small subset of the cladding modes resonances increase at the location of the observed SP thereby confirming the possibility of measuring ambient RI changes. Figure 4.17 shows some selected transmission spectra of the response of the SPR to SRI variation. It is observed that the SPR red-shifts as the RI of the index gels increases immediately when the Au-coated 6°-TFG is submerged. The anomalous resonances which appear are quite different from those observed with uncoated S-TFG. The SPR was observed for index gel with RI range between 1.340 – 1.412. The plot of SPR wavelength shift as a function of SRI variation is well approximated by a linear fit with a slope of 469.97 ± 15.2911 nm/RIU as shown in Figure 4.18 (the inset shows the regular residual plot of the linear fitting). The sensitivity of ~ 469.97 nm/RIU shows the SPR is highly sensitive to SRI variation.

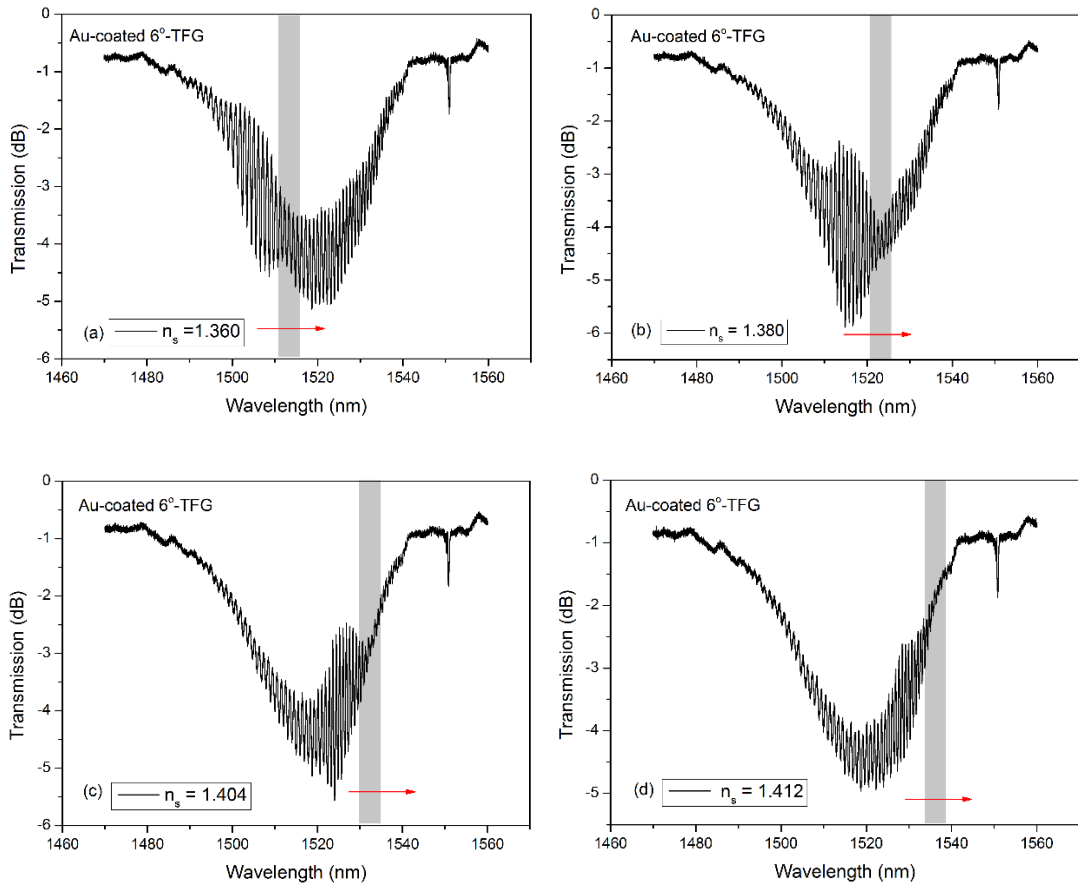


Figure 4.17: Transmission spectra of Au-coated 6°-TFG showing red-shift of the SPR as SRI changes (a) $n_s = 1.360$ (b) $n_s = 1.380$ (c) $n_s = 1.404$ (d) $n_s = 1.412$

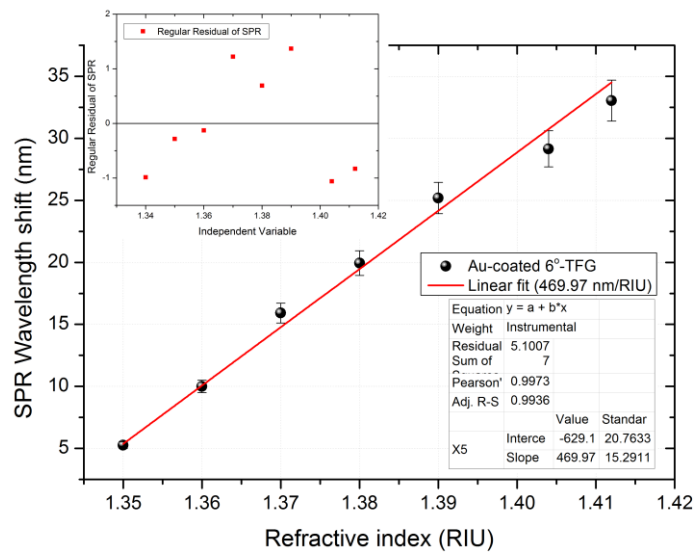


Figure 4.18: Plots of SPR wavelength shift of 6°-TFG against SRI variation; inset: regular residue plot.

4.4.4 Conclusion

The SPR signature has been observed as an evidence of surface plasmon resonance in a gold coated small angle tilted fibre grating (internal tilt of 6°) fabricated in standard single mode fibre. The Au-coated 6° -TFGs have been employed as an SRI sensor with a sensitivity of 469.97 nm/RIU. This sensor could find application in chemical monitoring, food processing or environmental monitoring.

4.5 Chapter conclusion

The nano-characterisation of optical fibre grating surface has been investigated for enhanced sensitivity to external perturbation using nanoparticles such as CNT, ZnO and AuNPs. Different deposition morphologies on Ex-TFGs have been explored and experimental results have shown RI sensitivity enhancement. Session 4.2 has demonstrated a highly sensitive ambient RI sensor based on 81° excessively tilted fibre grating structures UV-inscribed in standard telecom fibre with carbon nanotube (CNT) overlay deposition. The surrounding RI change has not only induced the resonant wavelength shift but also the power intensity change of the attenuation band in the transmission spectrum.

The nano-deposition of ZnO on single-mode excessively tilted grating structures (Ex-TFGs) using discrete morphologies has been presented in session 4.3 for enhanced refractive index sensing. Sensitivity enhancement as a function of cladding diameter and different deposition morphology has been extensively investigated. With respect to the bare fibre gratings, Samples A and B showed significant improvement in sensitivities by ~ 19% increment (~ 409.5 nm/RIU) and ~ 21% (~ 522 nm/RIU) for PS-ZnO morphology respectively.

Finally, session 4.4 presents Au-coated 6°-TFGs observed for SPR signature and employed as an RI sensor. Also, it has been shown that the excitation of SP by Au-coated 6° S-TFGs is polarisation dependent.

References

- [1] A. A. Badmos, Q. Sun, Z. Yan, R. N. Arif, J. Zhang, A. Rozhin and L. Zhang, "High sensitivity refractive index sensor based on large-angle tilted fibre grating with carbon nanotube deposition," *Proc. SPIE 9899*, Optical Sensing and Detection IV, 989916, 2016.
- [2] A. A. Badmos, P. Lutsyk, J. Zhang, Z. Sun, Lifeng Hang, Z. Yan, K. Zhou and L. Zhang, "Nanodeposition of ZnO on single-mode excessively tilted grating structures (Ex-TFGs) using discrete morphologies for enhanced refractive index sensing", (*In press*) 2017.
- [3] S. Giordani, S. D. Bergin, V. Nicolosi, S. Lebedkin and M. M. Kappes, "Debundling of single-walled nanotubes by dilution: observation of large populations of individual nanotubes in amide solvent dispersions," *J. Phys. Chem. B* vol. 110, pp. 15708–15718, 2006.
- [4] T. Hasan and V. Scardaci, "Stabilization and "debundling" of single-wall carbon nanotube dispersions in N-methyl-2-pyrrolidone (NMP) by polyvinylpyrrolidone (PVP)," *J. Phys. Chem. C* vol. 111, pp. 12594–12602, 2007.
- [5] S. Y. Set, H. Yaguchi, Y. Tanaka and V. Jablonski, "Laser mode locking using a saturable absorber incorporating carbon nanotubes," *J. Lightwave Technol.* vol. 22, pp. 51–56, 2004.
- [6] Y. Wang and J. T. Yeow, "A review of carbon nanotubes-based gas sensors," *J. Sensors*, pp. 1 - 24, 2009.
- [7] D. B. Stegall and T. Erdogan, "Leaky cladding mode propagation in long-period fibre grating devices," *IEEE Photon. Technol. Lett.* vol. 11, pp. 343–345, 1999.
- [8] H. A. Macleod, "Thin-Film Optical Filters, fourth ed.," *CRC Press/Taylor & Francis*, Boca Raton, FL, ch.4, 2010.
- [9] K. Zhou, L. Zhang, X. Chen and I. Bennion. "Optic sensors of high refractive-index responsivity and low thermal cross sensitivity that use fibre Bragg gratings of 80° tilted structures," *Optics Letters* vol. 31(9), pp. 1193-1195, 2006.
- [10] Y. C. Tan, W. B. Ji, V. Mamidala, K. K. Chow, "Carbon-nanotube-deposited long period fibre grating for continuous refractive index sensor applications," *Sensors and Actuators B* vol. 196, pp. 260-264, 2014.
- [11] K. Zhou, Z. Yan, L. Zhang and I. Bennion, "Refractometer based on fibre Bragg grating Fabry-Perot cavity embedded with a narrow microchannel," *Optical Express* vol. 19, pp. 11769-11779, 2011.
- [12] J. H. Wo, G. H. Wang, Y. Cui, Q. Z. Sun, R. B. Liang, P. P. Shum, and D. M. Liu, "Refractive index sensor using microfibre-based Mach-Zehnder interferometer," *Opt. Lett.* vol. 37, pp. 67–69, 2012.

- [13] J. Tian, Y. Lu, Q. Zhang, and M. Han, "Microfluidic refractive index sensor based on an all-silica in-line Fabry-Perot interferometer fabricated with micro-structured fibres," *Opt. Express* vol. 21, pp. 6633-6639, 2013.
- [14] P. Lu, L.Q. Men, K. Sooley, and Q. Y. Chen, "Tapered fibre Mach-Zehnder interferometer for simultaneous measurement of refractive index and temperature," *Appl. Phys. Lett.* vol. 94, 2009.
- [15] W. B. Ji, H. H. Liu, S. C. Tjin, K. K. Chow, and A. Lim, "Ultra-high sensitivity refractive index sensor based on optical microfiber," *IEEE Photon. Technol. Lett.* vol. 24 pp. 1872–1874, 2012.
- [16] P.F. Wang, G. Brambilla, M. Ding, Y. Semenova, Q. Wu, and G. Farrell, "High-sensitivity, evanescent field refractometric sensor based on a tapered multimode fibre interference," *Opt. Lett.* vol. 36, pp. 2233–2235, 2011.
- [17] P.K. Maharana, P. Padhy, and R. Jha, "On the field of enhancement and performance of an ultra-stable SPR biosensor based on graphene," *IEEE Photon. Technol. Lett.* vol. 25, pp. 2156-2159, 2013.
- [18] X. Wu, J. Zhang, J. Chen, C. Zhao, and Q. Gong, "Refractive index sensor based on surface-Plasmon interference," *Opt. Lett.* vol. 34, pp. 392-394, 2009.
- [19] B. N. Shivananju, S. Yamdagni, R. Fazuldeen, A. K. Kumar, S. P. Nithin, M. M. Varma and S. Asokan, "Highly Sensitive Carbon Nanotubes Coated Etched Fibre Bragg Grating Sensor for Humidity Sensing," *IEEE Sensors Journal*, vol. 14, pp. 2615-2619, 2014.
- [20] L. Coelho, D. Viegas, J. L. Santos, J. M. M. de Almeida, "Characterisation of zinc oxide coated optical fibre long period gratings with improved refractive index sensing properties," *Sens. and Actuators B* vol. 223, pp. 45-51, 2016.
- [21] S. Silva, O. Frazao, J. L. Santos, F. X. Malcata, "A reflective optical fibre refractometer based on multimode interference," *Sens. Actuator B* vol. 161, pp. 88-92, 2012.
- [22] K. Zhou, L. Zhang, X. Chen, I. Bennion, "Low thermal sensitivity grating devices based on ex-45° tilting structure capable of forward-propagating cladding modes coupling," *J. Lightwave Technol.* vol. 24, pp. 5087–5094, 2006.
- [23] N. A. Yebo, P. Lommens, Z. Hens, and R. Baets, "An integrated optic ethanol vapor sensor based on a silicon-on-insulator micro ring resonator coated with a porous ZnO film," *Opt. Express* vol. 18(11), pp. 11859-11866, 2010.
- [24] Q. Wan, Q. H. Li, Y. J. Chen, T. H. Wang, X. L. He, J. P. Li and C. L. Lin, "Fabrication and ethanol sensing characteristics of ZnO nanowire gas sensors," *Appl. Phys. Lett.* vol. 84(18), pp. 3654-3656, 2004.
- [25] W. Y. Wu, J. M. Ting, and P. J. Huang, "Electro spun ZnO Nano-wires as gas sensors for ethanol detection," *Nanoscale Res. Lett.* vol. 4(6), pp. 513-517, 2009.
- [26] Y. Yin, Y. Sun, M. Yu, X. Liu, T. Jiang, B. Yang, D. Liu, S. Liu and W. Cao, "ZnO Nano-rod array grown on Ag layer: A highly efficient fluorescence enhancement platform," *Scientific Reports* vol. 5, pp. 8152, 2015.

- [27] Z. Wang, J. R. Heflin, R. H. Stolen and S. Ramachandran, "Analysis of optical response of long period fibre gratings to nm-thick thin-film coatings," *Opt. Express* vol. 13(8), pp. 2808-2813, 2005.
- [28] I. D. Villar, I. R. Matias, F. J. Arregui and M. Achaerandio, "Nano-deposition of materials with complex refractive index in long -period fibre gratings," *J. Lightwave Technol.* vol. 23(12), pp. 4192-4199, 2005.
- [29] N. D. Rees, S. T. James, R. P. Tatam and G. J. Ashwell, "Optical fibre long-period gratings with Langmuir-Blodgett thin-film overlays," *Opt. Lett.* vol. 27(9), pp. 686-688, 2002.
- [30] Z. Yan, Z. Sun, K. Zhou, B. Luo, J. Li, H. Wang, Y. Wang, W. Zhao and L. Zhang, "Numerical and experimental analysis of sensitivity-enhanced RI sensor based on Ex-TFG in thin cladding fibre," *J. Lightwave Technol.* vol. 33(14), pp. 3023-3027, 2015.
- [31] H. Patrick, A. Kersey and F. Bucholtz, "Analysis of the response of long period fibre grating to external index of refraction," *J. Lightwave Technol.* vol. 16(9), pp. 1606-1612, 1998.
- [32] A. Mortezaali, O. Taheri and Z. S. Hosseini, "Thickness effect of nanostructured ZnO thin films prepared by spray method on structural, morphological and optical properties." *Microelectronic Engineering* vol. 151, pp. 19-23, 2016.
- [33] B. L. Zhu, X. H. Sun, S. S. Guo, X. Z. Zhao, J. WU, R. WU and J. Liu, "Effect of thickness on the structure and properties of ZnO thin Films prepared by pulsed laser deposition," *Japanese Journal of Applied Physics* vol. 45, pp. 7860-7865, 2006.
- [34] F. Chowdhury, "Influence of thickness variation on the optical properties of ZnO thin films prepared by thermal evaporation method," *Journal of Electron Devices* vol. 10, pp. 448-455, 2011.
- [35] F. Sun, W. Cai, Y. Li, B. Cao, Y. Lei, and L. Zhang, "Morphology-controlled growth of large-area two-dimensional ordered pore arrays," *Adv. Funct. Mater.* vol. 14, pp. 283-288, 2004.
- [36] S. W. James, I. Ishaq, G. J. Ashwell and R. P. Tatam, "Fibre optic sensing using Langmuir-Blodgett thin film overlays," *Proc. SPIE 5502*, pp. 308-312, 2004.
- [37] L. Coelho D. Viegas, J. L. Santos and J. De Almeida, "Enhanced refractive index sensing characteristics of optical fibre long period grating coated with titanium dioxide thin films," *Sens. Actuators B: Chem.* vol. 202, pp. 929-934, 2014.
- [38] I. D. Villar, I. R. Matias, F. J. Arregui, and P. Lalanne, "Optimization of sensitivity in long period fibre gratings," *Opt. Express* vol. 13(1), pp. 56-69, 2005.
- [39] R. Alonso, J. Subias, J. Pelayo, F. Villuendas and J. Tornos, "Single-mode, optical-fibre sensors and tunable wavelength filters based on the resonant excitation of metal-clad modes," *Appl. Opt.* vol. 33, pp. 5197-5201, 1994.
- [40] R. C. Jorgenson and S. S. Yee, "A fibre-optic chemical sensor based on surface plasmon resonance," *Sens. Actuators B* vol. 12, pp. 213-220, 1993.

- [41] Y. J. He, Y. L. Lo and J. F. Huang, "Optical-fibre surface-plasmon-resonance sensor employing long-period fibre gratings in multiplexing," *Opt. Soc. Am. B* vol. 23, pp. 801-811, 2006.
- [42] G. Nemova and R. Kashyap, "Fibre-Bragg-grating-assisted surface plasmon-polariton sensor," *Opt. Lett.* vol. 31, pp. 2118-2120, 2006.
- [43] J. Homola, "Surface plasmon resonance sensors for detection of chemical and biological species," *Chem. Rev.* vol. 108, pp. 462-493, 2008.
- [44] H. Raether, "Surface Plasmon," *Springer-Verlag*, 1988.
- [45] Y. Y. Shevchenko and J. Albert, "Plasmon resonances in gold-coated tilted fibre Bragg gratings," *Opt. Lett.* vol. 32(3), pp. 211-213, 2007.
- [46] G. Laffont and P. Ferdinand, "Tilted short-period fibre-Bragg-grating-induced coupling to cladding modes for accurate refractometry", *Meas. Sci. Technol.* vol. 12, pp. 765-770, 2001.
- [47] J. Albert, L. Y. Shao and C. Caucheteur, "Tilted fibre Bragg sensors," *Laser Photonics Rev.*, pp. 1-26, 2012.
- [48] Y. Y. Shevchenko, C. Chen, M. A. Dakka and J. Albert, "Polarisation-selective grating excitation of plasmons in cylindrical optical fibres," *Opt. Lett.* vol. 35(5), pp. 637-639, 2010.

Chapter 5

In-fibre grating based biosensors for pathogen detection [1, 2]

5.1 Introduction

In this chapter, the earlier reported optical fibre gratings are utilised as in-fibre grating based biosensors. The surfaces of the optical fibre gratings were functionalized with different bioreceptors such as enzymes and antibodies/antigens (IL-6, Trx), for receptor-analyte interaction.

The significance of such label free biosensors lies in their ever increasing demand in the food industry where biosensors are used to identify and detect microbial contamination with a view to preventing spread of infectious diseases. Also, in medical diagnostic field, in-fibre grating based biosensors are gradually finding their way into the clinical diagnostic market by offering real time monitoring and specific detection of human health such as detection of amount of sugar in the blood. Finally, their vast usage lies in environmental applications such as monitoring of harmful bacteria in drinking water and industrial effluents.

5.2 Enzyme-functionalized biosensor based on single mode 80 μ m-cladding dual-peak LPFG for glucose detection [1, 2]

5.2.1 Introduction

Glucose being the pivotal nutriment for human brain, muscles and other body parts, essentially requires monitoring for any level-imbalance to prevent malfunction and ensure healthy brain performance. Recent research findings have reported optical fibre based biosensors with targeted applications in food safety [3], medical diagnosis [4, 5] and environmental monitoring [6-8]. Long period fibre grating (LPFG) having the fundamental core mode coupled to the forward propagating cladding modes enables interaction between the propagating light and the ambient medium through the radiation (or/and cladding) modes. This attribute allows LPFG to be utilised as biosensor for direct probing of surrounding medium.

LPFG sensors have been reported to produce high sensitivity resonant wavelength shift with the variation in refractive index of ambient medium thereby offering label-free detection. Prominent citations on applications of LPFG based biosensors include: antibody-antigen detection [9], chemical sensing [10], pH sensing [11], glucose detection [12], DNA [13], bacterial detection and other medical diagnostic applications [14, 15].

Functionalizing the LPFG surface with molecular recognition elements such as enzymes, nucleic acids (DNA), antibodies and antigens involves several bio-receptor immobilization methods which include covalent bonding [16, 17], ionic bonding [18, 19], absorption [20], avidin-biotin interaction and cross-linking through multifunctional reagent [21, 22]. While covalent bonding has been considered mostly effective of all the methods because it allows the active sites to remain chemically reactive and unobstructed, enzymes have also been considered usefully utilised as molecular recognition elements.

Dispersion turning point associated with dual-peak LPFG determines the condition of maximum sensitivity of cladding modes and occurs at longer wavelengths for lower order cladding modes with a shift to the shorter wavelength as the mode order increases [23]. The high sensitivity exhibited by the dual-peak LPFG structure especially made in thin cladding (80 μ m diameter) fibre has prompted us to functionalize the dual-peak LPFG with enzyme for immuno-sensing of glucose. This serves as alternative detection device to the prevalent electrochemical methods of glucose analysis. Here, we present an enzyme-functionalized, aqueous dispersed and actively targeted dual-peak LPFG with dispersion turning point in near-infrared (NIR) region as highly specific probe for sugar level and glucose detection.

In previous reports, unmodified LPFG have been used for non-selective analysis of very high concentrated glucose solutions (≥ 300 mg/ml) [24, 25] but it offered insignificant changes in the refractive index and consequently no resonant wavelength shift. However, covalent immobilization methodology (conversion of glucose to gluconic acid) has been investigated for selective analysis of low concentrated glucose solutions (0.1 – 3.0 mg/ml) [12] and significant changes in the refractive index were obtained. This selective method was used in our research to show the correlation of the resonant wavelength shift of a dual-peak LPFG in a thin cladding fibre to a range of D-(+)-Glucose concentrations.

5.2.2 LPFG inscription and spectral characteristics

The prevalent point-by-point inscription method was used to fabricate dual-peak LPFGs of 300 μ m period on single mode thin-cladding boron-germanium doped fibre (80 μ m B/Ge CA3596/877F/C - Nortel). Ultra-violet (UV) light source from a frequency doubled argon (Ar⁺) laser at 244nm (Sabre Fred, Coherent) was used for the LPFG inscription. The grating fabrication parameters include a period of 300 μ m, grating length of 12mm, scanning speed of 0.2mm/s, and laser power of 145mW. UV radiation propagating through the fibre core causes index modulation according to the phase matching condition (Eqn. 5.1) [26].

$$\text{Equation 5.1} \quad \beta_{01} - \beta_{cladding}^m = \frac{2\pi}{\Lambda}, m = 2, 3, 4, 5, \dots$$

Where β_{01} and $\beta_{cladding}^m$ are the propagation constants of the fundamental core mode and the m^{th} order co-propagating cladding mode respectively, and Λ is the grating period. As a result of the parabolic characteristic of group index of higher order cladding modes, a dispersion turning point was observed on the LPFG phase curve as $|d\lambda_{res} / d\Lambda| \rightarrow \infty$. For a given radius, the phase matching condition is met concurrently with one cladding mode in the positive dispersion region and the other in the negative dispersion region, thereby generating dual-peak resonances [23]. We have theoretically simulated the cladding mode curves of the 80 μ m diameter cladding fibre with 4.8 μ m core size for LPFGs with different periods and the results are plotted in Figure 3.17(a). Due to the reduction in the fibre cladding diameter (80 μ m), the dispersion turning point has shifted to lower order cladding mode curve region as compared with the normal 125 μ m cladding fibre. As our calculation result have shown, the turning point for an LPFG with 300 μ m period in 80 μ m thin cladding fibre is associated with the cladding mode HE_{1,4}.

According to the mode curves shown in Figure 3.17(a), we see the paired attenuation bands of the dual-peak LPFG with a 300µm period in a 80µm cladding fibre would appear at the HE_{1,6} with wavelengths of 1520nm and 1740nm. The real-time transmission spectrum evolution of the dual-peak LPFG with 300µm grating period monitored on an optical spectrum analyzer (AQ6375B-YOKOGAWA) as shown in Figure 5.1 exhibits dual-peak feature with the first of the dual attenuation-peaks appearing at ~1567.53nm termed 'Peak 1' while the other peak at the longer wavelength, ~1787.16nm, is termed 'Peak 2'. Both resonance wavelengths are broadly in agreement with the simulated wavelengths of the dual peaks.

These dual attenuation peaks are generated from the light coupling from the core mode to high sensitivity HE_{1,6} (dual-peak) cladding modes, thereby interacting with the surrounding medium more responsively via evanescent fields. External perturbation effect on the evanescent fields induces changes in the effective index of the cladding mode, thus causing optically measurable wavelength shifts of the LPFG dual-peaks according to (Eqn. 5.2) [27].

Equation 5.2
$$\lambda_{m,res} = \left[n_{eff,core}^{01}(\lambda_m, n_1, n_2) - n_{eff,clad}^{0m}(\lambda_m, n_1, n_3) \right] \Lambda$$

Where $\lambda_{m,res}$ is the resonant wavelength due to coupling between fundamental core mode and the m^{th} cladding mode, $n_{eff,core}^{01}$ and $n_{eff,clad}^{0m}$ are the effective indices of the fundamental core mode and the cladding mode respectively, while the refractive indices of the core, cladding and ambient medium are denoted by n_1, n_2, n_3 respectively. It is clear from this mechanism that LPFGs are capable of detecting changes when a target bio-analyte interacts with a recognition element on their surfaces [28, 29].

In the evaluation, the response of the dual-peak LPFG to external perturbations was carried out by exposure to wide range of surrounding refractive-index gels (1.305 – 1.444 RIU), sugar solutions of different concentrations (0% - 60%) and finally, different glucose concentrations (0.0–3.2 mg/ml) after the surface has been enzyme functionalized.

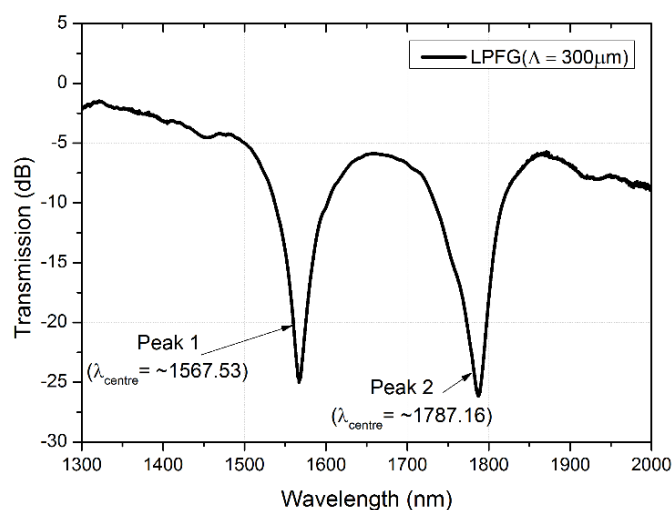


Figure 5.1: Enzyme functionalization of LPFG surface

5.2.3 Enzyme functionalization of LPFG surface

The entire sample solutions were prepared by analytical grade reagents and de-ionized water. All reagents used were purchased from Sigma Aldrich: Sodium Acetate buffer (form: liquid; S7899); D-(+)-Glucose (form: powder; G7021); (3-Aminopropyl) tri-ethoxysilane (APTES) (form: liquid; A3648) and Glucose Oxidase (form: Aspergillus Niger) (form: buffered aqueous solution; G0543). The LPFG enzyme functionalization started with the cleaning process (Figure 5.2(a)). Here, the fibre was absolutely immersed in HNO_3 solution (5% v/v; ~2h; 40°C) with a view to removing all contaminations, then washed thoroughly with de-ionized water and ethanol intermittently. Thereafter, the contamination-free fibre was immersed in H_2SO_4 solution (95% v/v in H_2O_2 ; ~1h; room temp.) to activate the hydroxyl-groups (-OH) on the fibre surface. The fibre was left to dry under an incandescent lamp (40W; 240V; ~24h; ~40°C). Afterwards, it was submerged in (3-Aminopropyl) tri-ethoxysilane (APTES/ethanoic solution, 10% v/v) which incubates the -OH activated fibre in the silanization process for 30 minutes at room temperature in order to covalently link the NH_3^+ groups of the APTES molecules to the -OH group on the fibre surface (Figure 5.2(b)). Note, the NH_3^+ group of the APTES molecules has been reportedly used to absorb bio-molecules with negative charges like glucose oxidase and Escherichia coli bacteria [12, 14]. Then, it was rinsed with de-ionized water and ethanol to remove non-covalently absorbed silane compounds.



Figure 5.2: Enzyme functionalization of LPFG surface: (a) Cleaning process (b) Silanization process and (c) Glucose-oxidase immobilization.

Finally, glucose oxidase was immobilized on the -NH_2 functionalized dual-peak LPFG surface (Figure 5.2 (c)) by immersion in 5 mg/ml buffered solution (Sodium Acetate) of glucose oxidase for ~2hours. During the incubation, glucose oxidase -COOH groups bonded with the NH_3^+ groups of the APTES molecules through covalent interaction. The enzyme functionalized surface was later rinsed with Sodium Acetate (SA) buffer and left to dry in air. Each stage of the enzyme functionalization processes was examined under optical microscope (Zeiss Axioskop 2 mot plus upright Microscope) and the micrograph images taken are as shown in Figure 5.3.



Figure 5.3: Optical microscopic images of: (a) cleaned fibre, (b) silanized fibre, (c) enzyme-functionalized fibre observed under transmitted light, and (d) enzyme's (fluorescent) presence on fibre surface.

The optical microscope transmission path (100W halogen – HAL 100) was used to observe the cleaned fibre, APTES treated fibre and glucose oxidase immobilized fibre (Figure 5.3(a-c)). Optical recognition of the presence of glucose oxidase was as a result of its fluorescence property when observed under optical fluorescent microscopy (100×; ex. 479 nm; light source: 200W metal halide arc lamp; 110-250VAC; 2A; 50-60 Hz; 5-30°C – Lumen 200PRO) (Figure 5.3 (d)).

For better controlled measurement, the APTES treated fibre was first observed under the fluorescent microscopy but no fluorescence property was detected; therefore, the fluorescence property is only attributed to the presence of glucose oxidase molecules. From the optical microscopic images obtained in Figure 5.3, with each micrograph depicting each functionalization stage, it is evident that the surface of the fibre has been uniformly functionalized with the protocol used for the silanization and enzyme immobilization.

5.2.4 Experimental setup for RI, sugar solution and glucose detection

The experimental setup for the RI, sugar solution and glucose detection is as shown in Figure 3.39 where the dual-peak LPFG fibre was mounted at each end on two 3D translation stages with the grating region centralized above a test solution platform which was fixed to a micrometre stage that is capable of vertical movement in either direction. Clean glass slides were placed intermittently on the platform as each solution of different RI was applied. One end of the fibre was connected to a supercontinuum light source (950nm – mid-IR; Fianium) and the other end to the input port of the OSA. When light was transmitted through the fibre while still in air, spectral measurement was obtained on the OSA and recorded as reference. Subsequent submergence of the fibre in different solutions caused wavelength shift with respect to the reference as observed on the OSA and all transmission spectra were recorded.

5.2.5 Results and discussion

5.2.5.1 RI and sugar level detection measurements

According to Eqn. 5.2, the LPFG resonant wavelength depends on the effective index of the cladding mode which in turn is dependent on the RI of surrounding medium. Therefore, as the surrounding medium RI increases there is a corresponding shift in the resonant wavelength. Before the glucose detection which requires surface-functionalization of the fibre, the dual-peak LPFG was evaluated for RI and sugar solution measurement at constant room temperature of $\sim 21^{\circ}\text{C}$.

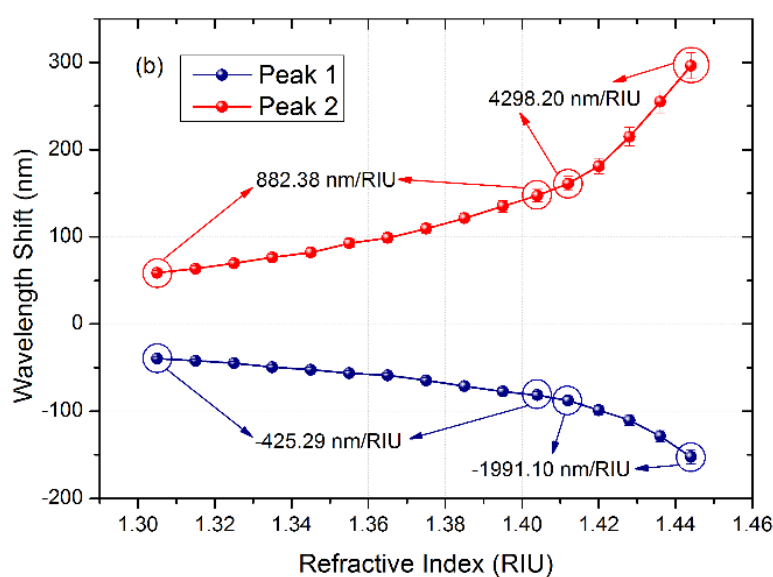


Figure 5.4: Plots of resonant wavelength shift against surrounding medium RI variation of the $300\mu\text{m}$ period dual-peak LPFG in thin cladding fibre.

To evaluate the RI sensitivity of the dual-peak LPFG, a series of index gels, 1.305 - 1.444 (Cargile), were employed to probe the response of the dual-peak LPFG to surrounding medium refractive index (SRI) variation. High SRI sensitivities were obtained, as shown in Figure 5.4, Peak 1 and Peak 2 recorded sensitivities of -425.29 nm/RIU and 882.38 nm/RIU in the RI range of 1.305 – 1.404 and -1991.10 nm/RIU and 4298.20 nm/RIU in the RI range of 1.412 – 1.444. It is interesting to note that both peaks show higher RI sensitivity in the second RI range, but the RI sensitivity of Peak 2 is almost twice that of Peak 1. This is a maximum recorded total peak separation of ~460 nm which is 23% improvement to ~374 nm earlier reported for light cladding-etched dual-peak LPFG [30]. Although, a much higher sensitivity of ~8734 nm/RIU [31] and giant sensitivity of ~9100 nm/RIU [32] have been achieved by cladding-etched dual-peak LPFGs from original 80 μ m to only 35 μ m, undoubtedly reducing the mechanical strength of the grating and increasing its fragility, thus limiting its applicability.

Raw sugar (turbinado sugar) has been known to contain several useful nutrients (100g of turbinado sugar contains – 100mg potassium, 85mg calcium, 23mg magnesium, 3.9mg phosphorous and 1.3mg iron) and less calories therefore healthier than white sugar [33]. Solutions of different concentrations (0% - 60%) were made with the turbinado sugar and de-ionized water for sugar-level sensing using the same dual-peak LPFG at room temperature. Figure 5.5(a) shows the real time shifting of the dual peak LPFG in opposite directions with Peak 1 shifting towards shorter wavelengths (blue-shifting) while Peak 2 drifts towards longer wavelengths (red-shifting) as the concentration of the sugar solution increases. Both peaks recorded relatively high sensitivities to sugar-level detection with Peak1 showing a negative correlation coefficient of -0.8550 nm/% and -2.4642 nm/% for the sugar concentration levels of 0% – 30% and 30 – 60% respectively, while Peak 2 shows stronger positive correlation coefficients of 1.4592 nm/% and 4.6696 nm/% for the same two ranges (Figure 5.5(b)). From Figure 5, it can be observed that Peak 1 blue-shifts by ~100 nm while Peak 2 red-shifts by ~200 nm for the entire sugar concentration (0% - 60%) which are significantly higher than ~19.8 nm peak red-shift reported for concentration of hemoglobin in sugar solution [30] as the sensitivity of our thin-cladding dual-peak LPFG has achieved over one order of magnitude improvement.

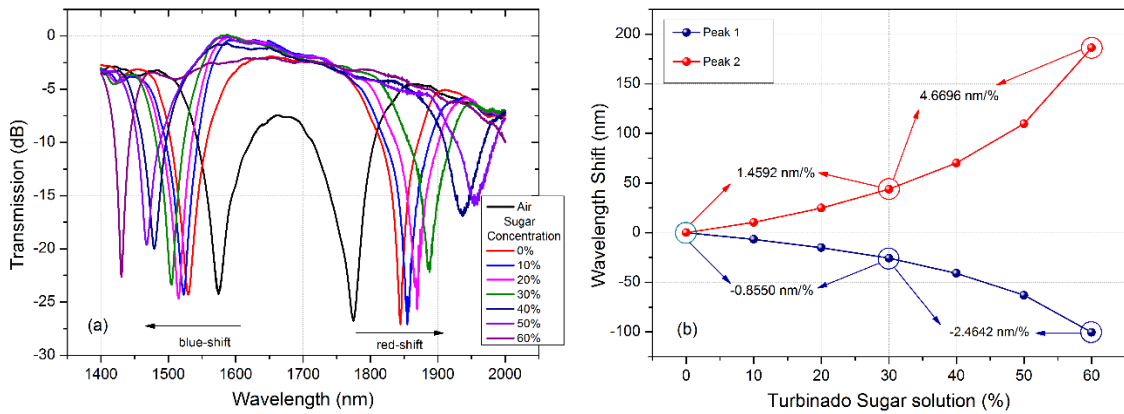
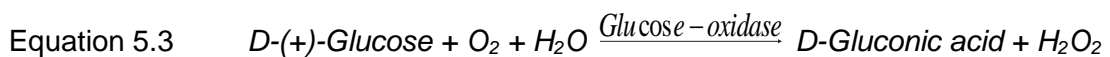


Figure 5.5: (a) Transmission spectral evolution of 80µm-cladding dual-peak LPFG to varying concentration of turbinado sugar solution; (b) Plot of resonant wavelength shift of Peak 1 and Peak 2 against sugar solution.

Since sucrose is sugar found naturally in fruits, vegetables and sugar cane, monitoring of sugar level in industrial aqueous solutions can utilize this sensor for broader applications. The inclusion of the RI sensing and raw sugar solution detection experiments are specifically used to show the versatility of this sensor as not only being restricted to bio-sensing but also could find applications in food processing and environmental monitoring.

5.2.5.2 Glucose detection with enzyme-functionalized dual-peak LPFG

The enzyme functionalization of the dual-peak LPFG made it a biosensor for bio-molecule detection. The specific enzyme (glucose oxidase) immobilized on the surface of the LPFG enables interaction with surrounding glucose solution. Different concentrations of D-(+)-Glucose was prepared in Sodium Acetate (SA) buffer (pH 5.2), which is a suitable reagent for this catalytic reaction. Eqn. 5.3 expresses the interaction of the glucose solution with glucose oxidase showing the conversion of D-(+)-Glucose to gluconic acid with concurrent release of hydrogen peroxide (1 unit of glucose oxidase (200units/mg) oxidizes 1.0µm of D-(+)-Glucose to D-gluconic acid and H₂O₂ per minute at pH ~5.1, 35°C).



This interaction causes changes in refractive index of the ambient medium and thus induces resonant wavelength shift in the transmission spectrum as observed on the OSA. After applying each glucose solution, de-ionized water was used to rinse the solution off the fibre surface to restore resonant peak back to the reference point in readiness for next measurement of subsequent solutions.

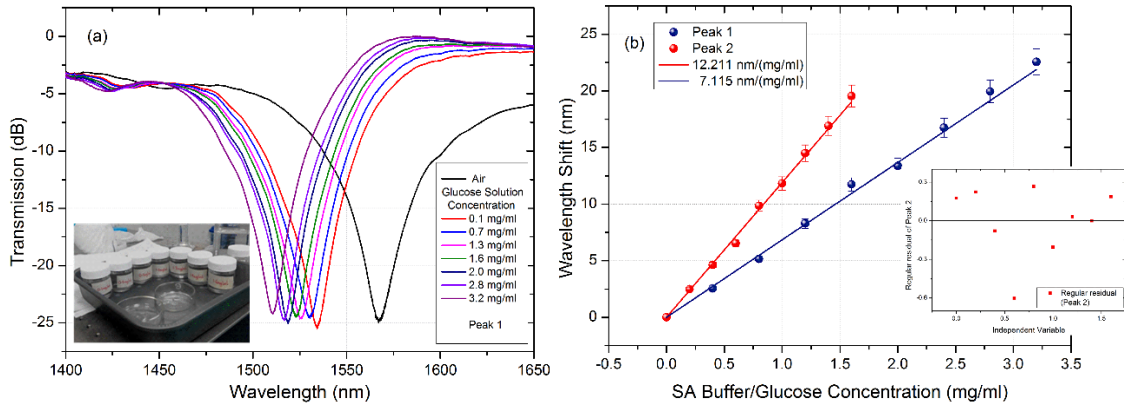


Figure 5.6: (a) Transmission spectral evolution of Peak 1 (of the dual-peak LPFG) to varying concentration of SA Buffer/D-(+)-Glucose solution at different concentration (inset: glucose solution (0.1 – 3.2 mg/ml)) and (b) Plots of resonant wavelength shift of the dual-peak LPFG against glucose concentration (inset: regular residual of Peak 2).

An average interaction time of ~60s was observed for each test solution (glucose solution). It was also observed that after enzyme functionalization of the LPFG surface the dual-peak shifted around ~15 nm from initial position in air. Peak 1 was observed at around ~1565 nm and Peak 2 around ~1802 nm as against initial positions. Figure 5.6(a) shows the transmission spectral evolution of Peak 1 of the dual-peak LPFG in glucose solutions of different concentrations, showing the resonant peak drifting away from initial reference position towards the shorter wavelength.

The test solutions (SA buffer/glucose) covers the glucose concentration range 0.1–3.2 mg/ml (Figure 5.6(a): inset). The obtained transmission spectra (Peak 1) shows approximately ~30nm blue-shift with respect to the varying glucose solutions. However, as Peak 2 red-shifts, the concentration range was limited to lower values of between 0.1–1.6 mg/ml to be measured as the longest wavelength the light source can emit is at around 2 μ m. As shown in Figure 5.6(b), for the glucose concentration range 0.1 – 3.2 mg/ml, Peak1 has exhibited a linear response with a sensitivity of 7.115 ± 0.119 nm/(mg/ml), while for the lower glucose concentration range 0.1 - 1.6 mg/ml, Peak 2 recorded a higher sensitivity of 12.211 ± 0.189 nm/(mg/ml). From the results, we observe that the enzyme functionalized dual-peak LPFG gives a linear response in the glucose concentration range (0.1–3.2 mg/ml). In comparison with previous reports, the sensitivity ~7.115nm/(mg/ml) for Peak 1 is approximately one order of magnitude higher than ~0.806nm/(mg/ml) reported for normal LPFG [12] and ~0.298 nm/(mg/ml) reported for 81 $^\circ$ -TFG [34] in similar glucose concentration range (0.1 – 3.2 mg/ml). The higher sensitivity of this sensor in comparison with earlier reports in [12, 34] coupled with high mechanical strength as against [35] makes this dual-peak LPFG sensor a viable and reusable alternative for supporting the instantaneous detection of the glucose

concentration. Note, to ensure reproducibility of result, the experiment was repeated three times with the glucose oxidase replenished for each repeated experiment, and the whole procedure shown in Fig. 2 was reiterated. The repeatability standard deviation of the experimental data was calculated to be 0.02.

5.2.6 Conclusion

In summary, enzyme functionalized dual-peak LPFG inscribed in B/Ge co-doped 80 μ m-cladding single mode fibre has been demonstrated and investigated for sugar level and glucose concentration detection. Before the enzyme functionalization, the dual-peak LPFG has been investigated for RI sensing and a sensitivity of 4298.20 nm/RIU has been achieved, which is a significant 23% improvement in total-peak separation as against earlier report on light cladding-etched dual-peak LPFG. Also, sugar solution has been investigated for level-concentration range 0% - 60%, significant peak-wavelength shift of ~200nm has been achieved for the entire concentration range which is remarkably higher than ~19.8 nm peak-wavelength shift earlier reported for concentration of hemoglobin in sugar solution. After the enzyme functionalization of the fibre surface, the dual-peak LPFG has been investigated for glucose concentration detection. The glucose detection has shown markedly high sensitivities of 12.211 ± 0.189 nm/ (mg/ml) (0.1 - 1.6 mg/ml) for Peak 2 and 7.115 ± 0.119 nm / (mg/ ml) (0.1–3.2 mg/ml) for Peak 1 which is one order of magnitude higher than earlier glucose detection results reported for normal LPFG and 81^o-TFG. This dual-peak LPFG sensor, as useful alternative, may find applications in food safety, medical diagnosis and environmental monitoring.

5.3 Label-free biosensor based on Trx-antibody immobilized 81^o-TFG in 80 μ m-cladding B/Ge co-doped optical fibre for high-specific thioredoxin (Trx) detection

5.3.1 Introduction

Thioredoxin (Trx) is a small ubiquitous redox-active multifunction protein which acts as potent antioxidant, promotes cell growth, control cellular redox balance, control modulation of inflammation and inhibit apoptosis. The thioredoxin system comprises thioredoxin (Trx), thioredoxin reductase (TrxR) and Nicotinamide adenine dinucleotide phosphate (NADPH) as expressed in Equations 5.4 – 5.6 below. TrxR and NADPH reduce the active site disulphide of oxidized Trx (Trx-S₂) to a dithiol (Trx-(SH)₂) which is the cells major protein disulphide reductase [36-38].



Trx was originally identified in *Escherichia coli* for its ability to act as an electron donor for ribonucleotide reductase which was the first unique investigation in DNA synthesis [36]. Since then, the role of Trx in a wide range of human diseases and conditions have been subjected to intense investigation. In cancer, overexpression of Trx is considered deleterious because it introduces resistance to anti-cancer drugs or radiation-induced apoptosis thereby impairing the effectiveness of chemotherapy strategies [36]. Similarly, the growth promoting effects of Trx are detrimental in rheumatoid arthritis [40, 41] but turn out to be beneficial in neural-degenerative disease where recovery is enhanced by promotion of neural-cell growth [42]. However, Trx protects against injurious insults in ischaemia-reperfusion injury where apoptosis immensely contributes to the pathology [43]. Likewise in HIV infection, Trx has been identified to block HIV replication [41] but rather unfortunately, at the later stage of the disease in some patients, it contributes to immunosuppression [44]. The dichotomous role of Trx in disease pathophysiology necessitates clear understanding of which properties of Trx predominate in a particular situation which is a fundamental integral of successful therapeutic manipulation of Trx.

Early detection of overexpression of Trx in several primary tumours is desired because the growth-promoting effects of Trx on cancerous cells outweigh its beneficial antioxidant properties. When Trx is secreted, it exerts a range of effects on adjacent cells from growth arrest to autocrine activation [45]. In early 90s, measurement of changes in

extracellular concentrations of Trx in several diseases and conditions that are generally associated with oxidative stress and inflammation are enabled by the commercial development of ELISA kits [46-48]. Other methods include: direct NMR titration [49]; reduction of insulin [50]; and Trp28 fluorescence [51]. However, all these methods remain time-consuming and expensive.

The quest for specific, non-invasive, time-saving and cost effective alternative measurement remains the motivation that prompted this novel idea of employing a label-free biosensor based on excessively tilted fibre grating (81°-TFG) inscribed in 80µm-cladding B/Ge co-doped optical fibre which is the main significance of this work.

5.3.2 Materials and methods

5.3.2.1 Ex-TFG inscription and antibody immobilization

Excessively tilted fringes were UV-inscribed in 80µm-cladding B/Ge co-doped optical fibre with internal tilt angle of 81° using an amplitude mask of 25µm period. The fabrication and spectra characteristics of the 81°-TFG have been extensively discussed in session 3.5.1. Therefore, this session will only focus on the surface functionalization of the 81°-TFG with Trx antibody. Most of the analytical grade reagents used were purchased from Sigma Aldrich which include: Glutaraldehyde solution (G7776); Phosphate buffered saline (form: dry powder; P2194) and (3-Aminopropyl) triethoxysilane (APTES) (form: liquid; A3648). Thioredoxin (Trx) antibody (form: liquid; ab1754) was purchased from Abcam Cambridge, UK. The entire sample solutions were prepared using deionized water except where stated otherwise.

The chemical treatment of the 81°-TFG surface started by cleaning which was achieved by total immersion of the fibre in 200ml of 5% nitric acid (HNO₃) for 2 hrs at 90°C. This was done with a view to removing all contaminations from the fibre. Then, the fibre was thoroughly rinsed by repeatedly washing with sterile deionized (DI) water. Thereafter, the contamination-free fibre was silanized by immersion in 200ml of freshly prepared 10% (v/v) APTES in DI water (pH 3-4) for 1 hr at 75°C. The APTES mainly derivatize the fibre surface with primary amines (-NH₂) which activated the probe surface in preparation for antibody immobilization. It was then left to dry in the oven for 8 hrs at 80°C. After cooling, treatment with 1% (v/v) glutaraldehyde in DI water (pH 6-7) followed for 30 minutes at room temperature. Thereafter, the fibre was thoroughly rinsed with 0.01M Phosphate buffered saline (PBS: 0.137 M NaCl, pH 7.4) to remove any unbound molecules in preparation for antibody immobilization. Finally, the fibre was incubated overnight in 2ml of 1µg/ml thioredoxin (Trx) antibody in 10mM Phosphate buffered saline (PBS) with 0.1% FBS at 4°C to complete the surface functionalization of the 81°-TFG biosensor. The

experimental setup for this experiment is the same as that in Figure 3.39. When light is transmitted through the fibre after Trx immobilization, a shift in wavelength of $\sim 37\text{nm}$ with respect to the bare fibre was recorded on the OSA signifying the presence of the antibody on the surface of the fibre. As shown in Figure 5.7, the transmission spectrum of the 81° -TFG shifts in centre wavelength from $\sim 1590.47\text{nm}$ (bare fibre) to 1627.69nm (Trx-immobilized fibre) confirming surface functionalization.

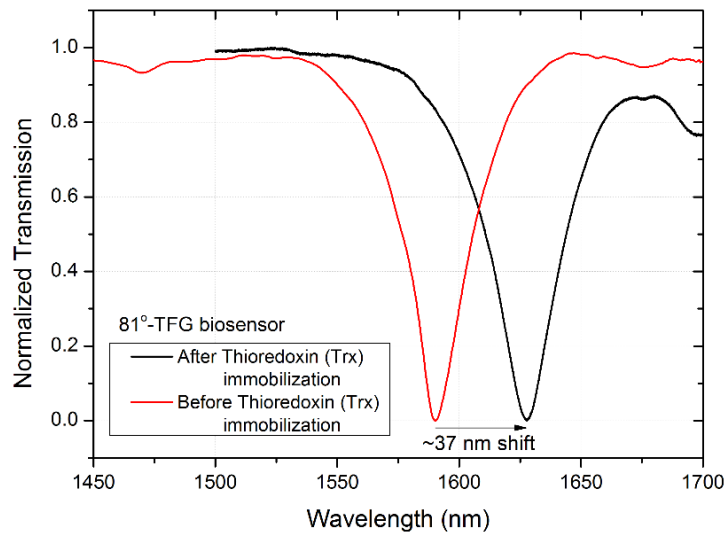


Figure 5.7: Spectra wavelength shift after immobilization of Thioredoxin (Trx) antibody on fibre surface

5.3.2.2 Trx antigen-antibody interaction on fibre surface

A schematic of the Trx-immobilized 81° -TFG biosensor is as shown in Figure 5.8 where the Trx-antibody is covalently bound to the fibre surface. The figure shows the antigen-antibody interaction through the antigen binding site as the biosensor is submerged in different concentrations of Trx antigen. In order to generate the standard curve, Trx-1 recombinant protein (R and D systems) was serially diluted (1.5ng/ml – 25ng/ml) in PBS with 0.1% FBS (fetal bovine serum) and incubated overnight at 4°C alongside the 81° -TFG biosensor submerged in the Trx-antibody.

At the beginning of the experiment, the Trx-immobilized 81° -TFG biosensor was mounted on the micrometre stage with the functionalized grating area centred on the test platform. Light from a supercontinuum laser source (Fianium) was transmitted through the fibre and as the excessively tilted fringes couple the core mode to the higher order cladding modes, evanescent waves are radiated to the surrounding medium thereby monitoring the signal generated by the sample concentration interaction. The Trx-antigen solutions, which have been serially diluted in the range 1.5ng/ml – 25ng/ml , were applied

as test/sample solutions. The applied sample solutions were at constant volume of 100 μ l so as to totally submerge the grating region of the Trx-immobilized 81 $^{\circ}$ -TFG biosensor for each interaction round of the experiment. The surface of the fibre was rinsed with PBS to restore the spectrum back to reference after each round of sample solution. The antibody-antigen interaction time was rapid and estimated to be approximately ~30sec as the transmission spectrum was almost immediately seen to red-shift when the sample solutions were administered. The signals generated from the antigen-antibody interaction were recorded as the signal/transmission spectra profile on the OSA.

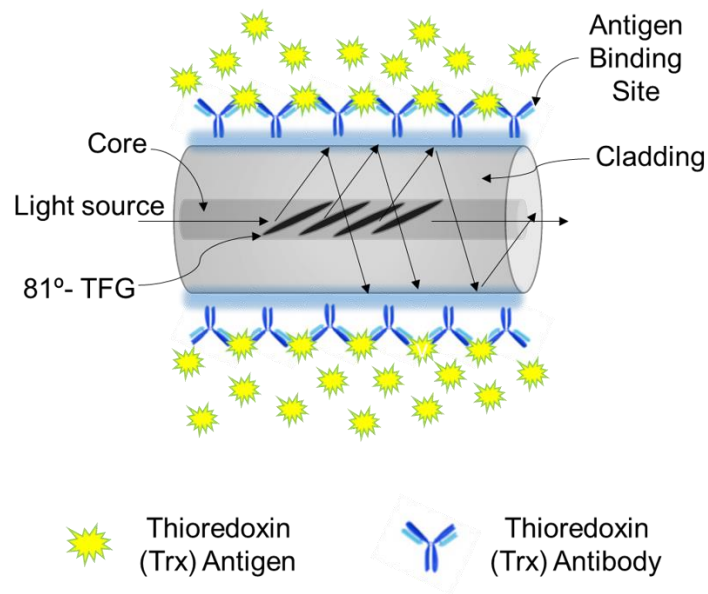


Figure 5.8: Schematic of Thio redoxin (Trx) antigen-antibody reaction on fibre surface

5.3.3 Results and discussion

To analyse the definite binding capability of Trx-antigen on the Trx-antibody immobilized 81 $^{\circ}$ -TFG biosensor, several concentrations of thio redoxin solutions were prepared. Before applying the test solutions, the fibre was immersed in PBS solution and the recorded wavelength shift was used as reference (Figure 5.9). At first, serial dilutions from low to high concentrations of range (1.50 – 25 ng/ml) were used as sample concentrations. As earlier iterated, the immersion time for administering each concentration was observed as 30 sec followed by PBS rinsing to remove any unbound thio redoxin. An immediate response from the 81 $^{\circ}$ -TFG biosensor shows clearly a red-shift of the central wavelength as each sample concentration was applied. Figure 5.9 shows the transmission spectra evolution of the 81 $^{\circ}$ -TFG biosensor in response to the sample concentrations.

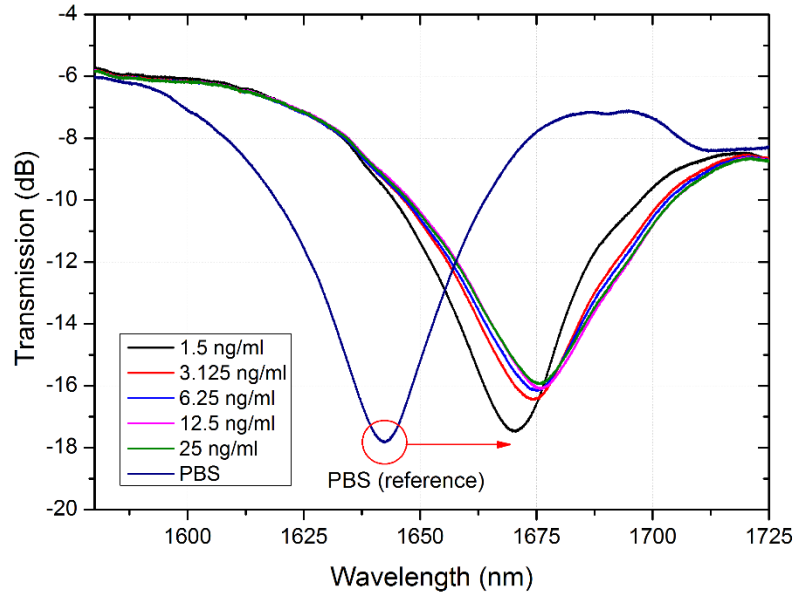


Figure 5.9: Transmission spectra evolution of the 81°-TFG biosensor in response to Thioredoxin (Trx) antigen-antibody interaction; red-shift from reference as sample concentration increases.

The binding interaction of antibody-antigen is analysed using the Hill model. The Hill equation [52, 53] is used to describe our sensor's binding affinity response as follows:

Equation 5.7
$$\Delta\lambda_{res} = \Delta\lambda_{max} \times \frac{[S]^n}{K_m + [S]^n} ,$$

where the maximum resonant wavelength shift $\Delta\lambda_{max}$, is the saturation value; $[S]$ is the concentration of thioredoxin; dissociation constant K_m , is the substrate concentration at which the rate of reaction is half its maximum; and n is the Hill coefficient. The lower the value of K_m , the higher the sensitivity of the biosensor to lower substrate concentration and the greater its efficiency.

From the curve fitting in Figure 5.10, the saturation value $\Delta\lambda_{max}$ of the reaction is 33.19 ± 0.15 nm. This characterises the maximum velocity of the reaction which is the highest reaction rate achieved at saturating substrate concentrations. Also the apparent affinity for the protein under study is high as the value of dissociation constant K_m is 0.65 ng/ml. this shows that it takes a lower substrate concentration to reach 50% saturation which is a good sign that our biosensor will even be more sensitive to lower substrate concentration. Therefore, our results have shown a high reaction speed at lower substrate concentration which is quite novel. The experiment was repeated three times for repeatability assurance and a repeatability standard deviation of 0.05 was obtained. For each set of repeated experiment, the protocol of cleaning the fibre was repeated and

the surface of the fibre was re-functionalized with fresh Trx-antibody so as to prevent the antibody from forming crystals on the surface of the 81⁰-TFG biosensor.

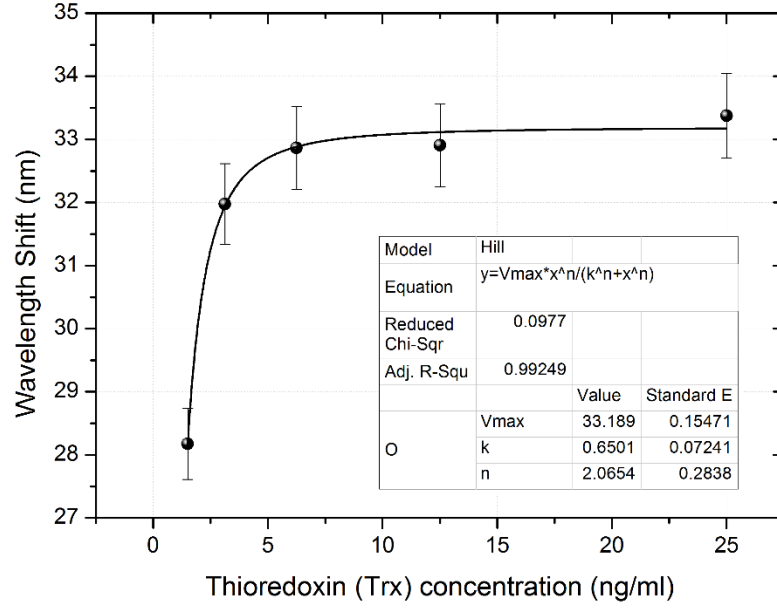


Figure 5.10: Plot of resonant wavelength shift against variation in Thioredoxin-antigen solution concentration (1.50 – 25 ng/ml).

The sensitivity and detection limit are two important factors of rating any biosensor. Therefore, in order to obtain the sensitivity of the sensor reference is made to the expression in [54] as follows:

Equation 5.8
$$S_R = \frac{\Delta\lambda_{max}}{\xi_{max}},$$

where the sensitivity response of our biosensor is S_R , $\Delta\lambda_{max}$ is the maximum resonant wavelength shift, and ξ_{max} is the surface density of the Trx-antibody when all Trx-antigen binding sites are occupied [55] and can be determined by the expression [54],

Equation 5.9
$$\xi_{max} = \frac{M_{[S]}}{N_A + L_{[S]}^2},$$

where $M_{[S]} = 12\text{kDa}$ (12000g/mol) is the molecular mass of thioredoxin [56], N_A is the Avogadro's number ($6.02 \times 10^{23} \text{ mol}^{-1}$), and $L_{[S]} = 105\text{\AA}$ (10.5 nm) [57] is the average length of one molecule of thioredoxin. Also, to estimate the thioredoxin detection limit, the K_m calculated with Hill model shows that the dissociation constant is strongly related to Trx antibody-antigen recognition and is used to obtain the detection limit as follow [55]:

Equation 5.10

$$D_{Limit} = K_m \times \frac{R_\lambda}{\Delta\lambda_{max} - R_\lambda} ,$$

where R_λ is the OSA resolution of 0.05 nm and K_m is dissociation constant. From Eqn. 5.10, it can be deduced that the smaller the dissociation constant the lower the detection limit. Therefore, with $\Delta\lambda_{max} = 33.19$ nm, the sensitivity response of the Trx-immobilized 81^o-TFG biosensor is calculated to be 183.57 nm/(ng/mm²) and the limit of detection is obtained as $\sim 9.81 \times 10^{-4}$ ng/ml (0.003 nM) which is far lower than 0.02nM reported in [58] and 19nM obtained in [59].

Furthermore, as a fallout from the first experiment, lower concentrations of Trx-antigen solutions serially diluted in the range 0.07ng/ml – 2.5ng/ml, were applied as the new sample solutions. The applied sample solutions still retained the constant volume of 100 μ l for total submergence of the Trx-immobilized 81^o-TFG biosensor. From the curve fitting in Figure 5.11 the max speed of reaction $\Delta\lambda_{max}$ has a lower value of 17.66 nm and a dissociation constant K_m of 1.39×10^{-4} ng/ml compared with previous experiment of higher substrate concentration. The sensitivity response of the lower concentration range is estimated to be 97.68 nm/(ng/mm²) and the limit of detection is 3.95×10^{-7} ng/ml.

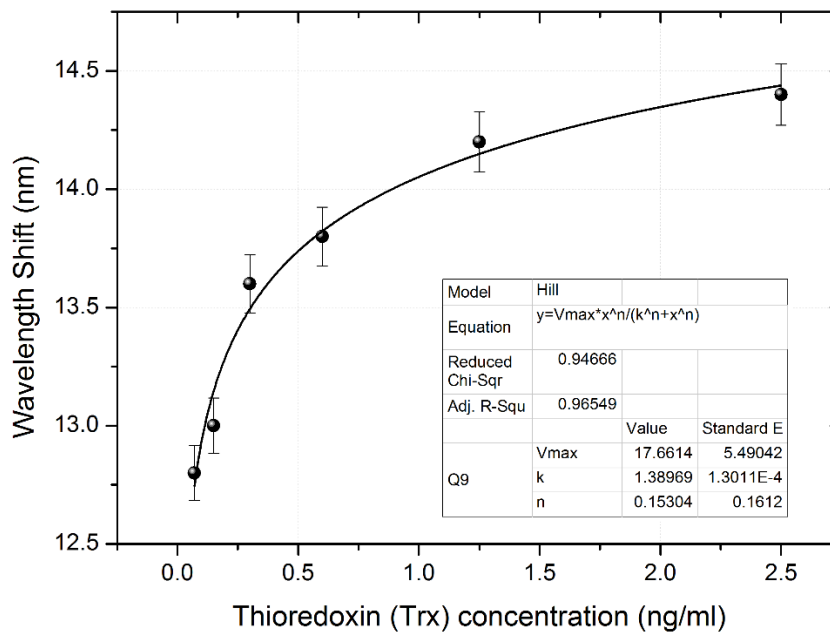


Figure 5.11: Plot of resonant wavelength shift against variation in Thioredoxin-antigen solution concentration (0.07 – 2.5 ng/ml)

From the lower substrate concentration experimental results, it can be seen that the rate of reaction decreases significantly as compared with that of higher concentrations and the apparent affinity of the binding protein is lower since a far higher value was obtained

for the dissociation constant (K_m). Also, from the curve fitting in Figure 5.11, it can be observed that the rate of reaction was rapid for the 0.07ng/ml, 0.15ng/ml and 0.3ng/ml substrate concentrations showing higher binding efficiency of 3.55nm/(ng/ml). As saturation gradually set in with 0.6ng/ml, 1.25ng/ml and 2.5ng/ml substrate concentrations, the binding efficiency reduced to 0.29 nm/(ng/ml).

However, this sensor has efficiently exhibited effective sensing for lower concentration range measurement which has been the shortfall of the ELISA test employed in [56, 57]. Also, the limit of detection is still remains lower than those reported in [58, 59]. For repeatability and reproducibility, the experiment was also repeated three times and a repeatability standard deviation of 0.06 was obtained.

To ascertain the specificity and selectivity of our Trx-immobilized 81^o-TFG biosensor, one pooled plasma sample (from human: P9523) purchased from Sigma Aldrich was used in this study. Since plasma is an embodiment of several proteins, the specificity and selectivity of our biosensor is experimentally validated by subjecting it to plasma solutions of different concentrations to specifically detect Trx amidst other interfering agents/proteins present in plasma.

For the specificity validation, the human plasma was serially diluted with PBS in the ratio 1:8, 1:4, 1:2, 1:1 so as to ascertain the detection limit. Note; the light source employed for plasma concentration measurement is different from the earlier one used for Trx-substrate concentrations. Although they are both supercontinuum laser sources, the latter has a lower output power than the former and the light is not filtered to separate the 'unused visible light range' from the required mid-infrared range, hence the cause of the inherent ripples in the transmission spectrum as obvious in Figure 5.12(a). These ratios correspond to plasma concentrations of 0.0625 mg/ml, 0.125 mg/ml, 0.25 mg/ml, 0.5 mg/ml and 1 mg/ml respectively. These new substrate concentration were applied to our biosensor and the respond recorded on the OSA. Figure 5.12(a) shows the spectra evolution of the 81^o-TFG biosensor in response to variation in plasma concentrations.

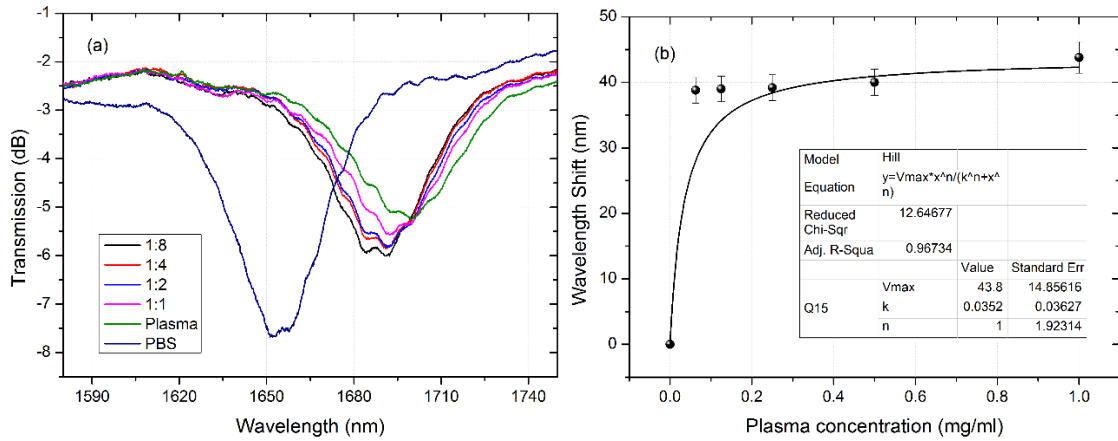


Figure 5.12: (a) Spectra evolution of the 81°-TFG biosensor in response to plasma concentrations, and (b) Plot of resonant wavelength shift of Trx-immobilized 81°-TFG biosensor against variation in human plasma solution of different concentrations: (0.0625 – 1.0 mg/ml).

From the curve fitting in Figure 5.12(b), it can be seen that the rate of reaction is very high with a value of $\Delta\lambda_{max} = 43.8\text{nm}$. This shows that the saturation occurs even at the lowest concentration measured. This may be because of background interference or non-specific binding of other proteins. This is a limitation as plasma is known to be a complex matrix with lots of factors that can cause non-specific signals.

5.3.4 Conclusion

A novel Label-free biosensor based on antibody (Trx) immobilized 81°-TFG in 80 μm -cladding B/Ge co-doped optical fibre has been demonstrated for high-specificity thioredoxin (Trx) detection. The 81°-TFG biosensor recorded a high saturation value $\Delta\lambda_{max}$ of $33.19 \pm 0.15\text{nm}$ and dissociation constant K_m of 0.65ng/ml for high concentrations range (1.50 – 25ng/ml) which shows high affinity binding. A detection limit and sensitivity response of 9.81×10^{-4} ng/ml and 183.57nm/(ng/mm²) were obtained respectively. Also, this biosensor has efficiently exhibited effective sensing for lower concentration range measurement which has been the major shortfall of the ELISA test. The investigated lower substrate concentration range is 0.07ng/ml – 2.5ng/ml, and values of 17.66nm and 1.39×10^{-4} ng/ml were obtained for $\Delta\lambda_{max}$ and K_m respectively. Lower sensitivity response of 97.68 nm/(ng/mm²) and a detection limit of 3.95×10^{-7} ng/ml were obtained in comparison with the higher concentration as expected. Finally, the specificity of the biosensor was attempted by using human plasma and results have shown that the saturation occurs even at the lowest concentration measured. This has been identified as the limitation of this sensor as the complexity of human plasma allows for background interference or non-specific binding of other proteins.

5.4 Fibre optic biosensor based on antibody-functionalized 81^o-TFG for label-free specific recognition of interleukin-6 (IL-6) protein

5.4.1 Introduction

Interleukin-6 (IL-6) is a pleiotropic cytokine which is soluble mediator in both physiological and pathophysiological processes. It is secreted in the course of immunologic and inflammatory responses typically including endotoxic lung, trauma, endotoxemia and acute infections [60, 61]. Earlier researches have reported some circumstantial evidence that cytokines may play important role as direct effectors of pathologic and clinical manifestations that abound in several central nervous system diseases [62-64]. Also, besides their involvement in the generation of immunity against chronic intracellular infections, circulation of IL-6 with other alarm cytokines *TNF α* and IL-1 produces acute phase proteins many of which are protease inhibitors [65, 66]. Apparently, clarification of the functional role of IL-6 in disease pathophysiology is therefore important to aid better understanding of the molecular mechanisms of inflammation and hence proffering appropriate therapeutic strategies.

Biosensors capable of specific detection and quantification of biomarkers are therefore desired for better understanding of the role of these protein in disease progression. Fibre optic biosensors have been widely employed in the field of biological applications such as food processing and security [67], environmental monitoring and protection [68] and clinical diagnosis [69] due to their high sensitivity, portability for point-of-care usage, cost effectiveness, rapid response time and anti-electromagnetic interference which make them highly safe for *in vivo* usage. Optical fibre gratings capable of evanescent wave induction to the surrounding have been employed using two highly sensitive techniques: fluorescence technique and label-free technique. While the two techniques have been proven to be highly sensitive they have their shortfall of selectivity depending on condition of usage. The fluorescence based technique may be blind to the presence of some auto-fluorescence from non-specific binding of other interfering proteins [70]. Also, signals from non-specific binding of other interfering proteins could reduce the selectivity of the label-free technique [71, 72] especially when used in fluids containing large amounts of interfering proteins [72]. However, they still remain the best methods available as researchers tenaciously find solution to this shortfall.

Various methods earlier reported on fibre optic biosensors construction include: LPFGs [73], TFGs [74], Michelson interferometer [75], Mach-Zehnder interferometer [76], Fabry-Perot interferometer [77] and tapered fibre probes [76, 78]. This work demonstrates highly sensitive and highly specific label-free fibre optic biosensor for the recognition of

interleukin-6 (IL-6) protein based on antibody-functionalized 81^o-TFG. With this 81^o-TFG biosensor, interleukin-6 (IL-6) protein has been successfully detected down to a concentration of 0.015 pg/ml.

5.4.2 Materials and methods

5.4.2.1 Fabrication of the IL-6 immobilized 81^o-TFGs biosensor

Similar sets of 81^o-TFGs UV-inscribed in 80 μ m-cladding B/Ge co-doped optical fibre earlier reported for Trx-antigen detection was also employed here. The detailed fabrication procedure and spectral characterisation of the 81^o-TFGs have been discussed in session 3.5.1.

Also, the entire sample solutions were prepared either by analytical grade reagents or de-ionized water. All reagents used are the same as those reported for Trx in session 5.3.2.1 except for the antibody which is now interleukin-6 (IL-6) antibody (format: Purified; MABF41). Also, the chemical treatment of the 81^o-TFG surface and antibody immobilization follow exactly the same procedure as that of Trx earlier discussed.

When light is transmitted through the fibre after IL-6 immobilization, a shift in wavelength of ~36nm with respect to the bare fibre was recorded on the OSA signifying the presence of the IL-6 antibody on the surface of the fibre. Figure 5.13 shows the transmission spectrum of the 81^o-TFG biosensor as the centre wavelength shifts from ~ 1605.19nm to ~1640.90nm before and after IL-6 immobilization respectively.

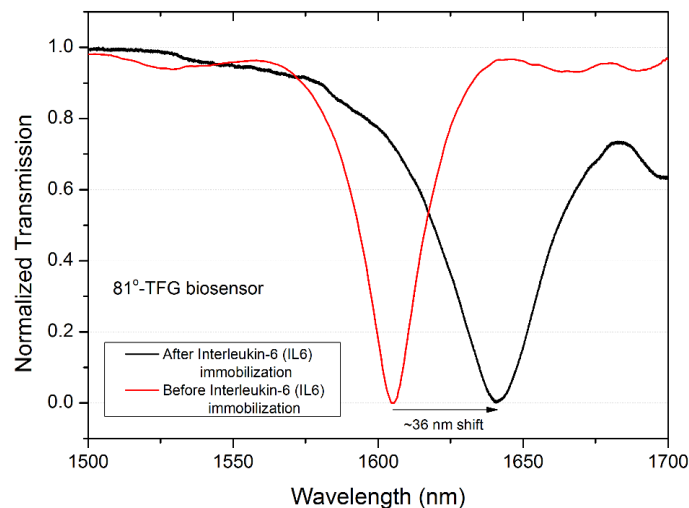


Figure 5.13: Spectra wavelength shift after immobilization of Interleukin-6 (IL-6) antibody on fibre surface

5.4.2.2 Chemical interaction on the surface-modified 81°-TFG biosensor

Figure 5.14 shows the IL-6 antibody covalently bound to the fibre surface and the antigen antibody reaction when submerged in different concentrations of IL-6 antigen. To generate standard curve, IL-6 recombinant protein was serially diluted (0.375pg/ml – 25pg/ml) in PBS/0.1% FBS and incubated overnight at 4°C. Also, the 81°-TFG biosensor was submerged in 2ml of 1µg/ml IL-6 antibody in 10mM Phosphate buffered saline (PBS) with 0.1% FBS and equally incubated overnight at 4°C.

Light from a supercontinuum laser source (Fianium) was transmitted through the fibre which was mounted on a micrometre stage with the functionalized grating area centred on the test platform. The excessively tilted fringes couple the core mode to the higher order cladding modes and the evanescent waves radiated to the surrounding medium monitors the signal generated by the IL-6 antibody-antigen interaction. The IL-6 antigen solutions, which has been serially diluted were applied as the sample solutions. Similar with Trx, the applied sample solutions were kept at constant volume of 100µl so as to totally submerge the grating region of the IL-6 immobilized 81°-TFG biosensor. At the end of each subsequent application of sample solution, the surface of the fibre was rinsed with PBS to restore the spectrum back to reference. The immediately response of the biosensor is obvious in its transmission spectrum as the centre wavelength red-shifts when the sample solutions were applied, indicating the rapidity in antibody-antigen interaction. The signals generated from the antigen-antibody interaction were recorded as the spectra profile on the OSA. Figure 5.14 shows the binding of the interleukin (IL-6) antibody to the fibre surface and the antibody-antigen interaction as light is transmitted through the fibre.

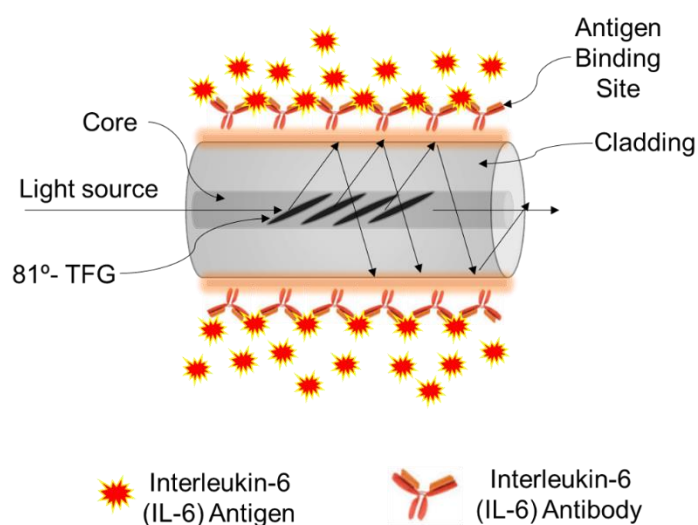


Figure 5.14: Schematic of Interleukin-6 (IL-6) antigen-antibody reaction on fibre surface

5.4.3 Results and discussion

Once removed from the capture IL-6 antibody solution, the interleukin (IL-6) immobilized 81°-TFG biosensor was immersed in PBS solution and the spectrum was recorded as reference. Thereafter, it was subjected to IL-6 antigen solutions of different concentrations and wavelength shifts were recorded. Equations 5.7 – 5.10 are used to analyse the definite binding capability of IL-6 antigen on the IL-6 antibody immobilized 81°-TFG biosensor which were recorded in form of optical signals on the OSA.

The first experiment used sample solutions serially diluted from low to high concentrations range 0.375pg/ml – 25pg/ml. The immersion time for administering each concentration was controlled at ~30 sec which was followed by PBS rinsing to remove any unbound interleukin. The signal spectra profiles as the 81°-TFG biosensor showed immediate response by red-shifting from initial reference point with respect to the substrate concentration were monitored real time on the OSA. The recorded transmission spectra evolution of the (IL-6) immobilized 81°-TFG biosensor in response to the sample concentrations are as shown in Figure 5.15.

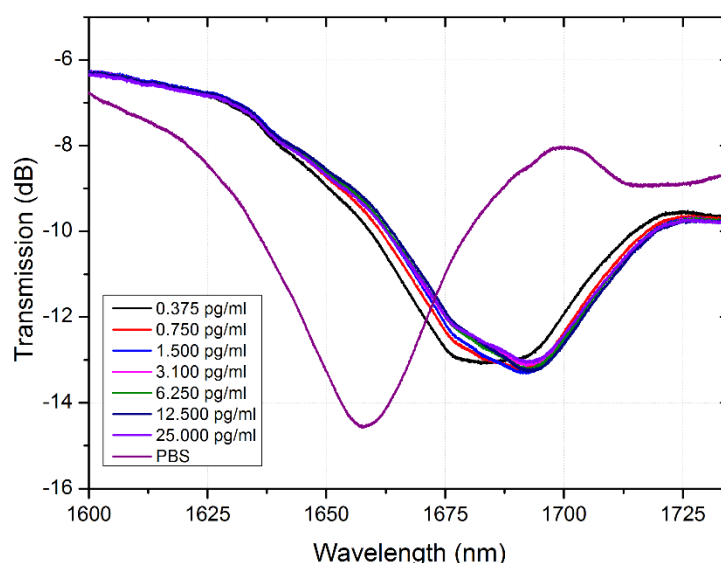


Figure 5.15: Transmission spectra evolution of the 81°-TFG biosensor in response to Interleukin (IL-6) antigen-antibody interaction; red-shift from reference as sample concentration increases

In Figure 5.16, the curve fitting shows the highest reaction rate achieved at saturating substrate concentrations $\Delta\lambda_{\max}$ was obtained as 35.05 ± 0.27 nm and the dissociation constant K_m obtained as 0.27 pg/ml. With these results, the apparent affinity for the protein under study is high. Therefore, our results have shown a high rate of reaction at higher substrate concentration. Furthermore, with the molecular mass of human interleukin-6, $M_{[S]} = 21006.11\text{Da}$ (21006.11g/mol) and molecular length $L_{[S]} = 185\text{\AA}$

(18.5 nm) [79], a detection limit and sensitivity response of 3.77×10^{-4} pg/ml (~ 0.001 nM) and $343.77 \text{ nm}/(\text{pg}/\text{mm}^2)$ were obtained respectively. The experiment was repeated three times for repeatability assurance and a repeatability standard deviation of 0.06 was obtained. For each set of repeated experiment, the protocol of cleaning the fibre was repeated and the surface of the fibre was re-functionalized with fresh IL-6 antibody for similar reasons as earlier mentioned with Trx-biosensor.

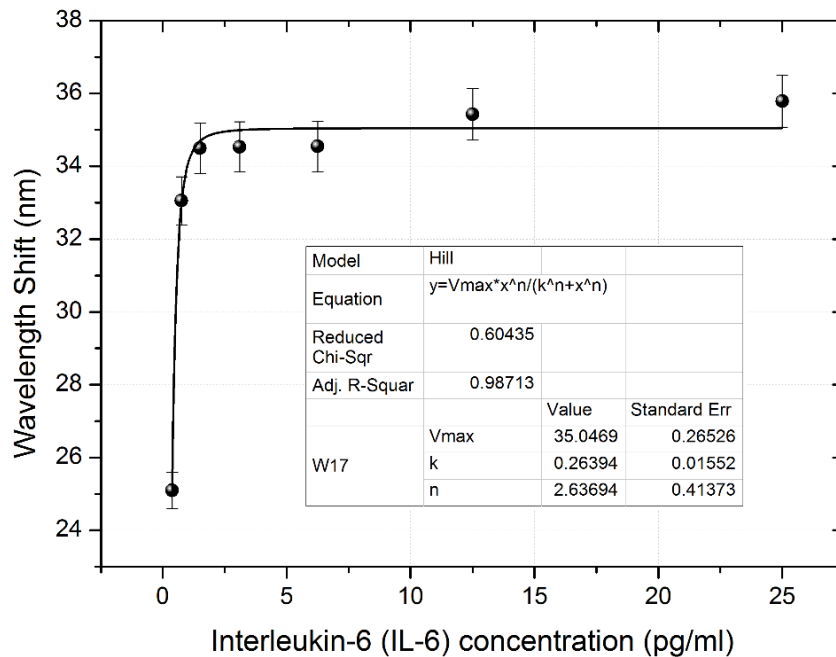


Figure 5.16: Plot of resonant wavelength shift against variation in IL-6 antigen solution concentration (0.375 pg/ml – 25 pg/ml), (Inset: regular residual plot)

The second experiment used sample solutions serially diluted purposely for low substrate concentrations: 0.015 pg/ml, 0.035 pg/ml, 0.07 pg/ml, 0.15 pg/ml, 0.3 pg/ml, 0.6 pg/ml, 1.25 pg/ml and 2.5 pg/ml. From the curve fitting in Figure 5.17, the max speed of reaction $\Delta\lambda_{\max}$ has a lower value of 19.82 ± 2.30 nm and lower dissociation constant K_m of 1.29×10^{-5} pg/ml compared with previous experiment of higher substrate concentration. The sensitivity response was estimated to be $194.41 \text{ nm}/(\text{pg}/\text{mm}^2)$. From the lower substrate concentration experimental results, it is obvious that the speed of reaction is significantly high and the apparent affinity of the binding protein is higher since a lower value was obtained for K_m . This experiment was also repeated three times and same repeatability standard deviation of 0.06 as that of higher concentration range was obtained.

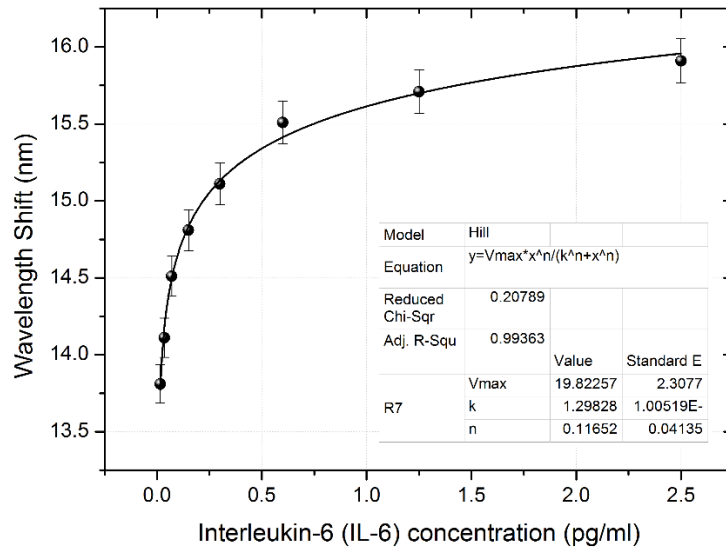


Figure 5.17: Plot of resonant wavelength shift against variation in IL-6 antigen solution concentration (0.015 pg/ml – 2.5 pg/ml).

The specificity validity of the interleukin (IL-6) immobilized 81^o-TFG biosensor for detection of IL-6 antibody-antigen interaction was put to test by subjecting it to plasma solutions of different concentrations to specifically detect IL-6 protein amidst other interfering proteins present in plasma. The same pooled plasma sample used for validating specificity of thioredoxin was also used in this study. The serial dilution follows same ratio of 1:8, 1:4, 1:2, and 1:1, which also correspond to plasma concentrations of 0.0625 mg/ml, 0.125 mg/ml, 0.25 mg/ml, 0.5 mg/ml and 1 mg/ml respectively.

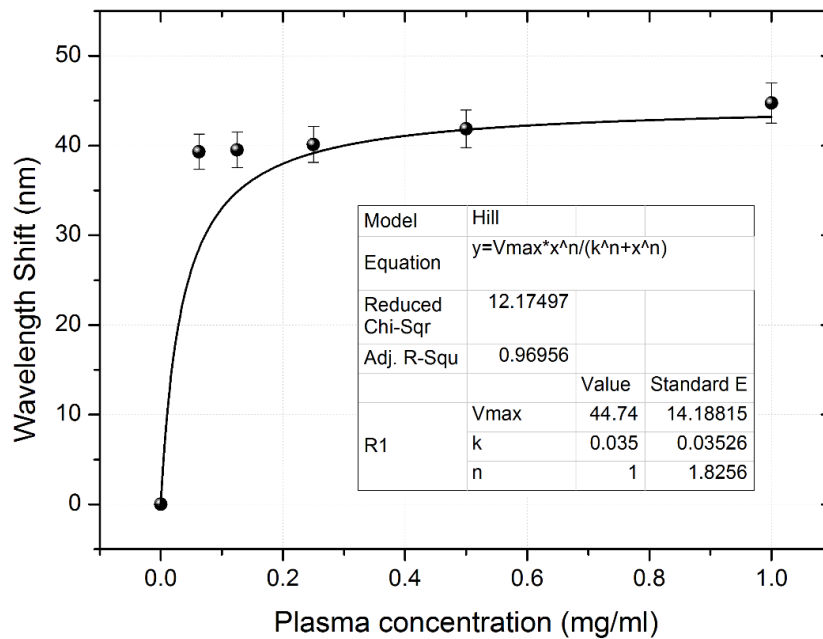


Figure 5.18: Plot of resonant wavelength shift of IL-6 immobilized 81^o-TFG biosensor against variation in human plasma solution of different concentrations (0.0625 – 1.0 mg/ml).

The IL-6 immobilized 81^o-TFG biosensor was immersed in the human plasma as the new substrate solutions of different concentrations for specific detection of interleukin protein in the presence of other interfering proteins. The resonant wavelength response was recorded on the OSA real time. Results from the curve fitting in Figure 5.18 shows $\Delta\lambda_{\max}$ has a high value of 44.74 nm which is similar to that obtained with Trx and same limitation imposed by the complexity of human plasma was experienced with IL-6 antibody with saturation occurring even at the lowest concentration.

5.4.4 Conclusion

A fibre optic biosensor based on IL-6 antibody-functionalized 81^o-TFG has been presented for label-free specific recognition of interleukin-6 (IL-6) protein. The 81^o-TFG biosensor recorded a high saturation value $\Delta\lambda_{\max}$ of 35.05 ± 0.27 nm and a dissociation constant K_m of 0.27 pg/ml for high concentrations range 0.375pg/ml – 25pg/ml which confirms high affinity binding. A detection limit and sensitivity response of 0.0004pg/ml and 343.77nm/(pg/mm²) were obtained respectively. Also, for lower substrate concentration range 0.015 pg/ml – 2.5 pg/ml, the biosensor recorded values of 19.82 ± 2.30 nm and 1.29×10^{-5} pg/ml for $\Delta\lambda_{\max}$ and K_m respectively. The sensitivity response was estimated to be 194.41 nm/(pg/mm²). Similar with Trx, the specificity of the biosensor in the presence of interfering proteins was validated using human plasma but results indicate background interference or non-specific binding of other proteins which is the limitation of this sensor.

5.5 Chapter conclusion

This chapter has presented in-fibre optical grating based biosensors for pathogen detection and sensing applications. First, enzyme functionalized biosensor based on dual-peak LPFG inscribed in B/Ge co-doped single mode fibre with 80 μ m-cladding has been demonstrated and investigated for sugar level and glucose concentration detection. Prior to enzyme functionalization, the dual-peak LPFG has been shown to have high sensitivity sugar level concentration solution (Peak 1: -2.4642 nm/%; Peak 2: 4.6696 nm/%) and after enzyme functionalization, the glucose detection has shown high sensitivities of 12.211 ± 0.189 nm/ (mg/ml) (0.1 - 1.6 mg/ml) for Peak 2 and 7.115 ± 0.119 nm / (mg/ ml) (0.1–3.2 mg/ml) for Peak 1.

Then, a label-free biosensor based on antibody (Trx) immobilized 81^o-TFG in 80 μ m-cladding B/Ge co-doped optical fibre has been demonstrated for high-specificity thioredoxin (Trx) detection. The (Trx) immobilized 81^o-TFG biosensor recorded a high saturation value $\Delta\lambda_{\max}$ of 33.19 ± 0.15 nm and dissociation constant K_m of 0.65 ng/ml for high concentrations range (1.50 – 25 ng/ml) with detection limit and sensitivity response of 0.003nM and 183.57 nm/(ng/mm²) respectively.

Finally, a fibre optic biosensor based on IL-6 antibody-functionalized 81^o-TFG has been presented for label-free specific recognition of interleukin-6 (IL-6) protein. The 81^o-TFG biosensor also recorded a high saturation value $\Delta\lambda_{\max}$ of 35.05nm and a dissociation constant K_m of 0.27 pg/ml for high concentrations range 0.375pg/ml – 25pg/ml which confirms high affinity binding. A detection limit and sensitivity response of 3.77×10^{-4} pg/ml and 343.77 nm/(pg/mm²) were obtained respectively. The specificity of the biosensor was attempted by using human plasma and results have shown that the saturation occurs even at the lowest concentration measured. This has been identified as the limitation of this sensor. Further and more comprehensive experiment should be carried out not just to optimise the sensor performance but also identify the application limitation of such sensors.

References

- [1] A. A. Badmos, Q. Sun, Z. Sun, J. Zhang, Z. Yan, P. Lutsyk, A. Rozhin and L. Zhang, "Enzyme-functionalized thin-cladding long period fibre grating in transition mode at dispersion turning point for sugar level and glucose detection", *J. Biomed. Opt.* vol. 22(2), 2017. (doi: 10.1117/1.JBO.22.2. 027003)
- [2] A. A. Badmos, Q. Sun, Z. Sun, Z. Yan, and L. Zhang, "Near-infrared enzyme-immobilized dual-peak long period fibre grating (LPFG) as sugar concentration and glucose detection biosensor", 2550682 *Chemical and Gas Sensing 6th Asia Pacific Optical Sensors Conference*, 12 October, 2016.
- [3] M. D. P. T. Sotomayor, I. M. Raimundo, G. O. Neto and L.T. Kubota, "Bi-enzyme optode detection system for oxalate determination based on a natural source of enzyme," *Analytica Chimica Acta*, vol. 447, pp. 33-40, 2001.
- [4] C. DiCesare, I. Biran and D. R. Walt, "Individual cell migration analysis using fibre-optic bundles," *Anal. Bioanal. Chem.* vol. 382, pp. 37-43, 2005.
- [5] D. Atias, Y. Liebes, V. Chalifa-Caspi, L. Bremand, L. Lobel, R. S. Marks and P. Dussart, "Chemiluminiscent optical fibre immunosensor for the detection of IgM antibody to dengue virus in humans," *Sens. Actuators B* vol. 140, pp. 206-215, 2009.
- [6] V. G. Andreou and Y. D. Clonis, "A portable fibre-optic pesticide biosensor based on immobilized cholinesterase and sol-gel entrapped bromocresol purple for in-field use," *Biosens. Bioelectron.* vol. 17, pp. 61-69, 2002.
- [7] K. L. Brogan and D. R. Walt, "Optical fibre-based sensor: application to chemical biology," *Curr. Opin. Chem. Biol.* vol. 9(5), pp. 494-500, 2005.
- [8] M. E. Bosch, A. J. R. Sanchez, F. S. Rojas and C. B. Ojeda, "Recent development in optical fibre biosensors," *Sensors* vol. 7(6), pp. 797-859, 2007.
- [9] M. P. DeLisa, Z. Zhang, M. Shiloach, S. Pilevar, C. C. Davis, J. S. Sirkis and W. E. Bentley, "Evanescent wave long-period fibre Bragg grating as an immobilized antibody biosensor," *Anal. Chem.* vol. 72(13), pp. 2895-2900, 2000.
- [10] J. A. Barnes, R. S. Brown, A. H. Cheung, M. A. Dreher, G. Mackey and H. P. Look, "Chemical sensing using a polymer coated long-period fibre grating interrogated by ring-down spectroscopy," *Sens. Actuators B* vol. 148 (1), pp. 221-226, 2010.
- [11] J. Goicoechea, C. R. Zamarreno, I. R. Matias and F. J. Arregui, "Optical fibre pH sensors based on layer-by-layer electrostatic self-assembled Neutral Red," *Sens. Actuators B* vol. 132(1), pp. 305-311, 2008.
- [12] A. Deep, U. Tiwari, P. Kumar, V. Mishra, S. C. Jain, N. Singh, P. Kapur and L. M. Bharadwaj, "Immobilization of enzyme on long period grating fibres for sensitive glucose detection," *Biosens. Bioelectron.* vol. 33, pp. 190-195, 2012.
- [13] H. M. R. Goncaives, L. Moreira, L. Pereira, P. Jorge, C. Gouveia, P. Martins-Lopes and J. R. A. Fernandes, "Biosensor for label-free DNA quantification based on functionalized LPGs," *Biosens. Bioelectron.* vol. 84, pp. 30-36, 2015.

- [14] S. M. Tripathi, W. J. Bock, P. Mikulic, R. Chinnappan, A. Ng, M. Tolba and M. Zourob, "Long period grating based biosensor for the detection of Escherichia coli bacteria," *Biosens. Bioelectron.* vol. 35(1), pp. 308-312, 2012.
- [15] C. L. Eggen, Y. S. Lin, T. Wei and H. Xiao, "Detection of lipid bilayer membranes formed on silica fibres by double-long period fibre grating laser refractometry," *Sens. Actuators B Chem.* vol. 150(2), pp. 734-741, 2010.
- [16] D. M. Disley, J. Blyth, D. C. Cullen, H. Yout, S. Eapen and C. R., Lowe, "Covalent coupling of immunoglobulin G to a poly(vinyl)alcohol-poly(acrylic acid) graft polymer as a method for fabricating the interfacial-recognition layer of a surface plasmon resonance immunosensor," *Biosens. Bioelectron.* vol. 13 (3-4), pp. 383-396, 1999.
- [17] C. J. Stanford, G. Ryu, M. Dagenais, M. T. Hurley, K. J. Gaskell and P. DeShong, *J. Sens.*, 2009.
- [18] C. Elosua, C. Bariain, I. R. Matias, F. J. Arregui, A. Luquin and M. Laguna, "Volatile alcoholic compounds fibre optic nanosensor," *Sens. Actuators B* vol. 115(1), pp. 444-449, 2006.
- [19] Z. Wang, J. R. Hefflin, K. Van Cott, R. H. Stolen, S. Ramachandran and S. Ghalmi, "Biosensors employing ionic self-assembled multilayers adsorbed on long-period fibre gratings," *Sens. Actuators B* vol. 139 (2), pp. 618-623, 2009.
- [20] X. Liu, W. Farmerie, S. Schuster and W. Tan, "Molecular beacons for DNA biosensors with micrometer to submicrometer dimensions," *Anal. Biochem.* vol. 283 (1), pp. 56-63, 2000.
- [21] R. Marks, A. Novoa, D. Thomassey and S. Cosnier, "An innovative strategy for immobilization of receptor proteins on to an optical fibre by use of poly (pyrrole–biotin)," *Anal. Biochem.* vol. 374 (6), pp. 1056-1063, 2002.
- [22] M. Lee and D. R. Walt, "A fibre-optic microarray biosensor using aptamers as receptors," *Anal. Biochem.* vol. 282 (1), pp. 142-146, 2000.
- [23] X. W. Shu, L. Zhang and I. Bennion, "Sensitivity characteristics of long-period fibre gratings," *J. Lightwave Technol.* vol. 20(2), pp. 255-266, 2002.
- [24] D. W. Kim, Y. Zhang, K. L. Cooper and A. Wang, "In-fibre reflection mode interferometer based on a long-period grating for external refractive-index measurement," *Appl. Opt.* vol. 44 (26), pp. 5368-5373, 2005.
- [25] T. M. Libish, J. Linesh, M. C. Bobby, B. Nithyaja, S. Mathew, C. Pradeep and P. Radhakrishnan, "Glucose concentration sensor based on long period grating fabricated from hydrogen loaded photosensitive fibre," *Sens. Transducers* vol. 129 (6), pp. 142-148, 2011.
- [26] A. M. Vengsarkar, P. J. Lemaire, J. B. Judkins, V. Bhatia, T. Erdogan and J. E. Sipe, "Long-period fibre gratings as band-rejection filters," *J. Lightw. Technol.* vol. 14 (1), pp. 58-65, 1996.
- [27] H. J. Patrick, A. Kersey and F. Bucholtz, "Analysis of the response of long period fibre gratings to external index of refraction," *J. Lightwave Technol.* vol. 16, pp. 1606-1611, 1998.

- [28] X. Chen, L. Zhang, K. Zhou, E. Davies and K. Sugden, "Real-time detection of DNA interactions with long-period fibre-grating-based biosensor," *Opt. Lett.* vol. 32, pp. 2541-2543, 2007.
- [29] H. S. Jang, K. N. Park, J. P. Kim, S. J. Sim and O. J. Kwon, "Sensitive DNA biosensor based on a long-period grating formed on the side-polished fibre surface," *Opt. Express* vol. 17, pp. 3855-3860, 2009.
- [30] X. Chen, K. Zhou, L. Zhang and I. Bennion, "Dual-peak long-period fibre gratings with enhanced refractive index sensitivity by finely tailored mode dispersion that uses the light cladding etching technique," *Applied Optics* vol. 46 (4), pp. 451-455, 2007.
- [31] I. D. Villar, J. L. Cruz, A. B. Socorro, J. M. Corres, and I. R. Matias, "Sensitivity optimization with cladding-etched long period fibre gratings at dispersion turning point," *Opt. Express* vol. 24 (16), pp. 17680-17685, 2016.
- [32] P. Pilla, C. Trono, F. Baldini, F. Chiavaioli, M. Giordano, and A. Cusano, "Giant sensitivity of long period grating in transition mode near the dispersion turning point: an integrated design approach," *Opt. Lett.* vol. 37 (19), pp. 4152-4154, 2012.
- [33] M. A. Godshall and A. J. DeLucca, "Acetic acid, a major volatile constituent of brown sugar: its origin and measurement," *J. Agric. Food Chem.* vol. 32 (2), pp. 390-393, 1984.
- [34] B. Luo, Z. Yan, Z. Sun, J. Li and L. Zhang, "Novel glucose sensor based on enzyme-immobilized 81 tilted fibre grating," *Optics Express* vol. 22(25), pp. 30571-30578, 2014.
- [35] Y-C. Kim, W. Peng, S. Banerji and K. S. Booksh, "Tapered fibre optic surface plasmon resonance sensor for analyses of vapour and liquid phases," *Optics Letters* vol. 30(17), pp. 2218-2220, 2005.
- [36] A. Holmgren, "Thioredoxin," *Ann. Rev. Biochem.* vol. 54, pp. 237-271, 1985.
- [37] A. Holmgren, C-I. Branden, H. Jornvall and B-M. Sjoberg, editors, "Thioredoxin and glutaredoxin systems: structure and functions," *NY: Raven Press*, 1986.
- [38] J. L. Martin, "Thioredoxin: a fold for all reasons," *Structure* vol. 3, pp. 245-250, 1995.
- [39] T. C. Laurent, E. C. Moore and P. Reichard, "Enzymatic synthesis of deoxyribonucleotides VI. Isolation and characterisation of thioredoxin, the hydrogen donor from *Escherichia coli* B," *J. Biol. Chem.* vol. 239, pp. 3436-3444, 1964.
- [40] G. Powis, D. Mustacich and A. Coon, "The role of redox protein thioredoxin in cell growth and cancer," *Free Radic. Biol. Med.* vol. 29(3-4), pp. 312-322, 2000.
- [41] S. Gromer, S. Urig and K. Becker, "The thioredoxin system – from science to clinic," *Med. Res. Rev.* vol. 24, pp. 40-89, 2004.
- [42] H. Masutani, J. Bai, Y. C. Kim and J. Yodoi, "Thioredoxin as a neurotropic cofactor and important regulator of neuroprotection," *Mol. Neurobiol.* vol. 29, pp. 229-242, 2004.

- [43] L. Tao, E. Gao, N. S. Bryan, Y. Qu, H. R. Liu, A. Hu, T.A. Christopher, B. L. Lopez, J. Yodoi, W. J. Koch, M. Feelisch and X. L. Ma, "Cardioprotective effects of thioredoxin in myocardial ischemia and reperfusion: role of S-nitrosation," *Proc. Natl. Acad. Sci. U. S. A.* vol. 101(31), pp. 11471-11476, 2004.
- [44] H. Nakamura, S. C. De Rosa, J. Yodoi, A. Holmgren, P. Ghezzi, L. A. Herzenberg, and L. A. Herzenberg, "Chronic elevation of plasma thioredoxin: inhibition of chemotaxis and curtailment of life expectancy in AIDS," *Proc. Natl. Acad. Sci. U. S. A.* vol. 98, pp. 2688-2693, 2001.
- [45] A. Rubartelli, A. Bajetto, G. Allavena, E. Wollman and R. Sitia, "Secretion of thioredoxin by normal and neoplastic cells through a leaderless secretory pathway," *J. Biol Chem.*, vol. 267 (34), 24161-24164, 1992.
- [46] H. Nakamura, J. Vaage, G. Valen, C. A. Padilla, M. Björnstedt and A. Holmgren, "Measurements of Plasma Glutaredoxin and Thioredoxin in Healthy Volunteers and During Open-Heart Surgery," *Free Radic. Biol. Med.* vol. 24, pp. 1176-1186, 1998.
- [47] H. Nakamura, S. De Rosa, M. Roederer, M. T. Anderson, J. G. Dubs, J. Yodoi, A. Holmgren, L. A. Herzenberg and L. A. Herzenberg., "Elevation of plasma thioredoxin levels in HIV-infected individuals," *Inter. Immunology* vol. 8, pp. 603-611, 1996.
- [48] K. Miyazaki, N. Noda, S. Okada, Y. Hagiwara, M. Miyata, I. Sakurabayashi, N. Yamaguchi, T. Sugimura, M. Terada and H. Wakasugi., "Elevated serum level of Thioredoxin in patients with Hepatocellular Carcinoma," *Biotherapy* vol. 11, pp. 277-288, 1998.
- [49] M. F. Jeng, A. Holmgren and H. J. Dyson, "Proton sharing between cysteine thiols in Escherichia coli thioredoxin: implications for the mechanism of protein disulfide reduction," *Biochemistry* vol. 34, pp. 10101-10105, 1995.
- [50] A. Holmgren and M. Bjornstedt, "Thioredoxin and thioredoxin reductase," *Methods Enzymol.* vol. 252, pp. 199-208, 1995.
- [51] M. F. Jeng, A. P. Campbell, T. Begley, A. Holmgren, D. A. Case, P. E. Wright and H. J. Dyson, "High-resolution solution structures of oxidized and reduced Escherichia coli thioredoxin," *Structure* vol. 2, pp. 853-868, 1994.
- [52] K. W. Kim, J. F. Song, J. S. Kee, Q. Liu, G. Q. Lo and M. K. Park, "Label-free biosensor based on an electrical tracing-assisted silicon micro-ring resonator with a low cost broadband source," *Biosens. Bioelectron.*, vol. 46, pp 15-21, 2013.
- [53] Chang Raymond, "Physical Chemistry for the Biosciences," *Sausalito, CA: University Science*, pp 363-371, 2005.
- [54] L. H. Chen, C. C. Chan, K. Ni, P. B. Hu, T. Li, W. C. Wong, P. Balamurali, R. Menon, M. Shailender, B. Neu, C. L. Poh, X. Y. Dong, X. M. Ang, P. Zu, Z. Q. Tou and K. C. Leong, "Label-free fibre-optic interferometric immunosensors based on waist-enlarged fusion taper," *Sens. Actuators B: Chem.* vol. 178, pp 176-184, 2013.
- [55] S. Maguis, G. Laffont, P. Ferdinand, B. Carbonnier, K. Kham, T. mekhalif and M. C. Millot, "Biofunctionalized tilted fibre Bragg gratings for label-free immunosensing," *Opt. Express* vol. 16, pp. 19049-19062, 2008.

- [56] B. Sahaf, A. Söderberg, G. Spyrou, A. M. Barral, K. Pekkari, A. Holmgren and A. Rosén, "Thioredoxin Expression and Localization in Human Cell Lines: Detection of Full-Length and Truncated Species," *Exp. Cell Res.* vol. 236(1), pp. 181-192, 1997.
- [57] A. Weichsel, J. R. Gasdaska, G. Powis and W. R. Montfort, "Crystal structures of reduced, oxidized, and mutated human thioredoxins: evidence for a regulatory homodimer," *Structure* vol. 4, pp. 735-751, 1996.
- [58] W. Yu, T. Lang, J. Bian and W. Kong, "Label-free fibre optic biosensor based on thin-core modal interferometer," *Sensors and Act. B* vol. 228, pp. 322-329, 2016.
- [59] L. Marques, F. U. Hernandez, S. Korposh, M. Clark, S. Morgan, S. W. James and R. P. Tatam, "Sensitive protein detection using an optical fibre long period grating sensor anchored with silica core gold shell nanoparticles," *Proc. SPIE* 9157, pp. 1-4, 2014.
- [60] T. Kishimoto, S. Akira and T. Taga, "Interleukin-6 and its receptor: a paradigm for cytokines," *Science* vol. 258, pp. 593-597, 1992.
- [61] R. J. Zitnik and J. A. Elias, "Interleukin-6 and the lung, In Cytokines of the lungs," *J. Kelly editor, Marcel Dekker, Inc. New York*, pp. 229-280, 1993.
- [62] E. J. Goetzl, D. C. Adelman and S. P. Sreedharan, "Neuroimmunology," *Adv. Immunol.* vol. 48, pp. 161-190, 1990.
- [63] C. R. Plata-Salaman, "Immunoregulators in the nervous system," *Biobehavioral Rev.* vol. 15, pp. 185-215, 1991.
- [64] J. E. Merrill, "Tumor necrosis factor alpha, interleukin 1 and related cytokines in brain development: normal and pathological," *Dev. Neurosci. Rev.* vol. 14, pp. 1-10, 1992.
- [65] H. Baumann and J. Gauldie, "The acute phase response," *Immunol. Today* vol. 15, pp. 74-80, 1994.
- [66] Z. Xing, C. D. Richards, T. Braciak, V. Thibault and J. Gauldie, "Cytokine regulation of hepatic acute phase protein expression," *In Cytokines and the Liver, Falk Symposium 78*, W. Gerok, K. Decker, T. Andus, and V. Gross, editors. Kluwer Academic Publishers Group, Dordrecht, Netherlands, pp. 164-171, 1995.
- [67] X. J. Hao, X. H. Zhou, Y. Zhang, L. H. Liu, F. Long, L. Song and H. C. Shi, "Melamine detection in dairy products by using a reusable evanescent wave fibre optic biosensor," *Sens. Actuators B: Chem.* vol. 204, pp. 682-687, 2014.
- [68] S. K. Mishra, S. Rani and B. D. Gupta, "Surface plasmon resonance based fibre optic hydrogen sulphide gas sensor utilizing nickel oxide doped ITO thin film," *Sens. Actuators B: Chem.* vol. 195, pp. 215-222, 2014.
- [69] M. Yin, C. Wu, L. Shao, W. K. E. Chan, A. P. Zhang, C. Lu and H. Tam, "Label-free disposable fibre optic biosensors for DNA hybridization detection," *Analyst* vol. 138, pp. 1988-1994, 2013.
- [70] H-H. Zeng, R. B. Thompson, B. P. Maliwal, G. R. Fones, J. W. Moffett and C. A. Fierke, "Real-time determination of picomolar free Cu(II) in seawater using a fluorescence-based fibre optic biosensor," *Anal. Chem.* vol. 75(24), pp. 6807-6812, 2003.

- [71] D. J. Gentleman, L. A. Obando, J. F. Masson, J. R. Holloway and K. S. Booksh, "Calibration of fibre optic based surface plasmon resonance sensors in aqueous systems," *Analytica Chimica Acta*. vol. 512(2), pp. 291-302, 2004.
- [72] T. M. Battaglia, J. F. Masson, M. R. Sierks, S. P. Beaudoin, J. Rogers, K. N. Foster, G. A. Holloway and K. S. Booksh, "Quantification of cytokines involved in wound healing using surface plasmon resonance," *Anal. Chem.* vol. 77(21), pp. 7016-7023, 2005.
- [73] Z. Y. Wang, J. R. Heflin, K. V. Cott, R. H. Stolen, S. Ramachandra and S. Ghalmi, "Biosensors employing ionic self-assembled multilayers absorbed on long period fibre gratings," *Sens. Actuators B: Chem.* vol. 139, pp. 618-623, 2009.
- [74] S. Lepinay, A. Staff, A. Ianoul and J. Albert, "Improved detection limits of protein optical fibre biosensor coated with gold nanoparticles," *Biosens. Bioelectron.* vol. 52, pp. 337-344, 2014.
- [75] D. W. Kim, Y. Zhang, K. L. Cooper and A. Wang, "Fibre-optic interferometric immune-sensor using long period grating," *Electron. Lett.* vol. 42, pp. 324-325, 2006.
- [76] Y. Tian, W. Wang, N. Wu, X. Zou and X. Wang, "Tapered optical fibre sensor for label-free detection of biomolecules," *Sensors (Basel)* vol. 11, pp. 3780-3790, 2011.
- [77] Y. Zhang, H. Shibu, K. L. Cooper and A. Wang, "Miniature fibre-optic interferometric biosensor," *Opt. Lett.* vol. 30, pp. 1021-1023, 2005.
- [78] R. Kapoor, N. Kaur, E. T. Nishanth, S. W. Halvorsen, E. J. Bergey and P. N. Prasad, "Detection of trophic factor activated signalling molecules in cells by a compact fibre-optic sensor," *Biosens. Bioelectron.* vol. 20(2), pp. 345-349, 2004.
- [79] G. Y. Xu, H. A. Yu, J. Hong, M. Stahl, T. McDonagh, L. E. Kay and D. A. Cumming, "Solution structure of recombinant human interleukin-6," *J. Mol. Biol.* vol. 268, pp. 468-481, 1997.

Chapter 6

Conclusion and Future Research

6.1 Conclusion

This thesis has presented a systematic investigation and significant results on the sensitivity enhancement of advanced optical fibre gratings using different nanoparticle depositions and bioreceptor elements for biosensing applications. The main achievements can be summarised as a systematic study and realization in three areas: the fabrication and characterisation of advanced optical fibre gratings ranging from normal to complex grating inscriptions such as dual-peak LPFGs, apodized FBGs, S-TFGs and Ex-TFGs; the nano-structural functionalisation on optical fibre grating surfaces with nanoparticles such as carbon nanotubes (CNT), zinc oxide (ZnO) and gold film deposition, for sensitivity enhancement; and bio-functionalised optical fibre gratings as platform using bioreceptors such as enzymes, antibodies and antigens for biosensing.

The thesis started with a comprehensive literature review of historical perspectives on fibre grating, photosensitivity mechanism and enhancement for UV-induced refractive index change in silica glass fibres. The three UV-inscription techniques: two-beam holographic, phase mask scanning and point-by-point, have also been discussed together with the theories (couple mode theory and phase matching conditions) that underpin the mode coupling and spectral property of fibre gratings.

One of the main achievements of the work reported in this thesis is the use of the aforementioned UV-inscription techniques to fabricate advanced optical fibre gratings of

different structures. Particular emphasis was laid on the fabrication of dual-peak LPFGs in single mode fibres (SMF-28) and B/Ge co-doped thin-cladding single mode fibres at grating periods $140\mu\text{m}$ and $300\mu\text{m}$. Also, Ex-TFGs of different tilt angles are inscribed in SMF-28 and thin-cladding fibre using custom-made amplitude masks of different periods: $5.0\mu\text{m}$ (200 LPMM), $6.6\mu\text{m}$ (150 LPMM) and $25\mu\text{m}$ (40 LPMM). Inscription of FBGs and TFGs have utilised the holographic and phase mask scanning techniques based on simple exposure to periodic UV radiation along a specified length of the fibre. Since the holographic technique is not limited in the Bragg wavelength design, it has been employed to inscribe FBGs with different reflectivity ranges (4% - 99%). However, due to the limitation in length of grating which is imposed by the size of the two interfering beams, the phase mask scanning has been extensively used for most fabrications such as Gaussian apodized Bragg gratings and TFGs. The point-by-point inscription, being the most efficient and flexible method for LPFG inscription was employed for inscribing normal LPFGs and specifically dual-peak LPFGs in transition mode close to the dispersion turning points by the selection of appropriate grating period and simple control of the UV-radiation exposure with a programmable shutter.

Another significant achievement of this work is the surface modification of optical fibre gratings with different nanoparticles for sensitivity enhancement. Highly sensitive RI sensor based on excessively tilted fibre grating (81° Ex-TFGs) structures UV-inscribed in SMF-28 with carbon nanotube (CNT) overlay deposition has been demonstrated. The CNT which is a dark material with high absorption of light and high RI is responsible for the decrement in the intensity minima of the attenuation band while the 81° -TFG induces the wavelength shift as the SRI changes. Results show high sensitivities of 557.29 nm/RIU and 95.54 dB/RIU for the wavelength shift and intensity/power demodulation respectively. Nanodeposition of zinc oxide (ZnO) on Ex-TFGs inscribed in two different fibre types: SMF-28 and B/Ge co-doped thin-cladding SMF, have been investigated using dissimilar morphologies for enhanced RI sensing. With the PS-ZnO morphology, a significant improvement in sensitivity of $\sim 19\%$ (~ 409.5 nm/RIU) and $\sim 21\%$ (~ 522 nm/RIU) with respect to the bare fibre are obtained for the two fibre types respectively. Also, the polarisation dependence of Au-coated S-TFGs on excitation of surface plasmon resonance (SPR) has been investigated. SPR has been maximised for P-polarised light corresponding to complete extinction of a fractional part of the cladding mode resonances while for the S-polarised light, the SPR effect is not excited and the transmission spectrum remain similar to that of uncoated S-TFG. Coupling to the SPR occurs when the axial component of the cladding mode is equivalent to that of an SPR wave which is indicated by more attenuation of the specific cladding modes with respect

to other surrounding cladding modes signifying the SPR signature. The Au-coated 6^o-TFGs have been employed as an RI sensor with a high sensitivity of 469.97 nm/RIU.

The final significant contribution of this research is the surface functionalization of optical fibre gratings with different biological recognition elements, such as enzymes (glucose oxidase) and antibodies/antigens (IL6, Trx), for receptor-analyte interaction. Enzyme functionalized dual-peak LPFG inscribed in 80 μ m-cladding B/Ge co-doped SMF has been demonstrated for sugar concentration level and specific glucose detection. The glucose detection probe is attained by the surface functionalization of the dual-peak LPFG with glucose oxidase via covalent binding and optical micrographs confirmed the presence of the enzyme.

Sugar level concentration detection achieved a significant peak-wavelength shift of ~200nm which is remarkably higher than ~19.8 nm peak-wavelength shift earlier reported for concentration of hemoglobin in sugar solution [1]. Also, glucose detection shows ultra-high sensitivity of 7.115 ± 0.119 nm / (mg/ ml) (0.1–3.2 mg/ml) which is one order of magnitude higher than earlier glucose detection results reported for normal LPFG and 81^o-TFG [2, 3].

A novel label-free biosensor based on antibody (Trx) immobilized 81^o-TFG in 80 μ m-cladding B/Ge co-doped optical fibre has also been demonstrated for high-specificity thioredoxin (Trx) detection. High saturation value $\Delta\lambda_{\max}$ of 33.19 ± 0.15 nm and low dissociation constant K_m of 0.65 ng/ml have been obtained for high substrate concentration range (1.50 – 25 ng/ml) with sensitivity response of 183.57 nm/(ng/mm²) and detection limit of 9.81×10^{-4} ng/ml. Also, this biosensor has efficiently exhibited effective sensing for lower concentration range measurement which has been the major shortfall of the ELISA test. For the low substrate concentrations (0.07ng/ml – 2.5ng/ml), 17.66nm and 1.39×10^{-4} ng/ml were obtained for $\Delta\lambda_{\max}$ and K_m respectively.

In a similar vein, fibre optic biosensor based on antibody-functionalized 81^o-TFG has been presented for label-free specific recognition of interleukin-6 (IL-6) protein. High saturation value $\Delta\lambda_{\max}$ of 35.05 ± 0.27 nm and a dissociation constant K_m of 0.27 pg/ml for high concentrations range 0.375pg/ml – 25pg/ml which confirms high affinity binding were obtained. However, the specificity validation carried out using human plasma for both biosensor have shown that the saturation occurs even at the lowest concentration measured. This limitation requires further and more comprehensive experiment in order to optimise the sensor performance.

Since intensive industrialization and the use of chemicals have immensely contributed to the build-up of many toxic compounds in the environment, the significance of these label free in-fibre optical grating biosensors lies in their ever increasing demand in fields such as food quality controls, environmental monitoring, medical diagnostics and other industries that inevitably require accurate and portable biosensing systems.

6.2 Future research

The biosensing experiments presented in sessions 5.3 and 5.4 could be repeated and measured against time to further probe interactions between analyte in solution in addition to the results presented for measurement against concentration of substrates (Trx and IL-6). This is significantly important and a proposed future work endeared to further investigate the antibody-antigen interaction on the fibre surface is envisaged. Other proposed future works are expatiated below.

6.2.1 Label-free biosensor based on Ex-TFG in thin-core modal interferometer

Thin-core single mode fibre (TCSMF) based Mach-Zehnder interferometers (MZIs) have been employed as highly specific label-free biosensor for detection of various bio-molecules such as target DNA using probe DNA immobilization [4, 5]. Excessively tilted fibre gratings (Ex-TFGs) inscribed in TCSMF and sandwiched between two single-mode fibres (SMFs) have been proposed for biosensing. As illustrated in Figure 6.1, a TCSMF of length ' L ' is sandwiched between two SMFs. Since both the TCSMF and SMFs have the same cladding diameter ($125\ \mu\text{m}$) a fusion splicer in edge-aligned mode can be used to join the two fibre interfaces incurring less loss and making it mechanically strong. The core diameters of the SMFs are $8.2\ \mu\text{m}$ while that of the TCSMF is $2.1\ \mu\text{m}$ with a proposed length of $50\ \text{mm}$. The interfaces 1 and 2 function as mode splitter and combiner respectively.

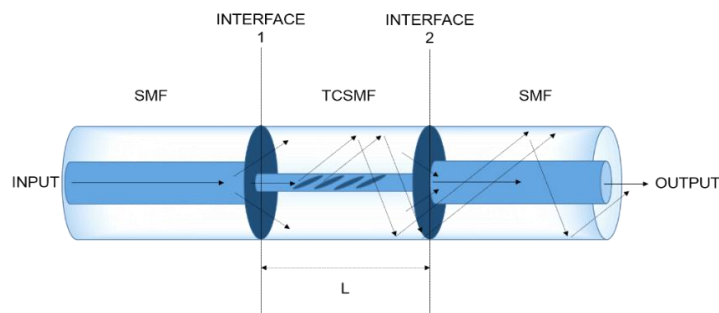


Figure 6.1: Schematic diagram of optical fibre sensor with a TCSMF sandwiched between two SMFs.

The difference in the core diameters allows for leakage of input light into the cladding of the TCSMF at the first interface thereby stimulating the cladding modes. In addition, if an Ex-TFG is inscribed in the thin-core, it will ensure some of the guided core-mode is coupled to higher order cladding modes which enhances the evanescence field of the fibre sensor. At interface 2, light propagating in the cladding mode is reconstituted into the core mode thereby generating an intermodal interference signal due to the optical

path difference. The interferometric phase matching condition as is expressed in Eqn. 6.1 [6],

$$\text{Equation 6.1} \quad 2\pi \left[n_{\text{eff}}^{\text{core}}(\lambda) - n_{\text{eff}}^{\text{clad},i}(\lambda, n_{\text{SRI}}) \right] \frac{L}{\lambda_z} = (2k + 1)$$

where $n_{\text{eff}}^{\text{core}}$ and $n_{\text{eff}}^{\text{clad},i}$ are the effective refractive indexes of core mode and i^{th} order cladding mode respectively, n_{SRI} is the refractive index of surrounding medium, λ_z is the interferometric wavelength of transmission, L is the proposed length of TCSMF and k is an integer. The phase matching condition for the Ex-TFG is as given in Eqn. 3.20. With both phase matching conditions simultaneously satisfied, the result is an enhanced evanescent field which is desired for high sensitivity biosensing.

Bio-functionalization of the proposed Ex-TFG thin-core interferometer further to be developed as label-free biosensor have been proposed to utilize pilot symbol assisted modulation (PSAM) deposition process. The PSAM consists of the polycation PDDA (Diallyldimethyl ammonium chloride) and the polyanion PSS (Styrenesulfonate sodium salt), defined as $(\text{PDDA} + \text{PSS})_n$ with 'n' being the number of bilayers [7]. The process can be repeated until the desired number of bilayers is achieved. Figure 6.2 shows the proposed procedure for surface modification of the Ex-TFG thin-core interferometer.

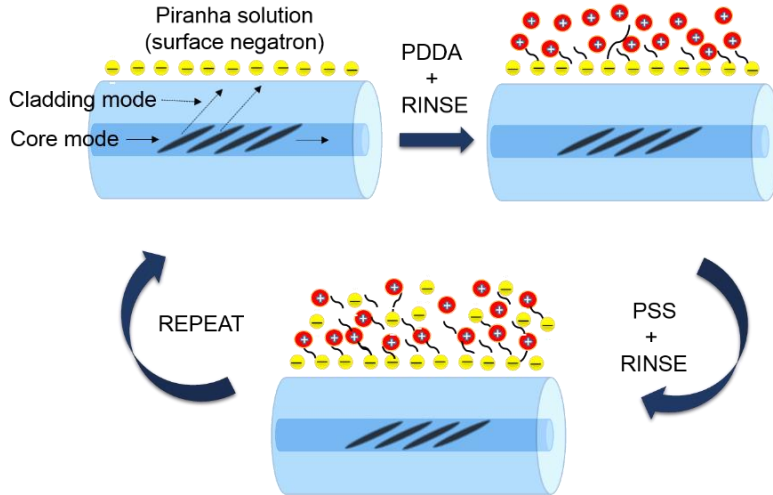


Figure 6.2: Schematic of optical fibre undergoing PSAM deposition.

A bioreceptor-analyte interaction pair, such as biotin-streptavidin bio-conjugate pair, can be immobilized on the prepared surface for bio-functionalization. The wavelength shift of the attenuation band in response to variation in concentration of the surrounding medium (analyte) will give the sensitivity of the proposed thin-core Ex-TFG biosensor.

6.2.2 Affinity surface plasmon resonance (SPR) biosensor

Affinity biosensors consist of a transducer, which could be electro-chemical [8], piezoelectric [9] or optical [10], and a biological recognition element which is able to interact with a selected analyte. The propagation constant of the SPW is extremely sensitive to changes in the refractive index of the dielectric because majority of the field of an SPW is concentrated in the dielectric. This property of SPW is the underlying physical principle of affinity SPR biosensors. For coupling to occur, the incident wave must be polarised in the plane of incidence and the metal layer thin enough to allow some light tunnel across. The tunneling wave excites the quasi-plasmon and the reflected wave loses power as a result of the coupling. A dip in the reflection spectrum, known as Kretschmann configuration, shows the presence of SPR when either the wavelength or the incident angle of light is changed.

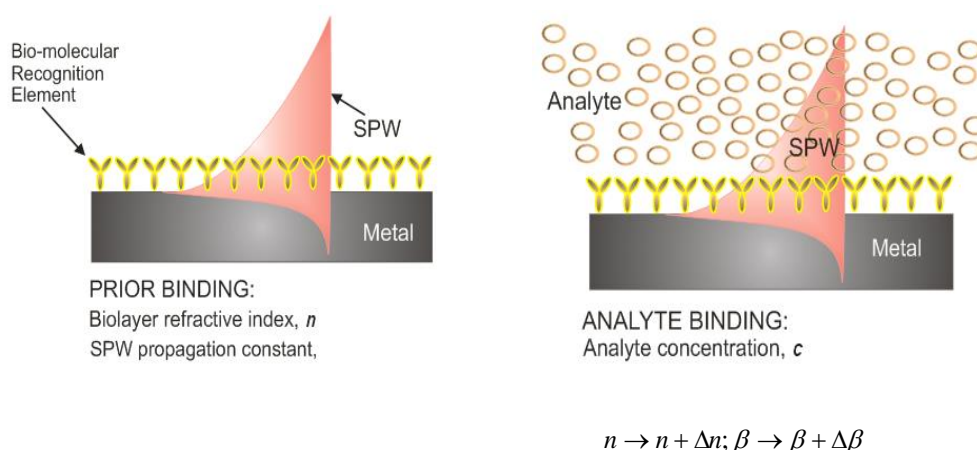


Figure 6.3: Schematic diagram depicting principle of SPR biosensing.

Figure 6.3 shows how the bio-molecular recognition elements on the surface of metal recognize and capture analyte present in a liquid sample thereby producing an increase in the refractive index at the metal surface. The increment in the refractive index gives rise to an increase in the propagation constant of SPW propagating along the metal surface and can be accurately measured by optical means. Figure 6.4 depicts the SPR probing showing the bio-molecular interaction occurring within a short distance from metal surface (Figure 6.4(a)) and the bio-molecular interaction occurring within the whole extent of the field of a SPW (Figure 6.4(b)).

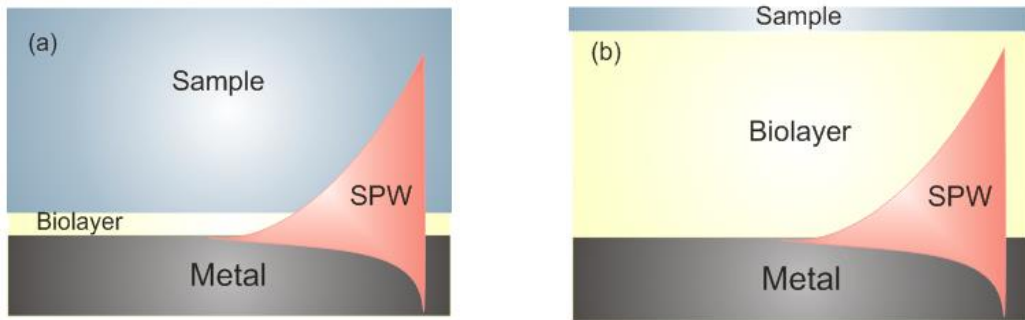


Figure 6.4: Schematic of SPR probing: (a) bio-molecular interaction occurring within a short distance from metal surface, (b) bio-molecular interaction occurring within the whole extent of the field of a SPW.

Extending this principle to TFGs could be straight forward since cladding modes are propagating waves inside the glass that are totally internally reflected by the cladding boundary. By coating the cladding with a thin metal layer, a cylindrically symmetric Kretschmann structure can be obtained.

While there has been couple of works reported on SPR biosensor [11-13], novel ideas can still emanate from the use of combination of LPFG and TFG as the optical transducer for affinity biosensor. The proposed novel work here looks in the direction of “Hybrid optical fibre gratings for efficient excitation of surface plasmon polariton” or “Plasmonic on-fibre bio-sensor in hybrid fibre gratings and plasmonic nanostructure”. It envisages the use of hybrid excessively tilted fibre gratings (Ex-TFGs) with long period fibre gratings (LPFGs) inscribed in small cladding fibre or in D-shaped fibre as the active transducer (Figure 6.5). The gratings are expected to be coated with thin metal layer to form the SPR; then the spectral profile. Several sensor platforms (such as protein detection, DNA, and or cancer biomarker) could be investigated and reported for appropriate application.

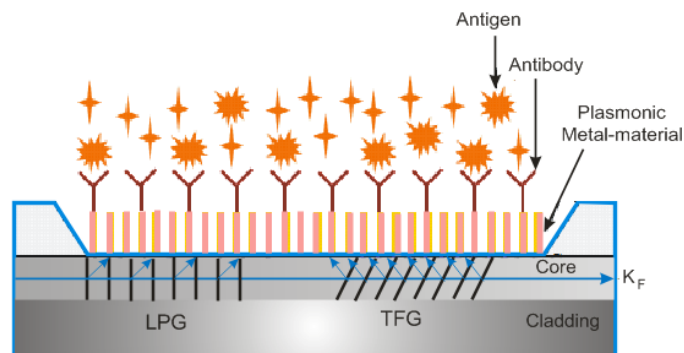


Figure 6.5: Hybrid fibre grating and plasmonic structure biosensor

6.2.3 Bacteriophage-functionalized Ex-TFG biosensor for specific E-coli detection

Detection of pathogenic bacteria has been a clear focus in the field of food processing, water safety and general public health. Phages are obligate intracellular parasites that suppress bacterial cell machinery for their replication. They recognise the bacteria receptors through their tail spike protein [14]. Consequently, they disseminate mature virions which allow binding to host surface receptors and inject genetic material into the bacterial cells thereby initiating a new cycle of propagation.

The strategy for immobilization of phage virions was initially based on physical absorption of the phages onto the detection platform which involves complementary metal-oxide semiconductor (CMOS), quartz crystal microbalance (QCM) flow cytometry and SPR as transduction platforms [15-18]. These result in weak binding and an inconsistent number of phages on the surface. Quest for stable anchoring of probes onto the surface of the detection platform, which enhances sensitivity and consistency of diagnosis, brought about immobilization by chemical functionalization such as streptavidin-mediated attachment of bacteriophages to directly express biotin on their capsid [19].

The approach produced a better attachment densities of 4.4 phage/ μm^2 which is 15-fold increase compared to simple physical absorption. Also, functionalization with sugars (dextrose and sucrose) or amino acids (histidine and cysteine) enhances the number of phage bound to the surface of the detection platform thereby improving coverage density. Compared to physical absorption, a cysteine modified gold surface exhibits 7-fold more phage and even improves to 37-folds when activated by a bi-linker such as glutaraldehyde [20].

Immobilization of phages on the Ex-TFG surface is proposed using established protocol reported in references [21-23]. The protocol consists of three main stages: firstly, silanization of the fibre surface by incubating the cleaned Ex-TFG in 3-aminopropyltris(trimethylsiloxy) silane (APTES); secondly, covalently immobilizing T4 bacteriophages on the activated surface of the Ex-TFG by immersing the samples in bacteriophage solution (10^{10} pfu/ml); and finally, incubating the Ex-TFG in bovine serum albumin (BSA) with a view to blocking the non-specific sites on the surface of the samples.

The bacteriophage-immobilized Ex-TFG is proposed for E.coli bacteria detection with high specificity. Figure 6.6 shows the aforementioned experimental protocol for covalent binding of T4 bacteriophage on the proposed Ex-TFG biosensor for specific E. coli detection.

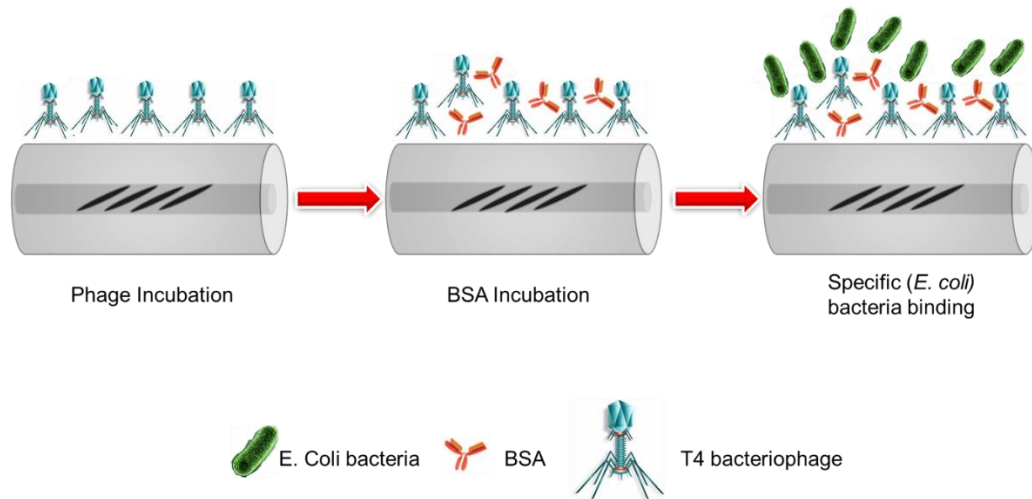


Figure 6.6: Schematic of experimental procedure for covalent binding of T4 bacteriophage on Ex-TFGs samples for *E. coli* bacteria detection.

References

- [1] X. Chen, K. Zhou, L. Zhang and I. Bennion, "Dual-peak long-period fibre gratings with enhanced refractive index sensitivity by finely tailored mode dispersion that uses the light cladding etching technique," *Applied Optics* vol. 46 (4), pp. 451-455, 2007.
- [2] A. Deep, U. Tiwari, P. Kumar, V. Mishra, S. C. Jain, N. Singh, P. Kapur and L. M. Bharadwaj, "Immobilization of enzyme on long period grating fibres for sensitive glucose detection," *Biosens. Bioelectron.* vol. 33, pp. 190-195, 2012.
- [3] B. Luo, Z. Yan, Z. Sun, J. Li and L. Zhang, "Novel glucose sensor based on enzyme-immobilized 81 tilted fibre grating," *Optics Express* vol. 22(25), pp. 30571-30578, 2014.
- [4] G. Y. Ma, P. Zhang, G. F. Yan, Y. B. Bai, Y. C. Hu and X. S. Ye, "Label-free DNA biosensor based on cladding-etched thin core fibre modal interferometer ," *Proc. SPIE* 84215, pp. 1-5, 2012.
- [5] M. Yin, C. Wu, L. Shao, W. K. E. Chan, A. P. Zhang, C. Lu and H. Tam, "Label-free disposable fibre optic biosensors for DNA hybridization detection," *Analyst* vol. 138, pp. 1988-1994, 2013.
- [6] W. Yu, T. Lang, J. Bian and W. Kong, "Label-free fibre optic biosensor based on thin-core modal interferometer," *Sensors and Act. B*, vol. 228, pp. 322-329, 2016.
- [7] C. Y. Gao, S. Leporatt, S. Moya, E. Donath and H. Mohwald, "Swelling and shrinking of polyelectrolyte microcapsules in response to swelling changes in temperature and ionic strength," *Chemistry*, vol. 9, pp. 915-920, 2003.
- [8] A. L. Ghindilis, P. Atanasov, M. Wilkins and E. Wilkins, "Immunosensors: electrochemical sensing and other engineering approaches," *Biosens. Bioelectron.* vol. 13, pp. 113–131, 1998.
- [9] X. Chu, Lin ZH, Shen GL and Yu RQM, "Piezoelectric immunosensor for the detection of immunoglobulin M," *Analyst* vol. 120, pp. 2829–2832, 1995.
- [10] G. Gauglitz, "Opto-chemical and opto-immuno sensors," *Sensor update*, vol. 1, VCH, Weinheim, 1996.
- [11] A. V. Kabashin, P. Evans, S. Pastkovsky, W. Hendren, G. A. Wurtz, R. Atkinson, R. Pollard, V. A. Podolskiy and A. V. Zayats, "Plasmonic nanorod metamaterials for biosensing," *Nature Materials*, vol. 8, pp. 867- 871, 2009.
- [12] J. Dostalek, J. Čtyroký, J. Homola, E. Brynda, M. Skalský, P. Někviňová, J. Špírková, J. Škvor and J. Schröfel, "Surface plasmon resonance based on integrated optical waveguide," *Sens. and Actuator B Chem.* vol. 76(1-3), pp. 8-12, 2001.
- [13] R. D. Harris and J. S. Wilkinson, "Waveguide surface plasmon resonance sensors," *Biosens. Bioelectron.* vol. 29(1-3), pp. 1-3, 1995.

- [14] E. Kutter and A. Sulakvelidze, "Bacteriophages: Biology and Applications," *CRC Press*, Boca raton, FL, 2004.
- [15] S. Balasubramanian, I. B. Sorokulova, V. J. Vodyanoy, and A. L. Simonian, "Lytic phage as a specific and selective probe for detection of *Staphylococcus aureus* - A surface plasmon resonance spectroscopic study," *Biosens. Bioelectron.* vol. 22(6), pp. 948 - 955, 2007.
- [16] R. Edgar, M. McKinsty, J. Hwang, A. B. Oppenheim, R. A. Fekete, G. Giulian, C. Merrill, K. Nagashima, and S. Adhya, "High-sensitivity bacterial detection using biotin-tagged phage and quantum-dot nanocomplexes," *Proc. Natl. Acad. Sci. U.S.A.* vol. 103(13), pp. 4841 - 4845, 2006.
- [17] V. Nanduri, I. B. Sorokulova, A. M. Samoylov, A. L. Simonian, V. A. Petrenko and V. Vodyanoy, , "Phage as a molecular recognition element in biosensors immobilized by physical adsorption," *Biosens. Bioelectron.* vol. 22(6), pp. 986 - 992, 2007.
- [18] E. V. Olsen, I. B. Sorokulova, V. A. Petrenko, I. Chen, J. M. Barbaree and V. J. Vodyanoy, "Affinity-selected filamentous bacteriophage as a probe for acoustic wave biodetectors of *Salmonella typhimurium*," *Biosens. Bioelectron.* vol. 21(8), pp. 1434 - 1442, 2006.
- [19] L. Gervais, M. Gel, B. Allain, M. Tolba, L. Brovko, M. Zourob, R. Mandeville, M. Griffiths and S. Evoy, "Immobilization of biotinylated bacteriophages on biosensor surfaces," *Biosens. Bioelectron.* vol. 125(2), pp. 615 - 621, 2007.
- [20] Y. Shevchenko , N. U. Ahamad, A. Ianoul, and J. Albert, "In situ monitoring of the formation of nanoscale polyelectrolyte coatings on optical fibres using Surface Plasmon Resonances," *Opt. Express* vol. 18, pp. 20409–20421, 2010.
- [21] A. Singh, N. Glass, M. Tolba, L. Brovko, M. Griffiths and S. Evoy, "Immobilization of bacteriophages on gold surfaces for the specific capture of pathogens," *Biosens. Bioelectron.* vol. 24, pp. 3645 - 3651, 2009.
- [22] M. Smietana, W. J. Bock, P. Mikulic, A. Ng, R. Chinnappan and M. Zourob, "Detection of bacteria using bacteriophages as recognition elements immobilized on long-period fibre gratings," *Optical Express*, vol. 19(9), pp. 7971 - 7978, 2011.
- [23] S. M. Tripathi, W. J. Bock, P. Mikulic, R. Chinnappan, A. Ng, M. Tolba and M. Zourob, "Long period grating based biosensor for the detection of *Escherichia coli* bacteria," *Biosens. Bioelectron.* vol. 35, pp. 308-312, 2012.

Journal

1. **A. A. Badmos**, Q. Sun, Z. Sun, J. Zhang, Z. Yan, P. Lutsyk, A. Rozhin and L. Zhang, "Enzyme-functionalized thin-cladding long period fibre grating in transition mode at dispersion turning point for sugar level and glucose detection", *J. Biomed. Opt.* 22(2), 2017. (doi: 10.1117/1.JBO.22.2. 027003)
2. **A. A. Badmos**, P. Lutsyk, J. Zhang, Z. Sun, Lifeng Hang, Z. Yan, K. Zhou and L. Zhang, "Nanodeposition of ZnO on single-mode excessively tilted grating structures (Ex-TFGs) using discrete morphologies for enhanced refractive index sensing", (In press)..
3. Z. Sun, Z. Yan, K. Zhou, Q. Sun, **A. A. Badmos** and L. Zhang, "UV-inscribed optical fibre gratings in mid-IR range and their laser applications", *Journal of Electronic Science technol.* Vol 13(4), pp. 328-342, 2015.

Conference

4. **A. A. Badmos**, Q. Sun, Z. Sun, Z. Yan, and L. Zhang, "Near-infrared Enzyme-immobilized Dual-peak Long Period Fibre Grating (LPFG) as Sugar Concentration and Glucose Detection Biosensor", 2550682 Chemical and Gas Sensing 6th Asia Pacific Optical Sensors Conference (12 October, 2016).
5. **A. A. Badmos**, Qizhen Sun,, Zhijun Yan, Raz N Arif, Junxi Zhang, Alex Rozhin, Lin Zhang, "High Sensitivity Refractive Index Sensor based on Large-angle Tilted Fibre Grating with Carbon Nanotube Deposition", Proc. SPIE 9899, Optical Sensing and Detection IV, 989916 (29 April 2016); doi: 10.1117/12.2227703.
6. C. Wang, Z. Yan, Q. Sun, Z. Sun, C. Mou, J. Zhang, **A. A. Badmos** and L. Zhang, "Fibre Bragg gratings fabrication in four core fibres", Proc. SPIE 9886, Micro-Structured and Specialty Optical Fibres IV, 98860H (April 27, 2016); doi: 10.1117/12.2227040.